

# Photosensitive Polymer Semiconductors

E. L. Aleksandrova

*Ioffe Physicotechnical Institute, Russian Academy of Sciences, Politekhnikeskaya ul. 26, St. Petersburg, 194021 Russia*

Submitted January 19, 2004; accepted for publication February 20, 2004

**Abstract**—Models of photogeneration of charge carriers and structural regularities of the photoeffect are analyzed for homologous series of the main classes of photosensitive polymer semiconductors and their donor–acceptor complexes with different sensitizers. The relationship between the chemical structure of polymers and their photophysical properties is studied on the basis of an analysis of the effect of the energy and spatial structure of the monomeric unit of a polymer and the complex molecules on the spectra of the quantum yield of carrier photogeneration. The existence of general regularities of changes in the quantum yield with changes in the parameters of the molecular structure is ascertained for the main classes of polymer semiconductors and donor–acceptor complexes. Comparison of the experimental results with the calculations on the basis of the structure-sensitive model of Onsager photogeneration made it possible to estimate the initial distances and the degree of charge transfer in the excited state of complex molecules and relate the obtained values of the dipole moments to the hyperpolarizability in nonlinear optical media formed on the basis of these polymers and complexes. The ascertained structural regularities of the photophysical processes make it possible to predict the ultimate quantum yield of photoprocesses in polymer organic semiconductors and their molecular complexes, as well as the ultimate value of photosensitivity of recording media on their basis. © 2004 MAIK “Nauka/Interperiodica”.

## 1. INTRODUCTION

Photosensitive polymer semiconductors are characterized by the combination of photoconductive properties (revealed for polymers at the end of the 1960s [1]) with thermal stability, mechanical, and other specific properties of polymers (in particular, the possibility of obtaining high resolution due to the features of their molecular structure). Hence, these semiconductors are promising candidates for optical recording media [1–5]. Polymer photoconductors have a number of technically important properties: optical transparency, film-forming ability, flexibility, and thermoplasticity. In addition, they are fairly conventional for preparation of layers at low cost. The attractive possibility of synthesizing new photoconductive polymers with specified properties also led to intense investigations that began in the early 1970s. Photosensitive polymer semiconductors are now more and more widely used as recording media of various types.

Photosensitive polymers were used previously in electrophotographic and photothermoplastic media and liquid crystals (LCs), which are applicable for photographic and holographic information recording. However, their application was limited due to their low competitiveness as compared with inorganic semiconductors.

Presently, along with these (conventional) applications, photosensitive polymers became indispensable in fabrication of photovoltaic elements for solar energy converters [6, 7]. In 1993, it was found that polymers have photorefractive properties caused by photopolarization of their molecules [8]. Since that time, on the basis of studying the nonlinear optical properties of polymers (generation of the second and third harmon-

ics and photorefraction) and processes of photopolarization of their molecules and photopolymerization of compositions, materials for laser media have been developed, as well as molecular media exhibiting photopolarization, photorefraction, and photopolymerization effects for static and dynamic holography.

Data recording using the noted classes of molecular media is based on photophysical processes in an electric field due to the photopolarization or internal photoeffect (the carrier photogeneration). These processes lead to the modulation of the refractive index (LCs and media with photorefraction, photopolarization, and photopolymerization) and the surface charge or potential (electrophotographic and photothermoplastic media). In photothermoplastic media, the charge modulation results in the modulation of thickness due to the thermoplasticity.

The noted fields of application of photosensitive polymers are related to the features of intermolecular interaction in these media and the possibility of forming donor–acceptor ( $D-A$ ) charge-transfer complexes (CTCs) in them. It is the complex-forming ability and the efficient charge transfer in complex molecules that lead to their polarization under illumination (and, therefore, photopolarization of a medium) and also to the specific features of photovoltaic and nonlinear optical properties related to the photopolarization.

The determination of the mechanism of electron transfer in CTC molecules is necessary for understanding the nature of biochemical processes: the electron transfer in photosynthesis in green leaves of plants containing chlorophyll and in protohemes entering the composition of enzymes and the electron (energy)

transfer in cell mitochondria and chromoproteids of blood (mioglobins and hemoglobins), whose structure is similar to that of photosensitive molecules of complexes of quinones with porphyrins (polyconjugated macrocycles formed of four five-member pyrrole rings) and their derivatives—phthalocyanines [9]. Aggregates of chlorophyll molecules form antennas absorbing solar photons and efficiently directing the light-induced excitons to the reaction centers where the light energy is transformed into the chemical energy of redox reactions [10]. The electron transfer in cells of living organisms lies in the basis of a modern method of cancer treatment. This method is based on the destruction of cancer cells under the action of active (singlet) oxygen, which is formed as a result of photochemical reactions in a cell involving a photosensitizer absorbing red light, which penetrates easily through tissues.

However, neither mechanisms of charge transfer nor the nature of primary photophysical processes in organic materials is clear. The specific features of molecular media—weak intermolecular interaction (and, in the presence of CTC molecules,  $D-A$  interaction in these molecules, which dominates over the intermolecular interaction)—lead to significant differences in the physical processes occurring in such media (both polymers and molecular crystals) from those in inorganic semiconductors. Therefore, at present, many questions concerning the charge transfer and the photogeneration of charge carriers with their subsequent transfer remain open for organic materials.

Most information on the photoprocesses occurring in molecules as a result of light absorption can be obtained by measuring the photosensitivity and the quantum yield of carrier photogeneration  $\eta$  (which determines the photosensitivity) in strong electric fields (the so-called electrophotographic mode [1]). The use of this mode, along with the determination of  $\eta$ , makes it possible to study the mechanism of carrier photogeneration and relate the physical characteristics of photogeneration to the parameters of chemical structure of molecules of photosensitive media [11–13]. Since the stage of carrier photogeneration in polymer semiconductors is preceded by electron transfer in a molecule absorbing light, the determination of the degree of the charge transfer  $\delta$  from the value of  $\eta$  makes it possible to estimate another important characteristic of molecules of photosensitive media: the dipole moment  $\mu_e$ , which is related to  $\delta$ . The value of this parameter is of interest not only for preparation of photosensitive media, such as electrophotographic and photothermoplastic media and LCs, but also for estimation of the polarizability of molecules in polymers with photopolarization and photopolymerization properties, which are used in holography and laser applications.

Thus, the methods of attaining high quantum yields of photophysical processes (in particular, the carrier photogeneration [12, 13]) and fabricating high-resolution molecular media with high photosensitivity  $S \propto \alpha\eta$

( $\alpha$  is the absorption coefficient) in the visible spectral range [14] based on these processes, developed for electrophotographic recording media, can be used not only in fabrication of electrophotographic and photothermoplastic media and LCs. They can also be used for a deliberate choice and synthesis of materials with CTC components for solar energy converters and photorefractive and photopolymerizing compositions, as well as for estimation of polarizability and dipole moments of photosensitive molecules. Knowledge of the mechanisms of the processes related to photogeneration—luminescence and carrier transport through a molecular medium—will allow one to design new electroluminescent devices based on organic semiconductors.

Traditionally, the development of photosensitive polymer materials ran in two directions [1, 10]: synthesis of polymers with a polyconjugated system and fabrication of systems based on the formation of CTCs in polymers. CTCs can either exist in polymers in the form of a monomeric unit or be formed by introducing low-molecular substances into polymers (the interaction of such substances with a polymer leads to both the increase in its photosensitivity and the extension of the spectral range of absorption and sensitivity, i.e., to the sensitization of the photoeffect (photoconduction) [1]. The following substances can be used for this purpose: dyes, which form centers of photoactive absorption in the visible or infrared (IR) spectral region in a polymer (the spectral sensitization of photoeffect), and acceptor or donor impurities (depending on the electronic properties of a polymer), which lead to the occurrence of one or several absorption bands due to the  $D-A$  interaction with aromatic fragments of the polymer (the structural chemical sensitization). It has been shown recently that, along with the two noted directions in the synthesis of photosensitive polymers, photoconductive properties can be obtained by forming supramolecular structures in a polymer due to hydrogen bonds [15] (it is the conjugation in these structures that is responsible for the photosensitivity [16]). However, the mechanism of photogeneration in polymer media containing CTC molecules remains unclear, and questions of practical interest about the relationship between the magnitude and spectrum of the quantum yield and the polymer structure and about the ultimate characteristics (in particular, photosensitivity) of molecular recording media on the basis of these polymers are still open. The solution of this problem encounters significant difficulties not only due to the low photosensitivity of polymer systems but also because there are a limited number of film-forming substances appropriate for fabrication of thin photoconductive films. Therefore, the photosensitive properties of polymer  $D-A$  complexes have been studied in more detail [1–3] because they are the most numerous and their structure can be easily varied.

In this study, analysis of existing models of carrier photogeneration in molecular media is performed and an attempt is made to relate the mechanism controlling the quantum yield of photogeneration (the internal pho-

toeffect) to the medium structure and to study the possibility of increasing the quantum yield by sensitizing the internal photoeffect. From this point of view, we consider the intrinsic photosensitivity of polymers with saturated and conjugated bonds and their sensitization (of structural, spectral, and injection types) by forming CTCs of different structure in them, including organometallic complexes and complexes formed at the interface between the photogeneration and transport layers in electrophotographic recording media. Analysis of the structural regularities of photosensitive properties of polymers was performed using the data in the literature referring to the most photosensitive electrophotographic recording media and the results of our studies of the quantum yields of photoprocesses in molecular complexes used in electrophotographic and photothermoplastic recording media, which were performed at the Vavilov State Optical Institute at the laboratory of Prof. Yu.A. Cherkasov.

### 1.1. Specific Features of Molecular Media and Photophysical Processes in These Media

Molecular media (both organic crystals and polymers and CTC-containing films) are solid-state systems formed due to intermolecular interaction. The intramolecular structure of covalently bonded atoms in a molecule (crystal) or the structure of CTCs formed due to the  $D-A$  interaction (in solid solutions of polymer complexes) remains almost unchanged when a solid is formed. Depending on the electronic structure of a molecule and the parameters related to the molecular structure (polarizability, dipole moments,  $D-A$  properties), the energy of intermolecular interaction may vary over a wide range: from  $10^{-3}$  eV (van der Waals interaction) to several eV ( $D-A$  bonds) [17].

### 1.2. Specific Features of Molecular Media Containing $D-A$ Complexes

The formation of a complex is related to intermolecular interactions of various types: van der Waals, Coulomb, dipole-dipole, polarization, induction, and others. A complex can be formed when the distance between the donor and acceptor molecules is small ( $\sim 0.35$  nm [18]) and they are oriented in such a way as to provide the most efficient overlap of their orbitals, which leads to the formation of a  $D-A$  or CTC complex. This process is related to the redistribution of the electron density due to the electron transfer from the highest occupied molecular orbital of the donor to the lowest unoccupied molecular orbital of the acceptor [18–22]. Depending on the state (ground or excited) of the complex in which partial or total charge transfer occurs, complexes are distinguished as strong (ion-radical salts), weak, and contact ones.

The quantum-chemical theory of  $D-A$  interaction (the main type of intermolecular interaction in binary compounds composed of two types of molecules with

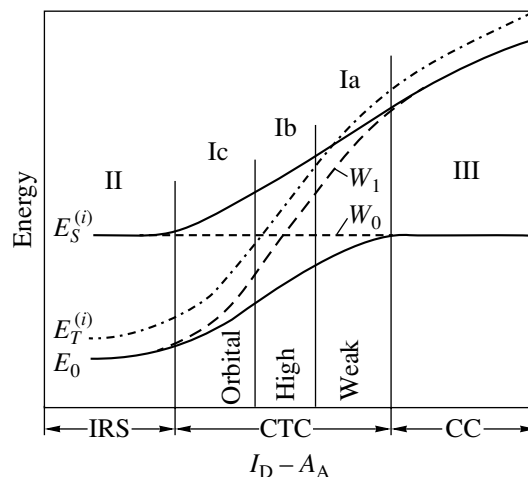


**Fig. 1.** Energy diagram for  $D-A$  complexes of different types [18]: CTC—complexes with charge transfer, IRS—ion-radical salts, and CC—contact complexes;  $E_0$  is the ground level,  $E_S^{(i)}$  is the singlet excited state,  $E_T^{(i)}$  is the triplet level,  $W_0$  is the state of the nonpolar CTC component (DA),  $W_1$  is the state of the polar CTC component ( $D^+A^-$ ),  $I_D$  is the ionization potential of the donor molecule, and  $A_A$  is the electron affinity of the acceptor molecule.

donor or acceptor properties) was developed by Mulliken in 1952 [23]. According to this theory, the  $D-A$  interaction arises due to the quantum-mechanical mixing of two states: nonpolar (DA), in which only van der Waals interaction occurs between donor and acceptor molecules, and polar ( $D^+A^-$ ), in which an electron is transferred from the donor to the acceptor. The average energy of the  $D-A$  interaction,  $W_{DA}$ , is determined by the resonance integral of the polar and nonpolar components, while the mixed state actually describes the dipole  $D^{+\delta}A^{-\delta}$ , where  $0 \leq \delta \leq 1$  is the degree of charge transfer. With respect to the energy, which is in the range from 0.05 to 1.0 eV, the intermolecular  $D-A$  interaction (in a complex) is intermediate between covalent interaction (several eV), on the one hand, and hydrogen (0.05–0.5 eV) and van der Waals ( $10^{-4}$ – $10^{-1}$  eV) interactions, on the other hand [17].

The generalized energy band diagram of  $D-A$  systems of different types is shown in Fig. 1. The above classification of molecular complexes is based on this diagram and the difference in the ionization energy of donor molecules and the electron affinity of acceptor molecules,  $I_D - A_A$ . For weak CTCs, which are mainly discussed here, the energy  $W_1$  of the state of the polar component  $D^+A^-$  significantly exceeds the energy  $W_0$  of the nonpolar state DA:  $W_1 \gg W_0$  [17]. Polar states can be occupied under photoexcitation as a result of optical transitions with charge transfer.

Since recording media containing molecular complexes are solid solutions of these molecules in polymers (in thermoplastic matrices in the case of photo-

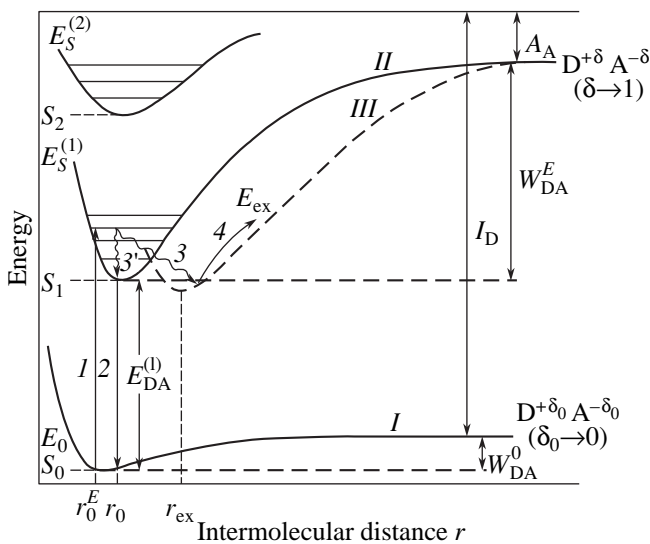


**Fig. 2.** Energy diagram for different  $D-A$  complexes, depending on the intermolecular distance  $r$ :  $E_0$  (curve I) is the energy of the ground state  $S_0$ ;  $E_S^{(1)}$  (curve II) and  $E_S^{(2)}$  are the energies of the first and second excited states,  $S_1$  and  $S_2$ , respectively; and  $E_{ex}$  (curve III) is the energy of the exciplex state.  $r_0^E$ ,  $r_0$ , and  $r_{ex}$  are the charge-transfer distances in a complex before the relaxation of vibrational energy, after the relaxation, and after the exciplex formation, respectively.  $W_{DA}^0$  and  $W_{DA}^E$  are the energies of the  $D-A$  interaction in the ground ( $\delta = \delta_0 \rightarrow 0$ ) and excited ( $\delta \rightarrow 1$ ) states. Transitions 1–4 are clarified in Subsection 1.3.2.

thermoplastic media), their plasticization results in another important feature of the media under consideration—low concentration of CTC molecules (lower than 5%) [1–3], which excludes their interaction with each other.

Thus, films with  $D-A$  complexes regarded as molecular solids are characterized by strong intramolecular ( $\sim 1$  eV [17, 24]) and weak ( $10^{-3}$ – $4 \times 10^{-2}$  eV [17]) interaction between complex molecules. Therefore, when complexes are formed, molecules retain their individuality, their energy structure changes insignificantly (Figs. 2, 3a, 3b) (the bandwidths are  $\sim 0.2$  eV [24]), and the optical and electric properties of the solid formed are controlled by the properties of the molecules and their complexes. The optical absorption shows molecular features and its spectrum is related to the energy structure of the complex molecules. Redistribution of the electron density upon formation of a complex leads to the formation of new bands in the absorption spectrum due to the charge transfer. The energies of these bands are determined by the equality [17]

$$\hbar\omega_{CT} = E_S^{(i)} - E_0 = I_D - A_A + R_E - E_0 - E_C + R_N, \quad (1)$$

where  $E_0$  and  $E_S^{(i)}$  are the energies of the ground and excited ( $i$ th) states of a CTC (Fig. 2 shows the energy of

the van der Waals interaction (curve I));  $I_D$  and  $A_A$  are the ionization potential of the donor molecule and the electron affinity of the acceptor molecule, respectively;  $E_C$  is the Coulomb energy, which stabilizes the complex in the excited states (see Fig. 2, curves II, III);  $R_E$  is the energy of destabilization of the excited complex due to the exchange polarization (resonance) interaction; and  $R_N$  is the charge-transfer energy, which stabilizes the complex. The energies  $R_E$  and  $R_N$  characterize the contribution of the  $D-A$  interaction in the excited and ground states, respectively, and their difference  $R_E - R_N$  is the change in the energy of the  $D-A$  interaction upon photoexcitation  $\Delta W_{DA} = W_{DA}^E - W_{DA}^0 \approx 1$  eV (Fig. 2). This value exceeds the energy of intermolecular interaction by more than two orders of magnitude [17], which ensures weak interaction between CTC molecules in a solid.

### 1.3. Specific Features of the Mechanism of Carrier Photogeneration

Weak intermolecular interaction in molecular solids leads to the pronounced localization of charge carriers at individual molecules (the localization time  $\tau_{loc} = 10^{-12}$ – $10^{-14}$  s [17]). This circumstance results in the electron lattice polarization by charge carriers (the polarization time  $\tau_{pol} = 10^{-16}$ – $10^{-15}$  s [5]) and controls the time of carrier hopping between neighboring localized states (the hopping time  $\tau_{hop} = 10^{-12}$  s [17]). As can be seen,  $\tau_{hop} > \tau_{lok} > \tau_{pol}$  and the carrier transport is described by incoherent hops between localized states [25–29]. The phenomenological model of hopping mobility is based on the following formula, which describes the rate of hops between two hopping centers with a difference in the electron binding energies  $\Delta_{ij}E$  located at a distance  $r_{ij}$  from each other [30]:

$$\Gamma_{ij} = \Gamma_0 \exp[-2\gamma r_{ij} - (\Delta_{ij}E/kT)\Theta(\Delta_{ij}E)], \quad (2)$$

where  $\gamma$  is the damping constant of the wave function of a localized electron, which is assumed to be spherically symmetric, and  $\Theta(x)$  is a unit step function [31, 32]. Obviously, if the spatial location of hopping centers and the type of distribution of the binding energies are specified, we deal with the random walk problem for an electron in a spatial lattice of nonisoenergetic centers. This problem is known in the literature as the  $r-E$  percolation problem. The first attempt to solve it was made in 1975 [26]. BäSSLER *et al.* [33–35] reduced the general  $r-E$  percolation problem to a problem for a regular (cubic) lattice. Later, this problem was solved using the Monte Carlo method [36].

The carrier-transport stage and the absorption of photons by complex molecules are generally described using the concept of charge-transfer states—excited neutral states of complexes (Fig. 3c), in which (in contrast to excitons, where an electron and a hole are localized at the same molecule and the distance between them is independent of time) an excited electron passes

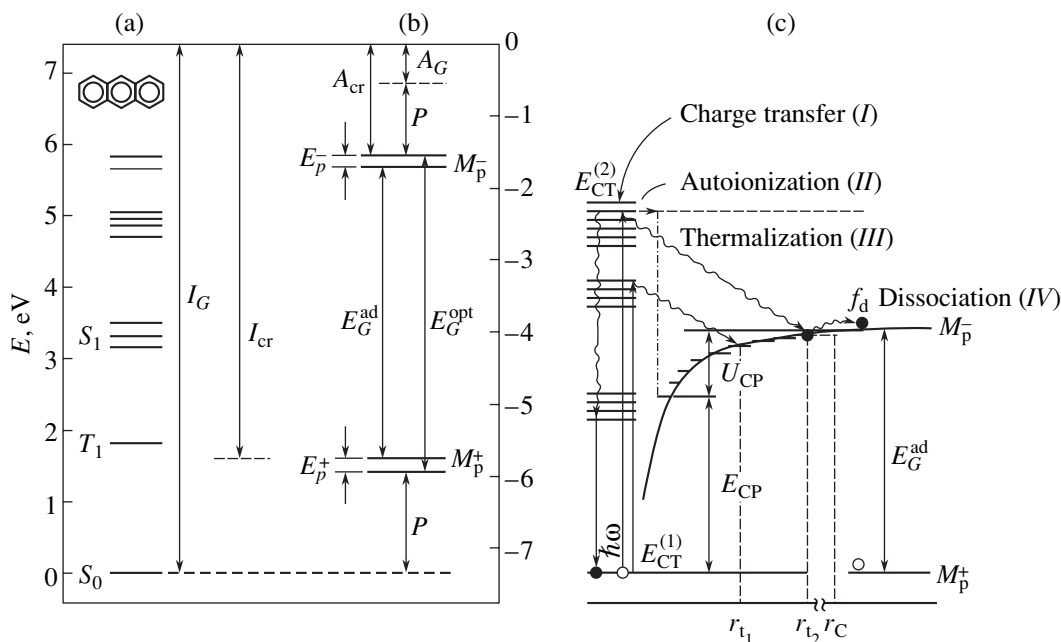


**Fig. 3.** Energy diagrams of the ionized states of (a) a molecule and (b) a molecular crystal and (c) the main stages of photogeneration in crystals using anthracene as an example.  $E_G^{opt}$  and  $E_G^{ad}$  are the optical and adiabatic energy gaps;  $E_p^+$  and  $E_p^-$  are the energies of formation of positive and negative polarons, respectively;  $P$  is the energy of electronic polarization;  $I_G$  and  $I_{cr}$  are the ionization potentials of the molecule and molecular crystal, respectively;  $A_G$  and  $A_{cr}$  are the electron affinities of the molecule and molecular crystal respectively;  $M_p^+$  and  $M_p^-$  are the levels of conductivity of molecular polarons;  $S_1$  and  $T_1$  are the singlet and triplet states of the molecule, respectively;  $r_{t_1}$  and  $r_{t_2}$  are the thermalization lengths of two possible states of a relaxed bound charge pair with the energies  $E_{CP}$  and  $U_{CP}$ ;  $E_{CT}^{(1)}$  and  $E_{CT}^{(2)}$  are the energies of the CT states; and  $r_C$  is the Coulomb radius of a bound pair. Other designations are clarified in Subsection 1.3.

to the nearest or the next nearest molecule but remains bonded to a hole by Coulomb forces [37–39]. The energies  $E_{CT}^{(i)}$  and  $E_{CP}$  of these nonconducting ionic states lie below the conduction band (Fig. 3c). When a molecule of a solid absorbs a photon, either autoionization occurs (Franck–Condon transition from the ground state to an excited state) [17] or direct excitation of the CT state [38–40], due to which a Coulomb pair is formed (the so-called charge-pair (CP) state). As a result, free charge carriers may arise (Fig. 3c).

Thus, the specific features of molecular media are related to the weak intermolecular interaction in them, leading to (i) the molecular character of light absorption and subsequent carrier photogeneration through the CP state with a quantum yield less than 1 and (ii) localization of charge carriers and their low mobility (in comparison with semiconductors, where the mobility  $\mu$  is not lower than  $1 \text{ cm}^2/(\text{V s})$ ). The weak intermolecular interaction and strong localization of charge carriers at individual molecules in a molecular solid cause carrier photogeneration through the CP state formed as a result of molecular absorption of a photon with possible direct excitation of CT states.

**1.3.1. Mathematical models of carrier photogeneration occurring through the CP state.** The carrier photogeneration in media with weak intermolecular interaction occurs through the CP state of a Coulomb pair of carriers of opposite sign [1, 17, 41–43]. The separation of such a pair of charges in an external electric field  $\mathcal{E}$  includes two stages: thermalization of a bound charge carrier and field-assisted thermal dissociation of the pair. The first (pre-Onsager) stage, in which the bound charge carrier (electron) loses the excess kinetic energy acquired from a photon and comes to equilibrium with phonons at a certain distance between the charges (the so-called thermalization length  $r_t$ ), is characterized by the quantum yield of formation of bound pairs  $\eta_0$ . The stage of field-assisted thermal dissociation, which consists in separation (facilitated by the external electric field) of thermalized bound pairs due to the interaction with phonons, is described by the dissociation probability  $f_d(r, \theta, \mathcal{E})$ . Hence [17],

$$\eta = \eta_0 f_d(r, \theta, \mathcal{E}) g(r, \theta) dr^3, \quad (3)$$

where  $g(r, \theta)$  is the function describing the distribution of pairs over their radii  $r$  and orientation with respect to the direction of the field  $\mathcal{E}$  and  $\theta$  is the angle between

the vectors  $\mathbf{r}$  and  $\mathcal{E}$ . At  $r_i < 10$  nm,  $g(r, \theta) = \delta(r - r_i)$  [34] and expression (3) takes the form

$$\eta = \eta_0 f_d(r_i, \mathcal{E}). \quad (4)$$

Since the separation of a bound pair of carriers in the field  $\mathcal{E}$  has a diffusion–drift character in the second stage, it can generally be described by the three-dimensional (3D) Smoluchowski equation [44]. This equation makes it possible to determine the space–time probability density, which is equal to the probability of mutual field-assisted thermal dissociation of charges bound by Coulomb forces  $f_d(r_i, \mathcal{E})$  having a constant microscopic mobility independent of time. The general solution of this equation can be reduced to an analytical form only in two cases: at  $\mathcal{E} = 0$  [17] and in a steady-state case [45].

In the steady-state case of an isotropic system of noninteracting pairs that are in equilibrium with a medium that has a constant permittivity and is maintained at a constant temperature  $T$ , the dissociation probability  $f_d(r_i, \mathcal{E})$  for a pair of charges located at a distance  $r_i$  from each other ( $r_i$  is independent of the field  $\mathcal{E}$ , temperature  $T$ , and the energy of photons) is determined by the 3D Onsager model [46, 47]

$$f_d = \left(1 - \frac{kT}{e\mathcal{E}r_i}\right) \sum_j \frac{e\mathcal{E}r_C}{kT} I_j\left(\frac{e^2}{\epsilon r_i kT}\right), \quad (5)$$

where  $e$  is the elementary charge,  $k$  is the Boltzmann constant,  $\epsilon$  is the permittivity,

$$I_j(x) = I_{j-1}(x) - \frac{x^j}{j!e^x}, \quad j > 1,$$

$$I_0(x) = 1 - e^{-x}.$$

For constant  $\mathcal{E}$  and  $T$ , expression (5) can be written as

$$f_d(r_i, \mathcal{E}) \propto \exp[1 - \exp(r_i/r_C)]. \quad (6)$$

The condition for the absence of pair–pair interaction is satisfied at distances between pairs significantly exceeding their radii  $r$ .

To remove the limitations of the classical Onsager model [46], a number of modifications were proposed: (i) the one-dimensional model [17] describing processes in linear systems; (ii) the ballistic model [42, 43, 48, 49], which takes into account the drift of bound carriers during their thermalization (at  $r_i > 5$  nm); (iii) the model of transient photogeneration [43, 50], which describes the probability kinetics  $f_d(r_i, \mathcal{E})$  at times  $t < 10^{-8}$  s; (iv) the model proposed by Mozumder [51], which yields the dependence of  $f_d(r_i, \mathcal{E})$  on the concentration of bound pairs; and (v) the model of optical transitions proposed by Bässler [38–40].

For anisotropic media, more general (as compared to the Onsager model) approaches were proposed by Scher and Racovsky [52] and Ries [53, 54]. These models assume the hopping character of separation of charge carriers in a pair and are based on the probabili-

ties of this process calculated by Monte Carlo methods [36, 37]. They make it possible to determine the range of validity of the isotropic Onsager model: according to these approaches, it is valid at  $r_i > 1$  nm and  $T > 200$  K [53].

The probability  $f_d(\mathcal{E})$  can also be calculated by the Pool–Frenkel model [55], which describes the probability of a mobile charge carrier (with a mobility exceeding  $1 \text{ cm}^2/(\text{V s})$ ) escaping from a Coulomb center under the assumption that the external electric field  $\mathcal{E}$  affects the activation energy of this process and reduces the height of the potential barrier by  $\sim \mathcal{E}^{0.5}$ . However, this model and its modifications require use of the band model, which is inadequate for molecular semiconductors [17].

Thus, among the aforementioned mathematical models of photogeneration through the CP state, the Onsager model most adequately describes the physical mechanism of this process for thermalized pairs. However, since this model does not describe the initial (pre-Onsager) stage, it does not allow one to take into account the photoexcitation and the effect of the  $D$ – $A$  interaction in the thermalization stage or find the dependence of  $\eta$  on the photon energy and the structure of the complex molecules. Therefore, a model should be developed that would describe the initial stage of photogeneration and take into account the features of the CTC structure.

**1.3.2. Physical models of photogeneration.** Different physical models of photogeneration consider different processes leading to the separation of pairs at the distance  $r_i$ . In hopping models [28, 56, 57], this process is a hop of a carrier from a complex molecule in an excited state to the neighboring intermediate state. In the dissociation–hopping model [58, 59], these are hops by localized states with the dissociation according to the Pool–Frenkel mechanism [55]. The dissociation models of Onsager photogeneration [38–40, 42, 43, 60–71] differ in the predissociation stages, depending on the medium structure, i.e., the character of the energy relaxation after photoexcitation.

Three models have been developed for molecular crystals (homomolecular media): the model of optical transitions [38–40], the ballistic model [42], and the excimer model [60]. For polyvinylcarbazole, it was shown that, in the range of singlet absorption bands, the quantum yield increases stepwise with increasing the radiation energy  $\hbar\omega$ , so that  $\eta$  and  $r_i$  remain constant within each band. For polyacene crystals, near the absorption threshold,  $\eta$  increases from  $10^{-3}$  to 0.5 with increasing number of aromatic rings [17, 72, 73]. Photogeneration in molecular crystals occurs via the CT states formed upon absorption of a photon (see Fig. 3c, transition  $I$ ) due to the excess vibrational energy of  $\sim 0.3$ – $0.4$  eV [17]. This energy is spent (transition  $III$ ) on the interaction with lattice phonons during 80–100 collisions at the distance  $r_i(T) = 6$ – $10$  nm (which depends on the field strength) [17]. As a result, a pair in the CP state with a thermalization length  $r_i$  is formed, which,

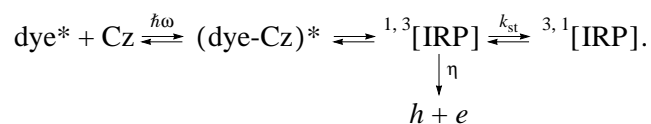


absorbing additional energy from the environment, can generate free charge carriers (Fig. 3c, transition IV). In the model considered,  $\eta$  and  $r_t$  depend on the photon energy [17, 43]. At higher energies, autoionization may occur (transition II).

For molecular media based on *D*–*A* complexes, along with the hopping [56] and dissociation–hopping [58] models, the exciplex [61–68] (for the case of structural chemical sensitization of the photoeffect) and ion–radical [69–71] (for spectral sensitization by dyes) models have been developed.

According to the exciplex model, photogeneration occurs as a result of the field-assisted thermal dissociation (Fig. 2, transition 4) of the unrelaxed state of the  $\text{Cz}^+-(\text{D}^+\text{A}^-)^{**}$  exciplex (Fig. 2, curve III) formed upon absorption of a photon (Fig. 2, transition I) by a donor molecule (the carbazolyl fragment Cz of polyvinylcarbazole) [65–67] or an acceptor molecule (both the donor and acceptor molecules are intramolecular CTCs (curve II) and subsequent thermalization of an electron (transition 3) [74, 75]. In this model, the thermalization length  $r_t = 2\text{--}3$  nm; it can be independent of  $\mathcal{E}$  and  $\hbar\omega$  in the absorption band due to the fast intramolecular relaxation (transition 3') of the molecule absorbing a photon.

In the case of spectral sensitization of the photoeffect, photogeneration occurs from the  $^1,^3[\text{IRP}]$  states of a bound ion–radical pair arising from the exciplex state of the dye molecule dye\* absorbing a photon and a carbazolyl group of the polymer Cz. The  $^1,^3[\text{IRP}]$  state formed from the (dye–Cz)\* state dissociates into free carriers. The  $^3,^1[\text{IRP}]$  state arising as a result of singlet–triplet conversion with a constant  $k_{st}$ , which depends on the magnetic field [75], gives neutral products [76]:



The above physical models of the photogeneration in molecular media based on CTCs do not yield dependences relating the magnitude and spectrum of  $\eta$  to the structure of CTC molecules, although such attempts were made in many studies. However, the attempts to relate the parameters of photophysical processes occurring after absorption of a photon by a molecule to the parameters of the chemical structure of complex molecules were successful for CTC-containing molecular media. In contrast to molecular crystals with a regular structure, for which a correlation with the band gap width was found [17], the class of CTC-containing media is wider and series of regularly changing structures of complexes can be chosen in it. From this point of view, the most promising are the media in which the CTC concentration is low and, therefore, CTC molecules retain their individuality. In addition, since the transport of photogenerated charge carriers in such media is performed by incoherent hops between localized states, the determination of the relationship

between the photogeneration and structural parameters requires such methods for measuring  $\eta$  that would allow one to take into account or exclude the effect of the transport stage on the measurable values. Therefore, an original method for measuring  $\eta$  was developed, which made it possible to relate the photogeneration parameters to the structure of organic semiconductors.

## 2. METHODS AND OBJECTS OF STUDY

### 2.1. Technique of Study

The technique of study included

(i) experimental method for determining the quantum yield  $\eta$  in strong electric fields (in the electrophotographic mode) and calculation of the photogeneration parameters;

(ii) choice of the objects of study as homologous series of both polymers themselves and *D*–*A* complexes formed by polymers.

**2.1.1. Electrophotographic method for determining the quantum yield of carrier photogeneration.** The quantum yield is the ratio of the number of molecules involved in a photochemical or photophysical process (in the case under consideration, the photophysical process of carrier photogeneration) to the number of absorbed photons.

The photogeneration quantum yield was measured for layers with a free charged surface in the electrophotographic mode by the technique reported in [1, 9]. As is well known [1], the electrophotographic method is based on the possibility of forming a double electric layer in a material under the action of an electrostatic field with subsequent localization of the modulation of its power (the product of the surface-charge density and the layer thickness) due to the photoconduction. The drift of light-generated charge carriers leads to the neutralization of the surface charge or to the decrease in the thickness of the double electric layer. According to the technique proposed in [1],  $\eta$  was determined from the slope of the photovoltage decay characteristic  $V(t)$  ( $V$  is the double-layer potential,  $t$  is time) at the initial instant of time as

$$\eta \propto \frac{\varepsilon \hbar \omega}{I \alpha d} \left( \frac{dV}{dt} \right)_{t=0}, \quad (7)$$

where  $\hbar\omega$  is the photon energy,  $d$  is the layer thickness,  $I$  is the energy illuminance,  $\alpha$  is the absorption coefficient, and  $\varepsilon$  is the permittivity of the layer. Formula (7) is valid at small variations in the layer potential.

The quantum yield  $\eta$  was measured at the electric field strength  $\mathcal{E} = 10^5\text{--}10^6$  V/cm by the “photogeneration-wedge” method [77], which makes it possible to monitor the conditions of complete collection of photogenerated charge carriers as a result of their transport through the layer. The relative error  $\Delta\eta/\eta$  of absolute and relative (at the given energy of photons) measurements was 40 and 15%, respectively. The injection effi-

ciency  $\eta_{inj}$  (which is equal to the number of charge carriers generated in the injection layer (Se or CdSe) and passed through the interface to the transport layer) was determined similarly for two-layer injection structures (in the electrophotographic mode).

**2.1.2. Technique for determining the photogeneration parameters.** The photogeneration parameters (the quantum yield of formation of bound pairs  $\eta_0$  and the thermalization length  $r_t$ ), which enter expression (3), are determined, according to [3], from the experimental values of  $\eta$  and its field dependences. The value of  $r_t$  was determined by comparing the slopes of the experimental and calculated (by formulas (3)–(5)) field dependences  $\eta(\mathcal{E})$ . The quantum yield of formation of bound pairs  $\eta_0$  was found, according to (4), from the value of  $f_d$  calculated for the thermalization lengths  $r_t$  determined by the above-described method.

The mechanism of photogeneration and possible ways of transformation of absorbed photon energy were studied by simultaneous photogeneration and luminescence measurements [1, 78]. The luminescence spectra were measured in the range 300–1200 nm at temperatures  $T = 4.2$ –300 K with the time resolution  $t_p = 2 \times 10^{-8}$ –10 s. The excitation of luminescence of complexes was performed in the absorption range of both complexes and their components by radiation of argon (337.1 nm), He–Cd (441.6 nm), and He–Ne (632.8 nm) lasers.

## 2.2. Objects of Study—Series with Systematically Varied Structure

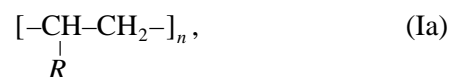
As was noted above, a polymer can have photosensitive properties only when either a conjugation system is present in its structure or  $D$ – $A$  complexes can be formed in it by introducing low-molecular impurities.

**2.2.1. Polymers.** Investigation of the behavior of changes in the intrinsic (i.e., with no sensitizing impurities introduced) photoconductivity of polymers of the vinyl series  $[-CRH-CH_2-]_n$  of different structures, for which the phenomenon of photoconduction in the UV spectral region [1] was found first, showed that, in order to increase  $\eta$ , it is expedient to synthesize polymers using the following procedures: (i) provide conjugation in the main chain by introducing double bonds or aromatic rings and (ii) choose fragments  $R$  in the lateral chain with low ionization potentials  $I_D$  (low values of  $I_D$  can be attained by increasing the  $\pi$  conjugation in aromatic systems (naphthalene, anthracene, phenanthrene) and introducing N, O, S, or Se heteroatoms with formation of carbazole, triphenylamine, oxazole, thiazole, and other heterocycles and their derivatives). The presence of fragments with low  $I_D$  leads, along with the increase in  $\eta$ , to the red shift of the absorption edge [1, 18], which makes it possible to extend the range of intrinsic photosensitivity of a polymer not only to the UV range but also to the visible range. Monomers and their aromatic fragments were chosen for synthesis of

photosensitive polymers in accordance with the above considerations. The most promising was the search for structures characterized by both large values of  $\eta$  and a wide photosensitivity range. The classes of photosensitive polymers with such structures obtained to date are listed in Table 1. Their range of intrinsic absorption is extended to 2.0–2.5 eV (while the initial range was 4–7 eV) [1]. The classes of  $\pi$ -conjugated polymers listed in Table 1 can be classified as either containing or not containing heteroatoms, in particular, nitrogen atoms, which play an important role in the complex formation.

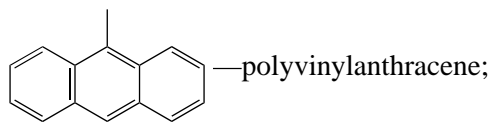
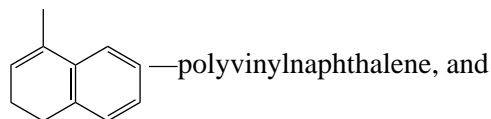
The following polymers containing no nitrogen atoms belong to the class of  $\pi$ -conjugated polymers:

(i) vinyl polymers with single bonds (the so-called polyene structure [1]) in the main chain (Table 1, series 1.1) with the general formula



where  $R = -\text{H}$ —polyethylene,

$-\text{C}_6\text{H}_5$ —polystyrene,



(ii) polymers with multiple (double) bonds (the so-called polyene structure [1]) in the main chain (Table 1, series 1.2) with the general formula



where  $R_1 = R_2 = -\text{H}$ —polyacetylene,

$R_1 = -\text{H}$  and  $R_2 = -\text{C}_6\text{H}_5$ —polyphenylacetylene, and

$R_1 = R_2 = -\text{C}_6\text{H}_5$ —polydiphenylacetylene;

(iii) polymers with the bonds



(the so-called polyschiff bases) [1]—polyphenylenes (Table 1, series 1.3):

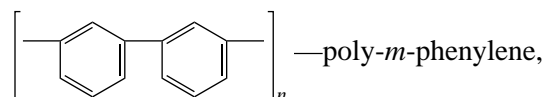
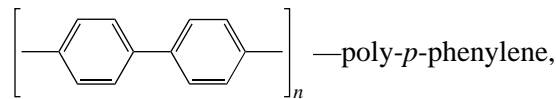


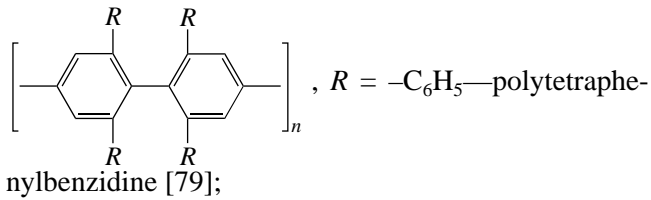


**Table 1.** Ionization potentials  $I_D$ , energies of optical and adiabatic gaps  $E_G^{\text{opt}}$  and  $E_G^{\text{ad}}$ , photoconductivities  $i_{\text{ph}}$ , quantum yields of photogeneration of free charge carriers  $\eta$ , and carrier mobilities for different classes of photosensitive polymers

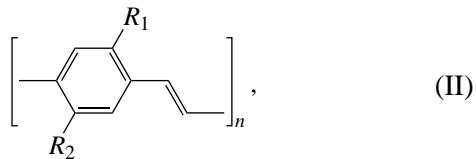
Structure of molecular chains	Polymers without nitrogen atoms								
	Series	Polymer	$E_G^{\text{opt}}$ , eV	$E_G^{\text{ad}}$ , eV	$\eta$	$i_{\text{ph}}$ , $\Omega^{-1} \text{cm}^{-1}$	$\mu$ , $\text{cm}^2 \text{V}^{-1} \text{s}^{-1}$	$I_D$ , eV	
Polyyne	1.1	$[-\text{CH}(\underset{\text{R}}{\text{R}})-\text{CH}_2-]_n$	–	–	–	–	–	–	
		polyethylene ( $R = \text{H}$ )	7.6	7.0 [1]	$10^{-4}$ – $10^{-5}$ [1]	–	$\sim 10^{-6}$	10.3	
		polystyrene ( $R = \text{C}_6\text{H}_5$ )	9.1	8.0 [1]	$10^{-5}$ – $10^{-2}$ [1]	–	$\ll 10^{-6}$	9.2	
		polyvinylanthracene	$\sim 4.0$	$\sim 3.6$ [1]	$(1-3) \times 10^{-4}$ [1]	–	–	8.1	
		polyvinylanthracene	$> 3.6$	3.1–3.4	$5 \times 10^{-4}$ – $8 \times 10^{-3}$ [1]	–	–	7.34	
Polyene	1.2	$[-\text{CR}_1=\text{CR}_2-]_n$	–	–	–	–	–	–	
		polyacetylene	5.6–5.0	–	$\sim 10^{-5}$ [1]	$10^4$	$10^{-4}$ – $10^{-5}$	–	
		polyphenylacetylene	$\sim 3.6$	7.1 [1]	$10^{-5}$ – $10^{-4}$ [1]	–	$\sim 10^{-4}$ [1]	8.2	
		polydiphenylacetylene	$\sim 3.1$	6.5 [1]	$10^{-5}$ – $3 \times 10^{-4}$ [1]	–	$\sim 10^{-3}$ [1]	7.4	
Phenylenes	1.3	poly( <i>p</i> -phenylenes)	$\sim 5.0$	$\sim 4.5$	$1.5 \times 10^{-5}$ [1]	–	$\sim 10^{-5}$ [1]	8.0	
		poly( <i>m</i> -phenylenes)	$\sim 5.2$	$\sim 4.9$	$2 \times 10^{-5}$ [1]	–	$\sim 10^{-5}$	8.2	
		poly( <i>p</i> -phenylenevinylenes)	2.5–2.7	2.4	–	$10^{-5}$ [79]	$10^{-5}$ – $10^{-4}$	7.7	
Polyacene	1.4	polyphenanthrene	–	3.6	–	$10^{-4}$ – $10^{-6}$	$10^{-5}$ – $10^{-3}$	8.1	
		polyalkylfluorene	–	–	–	$10^{-5}$ [79]	$\sim 3 \times 10^{-5}$ [79]	8.3	
		polydialkylhydropyrene	–	2.7 [81]	–	$\sim 10^{-2}$	–	$< 8.0$	
			polyphenyloxodiazole	–	–	–	$10^{-5}$	–	6.8
	1.5	polyphenylbutadiene	4.2	4.0 [1]	$3 \times 10^{-5}$ – $3 \times 10^{-3}$ [1]	–	$10^{-4}$ – $10^{-3}$ [1]	–	
		copolymer	–	2.0 [1]	$10^{-3}$ – $10^{-2}$ [1]	–	–	–	
Polymers with N, S, O, Cl, and like atoms									
	2.1	polyacrylonitrile ( $R = \text{CN}$ )	7.4	7.2 [1]	$10^{-4}$ [1]	–	–	–	
		polyvinyl chloride ( $R = \text{Cl}$ )	8.0	7.8 [1]	$10^{-4}$ – $10^{-5}$	–	–	–	
		polyvinylpyridine	$> 5.2$	4.9 [1]	$3 \times 10^{-4}$	–	$\sim 10^{-5}$	$\sim 8.3$	
		polyvinylindole	5.0	–	$10^{-3}$ – $3 \times 10^{-2}$ [3]	$10^{-6}$ [79]	$5 \times 10^{-6}$ [79]	7.9	
		polyvinylcarbazole	$> 4.6$	$> 3.1$	$10^{-3}$ – $5 \times 10^{-2}$ [1]	$\sim 10^{-6}$ [79]	$\sim 10^{-5}$	7.4–7.6	
			polyvinylpyrrolidone	$> 4.1$	–	$\sim 10^{-2}$ [1]	–	–	–
			polysiloxanes	3.6–3.2	3.1	$\sim 2 \times 10^{-1}$ [11]	–	$10^{-5}$	–
			polysililenes	–	–	–	$10^{-4}$ – $10^{-3}$ [85]	7.4	
			polygermylenes	–	–	–	$10^{-5}$ – $5 \times 10^{-3}$ [86]	–	
	2.2	polyiodophenylacetylene	$> 2.0$	$\sim 1.9$	$\sim 10^{-4}$ [1]	–	–	–	
polymethylethylpyridine		$\sim 5.0$	$\sim 4.8$	$3 \times 10^{-4}$ – $10^{-3}$ [1]	–	–	–		
polyamidines		$\sim 3.3$	$\sim 2.0$	$(2-8) \times 10^{-2}$ [16]	–	$\sim 10^{-5}$ [16]	–		
			–	–	–	$\sim 10^{-4}$ [16]	–		

**Table 1.** (Contd.)

Structure of molecular chains	Polymers without nitrogen atoms							
	Series	Polymer	$E_G^{\text{opt}}$ , eV	$E_G^{\text{ad}}$ , eV	$\eta$	$i_{\text{ph}}$ , $\Omega^{-1} \text{cm}^{-1}$	$\mu$ , $\text{cm}^2 \text{V}^{-1} \text{s}^{-1}$	$I_D$ , eV
	2.3	polyschiff bases of polyphenylvinylenes	>3.1	~3.0 [1]	$4 \times 10^{-5}$ – $2 \times 10^{-4}$ [1]	$10^{-5}$ [13]	$\sim 10^{-4}$ [1]	–
	2.4	polythienylvinylenes	–	2.1–2.3	–	$10^{-5}$ [79]	$10^{-4}$ – $10^{-5}$	–
		polythiophenes	–	–	–	$10^{-4}$ – $10^{-3}$	$10^{-5}$ – $10^{-3}$	–
		polypyrrole	2.45	–	–	$10^{-5}$ [79]	$\sim 3 \times 10^{-5}$ [79]	–
		polyphenyloxidiazole	3.1	–	–	$\sim 10^{-2}$	–	–
		polyamideimides	5.3	–	–	$10^{-5}$	–	–
	2.5	polyimides	–	–	$10^{-4}$ – $10^{-2}$ [91]	–	$\sim 10^{-5}$	7.5–9.7
		polyimides	>2.8	>2.0	$10^{-4}$ – $5 \times 10^{-1}$ [91]	$\sim 10^{-5}$	$10^{-6}$ – $10^{-3}$	6.7–9.2
		polymellitimides	>2.5 [5]	>1.9	–	–	–	6.7–9.2
		polyquinazolones	>2.3	>2.0	$3 \times 10^{-4}$ – $10^{-2}$ [94]	$\sim 10^{-5}$	$\sim 10^{-5}$ [5]	7.0–8.0

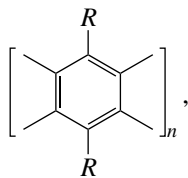


(iv) polyphenylenevinylenes (series 1.3) with the general formula [80–82]

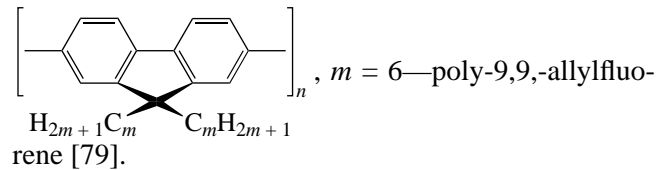
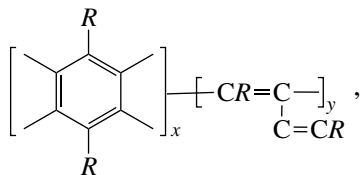


where  $R_1 = R_2 = -\text{C}_6\text{H}_5$ ;  $R_1 = \text{H}$ ,  $\text{OC}_8\text{H}_{17}$  and  $R_2 = -\text{CF}_3$ ;

(v) polymers with a double-conjugated system (the so-called polyacene structure, which is characteristic of molecular crystals of the anthracene, tetracene, and pentacene types) in the main chain (series 1.5) with the general formula



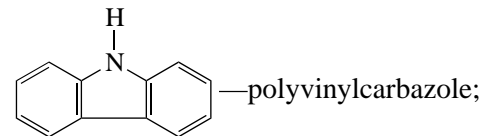
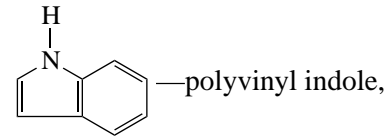
where  $R = -\text{C}_6\text{H}_5$ —polydiphenylbutadiene [1] and its copolymers:



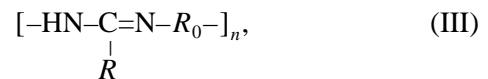
The analogs of the above polymers that contain, in contrast to them, heteroatoms (N, Cl, S, Se, O, and so on) are listed on the right-hand side of Table 1:

(i) series 2.1—polymers with the general formula (Ia), where

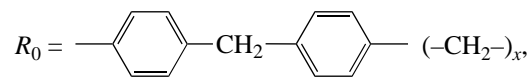
$R = -\text{CN}$ —polyacrylonitrile,  
 $-\text{Cl}$ —polyvinyl chloride,



(ii) series 2.2—polyamidines with the general formula [15]



where  $R = -\text{H}$ ,  $-\text{CH}_3$ , and  $-\text{C}_6\text{H}_5$ ;

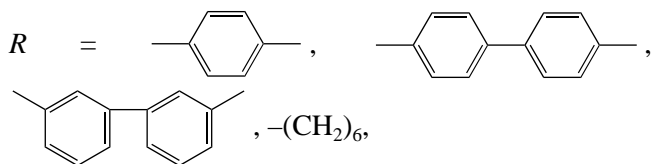
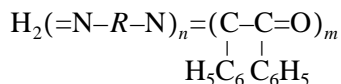


$x = 6, 8, 10$ ;

(iii) series 2.3—polymers with conjugated bonds



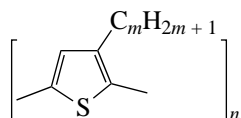
—polyschiff bases with the general formula



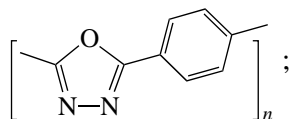
obtained by polycondensation of amines (*p*- or *m*-phenylenediamine and hexamethylamine) with benzyl;

(iv) series 2.4 from Table 1:

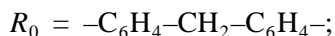
—polythiophenes with the general formula [83]



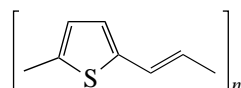
and polyphenyloxadiazoles [84]:



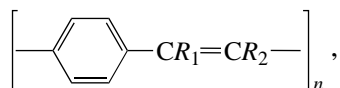
—polyamidines with the general formula (III) with



—polythienyls [81–83] with the general formula

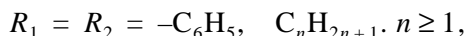
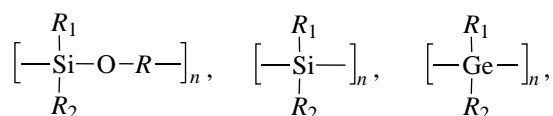


and poly-2,5-dialkoxyphenylenes with the general formula

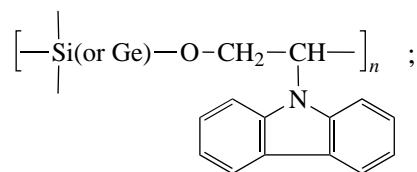


where  $R_1$ —phenyl,  $R_2 = -\text{H}(0)$ ;  $R_1 = R_2$ —phenyl (−0.35);  $R_1 = R_2$ —dimethoxyphenyl (−0.15);  $R_1 = R_2$ —diphenoxyphenyl (0.18) with an ionization potential increasing in the series (its relative change is indicated in brackets) and polyphenylenevinylene (formula (II)) with  $R_1 = -\text{H}$ ,  $-\text{OC}_8\text{H}_{17}$ ,  $R_2 = \text{CF}_3$ ;  $R_1 = -\text{OCH}_3$ ,  $R_2 = -\text{OC}_2\text{H}_5-\text{C}_4\text{H}_9$ ;  $R_1 = -\text{OC}_{10}\text{H}_{21}$ ,  $R_2 = -\text{H}$  [22];

—polysiloxanes [85] and polysilylenes and polymermylenes [86] with the general formulas

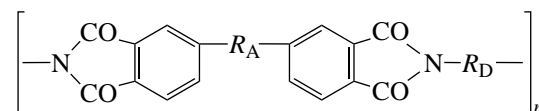


including triradial, tetradial, and linear carbazoyl-containing polyorganosiloxanes [85]

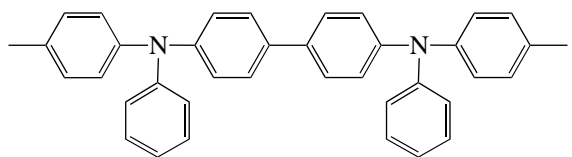


(v) series 2.5—polyimides and related compounds:

—polyimides with the general formula [87–93]

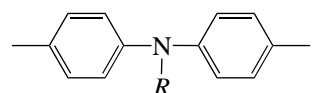


with donor (aromatic diamine) fragments  $R_D$  varied in a wide range described by the formulas



(1)–(1)

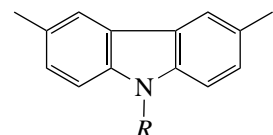
~6.7



where  $R = -\text{C}_6\text{H}_5$ ,  $-\text{CH}_3$ ,  $-\text{H}$ ;

(1) (2) (3)

6.88 7.0 7.14

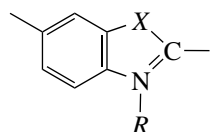


where  $R = -\text{CH}_3$ ,  $-\text{H}$ ;

(4) (5)

7.25 7.45

(the numbers in parentheses in the lines under the chemical formulas for the  $R$  fragments correspond to the numbers of experimental points in Fig. 4; the figures below are the corresponding values of  $I_D$  in eV)

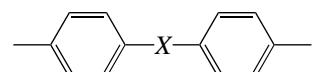


where  $X = -\text{N-}$ ,  $-\text{O-}$ ,  $-\text{S-}$ ,  $R = -\text{H}$ ;

(6) (7) (8)

or  $X = -\text{N-}$  and  $R = -\text{H}$ ,  $-\text{CH}_3$ ,  $-\text{C}_6\text{H}_5$ ;

(6a) (6b) (6c)



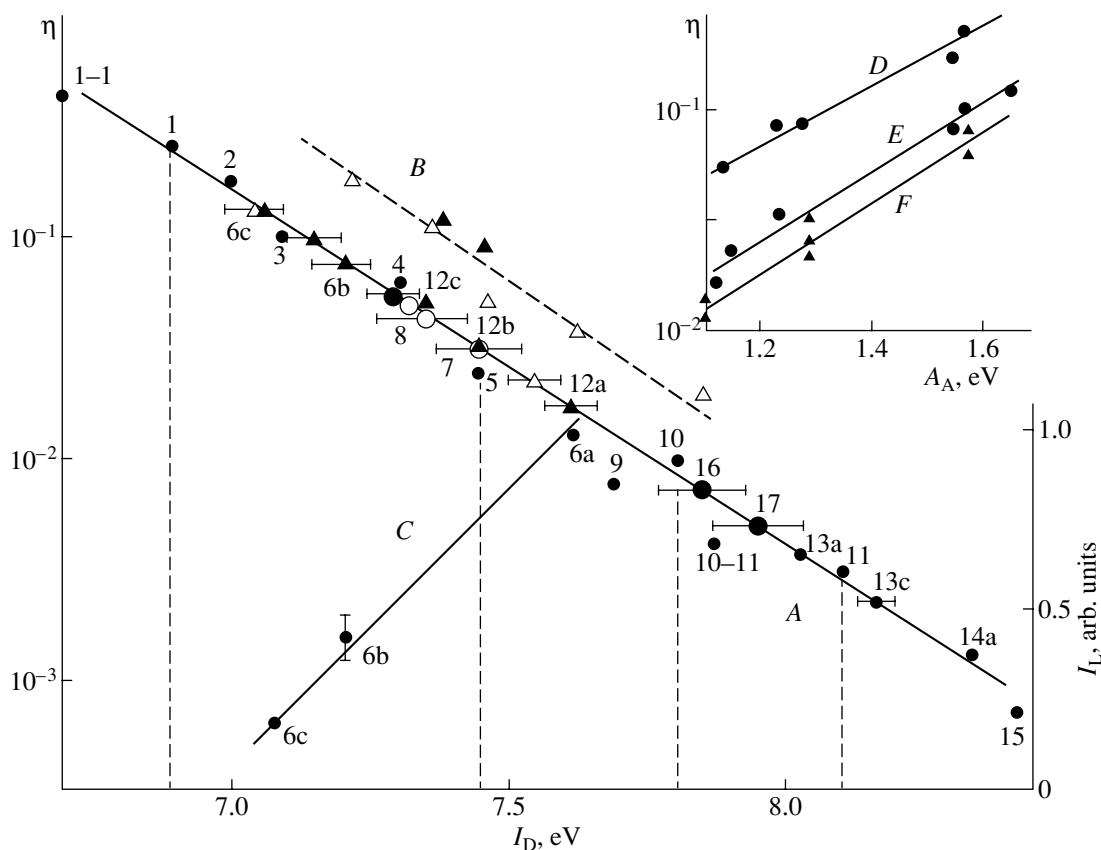


**Fig. 4.** Dependences of the (A, B) quantum yield of photogeneration  $\eta$  and (C) luminescence intensity  $I_L$  (C) on the ionization potential  $I_D$  of the donor fragment of polyimides (the types of fragments are indicated by numbers at points—see Subsection 2.2.1) for different acceptor fragments  $R_A$ : (A, C) diphenyl oxide and B  $(CF_3)_2$  [87–93]. The inset shows the dependences of  $\eta$  on the electron affinity  $A_A$  for the acceptor fragments from series I–VI at different  $R_D$ : (D) 1, (E) 6c, and (F) 12b.

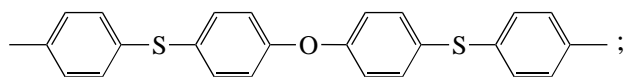
where  $X =$  —, —S—, —O— (diphenyl oxide (DPO))

(9) (10)

<7.8 7.8

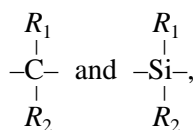
(11)

8.1



(10)–(11)

~7.9



here,  $R_1 = R_2 = -H$ , or  $R_1 = R_2 = -CH_3$ ,

(12a)

~8.5

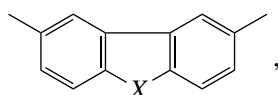
(12b)

~8.2

or  $R_1 = R_2 = -C_6H_5$ ;

(12c)

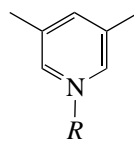
<8.0



where  $X = -CH_2-$ , —O—;

(14) (15)

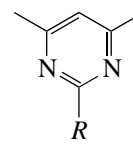
8.2 8.36



$R = H$ ,

(16)

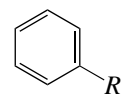
~7.8



$R = -C_6H_5$ ;

(17)

~7.9



(18)

where  $R = -H$ , —COOH, —CH<sub>2</sub>—CH—CH<sub>2</sub>—O—R',

(18a) (18b)

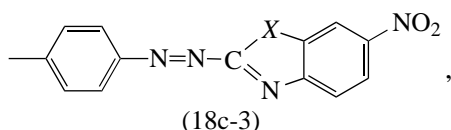
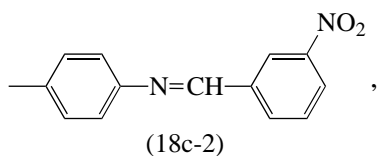
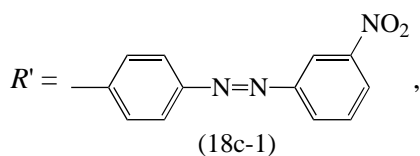
9.2

—



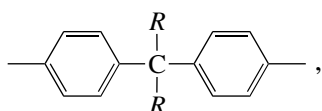
(18c)

—



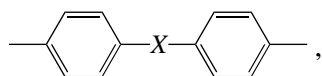
where  $X = \text{---O---}$  or  $\text{---S---}$   
(18c-3-1) (18c-3-2)

and acceptor (diimide) fragments  $R_A$ :



where  $R = \text{---CH}_3$ ,  $\text{---C}_6\text{H}_5$ ;

I  
1.10–1.14

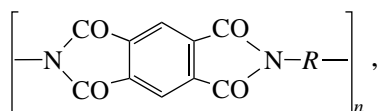


where  $X = \text{---CH}_2\text{---}$ ,  $\text{---O---}$ ,  $\text{---CO---}$ ,  $\text{---SO}_4\text{---}$ ,  $\text{---C} \begin{matrix} \diagup \text{CF}_3 \\ \diagdown \text{CF}_3 \end{matrix} \text{---}$

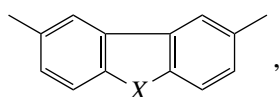
II III IV V VI  
1.19 1.30(1.12) 1.55(1.48) 1.57(1.48) 1.9

(here, Roman numerals denote series I–VI with  $R_A$  fragments in order of increasing electron affinity of the acceptor molecule  $A_A$ , which is indicated in the bottom line in eV);

—polymellitimides with the general formula

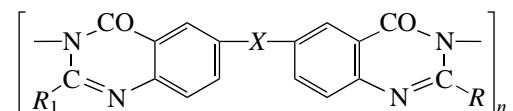


with  $R = \text{---} \text{C}_6\text{H}_4 \text{---} \text{X} \text{---} \text{C}_6\text{H}_4 \text{---}$ ,  $X = \text{---N(C}_6\text{H}_5)\text{---}$ ,  
 $\text{---NH---}$ ,  $\text{---S---}$ ,  $\text{---O---}$ ;

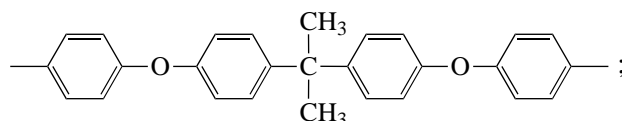
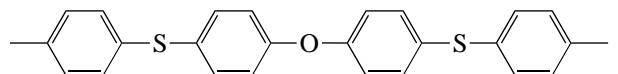


$X = \text{---NH---}$ ,  $\text{---N(CH}_3\text{)}\text{---}$ ,  $\text{---CH}_2\text{---}$ ,  $=\text{O}$ ;

—polyquinazolones with the general formula [94]

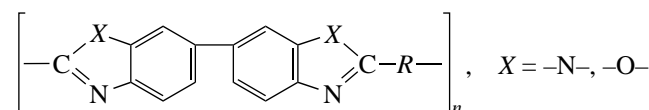


where  $R = \text{---} \text{C}_6\text{H}_4 \text{---} \text{Y} \text{---} \text{C}_6\text{H}_4 \text{---}$ ,

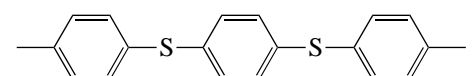
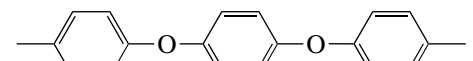


$Y = \text{---O---}$ ,  $\text{---CH}_2\text{---}$ ,  $R_1 = \text{---CH}_3$ ,  $\text{---C}_6\text{H}_5$ ,  $X = \text{---}$ ,  $\text{---CH}_2\text{---}$ ;

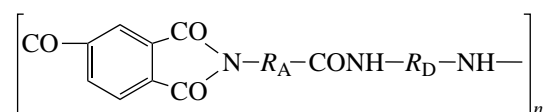
—poly-(N-phenyl)-benzimidazoles and polybenzoxazoles [5]



where  $R = \text{---} \text{C}_6\text{H}_3 \text{---}$ ,  $\text{---} \text{C}_6\text{H}_4 \text{---} \text{O} \text{---} \text{C}_6\text{H}_4 \text{---}$ ,



—polyamide-imides [92]



where  $R_A = \text{---}(\text{---CH}_2\text{---})_6\text{---}$ ,  $\text{---C}_6\text{H}_4\text{---}$ ;  $R_D = \text{DPO}$ , (18b) and (18c) from the corresponding structural formulas of the above polyimides.

## 2.2.2. Molecular D–A complexes.

**2.2.2.1. Structural parameters varied in the series of D–A complexes.** The objects of study were homologous series of molecules of D–A CTCs with systematically varied structure in which only one structural parameter is varied. The following characteristics were chosen as structural parameters: for the energy structure, the ionization potential of an isolated donor molecule (or donor fragment),  $I_D$ , and the electron affinity of an acceptor molecule or acceptor fragment,  $A_A$ ; for the spatial structure, the initial electron-transfer distance in a complex,  $r_0$ , and the distance between neighboring donor fragments,  $d$  (for polymer molecules). A homologous series of the molecules of D–A complexes is regarded as a sequence of molecules formed by a donor (acceptor) molecule with members of a homologous series of acceptor (donor) molecules. A homologous series of molecules with a systematically varied struc-

ture is regarded as a sequence of donor (acceptor) molecules (terms of the sequence) with similar spatial or energy structures; for each subsequent term of this sequence, one of the parameters of the spatial or energy structure ( $I_D$ ,  $A_A$ ,  $d$ , or  $r_0$ ) increases (decreases) with respect to the previous term, while the other parameters remain the same. The increase (decrease) in the parameter in this case is due to the difference in a single fragment of the molecular structure or a group of atoms in it.

Analysis of the results of [12] made it possible to conclude that  $\eta$  is independent of which of the parameters,  $A_A$  or  $I_D$ , is varied and is determined only by the difference  $A_A - I_D$ . Hence, this difference was used as the energy parameter. Since it is the variation in this parameter from one member of the series to another that is important in studying homologous series, the relative value was used:

$$A_A - I_D - (A_A - I_D)_{\min}, \quad (8)$$

where  $(A_A - I_D)_{\min}$  is the minimum value of the parameter in a given homologous series. The advantage of using the relative value is a significant increase in accuracy. For example, the methods for determining the values of  $A_A$  and  $I_D$  have an accuracy of  $\sim 0.5$  eV [95], whereas the methods for determining relative values (in particular, by maxima of absorption bands of  $D-A$  complexes) have an accuracy of 0.05 eV [96].

For the molecules of donors and acceptors that are intramolecular CTCs [97–99], the values of  $A_A$  and  $I_D$ , which enter (8), were determined from the parameters of their donor and acceptor fragments: the ionization potential of the donor fragment  $R_D$  of a donor molecule or acceptor molecule,  $I_D^D$  or  $I_A^D$ , respectively, or the electron affinity of the acceptor fragment  $R_A$  of a donor or acceptor molecule,  $A_D^A$  or  $A_A^A$ , respectively.

**2.2.2.2. Formation of homologous series of molecules of  $D-A$  complexes.** The homologous series of the molecules of  $D-A$  complexes are formed in such a way that the members of each series differ only in the parameter  $A_A - I_D$  and this parameter is larger for each subsequent member as compared with the previous one. The value of  $A_A - I_D$  is changed by systematic variation of either  $A_A$  or  $I_D$ , the other spatial parameters ( $d$  and  $r_0$ ) being the same. The values of  $d$  and  $r_0$  were set as constant parameters for a given homologous series. The parameter  $d$  for polymer molecules, in which monomeric aromatic donor fragments with a sufficiently low  $I_D$  are responsible for the charge transfer, was defined as the distance between these fragments. For monomer molecules,  $d$  was defined as  $d \propto N^{1/3}$ , where  $N$  is the concentration of molecules providing the charge transfer. The values of  $r_0$  were either taken from the literature [12] or, if such data were absent, were estimated based on the structural formulas of the molecules from the total length of chemical bonds with regard to the spatial position of the molecular fragments [11]. The constancy of the values of  $r_0$

and  $d$  in homologous series of complex molecules is obtained owing to the coplanar arrangement of varied donor or acceptor fragments [18].

The objects of study were thin (1–3  $\mu\text{m}$ ) films of solid solutions of molecular complexes in a polymer matrix [12]. The matrix is inert with respect to the complexes and their components (the ionization potential of matrix molecules  $I_{\text{matr}} > I_D$ ) and contains molecules providing transport of charge carriers (the ionization potential of these molecules  $I_{\text{tr}} \approx I_D$  and their concentration is 5–30%, which corresponds to a distance between transport molecules of 1–2 nm). The concentration of complex molecules in a matrix does not exceed 5% (for dyes and their complexes and fullerenes, lower than 1%). The polymer matrix is prepared on the basis of either a styrene copolymer with divinyl ( $I_{\text{matr}} = 8.5\text{--}9.2$  [95]) with transport carbazolyl-containing polymers ( $I_{\text{tr}} = 7.6$  eV [95]) or a polycarbonate ( $I_{\text{matr}} = 10.2$  eV [95]) with transport molecules on the basis of hydrazone derivatives [98], amines, carbazoles, and so on with  $I_{\text{tr}} = 6.88\text{--}7.6$  eV. In most cases, complexes were distributed in a matrix in the form of either individual molecules or aggregates of donor and acceptor molecules (up to 40), with an average distance between complexes of 20 nm [18]. In some other cases, they were distributed in the form of individual molecules at a planar interface between a photoconductor (layer of amorphous Se 10–400 nm thick or CdSe 70–90 nm thick [100]) and a polymer matrix (density  $10^{12}$   $\text{cm}^{-2}$ , distance between complexes  $\sim 10$  nm).

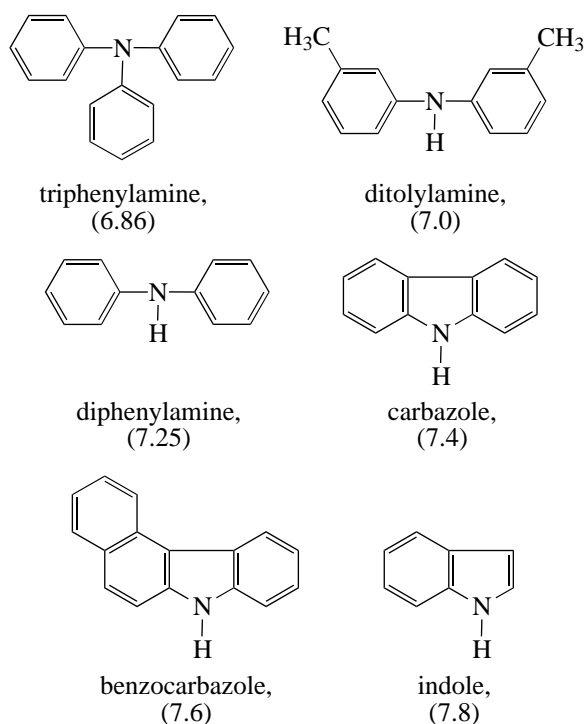
Homologous series of molecular complexes were formed on the basis of the homologous series of donor and acceptor molecules of various classes of organic (including organometal and organoselenium) compounds used in the preparation of electrophotographic recording media: carbazolyl-containing polymers (in particular, polyvinylcarbazole) and its polymeric and monomeric analogs—poly-9-substituted carbazoles [99] and aromatic vinyl polymers [85] and corresponding monomers ( $I_D$  was varied in the range 6.9–8.6 eV) with various acceptors ( $A_A$  was varied from  $-0.2$  to 2.7 eV). The following compounds were used as acceptors: fluorene derivatives, intramolecular complexes of heteryltricyanobutadienes, azides, azo pigments, squalenes, perylenes, and phthalocyanines; dyes of triphenylmethane, xanthene, and pyrylium classes; ternary complexes of dyes and ethylenethiolate complexes of transition metals; chloranil; bromanil; fullerenes ( $C_{60}$ ,  $C_{70}$ , and their mixture); polyimides (polymers with intramolecular charge transfer between donor and acceptor fragments), whose parameters were varied in a wide range ( $I_D = 6.7\text{--}8.7$  eV,  $A_A = 1.1\text{--}1.9$  eV); and polyphenylenevinyls. The distance  $r_0$ , constant for a given series, was varied by changing the complex structure (in going from one series to another). The series with a varied distance  $d$  was formed on the basis of poly-9-substituted carbazoles with monomeric units of different length. The classes of molecular complexes differed in the type of molecular orbitals of electrons

( $n$ ,  $\pi$ ,  $\sigma$ ) involved in the formation of a complex, the interaction energy (from weak nitrogen-containing complexes and exciplexes to ion-radical salts), and the preparation conditions (dispersion in an inert matrix or accumulation at the interface).

The samples with photosensitive media (see inset in Fig. 5b) consisted of a glass or Lavsan base covered with a conducting transparent (Ni or  $\text{In}_2\text{O}_3(\text{Sn})$ ) coating 0.01  $\mu\text{m}$  thick (for photothermoplastic media, this coating served as a thermal developing electrode), onto which one or two layers of a photosensitive medium were deposited. In the case of a single-layer medium, a layer of  $D$ - $A$  complexes dispersed in a polymer (thermoplastic) inert matrix was deposited. The matrix was a styrene-divinyl copolymer with the ionization potential  $I_{\text{matr}}$  much higher than  $I_D$  of the donor molecules under study. In the case of a two-layer (injection) medium, a photogeneration layer of either an inorganic injection sensitizer; or CdSe (0.1–0.8  $\mu\text{m}$ ), amorphous Se (up to 3  $\mu\text{m}$ ), or SeAsTe (~1  $\mu\text{m}$ ), which have acceptor elements with an unfilled  $p$  shell; or polyimide was deposited on a conducting coating, and this layer was covered with a transport layer of donor polymer or monomer molecules in a polymer matrix, which has thermoplastic properties in the case of photothermoplastic media.

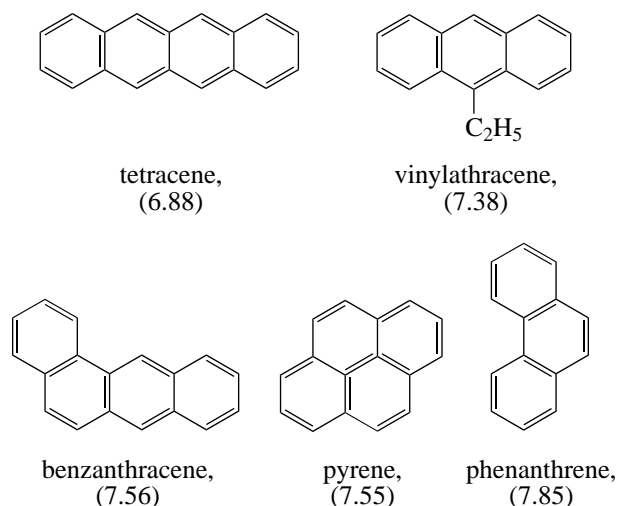
**2.2.2.3. Series of donor molecules used to form homologous series of  $D$ - $A$  complexes.** The following series of donors were considered: aromatic nitrogen-containing molecules and their analogs containing no nitrogen (series I and II, respectively), aromatic vinyl polymers (series III), and hydrazone derivatives (series IV).

The series of aromatic nitrogen-containing molecules (I) includes



with ionization potentials  $I_D$  increasing from 6.86 to 7.8 eV [95]. From here on, the figures in parentheses under the formulas indicate the values of  $I_D$  in eV.

The series of aromatic molecules containing no nitrogen (II) includes

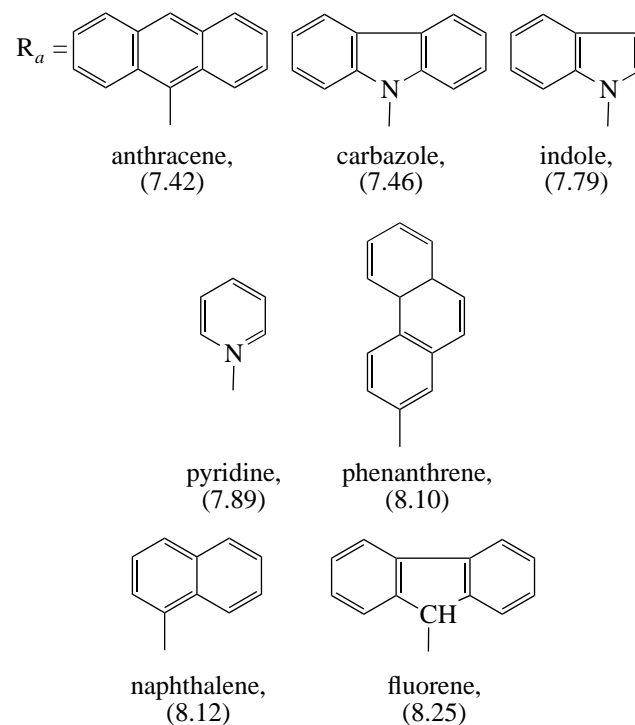


with  $I_D$  increasing from 6.88 to 7.85 eV [95].

The series of aromatic vinyl polymers (III) includes the compounds with the general formula



where



with  $I_D$  increasing from 7.42 to 8.25 eV [95].

The series of poly-9-substituted carbazoles (IV) contains compounds with the general formula  $[-\text{CzR}-]_n$ ,



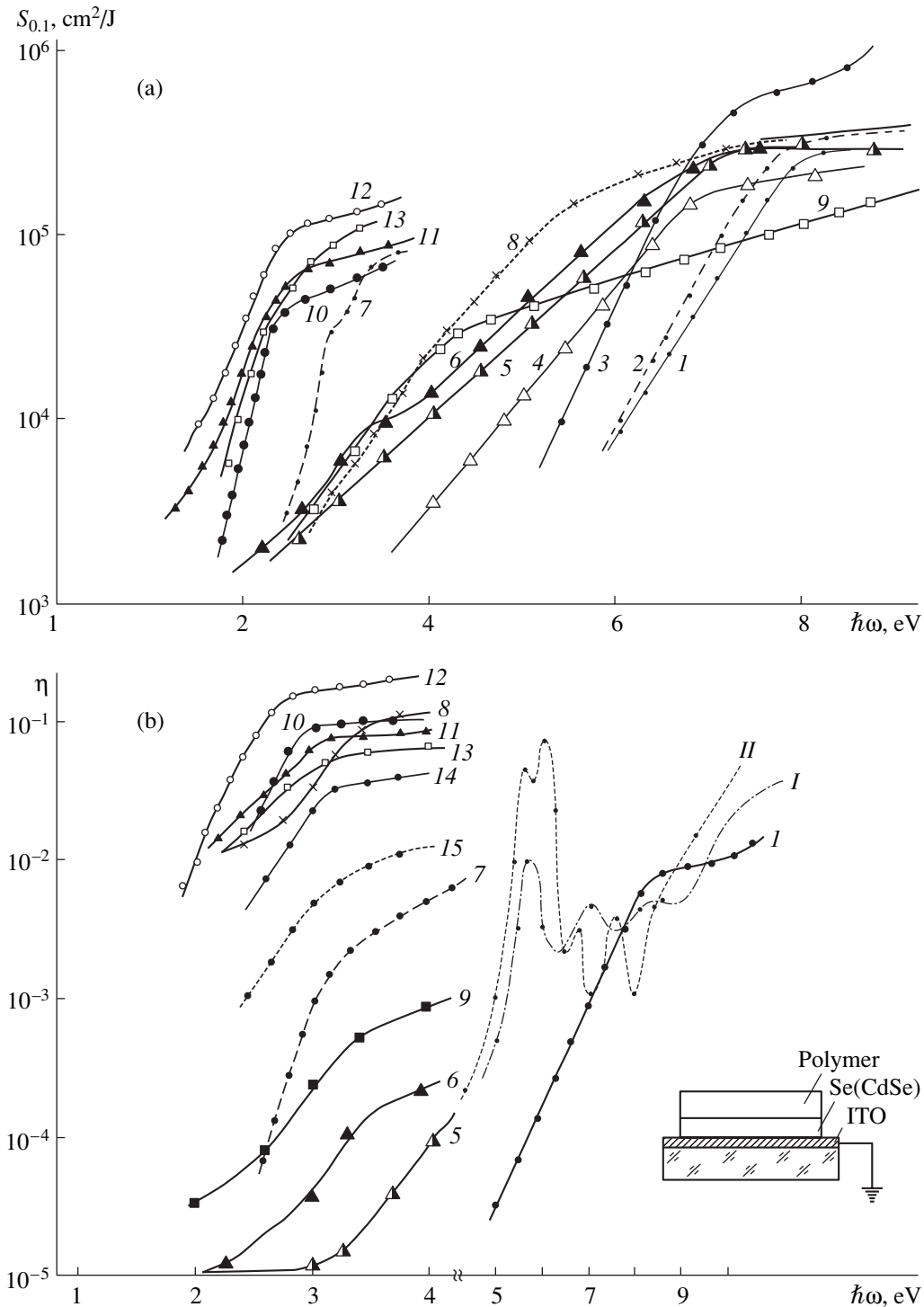
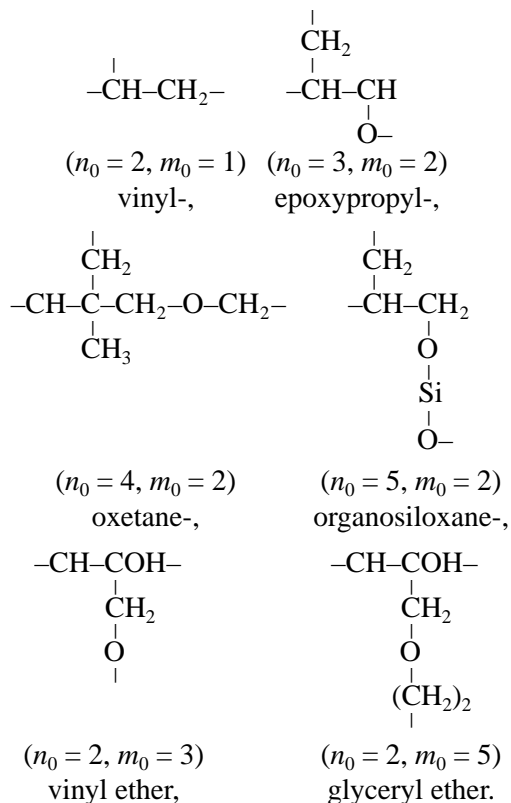


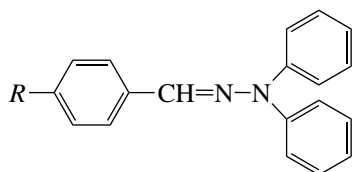
**Fig. 5.** Spectra of the (a) electrophotographic photosensitivity  $S_{0.1}$  and (b) quantum yield of photogeneration  $\eta$  of the polymers with saturated and conjugated bonds in the main chain: (1) polystyrene; (2) polyvinyl chloride; (3) polyacrylonitrile; (4) polyethylene; (5) polyphenylacetylene; (6) polydiphenylacetylene; (7) polyvinylanthracene; (8) polyvinylcarbazole; (9) polydiphenylbutadiene; (10) polyphenylenevinylene; (11) polyamidine; (12) triphenylamine-containing polyimide; (13) diphenyl oxide-containing polyquinazolone; and (14, 15) polyamideimides based on (14) phenyl-substituted benzimidazole and (15) diphenyl oxide ( $M_M = (3-5) \times 10^3$ ). The data are taken from (1-9) [1], (10) [80], (11) [16], (12) [90], (13) [93], and (14, 15) [92]. For comparison, the data on  $\eta$  of crystalline layers of (I) thymine and (II) adenine [1] are shown, whose structure is similar to that of the monomeric unit of polyimides and polyquinazolones. The inset shows the structure of the objects of study.

where Cz is carbazole and  $R$  are various alkyl and alky-nyl substituents:

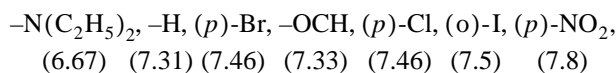


These substituents are intramolecular complexes with charge transfer between the nitrogen atom of carbazole  $\text{N}^{-\delta_0}$  and the alkynyl group  $\text{R}^{+\delta_0}$ . Here,  $\delta_0$  is the degree of  $p\pi$  conjugation between  $p$  electrons of nitrogen and  $\pi$  electrons of  $R$ , which determines the  $\sigma$  constants of alkynyl groups (they range from  $-0.04$  to  $-0.28$ ) [99]. The use of alkynyl groups with similar  $I_D$  but different distances  $d$  in this series made it possible to obtain series V, whose members differ in the parameter  $d$ .

The series of hydrazone derivatives (VI) contains compounds with the general formula [98]



with different groups  $R =$

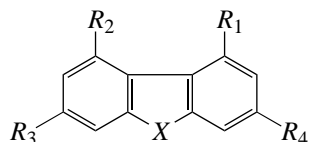


replacement of which leads to the variation in the value of  $I_D$  (indicated in parentheses).

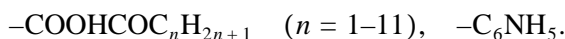
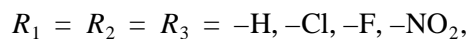
**2.2.2.4. Series of acceptor molecules used to form homologous series of D-A complexes.** To form series of acceptor molecules, fluorenes (series VII), dyes and their complexes (series VIII–XI), azides and azo pigments (series XII and XIII), perylenes (series XIV),

squalenes (series XV), fullerenes (series XVI), heteryl-tricyanobutadienes (series XVII), and elements with an unfilled  $p$  shell (series XVIII) were chosen.

Series VII contains compounds with the general formula [101–103]

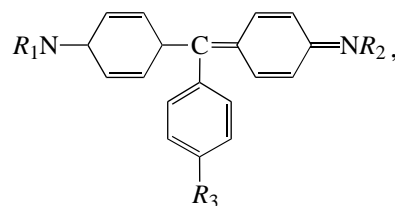


where  $X = \text{>O}, \text{>C}(\text{CN})_2$ ,

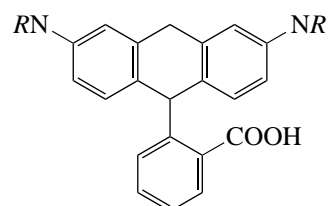


These compounds are intramolecular complexes with charge transfer of the  $p\pi$  or  $n\pi$  type between  $\pi$  electrons of the fluorene ring and  $p$  or  $n$  electrons of the acceptor radicals  $R_1$ – $R_4$ . The value of  $A_A$  is estimated as the sum of the electron affinities of all  $A_A^A$  groups; thus, the minimum value of  $A_A$  in the series is 1.65 eV (at  $X = 0, R_1 = R_2 = \text{H}, R_3 = R_4 = \text{Cl}$ ) and the maximum value of  $A_A$  is 2.55 eV (at  $X = \text{C}(\text{CN})_2, R_1 = R_2 = R_3 = R_4 = \text{NO}_2$ ) [95, 104].

Series VIII includes (i) dyes of the triphenylmethane class with the general formula



where  $R_1 = R_2 = (-\text{C}_2\text{H}_5)_2$  and  $R_3 = -\text{H}$  for brilliant green (the wavelength corresponding to the maximum absorption  $\lambda_{\text{max}} = 628$  nm);  $R_1 = R_2 = (-\text{CH}_3)_2, R_3 = \text{H}$  for malachite green ( $\lambda_{\text{max}} = 616$  nm);  $R_1 = R_2 = (-\text{CH}_3)_2, R_3 = -\text{HCH}_3$  for methyl violet ( $\lambda_{\text{max}} = 590$  nm); and  $R_1 = R_2 = R_3 = (-\text{CH}_3)_2$  for crystalline violet ( $\lambda_{\text{max}} = 589$  nm); (ii) xanthene dyes (rhodamine 4C, 6G); and (iii) dyes with the general formula

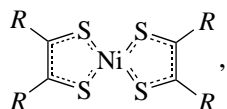


where  $R = (-\text{CH}_3)_2$  and  $(-\text{C}_2\text{H}_5)_2$ .

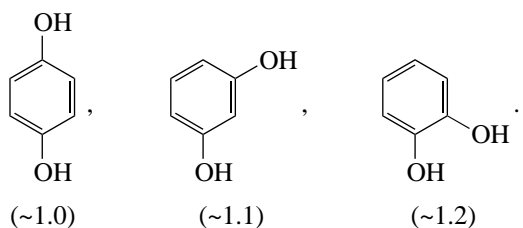
Series IX consists of dyes based on styryls and carbocyanines [105]. They include compounds with the general formula  $R^+-\text{ClO}^-$ , where  $R = R_a$  is pyrimidine and  $R_a$  are the derivatives of dimethylaminostyrylpyra-

zoles with a relative change in the electron affinity of the acceptor fragment  $A_A$  within 0.4 eV.

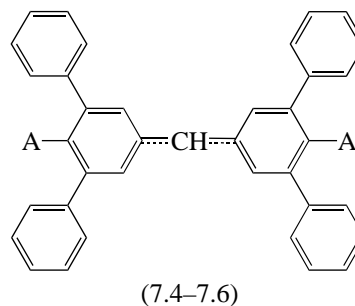
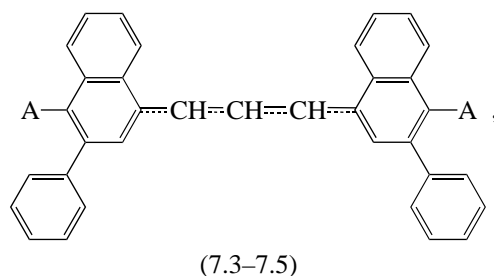
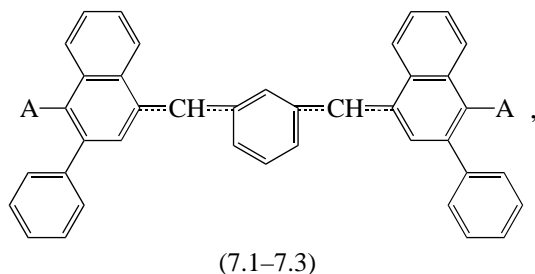
As dye complexes, the following were chosen: (i) ethylenethiolate complexes of transition metals (series X), in particular, Ni, with the general formula [106]



where  $R = -CH_3$ ,  $-C_6H_5$ , and  $-C_6H_4N(CH_3)_2$ , with maximum absorption at  $\lambda_{max} = 780, 830, 960,$  and  $1060$  nm, and (ii) ternary dye complexes (series XI) with the general formula  $TiL_3R_3$  [107], where  $L =$



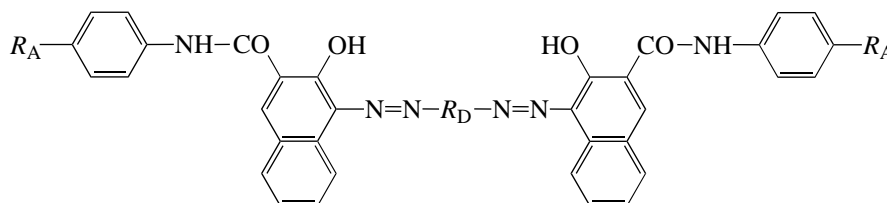
These are monomeric intramolecular CTCs formed via a ligand  $L$  by a metal (in particular, thallium) atom and a dye molecule  $R(A)$  containing an atom  $A$  (sulfur, selenium, oxygen). The value of  $A_A$  of this compound complex is varied by varying the dye molecule  $R(A) =$



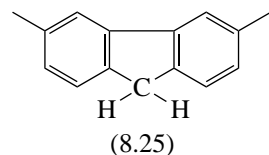
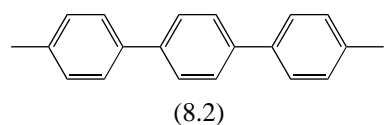
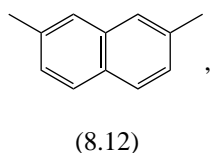
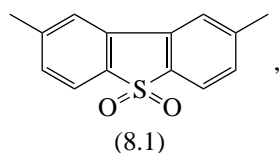
formed by an aromatic fragment with the ionization potential  $I_A^D = 7.1-7.5$  eV and an acceptor fragment formed by S, Se, or O atoms ( $A_A^A = 2.0, 2.1,$  and  $2.4$  eV [95], respectively). The value of  $A_A$  was determined by formula (8), taking into account the fact that it depends, along with the type of dye molecule (i.e., the value of  $I_A^D$ ), on the electron affinities of the ligand molecule  $A_A^L$  and the acceptor fragment of the dye molecule  $A_A^A$ , i.e.,

$$A_A = C_1 A_A^L + C_2 A_A^A + C_3 (I_A^D - \hbar\omega_{max}). \quad (9)$$

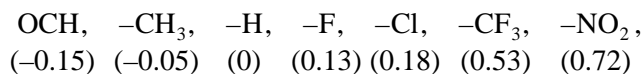
Series XII (azo pigments) contain compounds with the general formula [108]



They are monomeric intramolecular complexes with charge transfer of the  $n\pi$  type between  $\pi$  electrons of different donor bases  $-R_D^-$ ,

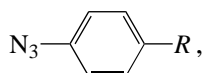


with the ionization potential  $I_A^D$  increasing from 8.1 to 8.25 eV and  $n$  electrons of different acceptor bases  $-R_A^-$ ,



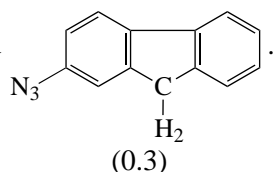
with different  $\sigma$  constants (from 0.15 to 0.8 [108]) and, accordingly, different values of  $A_A$  (indicated in parentheses).

Azides (series XIII) are compounds with the general formulas

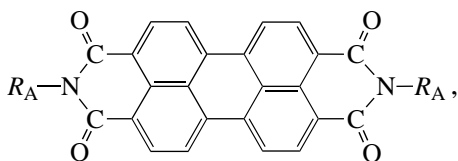


where  $R = -\text{OCH}_3$ ,  $-\text{COOH}$ ,  $-\text{NH}$ ,  $-\text{NO}_2$   
 (-0.17) (-0.05) (0.2) (0.54)

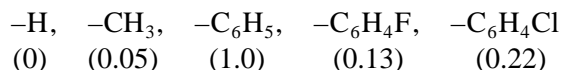
and



Perylenes (series XIV) are compounds with the general formula [110]

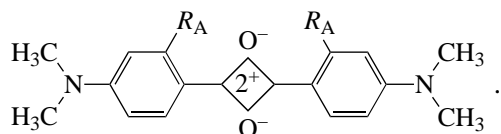


where  $R_A$  is

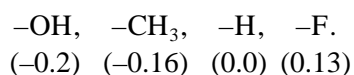


with the values of  $A_A$  increasing in the series (indicated in parentheses). They are intramolecular complexes with  $n\pi$  charge transfer between  $\pi$  electrons of perylene and  $n$  electrons of acceptor radicals  $R_A$ .

Squalenes (series XV) are compounds with the general formula [111]



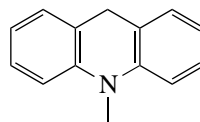
They are monomeric intramolecular complexes with  $\pi\sigma$  charge transfer between  $\sigma$  electrons of the O atom and  $\pi$  electrons of the amine group of different acceptor radicals  $R_A^-$ :



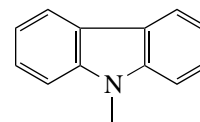
Series XVI includes fullerenes  $\text{C}_{60}$  ( $A_A \approx 2.6$  eV),  $\text{C}_{70}$  ( $A_A \approx 2.7$  eV), and their mixture (87%  $\text{C}_{60}$  and 13%  $\text{C}_{70}$ ). Their sensitizing ability is comparable with that of chloranils and bromanils, which have electron

affinities ( $\sim 2.6$  and  $\sim 2.8$  eV [95]) similar to those of fullerenes but different structure.

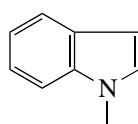
Heteryltricyanobutadienes (series XVII) include compounds with the general formula  $R_D-\text{CH}=\text{CH}-\text{C}(\text{CN})=\text{C}(\text{CN})_2$  [97]. They are intramolecular complexes with charge transfer of the  $n\pi$  type between  $\pi$  electrons of the varied donor fragment of the  $R_D$ -heterocycle and  $n$ -electrons of the N atom belonging to the CN group of tricyanobutadiene;  $R_D =$



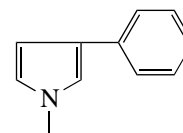
acridone (7.43),



carbazole (7.5),



indole (7.79)



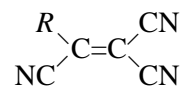
phenylpyrrole (8.09)

with  $I_A^D$  increasing from 7.43 to 8.06 eV [95]. The value of  $A_A$  for heteryltricyanobutadienes was determined from the known ionization potentials  $I_A^D$  of the donor fragments, which correspond to the absorption peaks found from the absorption spectra of the molecules [65]:

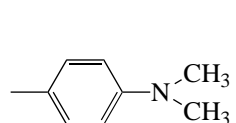
$$A_A = I_A^D - \hbar\omega_{\max} + C,$$

where  $C$  is a constant.

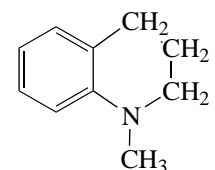
Tricyanovinylarylamines (series XVIII) [112] have the general formula



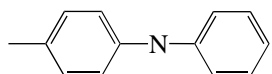
where  $R =$



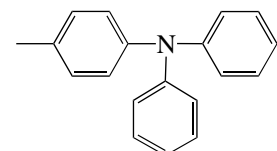
(540)



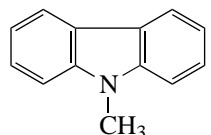
(545)



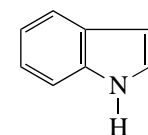
(520)



(550)



(510)

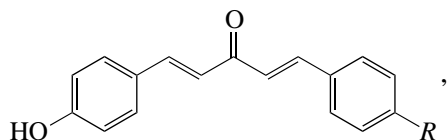


(475)

(the values of  $\lambda_{\max}$  are indicated in parentheses).

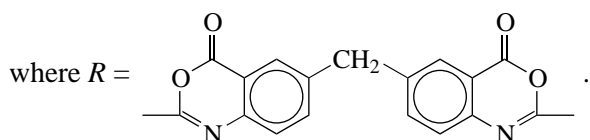
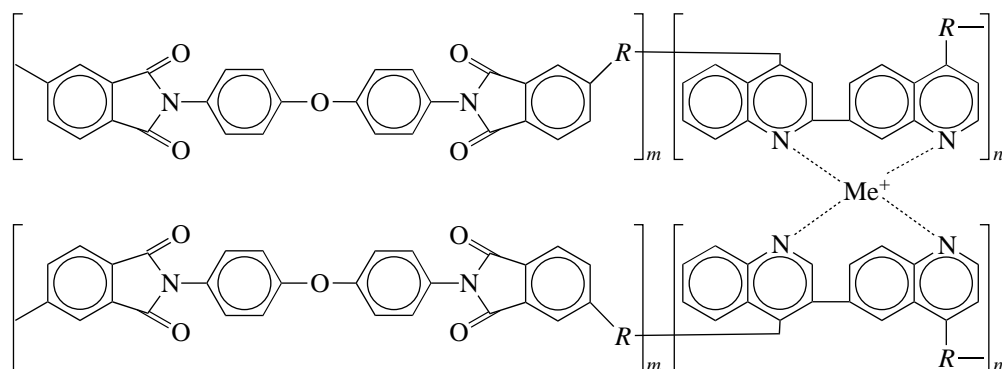
The elements with an unfilled  $p$  shell (series XIX) include S, Se, Te, and As with  $A_A = 1.9, 2.1, 2.4,$  and  $2.6$  eV, respectively [95].

The chromophores introduced into polyamides (series XX) have the general formula



where  $R = -N(C_2H_5)_2, -N(CH_3)_2, -OH, -NHCOCH_3,$   
 $(-0.93) \quad (-0.83) \quad (-0.37) \quad (-0.34)$   
 $-OC_3, \quad -H, \quad -F, \quad -NO_2$   
 $(-0.27) \quad (-0) \quad (-0.06) \quad (-0.79).$

Along with the above polymers, the following compounds have been studied: (i) polyimides (Table 1, series of polymers 2.5) sensitized by the acceptors 2,4,7-trinitro-9-fluorenone (the electron affinity  $A_G = 1.9$  eV [95]); 2,4,7-trinitro-9-dicyanomethylene-fluorene ( $A_G = 2.2$  eV [95]); chloranil ( $A_G = 2.5-2.6$  eV [95]); bromanil ( $A_G = 2.6-2.8$  eV [95]); fullerenes (a mixture of  $C_{60}$  and  $C_{70}, A_G = 2.65$  eV [113];  $C_{60}, A_G = 2.6$  eV;  $C_{70}, A_G = 2.7$  eV); and dyes (malachite green,  $A_G = 1.7$  eV; crystalline violet,  $A_G = 1.5$  eV [95]); rhodamine; coumarin; and ethylenethiolate complexes of metals [106] (the dye and fullerene concentrations were  $c_d = 0.2-1.0$  mol % and  $c_f = 0.7$  mol %, respectively); and (ii) organometallic complexes of biquinoyl- and bipyridine-containing polyimides with the general formula [114-116]



Me: Cu, Cd, Pt, Ru, Tb, Er.

**2.2.2.5. Homologous series of D-A complexes.** The chosen series of donor and acceptor molecules were used to form the homologous series of molecular D-A complexes, whose members differ in the energy parameter  $A_A - I_D$ , varied by varying  $I_D$  in the series of donors or  $A_A$  in the series of acceptors (with constant  $d$  and  $r_0$ ). The following homologous series (listed in order of increasing  $r_0$ ) were investigated (see Tables 2, 3):

series 2—porphyrins (donors)

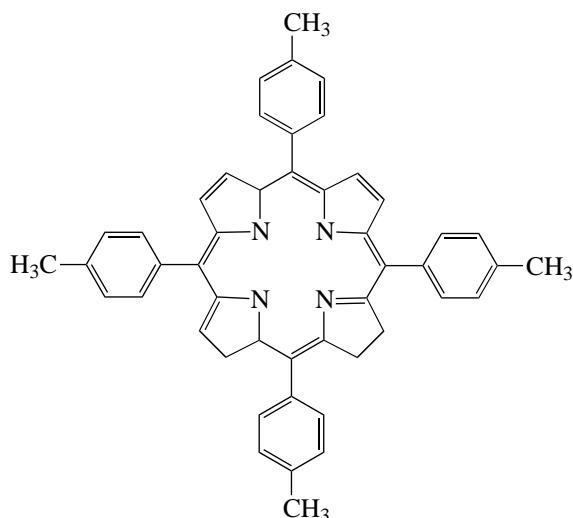


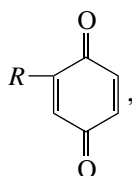
**Table 2.** Quantum yields of pair formation ( $\eta_0$ ) and photogeneration of free charge carriers ( $\eta$ ) and dipole moments  $\mu_e$  in the series of molecular  $D-A$  complexes, depending on the parameter  $A_A - I_D$ 

Series no.	Homologous series	$I_D$ , eV	$A_A$ , eV	$(A_A - I_D) - (A_A - I_D)_{\min}$ , eV	$\eta$	$\eta_0$	$\mu_e$ , D
2	porphyrins + quinines	—	—	0–0.35	0.24–0.85	0.3–1.0	3.1–11.2
3	PVC (series III) + acceptor (series VII)	7.6	1.6–2.5	0–0.9	0.003–0.35	0.05–0.65	0.7–8.4
4	TNDCMF (series VII) + donor (series III)	7.42–8.25	2.1	0–0.83	0.30–0.005	0.55–0.02	7.7–0.3
5	TNF (series VII) + donor (series IV)	7.29–7.77	1.9	0–0.38	0.03–0.32	0.15–0.40	0.7–5.6
7	PVC (series III) + $TiL_3R_3$ (acceptor) (series XI)	—	—	0–0.60	0.15–0.42	0.60–0.96	9.1–14.6
9	azo pigments (series XII) $R_D(AzoR_A)_2$ with: $R_A = H, R_D$	8.1–8.25	—	0–0.15	0.7–0.8	—	11.8–14.3
	$R_D = \text{fluorene}, R_A$	8.25	–0.15–0.72	0–0.87	0.44–0.86	—	—
11	perylene $R_A-Pr-R_A$	—	–0.05–0.17	0–0.22	0.04–0.32	—	0.7–5.5
13	squalenes $SqR_A R_A$	—	–0.20–0.13	0–0.33	0.08–0.35	—	1.5–6.9
14	azides (series) + $C_{60}$	—	2.6	–0.47–0	0.10–0.18	—	~20
2.5	polyimides with $R_A$ ,	—	1.1–1.9	0–0.8	<0.01–0.65	0.02–0.9	2.5–19.6
	$R_D$	6.7–8.9	—	0–2.2	—	—	—
2.5	polyimides + acceptor + dyes	~6.7	1.6–2.7	0–1.1	0.05–0.95	~1.0	15–26
1.3	PVC	—	–0.35–0.18	–0.17–0	0.07–0.25	0.12–0.5	0.5–1.1
15	PVC (series III) + HCB (series XVII)	7.6	7.43–8.09	0–0.66	0.35–0.24	0.65–0.59	14.8–13.5
18	Se + donor (series II)	6.88–7.85	2.2	0–0.97	0.65–0.01*	—	—

Note: Roman numerals correspond to the series of donors and acceptors defined in Subsections 2.2.2.3 and 2.2.2.4, respectively. Series of complexes denoted by numbers in the first column are formed of these donors and acceptors. See Table 1 for series 1.3 and 2.5. The following denotations are used: PVC—polyvinylcarbazole, TNDCMF—2,4,7-trinitro-9-dicyanomethylene-fluorene, TNF—2,4,7-trinitro-9-fluorenone, and HCB—heteryltricyanobutadiene.

\* Injection efficiency.

with quinones (acceptors)



where  $R = -H, -CHO, -CH_2C_6H_5$ ;

series 3–5—carbazolyl-containing polymers and their analogs with fluorene derivatives:

series 3—polyvinylcarbazoles (donor of series I–III, see Subsection 2.2.2.3) with fluorene acceptors (series VII, see Subsection 2.2.2.4);

series 4—2,4,7-trinitro-9-dicyanomethylene-fluorene (series VII) with vinyl aromatic donor polymers (series III);

series 5—2,4,7-trinitro-9-fluorenone (series VII) with poly-9-substituted carbazoles (series IV);

series 6—polyvinylcarbazoles with dyes (series IX);

**Table 3.** Initial charge-transfer distances  $r_0$  and degrees of charge transfer in the excited state,  $\delta$ , for homologous series of complex molecules

Homologous series	$r_0'$ , nm	$r_0''$ , nm	$\delta_{\max}$	$\delta_{\min}$
1	0.25–0.30	$0.31 \pm 0.03$	$0.95 \pm 0.05$	$0.2 \pm 0.1$
2–4	0.30–0.35	$0.33 \pm 0.03$	$0.95 \pm 0.05$	$0.2 \pm 0.1$
	0.35–0.03	$0.35 \pm 0.03$	$0.7 \pm 0.1$	$0.10 \pm 0.05$
6	0.4–0.6	$0.38 \pm 0.04$	$0.95 \pm 0.05$	$0.7 \pm 0.1$
7	0.4–0.5	$0.42 \pm 0.04$	—	—
8	0.3–0.5	$0.43 \pm 0.04$	—	—
9	0.4–0.6	$0.47 \pm 0.05$	—	—
10	0.6	$0.57 \pm 0.06$	$0.85 \pm 0.05$	$0.6 \pm 0.1$
13	—	$0.32 \pm 0.03$	$0.8 \pm 0.1$	$0.2 \pm 0.1$

Note:  $r_0'$  is estimated from the structural formulas of the molecules and  $r_0''$  is determined from the quantum yield  $\eta$ .

series 7—polyvinylcarbazoles with ternary complexes of dyes (series VIII and XI);

series 8—substituted polyphenylenevinylenes (series 2.3, see Table 1);

series 9—azo pigments (series XII);

series 10—polyimides (series 2.5, see Table 1);

series 11—perylene (series XIV);

series 12—polyimides with fullerenes;

series 13—squalenes (series XV);

series 14—azides (series XIII);

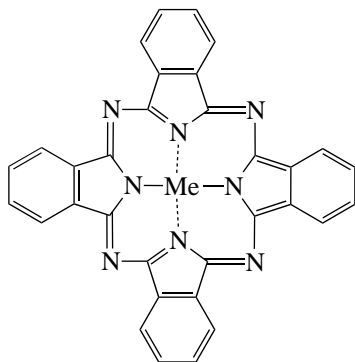
series 15—polyvinylcarbazoles with heteryltricyanobutadienes (series XVII);

series 16—azides with fullerenes;

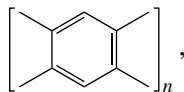
series 17—triphenylamine-containing polyimides with dyes.

Series of complexes forming at the interface (series 18 and 19) include complexes forming by aromatic molecules (series I) (either containing or not containing an N atom) dispersed in the neutral matrix of the transport layer and Se molecules of the injection layer (Se belongs to acceptors—elements with an unfilled  $p$  shell (series XVIII), series 18 and 19).

**2.2.3. Molecular crystals.** For comparison, the data for the two series of molecular crystals are given: (i) phthalocyanines (series 1) with the general formula [117–119]



with different metals (Me)—Ti, Zn, V, Co, and Cu ( $A_A = \sim 0.4, \sim 0.6, \sim 0.7, \sim 0.9,$  and  $\sim 1.5$  eV, respectively)—and without a metal ( $H_2$ ) and (ii) polyacenes—compounds with the general formula [17]



where  $n = 2-5$ .

### 3. RESULTS AND DISCUSSION

#### 3.1. Polymers and Molecular Crystals

**3.1.1. Spectral and structural regularities of photoeffect.** For the polymers of the vinyl series (series 1.1 and 2.1; all polymers are amorphous except polyethylene, which is in a crystalline state), it was ascertained [1] that the photoconductivity spectra of conjugated

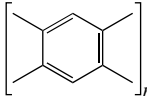
polymers are approximately the same in the UV spectral region (Fig. 5a). The position of the long-wavelength photosensitivity edge depends on the structure of a polymer and shifts to longer wavelengths with increasing  $\pi$  conjugation in the main chain and decreasing ionization potential  $I_D$  of the donor fragment or increasing electron affinity of the acceptor fragment, which serve as a radical  $R$  (in the lateral chain) in the following sequence [1]: phenyl ring, chlorine, cyano group, hydrogen, carbazolyl ring (Fig. 5a, curves 1–3, 7, 8). Obviously, in the case of the second and third of the above radicals, due to their acceptor properties, the electron transport is dominant; for the other radicals, the hole transport is dominant. Apparently, the higher photoconductivity and photosensitivity  $S$  of polyethylene (Fig. 5, curve 4), as compared with polystyrene (curve 1) (which has a lower potential  $I_D$ ), is related to the crystalline state of polyethylene. Investigation of the nature of the spectra  $S(\lambda)$  revealed that, in the short-wavelength range ( $\lambda = 120-135$  nm), where the valence electrons of the molecule are responsible for absorption, the quantum yield is constant; with an increase in wavelength, it sharply decreases.

For polymers with double bonds  $-C=C-$  (polyacetylene and its phenyl-substituted analogs), the shape of the spectrum  $S_{0,1}(\lambda)$  (Fig. 5a, curves 4–6) is somewhat different from the spectrum of vinyl polymers: the slope of the dependence  $S(\hbar\omega)$  in the vicinity of the absorption edge decreases. The likely reason is that, in the range  $\lambda = 135-180$  nm,  $\eta$  decreases with increasing number of double bonds and, in the range 180–220 nm,  $\eta$  increases due to the photoactive absorption [1]. The photosensitivity of conjugated polymers depends on their supramolecular structure, the molecular mass  $M_M$ , and the type of solvent. Aromatic solvents (toluene), which can interact with monomeric units and require much effort to remove them from a film (as compared to other solvents), reduce  $\eta$ . Taking into account the above considerations, the properties of polymers with the values of  $M_M$  of the same order of magnitude were compared for samples obtained under the most similar conditions of deposition: neutral solvents (not interacting with a polymer), measurement of  $\eta$  in the same spectral range, and the same measurement temperature  $T = 300$  K. The results of the analysis of the photosensitive characteristics of polymers—the energies  $E_G^{opt}$

and  $E_G^{ad}$ , determined from the values of the intrinsic absorption edge and photosensitivity from the corresponding spectra  $\alpha(\lambda)$  and  $S_{0,1}(\lambda)$ ; the quantum yields of photogeneration (for some polymers, photoconductivity  $i_{ph}$  [123, 124]); and the mobilities of charge carriers—are listed in Table 1. It can be seen from Table 1 that, with an increase in the  $\pi$  conjugation in the main chain, the energies  $E_G^{opt}$  and  $E_G^{ad}$  decrease, while the values of  $\eta$  and  $\mu$  increase. It is well known [1] that the energy  $E_G^{opt}$  for conjugated polymers decreases with



**Table 4.** Photosensitive characteristics (optical and adiabatic band gaps  $E_G^{\text{opt}}$  and  $E_G^{\text{ad}}$  and photosensitivities  $S_{0,1}$ ) and photo-generation parameters (quantum yields of bound-pair formation  $\eta_0$  and photogeneration of free charge carriers  $\eta$  and thermal-

ization lengths  $r_1$  near the intrinsic photoconductivity edge) of molecular crystals of polyacenes  and related compounds [17]

Crystal	$\Delta E_G^{\text{opt}}$ , eV	$\Delta E_G^{\text{ad}}$ , eV	$S_{0,1}$ ( $\text{lX s}^{-1}$ )	$\eta$	$r_1$ , nm	$\eta_0$
Naphthalene ( $n = 2$ )	4.95	4.7	$4.2 \times 10^{-5}$	$<10^{-4}$	45	$3 \times 10^{-3}$
Anthracene ( $n = 3$ )	4.35	4.1	$\sim 1.0 \times 10^{-4}$	$10^{-4}$ – $10^{-3}$ [1]	60	$\sim 10^{-3}$
Tetracene ( $n = 4$ )	3.45	3.13	$3.2 \times 10^{-3}$	$\sim 10^{-3}$	75	$\sim 10^{-2}$
Pentacene ( $n = 5$ )	2.82	2.47	$1.7 \times 10^{-2}$	0.05	85	0
Rubrene	3.0	–	–	–	–	0.3 [17]
Tetrathiotetracene	2.2	–	–	–	–	
Tetraselenotetracene	1.7	–	–	–	–	
Terphenyl	2.3	–	–	0.03	–	

increasing number of  $\pi$  electrons: it decreases the most significantly (from 7.8 to  $\sim 3.5$  eV) for polyines (series 1.1, see Table 1) and polyenes (series 1.2) and (from 6.0 to 2.1 eV) for polyacenes (series 1.3); for *m*- and *n*-phenylenes,  $E_G^{\text{opt}}$  decreases to a lesser extent (from  $\sim 6.0$  to 3.8 eV) [1].

A similar dependence is observed for molecular crystals of polyacenes. It was shown for them [17] that the energy  $E_G^{\text{opt}}$  (corresponding to the optical absorption edge) decreases in the series naphthalene–anthracene–tetracene–pentacene from 4.8 to 2.5 eV (Table 4) and the quantum yield increases from  $10^{-4}$  to  $5 \times 10^{-2}$ , respectively.

Fairly large values of  $\eta$  for conjugated polymers containing no nitrogen (at a level of  $10^{-4}$ – $10^{-3}$ ) were obtained for polymers with a high degree of  $\pi$  conjugation in the main chain (polydiphenylbutadiene and its block copolymer with phenylacetylene derivatives), as well as interacting aromatic chromophores in the lateral chain (polyvinylanthracene); in the latter case, the quantum yield is of the same order of magnitude as  $\eta$  of its crystalline analog—anthracene crystals [1, 17]. For polymers with different types of conjugation, introduction of nitrogen (replacement of anthracene by carbazole and naphthalene by indole) and –CN, –Cl, and –I groups leads to an increase in  $S$  and expansion of the sensitivity range to longer wavelengths (Fig. 5a, curves 2, 3, 8). For nitrogen-containing polyschiff bases, the maximum value of  $\eta$  is obtained for com-

pounds prepared on the basis of *p*-phenylenediamine and benzyl with an excess of diamine:  $\eta = 10^{-4}$  [1].

In going from polyphenylenes of different structures (series 1.3) to polyphenylenevinylenes (series 1.4) and polythiophenes (whose structure is similar to that of polyphenylenevinylenes) (series 2.4), enhancement of photosensitive properties is observed: photocurrent, quantum yield of photogeneration (Fig. 5b, curve 10), and carrier mobility increase. Introduction of various oxygen-containing lateral groups into polyphenylenevinylenes (series 2.4) leads to an increase in  $\eta$  by a factor of 5 [120, 121], whereas an introduction of a phenyl group results in an increase in  $\eta$  by no more than a factor of 2 (series 1.4). Polyphenylenevinylenes are characterized by relatively high (for polymers) mobilities of charge carriers (holes) in the range  $10^{-3}$ – $10^{-5}$   $\text{cm}^2/(\text{V s})$  [80, 122]. A value of about  $10^{-4}$   $\text{cm}^2/(\text{V s})$  is characteristic of the new class of photosensitive polymers—polyamidines (Fig. 5, curve 11), which contain amidine groups in the main chain. These groups can provide efficient two-center bonding with formation of cyclic and linear ensembles, which leads to the formation of a quasi-conjugated system and, therefore, the occurrence of photoconduction. For polyamidines, the photoconductive properties ( $\eta = (1.5$ – $8.5) \times 10^{-2}$  [16]) are due to the possibility of forming such supramolecular structures (Fig. 6). Apparently, linear structures (Fig. 6a) are responsible for the carrier transport, and cyclic structures (Fig. 6b) are responsible for the weak (up to 3% per 1  $\mu\text{m}$ ) absorption in the vicinity of 620 and 960 nm and for the ability to form complexes with acceptor

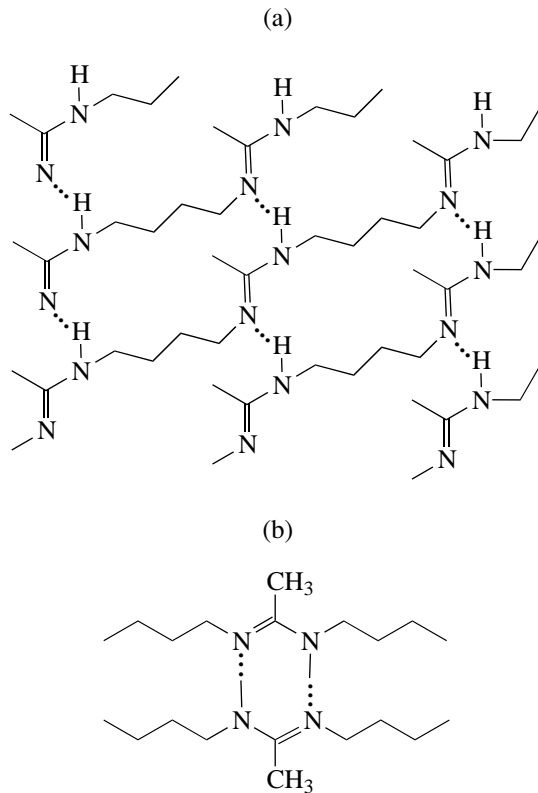


**Fig. 6.** (a) Linear and (b) cyclic supramolecular structures of polyamidines, which are responsible for the photoconductivity.

molecules of similar structure and the carrier photogeneration [16].

For polysilylenes and polygermylenes (Table 1, series 2.1), the mobility is determined by the nature of lateral substituents: for aromatic groups,  $\mu = 10^{-5}$ – $3 \times 10^{-3}$  cm<sup>2</sup>/(V s) and, for aliphatic groups,  $\mu = 2 \times 10^{-5}$ – $1.5 \times 10^{-4}$  cm<sup>2</sup>/(V s). In this case, the mobility activation energy increases by about a factor of 2 when aliphatic groups are replaced by aromatic ones [86]. For polytetraphenylbenzidine, the activation energy  $\Delta E$  ranges from 0.14 to 0.25 eV and depends on the electric field strength  $\mathcal{E}$ . When low-molecular impurities (which facilitate either hole or electron transport) are introduced,  $\Delta E$  increases to 0.6 eV and also depends on the field  $\mathcal{E}$  [86]:

$$\Delta E = A - k(c_d, \varepsilon_{1/2})\mathcal{E}^{1/2},$$

where  $k(c_d, \varepsilon_{1/2})$  is a function of the concentration  $c_d$  and the oxidation potential  $\varepsilon_{1/2}$  of the introduced transport molecules and  $A$  is a constant.

Analysis of the data on the intrinsic photoconductivity of polymers shows the following.

(i) As the polyconjugation regions develop, the ionization potential  $I_D$  decreases simultaneously with the increase in the electron affinity  $A_A$ , which leads to the decrease in the band gap width:

$$\Delta E_G = I_G - A_A - 2P, \quad (10)$$

where  $P$  is the energy of polarization of the medium by a charge carrier [1, 17] and  $I_G$  and  $A_A$  are the ionization potential and the electron affinity of molecules in the gas phase, respectively. The widths of the optical energy gap ( $E_G^{\text{opt}} \approx \Delta E_G$ ) and the adiabatic energy gap are related as follows:  $E_G^{\text{ad}} = E_G^{\text{opt}} - E_p$ , where  $E_p = \delta E$  (Fig. 3b) is the polaron-formation energy.

(ii) The decrease in the energy  $E_G^{\text{ad}}$  is accompanied by the increase in the quantum yield of photogeneration and carrier mobility.

### 3.1.2. Mechanism of carrier photogeneration.

The mechanism of carrier photogeneration in polymer semiconductors near the intrinsic absorption edge can be described by a model proposed for molecular crystals, which are characterized, as polymers, by weak intermolecular interaction. It was shown for these crystals [17] that, near the threshold, the spectral dependence of the quantum yield has the form

$$\eta(\hbar\omega, T, \mathcal{E}) \propto A(\mathcal{E}, T)(\hbar\omega - E_G^{\text{ad}})^n, \quad n = 2/5, \quad (11)$$

where  $A(\mathcal{E}, T)$  is a function of temperature  $T$  and electric field strength  $\mathcal{E}$ . The difference between the values of  $E_G^{\text{ad}}$  and  $E_G^{\text{opt}}$ , determined by the energy spacings between the levels of conductivity of excited relaxed CP states and unrelaxed CT states, is in the range 0.1–0.25 eV and is equal to the energy of formation of a molecular polaron,  $E_p$ , which is involved in the carrier photogeneration through the CP states (Fig. 3c). In molecular media, this process is multistep and is described by the so-called autoionization model of intrinsic photogeneration [17]. According to this model, the formation of CP states (which generate free carriers through field-assisted thermal dissociation) occurs in several successive stages (Fig. 3c): (i) photogeneration of a neutral exciton state (formation of CT states) (stage *I*); (ii) autoionization of the exciton state, as a result of which a positive ion and a quasi-free hot electron arise (stage *II*); and (iii) thermalization of the hot electron due to inelastic scattering by lattice vibrations, which leads to the formation of a thermalized CP state (stage *III*). In the final stage, the thermal dissociation (stage *IV*) of this state under the action of the Coulomb and external fields (according to the Onsager theory [46]) leads to the formation of charge carriers. The latter become free at a distance of about the Coulomb radius  $r_C \approx 15$ – $20$  nm [1], which is determined by the equality of the Coulomb and thermal energies.

Introduction of an efficient acceptor—fullerene—into a polymer gives rise to a new long-wavelength band at  $\hbar\omega < E^{\text{opt}}$  in the absorption spectra of the polymer. In addition (at a fullerene concentration of 5–7 mol %), photoconductivity of the polymer increases by a factor of 3–500, depending on the polymer structure [113, 125–127]. Photogeneration in such media occurs as a result of photoinduced electron transfer between the

photoconductive polymer (by the an exciton migrating in its chain) and  $C_{60}$  with subsequent formation of a polaron, which can either dissociate into free carriers (photogeneration) or relax (luminescence) [126]. Measurement of the absorption kinetics of polyvinylcarbazole- $C_{60}$  films showed that a CT state  $(Cz^+-C_{60}^-)^*$  is formed within  $10^{-12}$ – $10^{-11}$  s [127].

If conjugated segments in a polymer have different  $D$ - $A$  properties, at a sufficiently high degree of conjugation, favorable conditions for the formation of  $D$ - $A$  complexes arise. In this case, the values of  $I_G$  and  $A_A$  in expression (10) characterize the ionization potential of the donor fragment ( $I_G = I_D$ ) and the electron affinity of the acceptor fragment, respectively. Such polymers include polyimides and related compounds (series 2.5), as well as polymer  $D$ - $A$  complexes formed by aromatic fragments of polymers with acceptors or metals. When  $D$ - $A$  complexes are formed in a polymer, the energy of  $D$ - $A$  interaction  $E_{DA} = 5 \times 10^{-2}$ – $1$  eV [17] significantly exceeds the energy of intermolecular interaction (which is lower than  $10^{-2}$  eV [17]). Therefore, absorption of light and subsequent photophysical processes (carrier photogeneration, luminescence) are controlled by the properties of the molecules and thin-film polymers can be regarded as solid solutions of molecular complexes.

### 3.2. Polymer $D$ - $A$ Systems—Polyimides

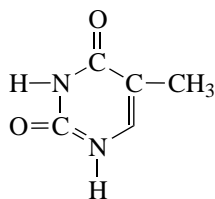
The specific feature of the structure of polyimides is that their monomeric units are intramolecular CTCs. Therefore, they form an intermediate (with respect to the properties) class between the above-considered polymers and molecular  $D$ - $A$  complexes. Aromatic polyimides are widely used in the electronics industry as film-forming, chemically resistant, and radiation-resistant materials with high thermal, optical, and dielectric properties [87]. Introduction of aromatic chromophore groups into the polyimide structure made it possible to obtain new (photosensitive and nonlinear optical) properties with conservation of high thermal stability. Polyimides can be used as photoconductive polymers due to the specific features of their molecular and supramolecular structure: the monomeric unit of a polyimide is a  $D$ - $A$  complex formed by a donor arylene diamine residue,  $R_D$ , and an acceptor diimide fragment of this unit,  $R_A$ . However, the photosensitivity of polyimides depends also on the formation of interchain complexes [89]. The photosensitive properties of polyimides are shown in Fig. 4 as functions of the energies  $A_A$  and  $I_D$  of the acceptor and donor fragments, respectively. It can be seen from Fig. 4 that  $\eta$  increases with decreasing  $I_D$  for polyimides with the same acceptor fragment (curve *A*) and the slope of the dependence remains constant when the acceptor fragment (energy  $A_A$ ) is varied (see inset, curves *D*–*F*). The value of the slope is  $d(\log \eta)/d(A_A - I_D) = 1.94$  (for the dependence of  $\eta_0$

on the difference  $A_A - I_D$ , the slope is 1.03). An increase in  $A_A$  by varying  $-X-$  in the acceptor fragment  $R_A$  (with a constant donor fragment) leads to an increase in  $\eta$  (inset in Fig. 4, curves *D*–*F*) in the series of  $R_A$  I–II–III–IV–V–VI (see Subsection 2.2.2.3). The value of  $\eta_0$  also increases with an increase in  $A_A$  (series III(1)–III(8), II(6)–II(14)) and a decrease in  $I_D$  (series VI(6)–VI(8), VI(16)); i.e., the dependences of  $\eta$  and  $\eta_0$  on  $(A_A - I_D)$  have the same character as those for other classes of molecular  $D$ - $A$  complexes [3, 12]. It can be seen that, for the donor fragments formed by substituted benzimidazoles (6a–6c, see Subsection 2.2.1), with a constant acceptor fragment ( $R_A$  is DPO), both  $S$  and  $\eta$  increase in the series  $-H$ ,  $-CH_3$ ,  $-C_6H_5$  with an increase in the donor properties of the substituents [92]; when  $R_D$  is phenyl-substituted benzimidazole (6c), the photosensitive properties increase with increasing acceptor properties in the series  $-O-$ ,  $-CO-$ ,  $-SO_2-$ ,  $-(CF_3)_2-$  (acceptors from series III–VI; see inset to Fig. 4, curve 4). The maximum value of  $\eta$  was obtained for the acceptor resorcin fragment. Obviously, the reason for this fact is in structural factors [92] and the increase in the length of the monomeric unit and related increase in  $r_t$ . The decrease in the quantum yield of luminescence (which competes with photogeneration (Fig. 4, curve *III*)) also correlates with the increase in  $\eta$  with decreasing  $I_D$ . The mobility of charge carriers in polyimides with the strongest donor properties ( $R_D$  are triphenylamine or diphenylanthracene) is  $2 \times 10^{-5}$ – $3 \times 10^{-3}$  cm<sup>2</sup>/(V s) [128, 129].

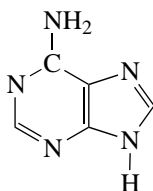
Polyimides with donor fragments containing phenyl or methyl groups ( $-C_6H_5$ ,  $-CH_3$ ) from series II(12a), II(12b), and I(12a)–V(12a) have high photosensitivity in the visible spectral range [93], as well as their triphenylamine-containing analogs [89, 90]. Note that the replacement of the  $-\overset{|}{C}-$  atom by the  $-\overset{|}{Si}-$  atom (transition from series 12 to series 13) leads to the decrease in  $S_{0.1}$  (by an order of magnitude) and  $\eta$  (by more than a factor of 4). The presence of a band at 660 nm (which is characteristic of ionized triphenylamine ( $TPA^+$ ) [96]) in the luminescence spectra of triphenylamine-containing polyimides and high values of  $S_{0.1}$  for polyimides containing phenyl rings in the donor fragment (the ionization potentials of these rings in the neutral state exceed those for ionized rings by more than 0.1 eV) also confirm the formation of interchain  $D$ - $A$  complexes in polyimides and their significant contribution to the carrier photogeneration.

Polyquinazolones, whose structure is similar to that of polyimides, also have high values of  $S$  and  $\eta$  in the visible spectral range [94]. Note that the values of  $\eta \approx 0.1$  are 2–3 orders of magnitude higher than those for the monomer molecules of crystals having the same

number of nitrogen atoms in the aromatic system (thymine and adenine) [130] (Fig. 5b, curves *I, II*):



thymine ( $\Delta E_G = 4.8$  eV and  $E_G^{\text{opt}} = 3.8$  eV),



adenine ( $\Delta E_G = 4.55$  eV and  $E_G^{\text{opt}} = 3.9$  eV).

Another class of polymers with a structure similar to that of polyimides (but, in contrast to them, insoluble) is polymellitimides, polybenzimidazoles, and polybenzoxazoles. For polymellitimides, which differ from polyimides in the acceptor group with a larger value of  $A_A = 1.9$  eV [92], the energies  $E^{\text{opt}}$  and the energies of activation of dark conductivity are lower [5]. The photoconductivity is *p*-type in polymellitimides and *n*-type in polybenzoxazoles [5]. The aromatic heterocyclic polymers under study form a series in the following order of ascending conductivity: polybenzoxazoles, poly-(*N*-phenyl)-benzimidazoles, and polymellitimides. For polybenzoxazoles, a correlation is observed between the conjugation efficiency and the energy parameters: the widths of the energy gaps and the energies of excited states increase with a decrease in the degree of conjugation [5]. The correlation between the conductivity-activation energy, the degree of conjugation, and other energy parameters suggests the existence of intermolecular complexes, which is confirmed by both the appearance of new absorption bands due to the introduction of donor or acceptor molecules [31, 32] and the ESR data [5]. In going from polyimides to polyamideimides, which have a similar structure (with the same donor fragments),  $\eta$  and  $S$  decrease by almost an order of magnitude. The exception is polyamideimides with  $R = -C_6H_4(COOH)$ . Obviously, this fact is related to the formation of the *D*-*A* complex  $NH^+ - COO^-$  with a high dipole moment  $\mu_e$  and a high efficiency of formation of bound pairs  $\eta_0 \propto \mu_e$ .

### 3.3. Molecular *D*-*A* Complexes

#### 3.3.1. Structural regularities of photoeffect.

**3.3.1.1. Regularities of changes in the quantum yield upon varying the energy parameters of the complex structure.** The dependences of the quantum yields of photogeneration  $\eta$  and formation of bound pairs  $\eta_0$

on the parameter  $A_A - I_D$  (which characterizes the energy structure of molecular complexes) for the investigated homologous series of molecules of *D*-*A* complexes are shown in Fig. 7 and listed in Table 2 (the regularities of changes in  $\eta$  for different structures were considered in more detail in [11, 12]). The dependences 6–20 in Fig. 7 are given for the molecules of the following complexes: polyvinylcarbazoles with dyes (6), carbazolyl-containing polymers with ternary complexes of dyes (7), substituted polyphenylenevinylenes (8), azo pigments (9), polyimides with varied donor and acceptor fragments (10), perylenes (11), polyimides with different donor fragments with a fullerene (12), squalenes (13), azides (14), complexes of poly-9-substituted carbazoles with heteryltricyanobutadienes (15), azides with the fullerene  $C_{70}$  (16), polyimides with a triphenylamine donor fragment and different acceptor dyes (17), complexes of polyimides with different donor fragments and acceptor elements with an unfilled *p* shell (19), and complexes of aromatic nitrogen-containing donor molecules with acceptor elements of Group VI of the periodic table with an unfilled *p* shell (20).

Tables 2 and 3 contain the ranges of values of the degree of charge transfer  $\delta$ , the distance of the initial electron transfer in a complex  $r_0$ , and the dipole moment  $\mu_e = \delta r_0$  determined from these values for the molecules of the complexes in the excited state. The values of  $A_A$  and  $I_D$  are taken for isolated molecules and their difference  $A_A - I_D$  is taken with respect to the difference for the first member of each series  $(A_A - I_D)_{\text{min}}$ . The energy of photons corresponds to the maximum of the absorption band; the value of  $\eta$  corresponds to the field strength  $\mathcal{E} = 8 \times 10^5$  V/cm; and  $\eta_0$  at thermalization lengths  $r_t < 3$  nm (characteristic of most series of complexes), as well as  $\delta$  and  $\mu_e$ , is independent of the field strength [3, 11, 12]. It can be seen from Fig. 7 and Tables 2 and 3 that, for each series, the value of  $\eta$  and the parameters of photoprocesses  $\delta$ ,  $\mu_e$ , and  $\eta_0$  unambiguously depend on the parameter  $A_A - I_D$  of the energy structure of the molecules of a complex. An increase in  $A_A - I_D$  in the range of about 1 eV leads to an increase in  $\eta$  up to three orders of magnitude.

Let us consider the structural regularities of changes in  $\eta$  with increasing  $r_0$  in a complex (Fig. 7 and Table 3). The smallest values of  $r_0$  (according to the estimates of [9, 12]) correspond to phthalocyanine crystals and complexes of porphyrins with quinones dispersed in a matrix (curves *I, 2*). The value of  $\eta$  increases with an increase in  $(A_A - I_D) - (A_A - I_D)_{\text{min}}$  regardless of the reason for the increase in this difference (due to either a decrease in the ionization potential  $I_D$  in the series of donor fragments with the same acceptor (symbols *a* in Fig. 7) or an increase in the electron affinity  $A_A$  in the series of acceptors with the same donor, i.e.,  $I_D = \text{const}$  (symbols *b* in Fig. 7)) [9, 117–119].

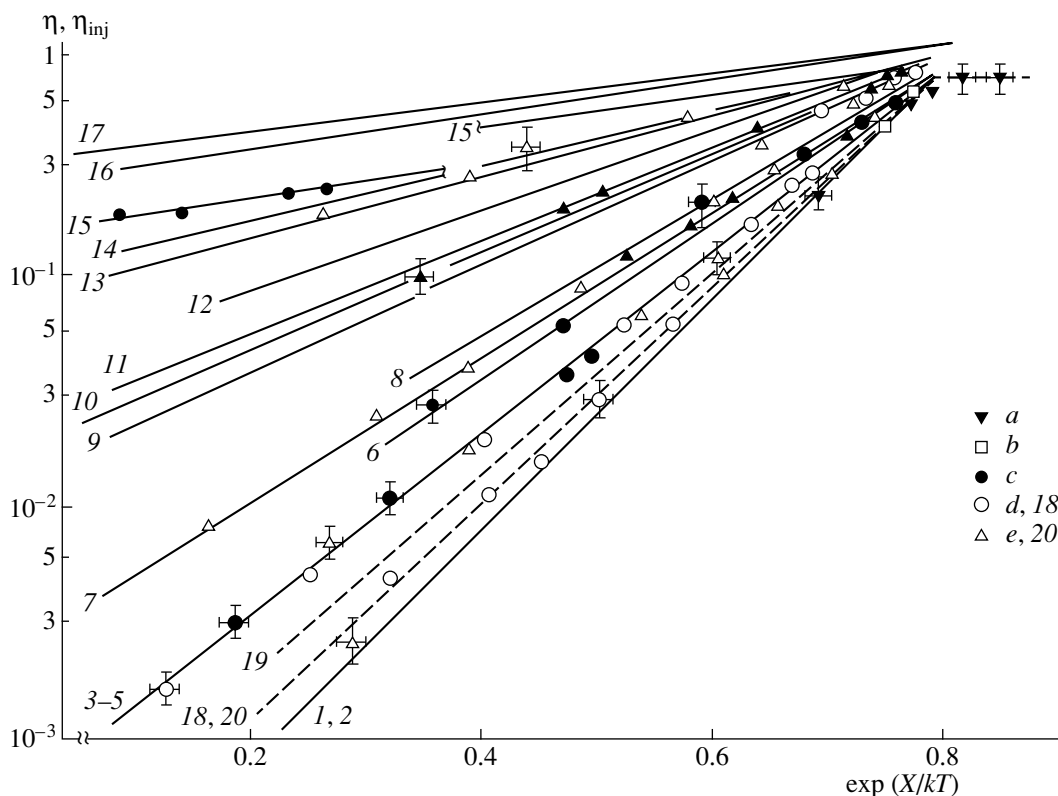


**Fig. 7.** Dependences of the (1–17) quantum yield of photogeneration  $\eta$  and (18–20) injection efficiency  $\eta_{inj}$  (dashed lines) on the energy parameter  $X = (A_A - I_D) - (A_A - I_D)_{min}$  at  $T = 300$  K for the series of the complexes (the numbers of the curves correspond to the numbers of series in Subsection 2.2.5.5. and Table 2) of (1, 2) porphyrins with (a) quinones and (b) phthalocyanines, (3–5) poly-9-substituted carbazoles (c is acceptor—2,4,7-trinitro-9-fluorenone) and vinyl aromatic polymers (d is acceptor—2,4,7-trinitro-9-dicyanomethylenefluorene) with acceptors of the fluorene series (e is donor—polyvinylcarbazole). The compounds characterized by dependences 6–20 are clarified in the text in Subsection 3.3.1.1. The series differ in the initial electron-transfer distance in a complex ( $r_0$ ), which increases with increasing number in a series.  $(A_A - I_D)_{min}$  is the difference in the energy parameters of the structure for the first member of each series. The energy of photons  $\hbar\omega$  corresponds to the maximum absorption and  $\mathcal{E}$  is the limiting field strength for a given complex. The data for curves 3–7, 10, 12, and 14–19 were obtained by us; the data for curves 2, 8–10, and 20 were obtained by us and compared with the data in the literature; and the data for curves 1, 11, and 13 are taken from the literature.

### 1. Polymer CTCs.

#### 1a. D–A complexes of carbazolyl-containing polymers and their aromatic analogs with fluorene derivatives.

The dependences of  $\eta$  and  $\eta_{inj}$  on the energy parameter  $A_A - I_D$  for the complexes of carbazolyl-containing polymers and their aromatic analogs (series 2–4) are shown in Fig. 7 (curves 3–5) and listed in Table 2 (series 2–4). As for series 2, the quantum yields  $\eta$  and  $\eta_0$  increase with an increase in the parameter  $(A_A - I_D) - (A_A - I_D)_{min}$  (which can be increased by either increasing  $A_A$  at  $I_D = \text{const}$  (points c in Fig. 7) or decreasing  $I_D$  at  $A_A = \text{const}$  (points d in Fig. 7)).

#### 1b. Complexes of carbazolyl-containing polymers with dyes and complexes of dyes.

The dependences of  $\eta$  on the parameter  $A_A - I_D$  varied by changing either the electron affinities of the ligand and atom A in the dye molecule ( $A_A^L$  and  $A_A^A$ , respectively) or the ionization potential of its donor

fragment,  $I_A^D$ , for the complexes of polyvinylcarbazole with dyes [105] and ternary complexes of dyes [107] are shown in Fig. 7 (curves 6 and 7). The data of [118, 119] indicate that  $\eta$  and  $\eta_0$  increase with the increase in  $A_A$ , which, according to (9), is due to either the increase in  $A_A^L$  in the series of ligands, or the increase in  $A_A^A$  of the A atom (in going from O to S and Se) of the dye molecule  $R(A)$ , or the decrease in  $I_A^D$  of the donor fragment of the dye molecule. The slope of the dependences increases in going from the dye molecule (curve 5) to more complex molecules of ternary dye complexes (curve 6).

#### 2. Intramolecular complexes in a polymer matrix.

The quantum yields of photoprocesses in intramolecular complexes in polymer matrices have been studied for the series of azo pigments, perylenes, squalenes, and azides (Fig. 7, curves 9, 11, 13, 14). The value of  $\eta$ , as for series 2–6, increases with increasing parameter  $(A_A - I_D) - (A_A - I_D)_{min}$ , regardless of the origin of this

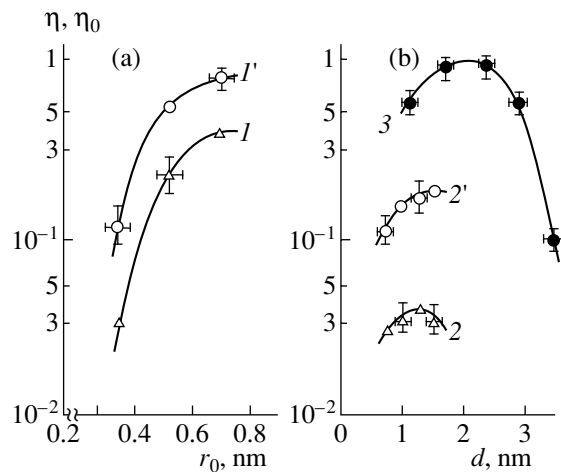


**Fig. 8.** Dependences of (1–3) the quantum yield of photogeneration  $\eta$  and (1', 2') the quantum yield of formation of bound pairs  $\eta_0$  on the spatial structural parameters of the molecules of  $D$ - $A$  complexes: (a) the initial electron-transfer distance  $r_0$  and (b) the distance  $d_0$  between the fragments through which bound charge carriers migrate. For the homologous series of molecules: (1) complexes of polyvinylcarbazole with acceptor molecules having similar  $A_A$ ; (2, 2') polymer 2,4,7-trinitro-9-fluorenone complexes; and (3) complexes of porphyrins and quinones [9] with different numbers of  $-\text{CH}_2-$  groups [3].

increase: due to either the increase in  $A_A$  (with the same donor fragment and  $I_D = \text{const}$ ) or the decrease in  $I_D$  (with the same acceptor and  $A_A = \text{const}$ ).

### 3. Complexes of aromatic polymers with intramolecular CTCs.

The behavior of the quantum yields in the complexes formed by aromatic polymers with intramolecular CTCs is considered using as an example complexes of carbazolyl-containing polymers (polyvinylcarbazoles and polyepoxypropylcarbazoles) with heteryltricyanobutadienes [97], tricyanovinylaryls [112], or fluorene derivatives, which are intramolecular CTCs ( $R$  is pipyridine) [102].

For molecular complexes in which one of the components is an intramolecular complex absorbing a photon, the structural regularities of the quantum yields have been studied as functions of the parameter  $(A_A - I_A^D) - I_D$  (the intramolecular CTC is an acceptor) and the parameter  $A_A - (A_D^A - I_D)$  (the intramolecular CTC is a donor). Examples of the complexes of the first type are the complexes of carbazolyl-containing polymers (polyvinylcarbazoles and polyepoxypropylcarbazoles) with heteryltricyanobutadienes. For these complexes, the dependences of  $\eta$  and  $\eta_0$  on the difference  $(A_A - I_A^D) - I_D$  varied by varying  $I_A^D$  of the heterocycle with constant  $A_A$  and  $I_D$  (Fig. 7, curve 15) indicate their increase with the increase in the energy parameter caused by the decrease in  $I_A^D$ . However, the slope of these dependences is lower than that for other series

(curves 1–14).  $\eta$  and  $\eta_0$  increase until the ionization potential of the donor fragment of the acceptor molecule  $I_A^D$  decreases to the ionization potential of the donor molecule  $I_D$  [97]. For complexes formed by donor molecules that are intramolecular CTCs, for example, azides with fullerenes as acceptors (series 16), the dependence of  $\eta$  on  $A_A$  changes and becomes reverse to the dependence observed for azide molecules dispersed in a neutral matrix (series 14). Since

$$\eta(A_A, A_D^A, I_D) \propto \exp(A_A - A_D^A - I_D),$$

$\eta$  decreases with increasing electron affinity of the acceptor fragment of the donor molecule  $A_D^A$  until the latter becomes as high as  $A_A$  of the acceptor molecule.

### 4. Polymer intramolecular complexes of polyimides sensitized by dyes and fullerenes.

For polyimides sensitized by acceptors (Fig. 7, curve 12),  $\eta$  increases with increasing electron affinity  $A_G$  (the symbol  $G$  is used in order not to confuse this parameter with  $A_A$ —the electron affinity of the acceptor fragment of a polyimide) of the acceptor molecule with a slope  $d\eta/d(A_G - I_D)$  that is lower than that for polyimides (curve 10) by a factor of 7.5; i.e., the same dependence is observed as for the series of carbazolyl-containing polymers with heteryltricyanobutadienes, in which both components are intramolecular CTCs (curve 15).

#### 3.3.1.2. Behavior of the change in the quantum yield upon varying the spatial-structure parameters.

##### 1. Dependences of $\eta$ on the initial charge-transfer distance $r_0$ .

For the series of complexes, the value of  $r_0$  is estimated from the structural formulas of the molecules with regard to the spatial position of their fragments [12]. For complexes of carbazolyl-containing polymers with heteryltricyanobutadienes, it is estimated from the radius  $r_{\text{ex}}$  ( $r_0 < r_{\text{ex}}$ ) of the exciplex formed by the excited acceptor molecule (heteryltricyanobutadiene) and the carbazolyl fragment of a polymer [18]. The radius of the exciplex  $r_{\text{ex}} = 0.6$  nm [97], which is equal to the distance between coplanar planes of aromatic fragments (heterocycle  $R_D$  and carbazolyl fragment). For the complexes formed by carbazolyl-containing polymers and ternary dye complexes,  $r_0$  is also estimated from the value of  $r_{\text{ex}}$ , which is defined as the distance between the exciplex-forming fragments of the molecule of the dye complex and the carbazolyl fragment of the polymer. The radius of the exciplex for the molecules of the class under consideration is  $r_{\text{ex}} = 0.8$  nm; thus,  $r_0 < 0.8$  nm [11].

To study the dependences of  $\eta$  and  $\eta_0$  on  $r_0$ , a sequence of complexes was chosen that does not correspond to the accepted definition of a homologous series. This sequence includes complexes on the basis of polyvinylcarbazoles ( $I_D = \text{const}$ ) with acceptors having the same values of  $A_A$  chosen from the series of fluorenes, heteryltricyanobutadienes, and dyes. As can be

seen from Fig. 8a (curves 1 and 1'), the values of  $\eta$  and  $\eta_0$  increase with increasing  $r_0$ , which is indicative of the dominant effect of the parameter  $r_0$  on  $\eta$  and  $\eta_0$ .

2. *Dependences of  $\eta$  on the distance between aromatic fragments of a polymer donor molecule.*

The dependences of  $\eta$  and  $\eta_0$  on the distance  $d$  between aromatic fragments of a polymer donor molecule, through which migration occurs, were determined for the complexes formed by 2,4,7-trinitro-9-fluorenones and 2,4,7-trinitro-9-dicyanomethylenefluorenes with poly-9-substituted carbazoles (donors of series 5) with varied  $d$  (Fig. 8b). It can be seen from Fig. 8b that  $\eta$  and  $\eta_0$  increase with increasing  $d$  until the latter attains some value  $d = d_0$ , after which  $\eta_0$  remains constant (curve 2') and  $\eta$  begins to decrease with a further increase in  $d$  (curve 2). A similar dependence is observed for the complexes of porphyrins with quinones [9], for which  $\eta$  also increases with increasing  $d$  to a certain value and drops at  $d > d_0$  (curve 3).

Thus, for the homologous series of the complexes studied, the dependences of  $\eta$  and  $\eta_0$  on the parameter

$$X = (A_A - I_D) - (A_A - I_D)_{\min}$$

are linear in the coordinates

$$\ln \eta = f(\exp X)$$

(Fig. 7), and it is known that the slope of the dependences

$$\ln \eta_0 = f(\exp X)$$

is lower by a factor of 2 [11, 12] (not shown in Fig. 7). The dependences are described by the functions [12]

$$\eta(A_A - I_D) = \exp\{-k^{(j)}[1 - \exp(X/kT)]\}, \quad (12)$$

$$\eta_0(A_A - I_D) = \exp\{-k_0^{(j)}[1 - \exp(X/kT)]\}, \quad (13)$$

where  $k^{(j)}$  and  $k_0^{(j)}$  are the slopes of the curves

$$\ln \eta = f(e^{X/kT}) \quad \text{and} \quad \ln \eta_0 = f(e^{X/k_0T}),$$

$j$  is the number of a homologous series, and  $\rho$  is a constant; note that  $k^{(j)} = nk_0^{(j)}$ , where  $n = 2$ . The values of  $k^{(j)}$  and  $k_0^{(j)}$  correlate with  $r_0$ . It can be seen from Fig. 7 and Table 3 that the slope is the highest for the series with the smallest  $r_0$  and the lowest for the series with the largest  $r_0$ , while the dependence of  $k_0^{(j)}$  on  $r_0$  is described by the function [3, 12]

$$k_0^{(j)}\left(\frac{r_0}{\rho}\right) \propto \exp\left(-\frac{r_0}{\rho}\right). \quad (14)$$

If the value of  $r_0$  is known for one series at least, formula (14) can be used to determine  $r_0$  for any series of complexes under study. The values of  $r_0''$  calculated by formula (14) (calculation error is 10%) are compared in

Table 3 with the values of  $r_0'$  estimated from the structural formulas of the molecules taking into account the spatial position of coplanar fragments but disregarding the angles between them (estimation error is 50%). It can be seen from Table 3 that the calculated values of  $r_0''$  are in the range of values of  $r_0'$  estimated from the structural formulas; however, the error in their determination is reduced from 50 to 10%. For the polymer series of polyimides, the value of  $r_0$  estimated from formula (14) is  $r_0 = 0.45\text{--}0.52$  nm; i.e., it is intermediate between the values of  $r_0$  for  $D\text{--}A$  complexes of polyvinylcarbazoles with fluorene derivatives (weak  $D\text{--}A$  complexes) and polyvinylcarbazoles with intramolecular CTCs.

The established structural regularities of changes in the quantum yields are described by the dependence of  $\eta$  on the structural parameters of the complex molecules ( $A_A - I_D$ ,  $r_0$ ,  $d$ ) ascertained in [11, 12] on the basis of the migration model of photogeneration [3]. This dependence has the form

$$\begin{aligned} & \ln[\eta(A_A - I_D, r_0, d)] \\ &= A - 2B_0 \exp\left[\frac{\sum f(r)}{\rho d} (1 - e^{X/kT})\right], \end{aligned} \quad (15)$$

where  $r = r_0 + nd$  and  $n$  is the number of transport events through donor molecules that is required to obtain the value of the thermalization length  $r_t$ .

At  $\eta > 0.4$ , expression (15) transforms into

$$\begin{aligned} & \eta(A_A, I_D, r_0, d) \\ & \approx \left[1 - \exp\left(-\frac{r_0 + nd}{\rho_0}\right)\right] \exp\left(-\frac{A_A - I_D - C}{kT}\right), \end{aligned} \quad (16)$$

where  $C$ ,  $n$ , and  $\rho_0$  are the constants obtained in [3].

Let us consider the physical meaning of the parameter  $A_A - I_D$  and the nature of the dependences of the quantum yields on this parameter. The difference  $A_A - I_D$  is the energy that must be spent to detach an electron from an isolated donor molecule and transport it to infinity with subsequent transport from infinity to an isolated acceptor molecule. Actually, the charge phototransfer occurs directly between interacting donor and acceptor molecules, and the transfer energy is reduced due to Coulomb and exchange (resonance) interactions between the donor and acceptor molecules and the polarization of the environment by these molecules [3, 17] by  $\Delta = E_C + E_{\text{res}} + 2P$ , where  $E_C$  and  $E_{\text{res}}$  are the energies of the Coulomb and exchange (resonance [1]) interactions, respectively, and  $P$  is the polarization energy. This energy is constant in series. Indeed, the Coulomb interaction, which is controlled by the electron density distribution and the sizes of the molecules, is almost constant in the series of molecules hav-



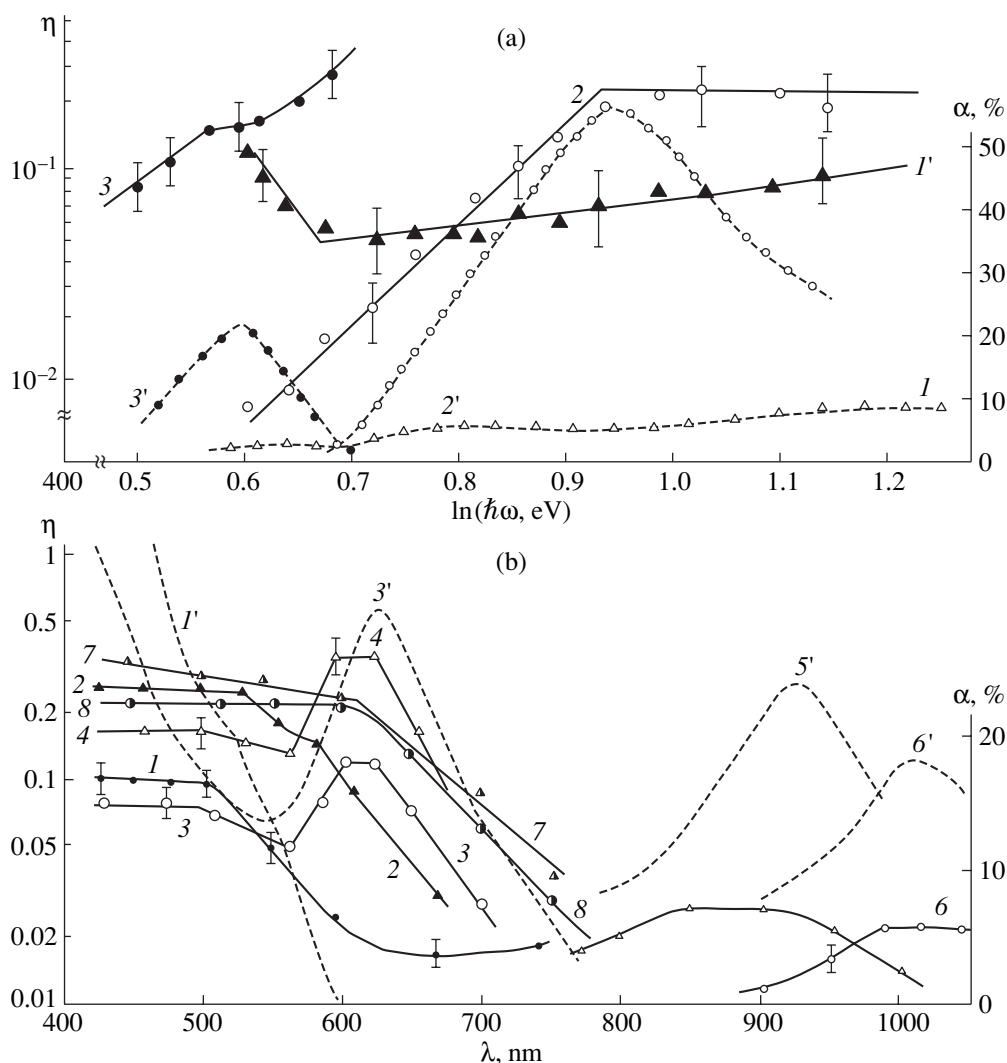


**Fig. 9.** Spectra of the quantum yield  $\eta$  (solid lines) and absorption  $\alpha$  (dashed lines) of (a) polyvinylcarbazole sensitized by (*I*, *I'*) fluorene derivative (2,4,7-trinitro-9-dicyanomethylenefluorene), (2, 2') heteryltricyanobutadiene, and (3, 3') ternary dye complex and (b) triphenylamine-containing polyimide sensitized by (3, 4) malachite green; (5, 5' and 6, 6') IR dyes with absorption maxima at 830 and 950 nm, respectively; (7) 2,4,7-trinitro-9-dicyanomethylenefluorene; and (8) fullerene. Curves *I* and 2 (b) refer to nonsensitized polyimides containing (*I*) one and (2) two triphenylamine groups [89, 90]. The concentrations of the sensitizers (2,4,7-trinitro-9-dicyanomethylenefluorene, dyes, and fullerene) are 3, 1, and less than 0.7 mol %, respectively.

ing a similar structure, and the polarization energy for aromatic organic molecules is also constant ( $\sim 1.5$  eV [17, 18]). Therefore, the difference  $I_D - A_A - \Delta$  in the homologous series has the meaning of electron-transfer energy in a molecule of a complex and  $\Delta$  is the energy  $W_{DA}$  of *D*-*A* interaction in this molecule. These quantities are determined from the energy parameters of isolated donor and acceptor molecules.

**3.3.2. Spectral behavior of the change in  $\eta$  in different structures of molecular complexes.** The shape of the spectra of the quantum yield  $\eta(\hbar\omega)$  depends on the type of sensitization (Fig. 9). For structural chemical sensitization, it has been ascertained experimentally that the spectrum  $\eta(\hbar\omega)$  depends on the complex structure [3] and, generally, does not correlate with the

absorption spectrum. Several characteristic regions can be distinguished in the dependences  $\eta(\hbar\omega)$  (Fig. 9a):

- (i)  $\eta$  decreases with decreasing  $\hbar\omega$ ;
- (ii)  $\eta$  increases with decreasing  $\hbar\omega$  (at low  $\hbar\omega$ —below a certain value  $\hbar\omega_0(A_A)$ , curve *I*); and
- (iii)  $\eta$  is independent of  $\hbar\omega$  in the absorption band of the acceptor molecule (curve 2).

The experimentally established spectral behavior of the change in the  $\eta$  for different structures of molecular complexes [7], as well as the structural behavior, can be explained on the basis of the migration mechanism of photogeneration proposed in [3]. This mechanism accounts for the shape and nature of the spectral dependences of  $\eta$  in the cases of both structural chemical and spectral types of sensitization, in particular, for aro-

matic polymers with low  $I_D$ , which are used to prepare recording media.

**3.3.2.1. Structural chemical sensitization of polymers by acceptors.** According to the model, the spectrum  $\eta(\hbar\omega)$  for different structures (types of  $D$ - $A$  interaction) can be found on the basis of the known spectra  $r_i(\hbar\omega)$  and  $\eta_0(\hbar\omega)$ . It was shown that the shape of the spectrum  $r_i(\hbar\omega)$  is controlled by the relaxation rate of the photoexcitation energy  $\Delta E/dt$  and can be described as

$$r_i(\hbar\omega) \propto \ln^m(\hbar\omega),$$

where  $m = 0$  at a high vibrational relaxation rate  $k_V$  (as compared to the pair-formation rate  $k_{CP}$ ;

$$m = 0.5 \text{ at } k_V < k_{CP} \text{ and } \Delta E/dt \propto r;$$

$$m = 1 \text{ at } k_V < k_{CP}, \quad \Delta E/dt = \text{const.}$$

The shape of the spectrum  $\eta(\hbar\omega)$  depends on the electric field strength  $\mathcal{E}$  and can be described as [3]

$$\begin{aligned} \eta(\hbar\omega) &= \text{const at } k_V > k_{CP}, \\ &\text{when } r_i(\hbar\omega) = \text{const;} \end{aligned} \quad (17)$$

$$\eta(\hbar\omega) \propto \exp(-\hbar\omega) \text{ for } \mathcal{E} < 8 \times 10^5 \text{ V/cm}$$

$$\begin{aligned} &\text{and } \eta(\hbar\omega) \propto \hbar\omega^\beta \text{ for } \mathcal{E} > 8 \times 10^5 \text{ V/cm} \\ &\text{at } k_V < k_{CP}. \end{aligned}$$

The dependences obtained coincide with those found experimentally (Fig. 9), except for the low-energy region, where, at  $\hbar\omega$  lower than  $\hbar\omega_0$ , an increase in  $\eta$  with decreasing  $\hbar\omega$  is observed, which is not characteristic of Onsager photogeneration (Fig. 9a, curve 1). It has been shown that this spectral shape is due to the migration of bound carriers without losing energy on electron-phonon interactions [3]. Migration of this type is possible when the carrier energy is comparable with the energy of phonons  $h\nu(A_A)$ , which depends on the energy parameters of the molecules. Then [3],

$$\eta(\hbar\omega) \propto \frac{1}{1 - C[\hbar\omega - E_{CT}^{(i)}(\nu = 0)]}, \quad (18)$$

where  $C$  is a coefficient.

The anti-Onsager shape of the spectra (18) is typical of structural chemical sensitization (Fig. 9a, curve 1) of carbazolyl-containing polymers by fluorene derivatives [3]. In the case of the structural chemical sensitization of polyvinylcarbazole polymers by acceptors forming complexes with several charge-transfer bands,  $r_i$  and  $\eta$  can be independent of  $\hbar\omega$  in each band; however, the step shape of the spectral dependences  $\eta(\hbar\omega)$  coincides, within experimental error, with the above-described ones. Hence, it does not seem to be possible to draw any conclusions on the validity of a particular shape of the dependence. With an increase in the acceptor (or donor) properties of one of the substituents  $R_i$  in the structural formulas of fluorene derivatives, the latter transform from acceptors (forming weak CTCs with

carbazolyl-containing polymers) into intramolecular CTCs and, absorbing a photon, form exciplexes with carbazolyl fragments. This process manifests itself in the change in the shape of the absorption and quantum yield spectra [102]:  $\eta$  becomes constant in the absorption band of the acceptor molecule instead of decreasing with decreasing  $\hbar\omega$ , which is typical of photogeneration caused by the photoexcitation of a  $D$ - $A$  complex [3]. At the same time,  $\eta$  decreases in the long-wavelength wing of the spectrum, which is characteristic of exciplexes.

**3.3.2.2. Sensitization of polymers by dyes and intramolecular CTCs.** The independence of  $\eta$  of  $\hbar\omega$  in the absorption band of an acceptor molecule (Fig. 9a, curve 2) is characteristic of the exciplex mechanism of photogeneration, which occurs in the case of the sensitization of polymers by intramolecular complexes, in particular, heteryltricyanobutadiene-containing ones [97], which form in the excited state an exciplex with the carbazolyl fragment of the polymer. The radius of the exciplex is  $r_{ex} = 0.6$  nm [97], which is equal to the distance between coplanar planes of aromatic fragments (heterocycle  $R_D$  and carbazolyl fragment). The occurrence (in the excited state) of a gradient of the electron affinity [3] between these aromatic fragments

$$\frac{\partial A_A}{\partial r} \propto \frac{I_A^D - I_D}{r_{ex}}$$

due to the difference in the values of  $I_A^D$  and  $I_D$  facilitates the separation of bound charge carriers in the CP state.

**3.3.2.3. Polyimides and their organometallic complexes.** In the case of spectral sensitization of polyimides, the photosensitivity spectrum  $S(\hbar\omega)$  coincides with the absorption spectrum  $\alpha(\hbar\omega)$  and the value of  $\eta$  becomes maximal in the absorption maximum. Let us consider the spectra using as an example the spectral sensitization of the most photosensitive polymer—triphenylamine-containing polyimide—by dyes (Fig. 9b) [88–91]. Sensitization of the polyimides containing one triphenylamine group by xanthene (rhodamine 6G) and triphenylmethane dyes (the most efficient is malachite green) (Fig. 9b, curves 3, 4) results in the value of  $\eta$  in the range of dye sensitization being approximately equal to  $\eta$  in the range of intrinsic sensitivity:  $\eta = 0.08$ – $0.15$  [90]. The effects of decreasing  $\eta$  beyond the absorption band (at the photon energies  $\hbar\omega$  either higher or lower than the energy corresponding to the maximum absorption at  $\hbar\omega_0(\lambda_{max})$ ) and the decrease in the radius  $r_i$  at  $\hbar\omega > \hbar\omega_0$  are described by the expressions derived in [3]. The values of  $\eta$ ,  $\eta_0$ , and  $r_i$  determined for polyimides with one triphenylamine group sensitized by different dyes are as follows:

$$\begin{aligned} \eta &= 0.10 \pm 0.03, \quad \eta_0 = 0.26 \pm 0.08, \\ &\text{and } r_i = (3.2 \pm 0.3) \text{ nm} \end{aligned}$$

for sensitization by rhodamine 6G [the peak of  $\eta(\lambda)$ , as well as the peak of  $\alpha(\lambda)$ , is at  $\lambda_{\max} = 530$  nm; the shape of the spectrum is similar to that shown in Fig. 9b (curves 3, 4)];

$$\eta = 0.12 \pm 0.04, \quad \eta_0 = 0.36 \pm 0.12,$$

$$\text{and } r_t = (2.8 \pm 0.3) \text{ nm}$$

for sensitization by malachite green ( $\lambda_{\max} = 650$  nm); and

$$\eta = 0.08 \pm 0.03, \quad \eta_0 = 0.3 \pm 0.1,$$

$$\text{and } r_t = (3.0 \pm 0.3) \text{ nm}$$

for sensitization by a dye based on a pyrylium salt ( $\lambda_{\max} = 630$  nm). For polyimides with two triphenylamine groups, the values of  $\eta$  and  $\eta_0$  increase, in comparison with the polyimides containing one triphenylamine group, by a factor of 2–3 (Fig. 9b, curve 2 with respect to 1) and  $r_t$  increases up to 1.5 times [90, 91].

The introduction of a dye for the visible spectral range, which changes the absorption region and the spectral sensitivity of polyimides, in particular, malachite green (Fig. 9b, curves 3 and 4 with respect to 1 and 2), regardless of its concentration  $c_{\text{dye}}$ , does not change the value of  $\eta_0$  but results in an increase in  $r_t$  by 0.5–1.0 nm and, therefore, an increase in  $\eta$  by ~20% (curves 3, 4) in comparison with the corresponding nonsensitized polyimides (curves 1, 2) [90].

Analysis of the effect of a dye structure on the value of photosensitivity  $S$  and the quantum yield  $\eta$  [90] showed that the maximum values of  $S$  and  $\eta$  in the case of sensitization of triphenylamine-containing polyimides are obtained for dyes of the triphenylmethane class, whose spatial structure is similar to that of the triphenylamine molecule. The data for carbazolyl-containing polymers, given for comparison, show a similar situation: the most efficient sensitizer for these polymers is the xanthene dye—rhodamine 6G—whose structure is similar to that of carbazole.

Triphenylamine-containing polyimides can also be efficiently sensitized in the IR spectral region. The following complexes were used as IR sensitizers: ternary complexes of dyes, which efficiently sensitize carbazolyl-containing polymers (in particular, polyvinylcarbazole [107]), and ethylenethiolate complexes of transition metals [106] (used for the first time as sensitizers of aromatic polymers). When aromatic polymers, in particular, triphenylamine-containing polyimides, are sensitized by ethylenethiolate complexes of transition metals [106], the maxima of the absorption and photosensitivity bands shift to longer wavelengths when Ni is replaced by Pt or Pd or when one (or several) substituent  $R$  with stronger donor properties is introduced into the chain region. For  $R = -C_6H_5$  and  $-C_6H_4N(CH_3)_2$ , in comparison with  $R = -H$  and  $-CH_3$ , the maxima shift from 1.51 and 1.44 eV to 1.26 and 1.03 eV, respectively (the maxima of the corresponding absorption bands of the dyes themselves are at 1.59, 1.48, 1.3, and 1.17 eV).

The data on the IR sensitization of triphenylamine-containing polyimides are shown in Fig. 9b (curves 5, 6). For all dyes, in the spectra with  $\lambda_{\max} = 780, 830, 950,$  and 1060 nm (for both polyimides, and polyvinylcarbazoles, and polyepoxypropylcarbazoles), a red shift by 0.10–0.15 eV with respect to the maximum of absorption of the dye itself is observed. The value of  $S_{0.1}$  for dyes in the IR-sensitization range is  $\sim 10^3$  cm<sup>2</sup>/J,  $\eta \approx 0.01$  [106], and the shape of the spectrum corresponds to that described in [3]. For polyimides with one triphenylamine group, in the case of sensitization by dyes with  $\lambda_{\max} = 830$  and 950 nm, the photogeneration parameters are  $\eta = 0.02$ ,  $\eta_0 = 0.05$ , and  $r_t = 2.0$  nm and  $\eta = 0.01$ ,  $\eta_0 = 0.02$ , and  $r_t = 1.8$  nm, respectively [91]. The value of  $S_{0.1}$  at wavelength  $\lambda = 1060$  nm is  $\sim 5 \times 10^3$  cm<sup>2</sup>/J, which is an order of magnitude larger than  $S$  in the case of sensitization by the most efficient sensitizer in the fluorene series [101]. In the case of dye sensitization of polyimides with two triphenylamine groups in the IR spectral region (Fig. 9b, curves 5, 6), the values of  $\eta$  and  $\eta_0$  decrease to 0.001–0.003 at a constant  $r_t$ .

The efficiency of IR sensitization (in the range 780–1200 nm), defined as the ratio of the photosensitivities in the dye-absorption maximum and in the range of intrinsic photosensitivity, is 1–3 for the long-wavelength band (650–840 nm) and 0.05–0.1 for the short-wavelength region.

For organometallic complexes of biquinolyl-containing polyimides [114–116], the value of photosensitivity  $S_{0.1}$  is  $3 \times 10^4$  cm<sup>2</sup>/J (in the range 400–750 nm for the Cu<sup>2+</sup>–biquinolyl complex and in a longer wavelength region for the Cd<sup>2+</sup>–biquinolyl complex) (Fig. 10). Thermal cyclization of a polymer (heating to 250°C) leads to a sharp decrease in  $S_{0.1}$  (by two orders of magnitude). The energies  $\hbar\omega_0$  of the maxima of the absorption bands due to the charge transfer in a complex and the quantum yield  $\eta$  depend on the ionization potential of the metal atom  $I_{\text{Me}}$ : the value of  $\hbar\omega_0$  decreases with increasing  $I_{\text{Me}}$  while  $\eta$ , in contrast, increases from 0.004 to 0.07 with increasing  $I_{\text{Me}}$  in the series Tb, Ru, Cu, Cd, Pt (see inset in Fig. 10, curves 1 and 2). This shape of the dependence of  $\eta$  on  $I_{\text{Me}}$ , the correlation of the dependence of the carrier mobility on  $I_{\text{Me}}$  (curve 3) with  $\eta(I_{\text{Me}})$ , and the strong dependence of  $\eta$  on the structure of the monomeric unit of a polyimide (which changes, in particular, due to the polymer cyclization) indicate a complex character of interaction of metal atoms with biquinolyl fragments and suggest that the photosensitivity is, apparently, due not only to the charge transfer in the complex but also to the significant effect of other functional groups of polyimides on the complex.

The experimentally established structural and spectral behavior of the photoeffect in molecular  $D$ – $A$  complexes can be described within the previously proposed model considering the migration mechanism of Onsager photogeneration [3], which takes into account

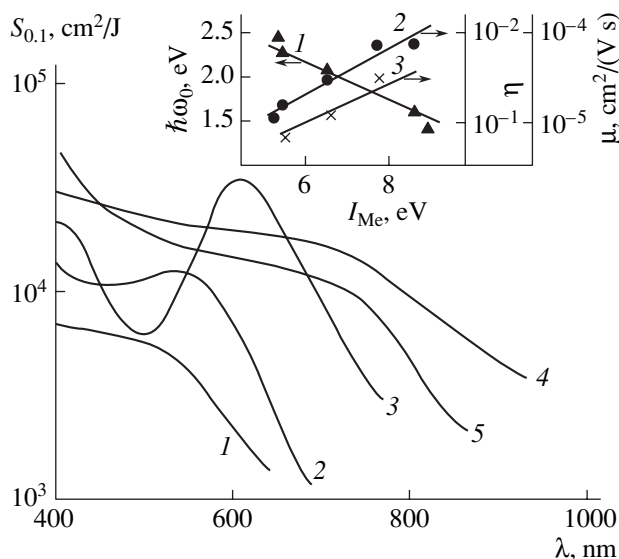


**Fig. 10.** Photosensitivity spectra of aromatic polyimides containing organometallic complexes of different metals in the lateral chain: (1)  $\text{Tb}^{+3}$ , (2)  $\text{Ru}^{+3}$ , (3)  $\text{Cu}^{+2}$ , (4)  $\text{Cd}^{+2}$ , and (5)  $\text{Pt}^{+2}$  [114–116] with (1, 2) bipyridyl and (3–5) biquinolyl aromatic fragments. The dependences of the (1) energy of maximum absorption of a complex  $\hbar\omega_0$ , (2) quantum yield  $\eta$ , and (3) mobility  $\mu$  as functions of the ionization potential of a metal  $I_{Me}$  are shown in the inset.

the above-considered features of molecular media containing CTCs.

### 3.4. Migration Mechanism of Onsager Carrier Photogeneration in Molecular Complexes

According to the model based on the migration mechanism [3], the carrier photogeneration, as in molecular crystals [17], occurs in two stages: *I–II* and *III* (Fig. 11). In the first (structure-sensitive) stage *I–II*, due to the absorption of a photon (Fig. 11, transition 1, stage *I*), an electron is transferred in the molecule of the complex at a distance  $r_{DA} \approx r_0$  with its subsequent transport as a result of “relay-race” migration of a hole through aromatic fragments of a polymer at distance  $r_t$  (transition 2), during which thermalized Coulomb electron–hole pairs are formed (stage *II*). The subsequent decomposition of the bound pairs in the external electric field (transition 3) occurs according to the model of field-assisted thermal Onsager dissociation (stage *III*) [46]. The pairs are formed by the electrons localized at the acceptor molecules and the holes localized at the donor molecules. The values of  $r_0$  and  $r_t$  are in the ranges 0.3–0.5 and 2.5–3.5 nm, respectively [1, 3, 18].

The transport over a distance  $r_0$  occurs due to the energy of an absorbed photon, which leads to a gradient in the electron affinity  $\partial A_A/\partial r$  along the transport path of the bound carrier [3]; the value of this gradient is determined by the energy of *D–A* interaction  $W_{DA}$  (Fig. 11). Since  $r_t$  significantly exceeds (for most mol-

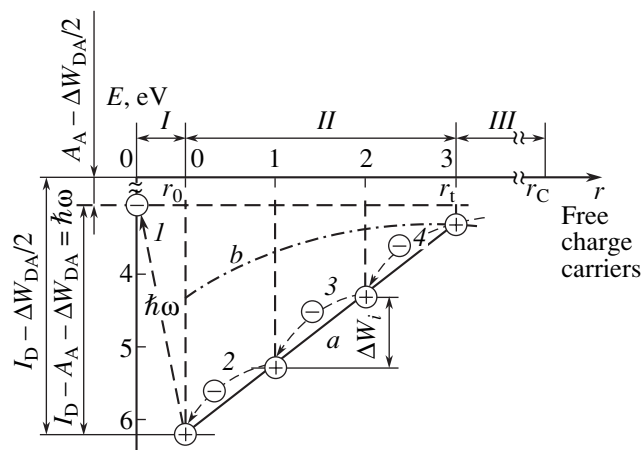


**Fig. 11.** Schematic diagram of the migration mechanism of the Onsager carrier photogeneration in molecular CTCs. The photogeneration stages are as follows: (*I*) charge transfer in a *D–A* complex, (*II*) thermalization, and (*III*) field-assisted thermal dissociation. Numbers of aromatic fragments (through which the migration occurs)  $n = (r - r_0)/d$  are indicated on the  $r$  axis.

ecules) the size of molecular complexes (0.2–0.5 nm [3, 18]), the possibility of transport is controlled by the value of  $d$ . For molecules of donor (or acceptor) polymers (for example, carbazolyl-containing polymers with fluorene derivatives), the transport is possible due to the presence of aromatic (in this case, carbazolyl) fragments, located at a distance  $d$  from each other. For monomeric complexes, for example, porphyrins with quinones, an increase in the number of  $-\text{CH}_2-$  fragments leads to the lengthening of the chain along which a carrier is transported. In the case of monomeric components of molecular complexes (squalenes, azo pigments, and so on), the presence of transport molecules is necessary to transport charge carriers over the distance  $r_t$ . Since, at distances  $r_t < 3.5$  nm, the electric field has almost no effect on the separation of bound carriers [3], the value of  $\eta_0$  is field-independent.

In the second (Onsager) stage of photogeneration, which was considered above in detail, the distance in the bound pairs increases from  $r_t$  to the Coulomb radius  $r_C = 20$  nm [1], at which the charge carriers become free. The probability of separation of carriers, especially in the initial stage, depends on the structural parameters of the complex molecules and the energy of *D–A* interaction.

The energy of *D–A* interaction  $W_{DA}$  is determined, according to [28], from the photoemission and luminescence spectra by the energy of the  $i$ th electronic transition  $E_{DA}^{(i)}$ :

$$E_{DA}^{(i)} = E_E^{(i)} = I_D^{(i)} - A_A - P - \Delta W_{DA}^{(i)},$$

where  $\Delta W_{DA}^{(i)}$  is the change in the energy of *D–A* interaction at a transition from the ground state with energy

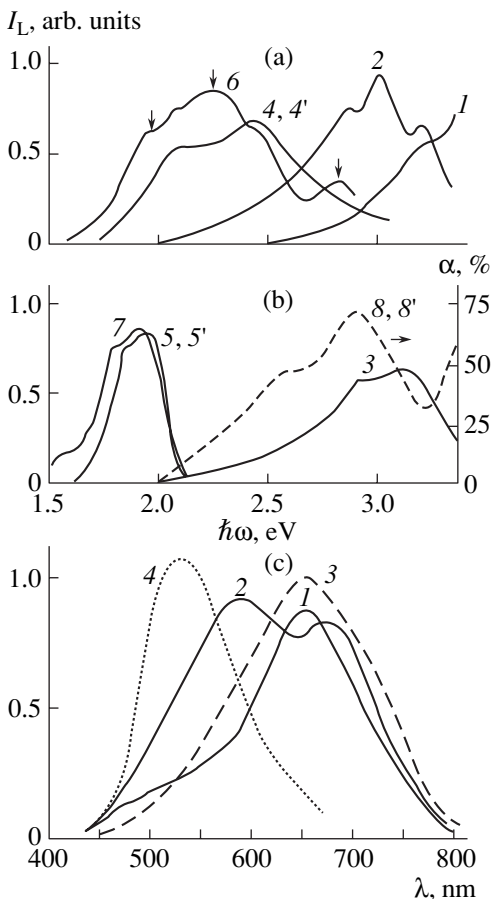


**Fig. 12.** Luminescence spectra of  $D-A$  complexes and exciplexes of polyvinylcarbazole (with fluorene derivatives) and their components (a, b) and triphenylamine-containing polyimide (c). (a, b) Spectra measured at  $T = 77$  K with time resolution  $t_p = 10^{-8}$  s for (1) PMMA, (2) polyvinylcarbazole, (3) PMMA-1,2,4-trifluoro-3-piperidine-7-nitro-9-dicyanomethylenefluorene, (4) 1,2,4-trifluoro-7-nitro-9-dicyanomethylenefluorene, (4') PMMA-1,2,4-trifluoro-3-piperidine-7-nitro-9-dicyanomethylenefluorene, (5) 1,2,4-trifluoro-3-piperidine-7-nitro-9-dicyanomethylenefluorene, (6) polyvinylcarbazole-2,4,7-trinitro-9-dicyanomethylenefluorene complex, and (7) polyvinylcarbazole-1,2,4-trifluoro-3-piperidine-7-nitro-9-dicyanomethylenefluorene exciplex. (8, 8') Absorption spectra of 1,2,4-trifluoro-3-piperidine-7-nitro-9-dicyanomethylenefluorene and polyvinylcarbazole-1,2,4-trifluoro-3-piperidine-7-nitro-9-dicyanomethylenefluorene exciplex at  $T = 300$  K [96]. (c) Spectra ( $T = 300$  K,  $t_p = 1$  s) of (1) a nonsensitized polyimide, (2, 3) polyimides sensitized by (2) malachite green and (3) fullerene and malachite green, and (4) a polyimide without a triphenylamine group.

$E_0^{(i)}$  to the excited state with energy  $E_E^{(i)}$ . Since, for the complexes under study, the degree of charge transfer  $\delta \ll \delta_0$  and  $E_0^{(i)} \ll E_E^{(i)}$ ,  $\Delta W_{DA}^{(i)} = W_{DA}^{(i)}$ —the energy of  $D-A$  interaction in the excited state:

$$W_{DA}^{(i)} = I_D^{(i)} - A_A - P - E_{DA}^{(i)},$$

where  $I_D^{(i)}$  and  $A_A$  are determined from the photoemission spectra and  $E_{DA}^{(i)}$  is determined from the lumines-

cence spectra by the maxima of the bands that arise in the spectra of complexes and are absent in the spectra of their components (indicated by arrows in Fig. 12a).

Typical luminescence spectra of molecules of  $D-A$  complexes, from which the energies  $E_{DA}^{(i)}$  can be determined, are shown in Fig. 12. The spectra can be separated into two groups, depending on the character of their change in going from the spectra of components to the spectra of complexes. The first group includes acceptors that do not contain piperidine and the second group includes piperidine-containing acceptors (1,2,4-trifluoro-7-nitro-9-dicyanomethylenefluorenes and 1,2,4-trifluoro-3-piperidine-7-nitro-9-dicyanomethylenefluorenes, respectively). For the first group (Fig. 12a), new bands (curve 6) (in comparison with the spectra of acceptor and donor molecules (curves 2, 4)) arise in the visible spectral range in the luminescence spectra of molecules in a matrix containing donor molecules with  $I_D = 7.4-7.6$  eV. These bands are absent in the luminescence spectra (curve 4') of molecules in a matrix containing PPMA molecules with  $I_D = 10.2$  eV (curve 1). For the second group of acceptors (Fig. 12b), a weak long-wavelength band (curve 7) arises in the luminescence spectra of the molecules in a matrix containing donor molecules with  $I_D = 7.4-7.6$  eV. This band is absent in the spectra of donor (Fig. 12a, curve 2) and acceptor (Fig. 12b, curves 3, 5) molecules and in the luminescence spectra of the matrix containing molecules with  $I_D = 10.2$  eV (curve 5'). The position of the maximum of the new long-wavelength luminescence band depends on the electron affinity  $A_A$  of the acceptor molecule [102]. This circumstance indicates the formation of an exciplex by the acceptor molecule and the carbazolyl fragment of the donor molecule. The formation of an exciplex is confirmed by the shape of the absorption spectra (curves 8 and 8') and the behavior of the quantum yield of photogeneration  $\eta$  [102].

The energies of electronic transitions  $E_{DA}^{(i)}$  determined from the maxima of the new bands correspond to the charge transfer between carbazolyl donor fragments and the acceptor molecule, and the energy of  $D-A$  interaction  $W_{DA}^{(i)}$  upon photoexcitation of molecular CTCs is equal to 0.6–1.2 eV and depends on the dipole moment of their molecules in an excited state  $\mu_e$ , on the degree of charge transfer  $\delta$ , and on the value of  $A_A$  (for donor molecules, on the difference  $A_A - I_D$ ). The dependence of  $W_{DA}^{(i)}$  on  $\mu_e^i$  is shown in Fig. 13 (curve 1). At small values of  $\mu_e$  (1–2 D),  $W_{DA}^{(i)}$  increases linearly with increasing  $\mu_e$  and tends to a constant value at large  $\mu_e$  (2–13 D). The general form of the dependence is described by the formula [102]

$$W_{DA}^{(i)}(\mu_e) = W_{DA}^{\min} + W_{DA}^{\max}[1 - \exp(-\mu_e/\mu_0)], \quad (19)$$

where  $W_{DA}^{\min} = W_0 = 0.1$  eV,  $W_{DA}^{\max} = 0.85$  eV, and  $\mu_0 = 0.9$  D. Expression (19) can be written as an expansion in powers of  $\mu_e/\mu_0$ :

$$W_{DA}^{(i)}(\mu_e) = W_{DA}^{\min} \quad (20)$$

$$+ W_{DA}^{\max} [\alpha(\mu_e/\mu_0) - \beta(\mu_e/\mu_0)^2 + \gamma(\mu_e/\mu_0)^3 + \dots],$$

where  $\alpha$ ,  $\beta$ , and  $\gamma$  are constants. Since the energy of  $D$ - $A$  interaction includes the difference in the energies of Coulomb and resonance interactions [17], which arise during the charge transfer, the second term in formula (20) corresponds to the Coulomb energy  $E_C \propto \mu_e^2$  (Fig. 13, curve 2) and the other terms correspond to the resonance energy  $E_{res}$ . It can be seen from Fig. 13 that  $E_C$  increases in the entire range of variation in  $\mu_e$  and attains  $\sim 6$  eV at  $\mu_e = 13$  D. The dependence of  $E_{res}$  (obtained as the difference  $W_{DA} - E_C$ ) on  $\mu_e$  is also shown in Fig. 13 (curve 3). It can be seen that  $E_{res}(\mu_e)$  is linear up to  $\mu_e = 4$  D and, at larger dipole moments, a deviation from linearity is observed. Along with the structural parameters, the energy of  $D$ - $A$  interaction also depends on the photon energy  $\hbar\omega$  and it can be written at small values of  $A_A - I_D$  (i.e., small  $\delta$  and  $\mu_e$ ) in the form [102]

$$W_{DA}(A_A, I_D, \hbar\omega) = W_{00} + C_1 \hbar\omega (A_A - I_D) / kT, \quad (21)$$

and, at large values of  $A_A - I_D$  (large  $\delta$  and  $\mu_e$ ), the factors are separated and dependence (21) turns into the dependence [102]

$$W_{DA}(A_A, I_D, \hbar\omega) = k_1(A_A - I_D) + k_2 \hbar\omega, \quad (22)$$

which was obtained previously [35]. In (21) and (22),  $C_1$ ,  $k_1$ , and  $k_2$  are coefficients. Expressions (21) (for ion-radical salts (dyes)) and (22) (for weak CTCs considered here) can be used to obtain (based on the migration mechanism [3]) the dependences of the quantum yield  $\eta$  on the structural parameters (expression (15) and its particular cases (11), (13), and (16)), as well as the spectra  $\eta(\hbar\omega)$  of  $D$ - $A$  complexes (17), including the spectrum at small  $\hbar\omega$  (18) and in the case of the exciplex mechanism of photogeneration, which occurs upon sensitization of carbazoyl-containing polymers by dyes and intramolecular CTCs.

In polyimides sensitized by dyes, photogeneration occurs also through the exciplex state formed by a dye molecule absorbing a photon and an aromatic fragment of the polyimide. The absorption of light by a dye molecule is accompanied by the localization of a negative charge at its anionic part ( $\text{ClO}_4^-$ ) and a positive charge at the cationic part (triphenylmethane derivative). Due to the difference in the ionization potentials of the dye cation and triphenylamine, dye cations can form exciplexes with triphenylamine fragments (with the luminescence maximum at  $\lambda > 660$  nm) (Fig. 12c, curve 1). Electric-field induced dissociation of these exciplexes is responsible for the carrier photogeneration [89].

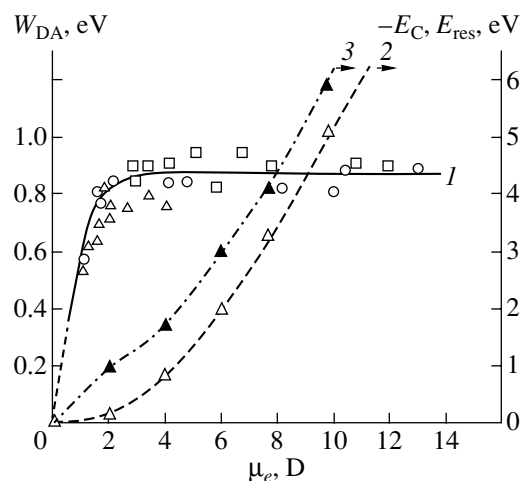


**Fig. 13.** Dependences of the (1) energy of the  $D$ - $A$  interaction in the excited state  $W_{DA}$  and the energies of (2) Coulomb and (3) resonance interactions (components of  $W_{DA}$ ) on the dipole moment of the complex molecule in an excited state using the complex of polyvinylcarbazole with fluorene derivatives (series VII) as an example [102].

Indeed, when the malachite green dye is introduced, the maximum at 660 nm disappears and two maxima at 590 and 690 nm arise (Fig. 12c, curve 2). The formation of an exciplex is confirmed by the increase in the value of  $r_t$  caused by the introduction of the dye (from 2.0 to 3.0–3.5 nm) or the increase in the size of the donor fragment (to 2.7–3.0 nm due to the introduction of the second triphenylamine fragment into a triphenylamine-containing polyimide with  $I_D = 6.7$  eV). The proposed mechanism of photogeneration is also confirmed by the experimental data on the carrier mobility in nonsensitized and sensitized polyimides [129]. When the dye is introduced, the hole conductivity with mobility  $\mu_h \approx 10^{-4}$  cm<sup>2</sup>/(V s) [129] changes to mixed conductivity with electron mobility  $\mu_e \approx 10^{-3}$  cm<sup>2</sup>/(V s) and hole mobility  $\mu_h \approx 4 \times 10^{-4}$  cm<sup>2</sup>/(V s) [129], which indicates that the fraction of triphenylamine fragments through which the hole transport occurs form complexes with dye cations and the other anions  $\text{ClO}_4^-$  provide the electron transport. The introduction of a stronger acceptor—fullerene—impedes the formation of an exciplex, its luminescence vanishes (Fig. 12c, curve 3), and charge carriers provide a high quantum yield  $\eta$  [3].

It has been ascertained [113] that, in the case of sensitization of polyimides by fullerenes, the efficient sensitization of aromatic donor molecules by fullerenes is caused by the formation of complexes, each consisting of a donor molecule and an acceptor fullerene molecule. The complex formation is confirmed by the appearance of a new band in the absorption spectra (at 1405 nm [113] and 760 nm [127] for the complexes formed by a fullerene with a triphenylamine-containing polyimide and polyvinylcarbazole, respectively). This



band is absent in the spectra of the complex-forming components. Additional evidence of the complex formation is the possibility of conformational transformations of the triphenylamine molecule from the neutral tetrahedral to the ionized planar conformation [96]. The intermediate conformation is coplanar with the planes of the  $C_{60}$  molecule. This circumstance, taking into account the sizes of both molecules, suggests that charge transfer is possible between these two conformations. The conclusion about the efficiency of sensitization by fullerenes is based on the fact that their introduction, even with low concentrations (less than 1 molecule per 1500 monomeric units of a polymer), into a medium containing aromatic molecules makes it possible to increase the photosensitivity of the medium by 0.5–2.0 orders of magnitude and extend the range of its spectral sensitivity to longer wavelengths by 0.2–0.5 eV, depending on the ionization potential of the aromatic molecule of the complex and the structure of the fullerene molecule [109]. In going from the  $C_{60}$  to  $C_{70}$  molecule, the efficiency of the fullerene sensitization of aromatic polymers increases by a factor of 2.5 and the maximum in the spectrum  $\eta(\hbar\omega)$  shifts to longer wavelengths by  $\sim 0.15$  eV [109].

The experimental fact that the introduction of a fullerene leads to the formation of complexes with  $d = 1.0$ ,  $r_0 = 0.65$  nm,  $\eta_0 = 1.0$  and  $r_t = r_0$  and  $\eta = 1.0$  [113] suggests that carriers become free after their transport to fullerene molecules, on the surface of which charges are delocalized. One of the possible reasons for this phenomenon is the occurrence of an image charge for such a surface, which reduces the binding energy in a Coulomb pair. The above mechanism differs from the mechanism of dye sensitization, according to which the sensitization is due to the increase in the number of absorbing centers with constant  $\eta$  and  $\eta_0$ .

The above-considered features of the mechanism of photogeneration in molecular media, in particular, polymers sensitized by acceptors and dyes, are due to the process of photocarrier separation, which occurs through the CP state of bound pairs of these carriers [1, 7, 130] and is characteristic of only such media. These pairs are considered to be noninteracting. Upon their interaction, which occurs under certain conditions, another phenomenon is observed (which is typical of only molecular media)—concentration photogeneration.

### 3.5. Concentration Photogeneration

The concentration photogeneration, which manifests itself in the increase in  $\eta$  by up to 10 or more times in comparison with the case of low photoexcitation densities [131], when  $\eta$  is independent of the density of absorbing centers [1], is observed under conditions where the radii of Coulomb pairs formed as a result of absorption of photons become comparable with the distances between the pairs (i.e., between the absorbing

centers). These conditions are satisfied at high photoexcitation densities and low temperatures.

**3.5.1. Photogeneration at high photoexcitation densities.** For short photoexcitation times ( $10^{-8}$  s), the quantum yield  $\eta$  increases with decreasing excitation time  $t_{\text{exc}}$  in molecular CTCs (in particular, in the typical polyvinylcarbazole–2,4,7-trinitro-9-fluorenone polymer complex [1]). This effect was confirmed in [131], where it was shown that it is due to the increase in the photoexcitation density  $F$  and occurs in substances in which the primary event of photoexcitation consists in the formation of an electron–hole pair bound by the Coulomb interaction. Due to the neutrality of these pairs, the probability of interpair recombination is low, and the dipole–dipole interaction between bound pairs, which increases with decreasing distance  $d$  between them, reduces the Coulomb interaction energy [132] and, accordingly, increases the quantum yield  $\eta$ . Thus, the so-called phenomenon of concentration photogeneration occurs. At an average distance  $d$  smaller than the Coulomb radius  $r_C$  at which carriers become free, the increase in  $\eta$  may exceed 300% [1]. However, this effect occurs also in solid solutions, where  $d \gg r_C$ , in particular, in electrophotographic and photothermoplastic media [131–133], and is absent in thin films of inorganic semiconductors, in particular, Se and CdSe [1].

The experimental dependences of  $\eta$  on  $F$  are shown in Fig. 14a. It can be seen that, with an increase in  $F$ ,  $\eta$  first remains the same, and, when  $F$  attains some value  $F_{\text{min}}$ ,  $\eta$  increases for some complexes. The value of  $F_{\text{min}}$  depends on  $\eta$  at  $F < F_{\text{min}}$ . Thus, we have the following relations:

$$\begin{aligned} \eta(F) &= \text{const at } F < F_{\text{min}}, \\ \eta(F) &= f(F) \text{ at } F > F_{\text{min}}. \end{aligned} \quad (23)$$

At  $\eta(F < F_{\text{min}}) \approx 0.03$  (curves 4, 5), the larger the value of  $\eta$ , the higher  $F_{\text{min}}$  and the lower the rate of increase in  $\eta - d\eta/dF$ ; at  $\eta(F > F_{\text{min}}) \approx 0.1$ ,  $\eta$  is independent of  $F$  up to  $3 \times 10^{24} \text{ cm}^{-3} \text{ s}^{-1}$  (curves 1–3).

The dependences revealed can be explained taking into account the dipole–dipole interaction of bound pairs upon photogeneration (Fig. 14c). If the energy of dipole–dipole interaction

$$W_{\text{d-d}}[d(F, t, r(t))] \propto r^4(t)/d^5(F, t)$$

exceeds the Coulomb energy ( $W_{\text{d-d}} > E_C[r(t)]$ ), the quantum yield  $\eta$  should increase, and, if this increase is due to the increase in  $F$ , concentration photogeneration occurs. The conditions for the concentration photogeneration are as follows:

$$\begin{aligned} d_{\text{max}}(F_{\text{min}}, t_0) &= r_{\text{max}}(t_0) = r_0(\epsilon_{\text{loc}}), \\ t &= t_0 \text{ at } r = r_0. \end{aligned} \quad (24)$$

These conditions were considered in detail in [131], where the dependence of  $\eta$  on the distance between pairs  $d$  (i.e., the density  $F$ ) was calculated and it was



shown that  $\eta(d) \propto \exp[k(r_i)/d^5]$ . Taking into account (24), we obtain the dependence in the form

$$\eta(F) \propto \exp[k(r_i)/F]^{5/3}, \quad (25)$$

where  $r_i$  is the thermalization length and  $k$  is a coefficient dependent on  $r_i$ . It can be seen from (25) that an increase in  $F$  should lead to an increase in  $\eta$ , which depends on  $r_i$ . However, a check of the validity of condition (24), which is necessary for the occurrence of concentration photogeneration, showed that it is not satisfied (i.e., the energy of dipole–dipole interaction does not exceed the Coulomb energy) under the assumption that all CTC molecules are at the same distance  $d$  from each other. Thus, the effect of the increase in  $\eta$  with increasing  $F$  at high densities cannot be explained by the above-considered mechanism of concentration photogeneration. To explain the observed effect, the dispersion of CTC molecules over the distance  $d$  between them was taken into account [131]. Obviously, in this case, condition (24) should be satisfied only for some fraction of molecules located at small  $d$  from each other.

In the case of dispersion of molecules over the distance  $d$  between them, the molecules having different radii  $r$  and located at different distances  $d$  from each other have different values of  $\eta_i[d(F), r]$ . The total quantum yield is [1]

$$\eta[d(F), r] = \sum_i \eta_i[d(F), r] A_i[d(F), r], \quad (26)$$

where  $A_i[d(F), r]$  is the fraction of excited CTC molecules with a radius  $r$  located at a distance  $d$  from each other. The dependence  $\eta(F)$  for this case—the so-called dispersion concentration photogeneration [131]—is calculated under the assumption that the distance between molecules is not the same, the distribution of unexcited molecules over  $d$  is Gaussian [48], and conditions (24) are satisfied. Since the absorption has a molecular character for the CTC molecules under consideration [1, 134], it ensures the independence of the absorption coefficient from the shape of the distribution of excited molecules; i.e., the latter remains Gaussian, as the initial distribution of unexcited molecules. The function  $A_i[d(F), r]$  [131] found under these assumptions was substituted into Eq. (26), and, taking into account the temperature dependence of the Coulomb radius  $r_C$  in the form [1]

$$r_C(T) = \frac{e^2}{4\pi\epsilon\epsilon_0 kT}, \quad (27)$$

the dependence of  $\eta$  on  $F$  and  $T$  was determined (this dependence is caused by the dipole–dipole interaction and leads to the increase in  $\eta$  at  $F > F_{\min}$ ):

$$\eta_{d-d}(F, T) = \eta(F < F_{\min}) \exp[B(r_t, c, \sigma) F^{5/3}/kT]. \quad (28)$$

Here,  $B(r_t, c, \sigma)$  is a function of the thermalization length  $r_t$ , the concentration of complex molecules  $c$ ,

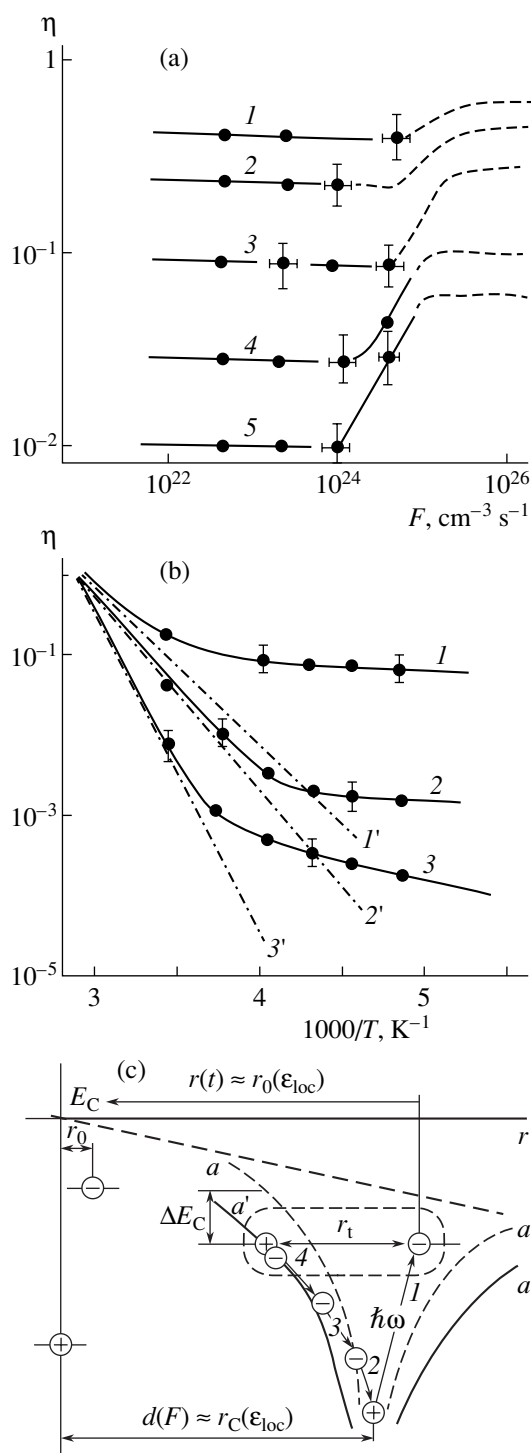


**Fig. 14.** Dependences of the quantum yield of photogeneration (a)  $\eta(F)$  and (b)  $\eta(T)$  at high photoexcitation densities  $F$  and low temperatures  $T$  for complexes of polyvinylcarbazole with (1) a dye, (2) heteryltricyanobutadiene, (3) 2,4,7-trinitro-9-dicyanomethylene-fluorene, (4) 2,4,7-trinitro-9-fluorenone, and (5) dinitrofluorenone. ( $I'$ – $3'$ ) Results of calculation according to the Onsager model disregarding the concentration photogeneration. (c) Schematic diagram of the concentration photogeneration with the Coulomb barrier reduced ( $a \rightarrow a'$ ) due to the dipole–dipole interaction; transitions  $I$ – $4$  are the same as in Fig. 11.

and their dispersion  $\sigma$  over intermolecular distances. It can be seen from (28) that the increase in  $\eta$  in the case of concentration photogeneration caused by the decrease in the energy of the dipole–dipole interaction between Coulomb pairs should also be observed at low temperatures, which would lead to a slower decrease in  $\eta$  with decreasing  $T$  in comparison with the decrease predicted by the Onsager model.

**3.5.2. Photogeneration at low temperatures.** At low temperatures, the phenomenon of concentration photogeneration [77] manifests itself in the decrease in the thermal-activation energy  $W_a$  of the quantum yield  $\eta$  with decreasing temperature below the threshold value, as a result of which  $\eta$  exceeds the expected value by a factor of 100 or more [131]. The experimental temperature dependences  $\eta(T)$  (Fig. 14b, curves 1–3) differ from the expected ones (curves 1'–3') and consist of two portions: a high-temperature portion ( $T > T_1$ ), where  $\eta(T) \propto \exp[-W_{a1}/kT]$ , and a low-temperature portion ( $T < T_2$ ), where  $\eta(T) \propto \exp[-W_{a2}/kT]$  with the activation energy  $W_{a2} < W_{a1}$ .

The temperature dependences of  $\eta$  were explained on the basis of the model of concentration photogeneration [131], which occurs when condition (24) is satisfied. In this case, the energy of the dipole–dipole interaction becomes comparable with the Coulomb energy and the thermal energy  $kT$ . The condition  $kT = W_{d-d}(r, d)$  can be used to find the temperature  $T_{d-d}$  at which the concentration photogeneration may begin:

$$T_{d-d} = e^2 r^4 / 4\pi\epsilon\epsilon_0 d^6 k. \quad (29)$$

For the low-temperature region ( $T < T_2$ ), where the effect of the dipole–dipole interaction is significant, the following dependence is valid:

$$\eta_{d-d}(T < T_2) = \eta_{\text{theor}}(T > T_1) \exp[B(c, \sigma)/kT], \quad (30)$$

where

$$\eta_{\text{theor}}(T > T_1) = \exp[-W_a/kT]$$

is the temperature dependence of the theoretically predicted quantum yield (disregarding the dipole–dipole interaction). It can be seen that a decrease in  $W_a$  by a factor of 5–10 leads to an increase in  $\eta$  by a factor of 100 or more.

The effect of low-temperature concentration photogeneration has the same characteristic features as the effect occurring at high photoexcitation densities: the quantum yield increases with respect to the theoretically predicted one, calculated disregarding the dipole–dipole interaction, and the concentration photogeneration manifests itself only in the case of dispersion of pairs over the distance between them. Some differences between the high- and low-temperature effects are due to the difference in the conditions of their occurrence. At high densities  $F$ , the distance between pairs  $d(F)$  tends to the radii of pairs  $r$  and, at some value of  $F$ , condition (24) is satisfied. At low  $T$ , the radii of pairs increase with decreasing  $T$  and tend to  $d$ ; thus, condi-

tion (24) is also satisfied. Obviously, condition (24) for the occurrence of concentration photogeneration is not satisfied for molecular media with low concentrations of CTCs, in particular, for polyimides ( $d \gg 30$  nm) [88]. For these media, the increase in  $\eta$  at low  $T$  [134], which is characteristic of concentration photogeneration [131], is not observed.

### 3.6. Molecular Complexes Formed at the Interface between the Photogeneration and Transport Layers in a Heterostructure That Are Responsible for High Injection Efficiency $\eta_{\text{inj}}$

It was shown previously [135] that, for heterostructures in which either donor molecules of the transport layer or acceptor molecules of the photogeneration layer are varied, the high efficiency of injection through the heterostructure interface (high transparency of the barrier overcome by the charge carriers injected from the photogeneration layer) is due to the formation of complexes at the interface under its illumination from the sensitivity region of the photogeneration injection layer. These complexes are formed by aromatic nitrogen-containing donor molecules of the transport layer and acceptor molecules containing elements with an unfilled  $p$  shell of the photogeneration layer (Se, SeTe, CdSe). The decisive role of nitrogen in the complex formation has been proven. The proof is based on (i) the results of investigations in which molecules blocking the nitrogen activity were introduced into a heterostructure (in this case, the value of  $\eta_{\text{inj}}$ , equal to 0.6 before this procedure, decreased to values much smaller than  $10^{-2}$ ) and then molecules restoring the nitrogen activity were introduced (after that,  $\eta_{\text{inj}}$  was restored to the initial value) and (ii) the comparison of the injection efficiency  $\eta_{\text{inj}}$  for donor molecules having the same spatial structure but either containing or not containing a nitrogen atom (Fig. 15a). For nitrogen-containing molecules,  $\eta_{\text{inj}}$  can be as high as 1.0, while, for molecules without a nitrogen atom,  $\eta_{\text{inj}} \ll 10^{-2}$  (Fig. 15a, curve 2). For nitrogen-containing aromatic molecules (Fig. 15a, curve 1),

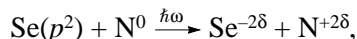
$$\eta_{\text{inj}} \propto \exp\{1 - \exp[C - (I_D - A_A)]\}, \quad (31)$$

where  $C$  is a constant [135]. At  $\eta_{\text{inj}} < 0.4$ , expression (31) transforms into the expression obtained previously [1], according to which the injection efficiency increases linearly with increasing  $A_A - I_D$  (Fig. 7, curve 18). Hence, to increase  $\eta_{\text{inj}}$ , it is necessary to either increase  $A_A$  (for example, by introducing Te molecules into a Se layer, since the value of  $A_A$  for Te exceeds that for Se by  $\sim 0.2$  eV) or use molecules with  $I_D < 7.0$  eV as donors [135].

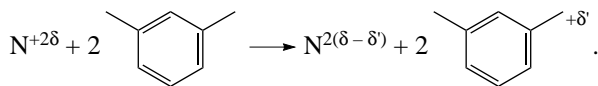
The formation of complexes in heterostructures containing two phases, one of which consists of a  $p$ -type element—amorphous Se—and the other is formed by aromatic molecules in a neutral matrix, with a highly transparent barrier at the interface is confirmed by the method of kinetic luminescence spectroscopy,

which is independent of the photoelectric spectroscopy [96]. Photoexcitation of the heterostructure interface changes the luminescence spectra at  $t_p = 10^{-6}$  s (Fig. 15, curves 1–3): the luminescence band of CdSe at  $\lambda = 720$  nm (curve 2) and new strong luminescence bands at  $\lambda = 460, 510, 570, 630,$  and  $750$  nm (indicated by arrows in Fig. 15b, curve 1) arise. These bands are absent in the spectra of CdSe and polyvinylcarbazole (curves 2 and 3). Obviously, they are due to photostimulated interaction since they arise only under illumination of the interface of the CdSe–polyvinylcarbazole heterostructure and can be assigned [96] to the luminescence of the  $D$ – $A$  complex formed by a carbazolyl fragment of polyvinylcarbazole with a S or Se atom at the interface. The positions of the luminescence peaks correspond to the electronic transitions in the complex between the three highest occupied levels of carbazole and the lowest unoccupied level of S or Se (acceptor) with the minimum vibrational energy [78].

The mechanism of formation of complexes by aromatic nitrogen-containing molecules and atoms of elements with an unoccupied  $p$  orbital was proposed in [96]. Due to the presence of a nitrogen atom (the case of polyvinylcarbazole), which readily supplies its unshared pair of  $n$  electrons to form the  $D$ – $A$  complex, the aromatic molecule serves as an  $n$ -type donor, while the  $p$ -type element with an unoccupied orbital serves as a  $v$  acceptor. The unshared pair of  $n$  electrons of the nitrogen atom is transferred upon photoexcitation to the free orbital of the  $v$  acceptor [96]:



where  $\delta$  is the degree of charge transfer. As a result of the phototransfer, the electron affinity of the nitrogen atom increases and the  $\pi$  electron density is transferred to it from the aromatic ring. An intramolecular complex of the  $n\pi$  type with the charge transfer between the aromatic ring ( $\pi$  donor) and the charged nitrogen atom  $\text{N}^{+2\delta}$  is formed in the carbazole molecule:



Due to the electron-density transfer to  $\text{N}^{+2\delta}$ , the electron affinity of the aromatic ring increases, which gives rise to the relay-race motion of charge through aromatic fragments according to the migration mechanism [3]. This motion leads to the efficient transport of photocarriers generated by light from the CdSe layer over the transport layer composed of aromatic molecules. As a result, a multicomponent  $D$ – $A$  complex formed by  $\text{Se}^{-2\delta}$  (or  $\text{S}^{-2\delta}$ ) and the intramolecular complex of the nitro-

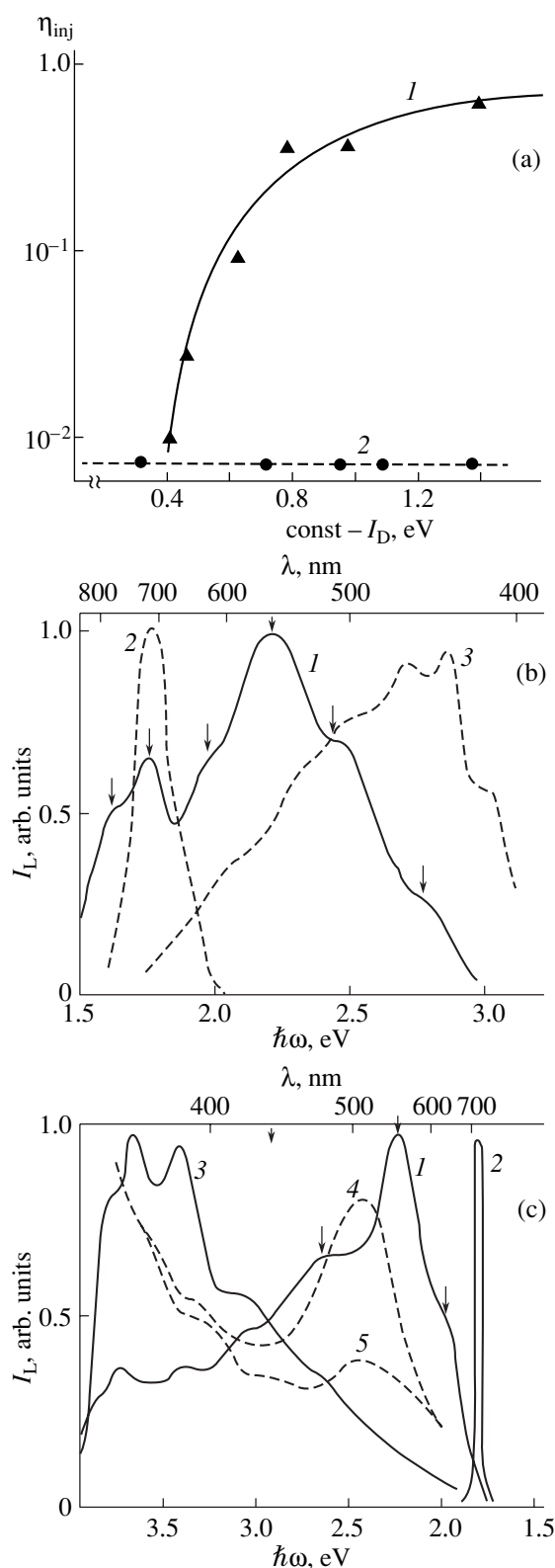
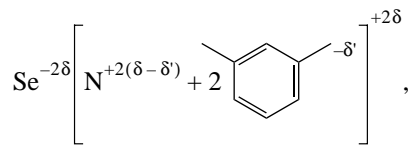


**Fig. 15.** (a) Dependences of the injection efficiency  $\eta_{inj}$  on the ionization potential  $I_D$  of the aromatic donor molecules containing (1) and not containing (2) a nitrogen atom, introduced into the transport layer [135]. (b, c) Luminescence spectra ( $T = 77$  K,  $t_p = 10^{-8}$  s) of the complexes arising at the interfaces of heterostructures formed of CdSe with (b) polymer polyvinylcarbazole or (c) monomer triphenylamine molecules and their components: (1) CdSe–polyvinylcarbazole heterostructure, (2) CdSe, and (3) polyvinylcarbazole (b) and triphenylamine (c). Dotted lines are the spectra of (4) a CdSe–vinylanthracene heterostructure and (5) vinylanthracene without a nitrogen atom [96].

gen-containing aromatic compound arises at the interface [96]:



i.e., a complex of the  $n\nu-n\pi$  type.

The decisive role of the nitrogen atom of donor aromatic molecules in the formation of complexes of these molecules with elements with an unoccupied  $p$  shell at the interface has been proven by (i) comparing the luminescence spectra measured from the interface between the phase containing elements with an unoccupied  $p$  shell and the phase containing monomeric donor aromatic molecules either with or without nitrogen atoms (Fig. 15c, curves 1 and 4, respectively) and (ii) controlling the complex formation (ensuring its presence or absence) by introducing molecules of *o*-chlorobenzoic acid, which is a quencher of nitrogen activity, and indole molecules, which restore this activity by forming complexes with acid molecules. It was shown that the new luminescence bands arise in the spectra of heterostructures with a high injection efficiency (the heterostructures formed by Se with triphenylamine and N-vinylcarbazole are characterized by an injection efficiency as high as 70%, while the efficiency of heterostructures with vinylanthracene is at least 100 times lower) and disappear (as well as the injection of photo-generated carriers through the interface) due to the introduction of the acid, but arise again after the introduction of indole.

### 3.7. Requirements for the Structure of Molecular Complexes with High Values of $\eta$

Based on the proposed mechanism of photogeneration, we can formulate the requirements for the structures of molecules of complexes with high quantum yields of photoprocesses. To attain high quantum yields of the primary photoprocesses ( $\delta$ ,  $\eta_0$ ), the donor molecule must have a low ionization potential (lower than 7.4 eV) and the acceptor molecule must have a high electron affinity (higher than 1.0 eV). To obtain a high quantum yield of photogeneration  $\eta$ , along with the above requirements, the following conditions should be satisfied: either

(i) the donor molecule with the ionization potential of aromatic fragments in the noted range (or the acceptor molecule with the electron affinity in the noted range) should be polymeric and have no less than five fragments periodically located at distances from 0.7 to 1.5 nm between neighboring fragments and the acceptor (donor) molecule should be an intramolecular complex composed of acceptor and donor fragments (differing in the electron affinities by no less than 1.0 eV), or

(ii) the donor and acceptor molecules forming a molecular complex should form a polymer with a

monomeric unit limited in size to the thermalization length (1.5–3.5 nm).

In the case of the spectral dye sensitization, one more requirement should be satisfied: the spatial structures of the donor fragment of the molecule and the dye cation should be similar. The structural regularities established for more than 15 series of molecular complexes and the requirements based on them for the structures with high quantum yields make it possible to predict the ultimate quantum yields of the photoprocesses and deliberately choose and synthesize photosensitive components of molecular complexes.

Thus, the presence of (i) rather extended conjugated segments and (ii) aromatic fragments with low  $I_D$  in the polymer chain leads, as is known, along with the increase in  $\eta$ , to the red shift of the absorption edge of the spectrum. This circumstance makes it possible to extend the region of intrinsic photosensitivity of polymers not only to the UV range but also to the visible wavelength range (Fig. 16a). The choice of monomers and their aromatic fragments for synthesis of photosensitive polymers was performed in these directions. The search for structures sensitive in both the UV and visible ranges turned out to be the most promising [136–139]. The photosensitive polymers obtained to date have the region of intrinsic absorption extended to 2.0–2.5 eV (in contrast to  $E_G = 4–7$  eV, as was initially [1]), which made it possible to develop recording media for the visible spectral range. The use of the principles of sensitization of polymers by dyes and formation of  $D-A$  complexes by dyes ensured control of the magnitude and spectrum of photosensitivity.

Along with the extension of existing and development of new classes of photosensitive polymers, the knowledge of the mechanisms of carrier photogeneration and antecedent primary photophysical processes makes it possible to choose promising molecular structures for nonlinear optical media on the basis of the ascertained structural regularities of the photoeffect [140–142], i.e., opens new possibilities of polymer systems. For media in which absorption of light is also accompanied by electron transfer within a molecule and the formation of high dipole moments  $\mu_e$  in the molecule and hyperpolarizability  $\gamma = f(\mu_e)$  [140], it was shown that not only  $E_G$  and  $\lambda_{\max}$  depend on the conjugation length of the monomeric unit (Fig. 16a) and the number of double bonds  $n$ ,

$$\lambda_{\max}(n) = A + \frac{B}{n},$$

where  $A$  and  $B$  are constants, but also the value of  $\gamma$  depends on these quantities (Fig. 16b),

$$\gamma \propto n^\beta, \quad \gamma \propto L^\beta,$$

where  $\beta = 3–5$  [140].

For polyimides and polyamideimides with azo dyes  $R$  introduced into the lateral chain (series (18a)–(18c)), at the degree of substitution of  $-H$  by  $-R$  (degree of

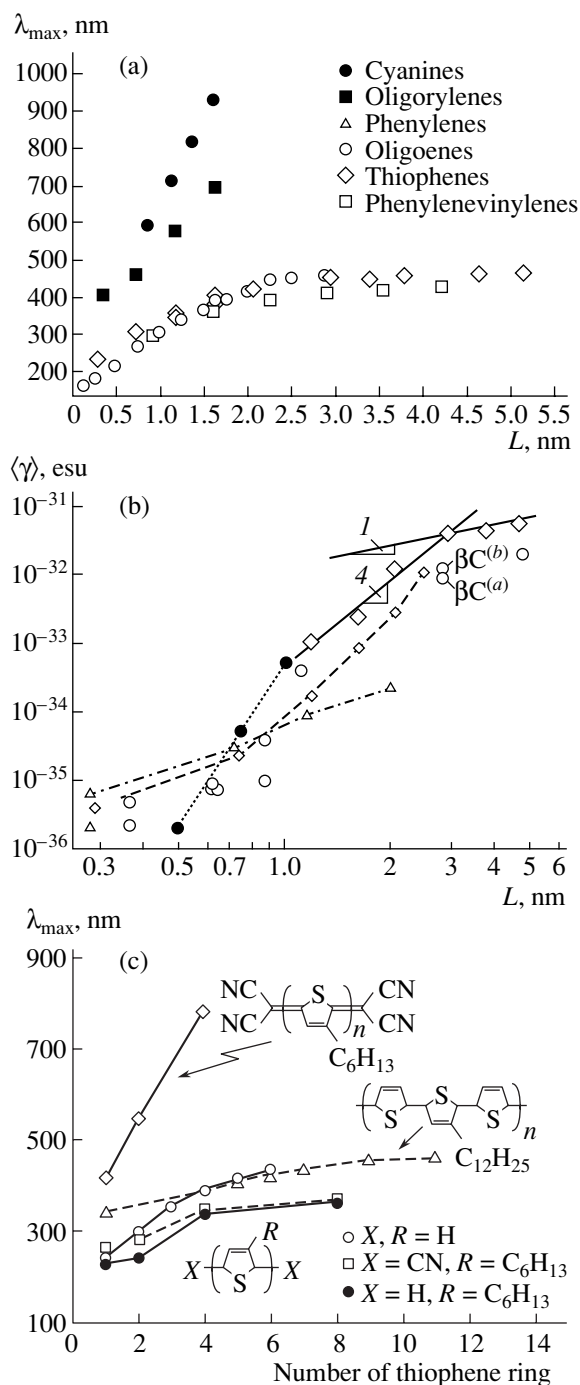


**Fig. 16.** Dependences of the energy of the (a) longest wavelength absorption band  $\lambda_{\max}$  and (b) hyperpolarizability  $\gamma$  on the length of a monomeric unit  $L$  for polyconjugated oligomers of different classes. (c) Dependences of  $\lambda_{\max}$  on the number of thiophene rings for oligothiophenes and their derivatives [140, 141].

esterification)  $n = 20, 30, 40, 60,$  and  $80\%$ , the values of  $S_{0,1}$  and  $\chi^{(2)} = f(\mu_e)$  increase with increasing number of dye fragments  $n$  [141]; however, the quantum yield  $\eta(n) = S_{0,1}(n)/\alpha(n)$  is independent of  $n$ . At  $n = 20$  and  $80\%$ , the values of  $S_{0,1}$  and  $\chi^{(2)}$  correlate with the ener-

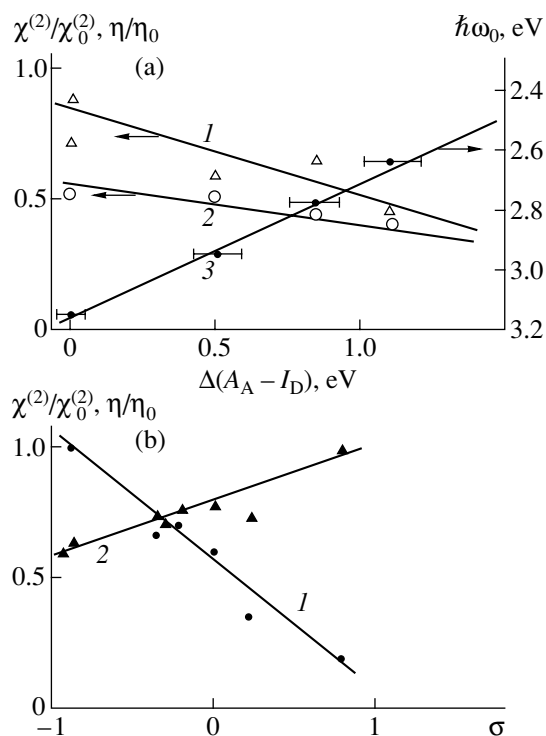


**Fig. 17.** Dependences of (1)  $\chi^{(2)}/\chi_0^{(2)}$ , (2)  $\eta/\eta_0$ , and (3)  $\hbar\omega_0$  on (a) the change in the energy parameter  $\Delta(A_A - I_D)$  and the constant  $\sigma$  for polyamideimides and polyimides with azo dyes of different structure and (b)  $\sigma$  for polyamidines with nonlinear optical chromophores.

gies of the absorption maxima of dyes  $\hbar\omega_0 = f(A_A - I_D)$  [143, 144] and, therefore, with the energies  $A_A$  and  $I_D$ , which control the positions of these bands (Fig. 17a). Such correlations are absent in the case of polyamidines into which nonlinear optical chromophores from series XX with different substituents  $R$  having constants  $\sigma$  from  $-0.83$  to  $0.79$  are introduced. For these systems,  $\chi^{(2)}$  is proportional to  $\sigma$  (Fig. 17b, curve 1), increasing by up to six times with an increase in the constant  $\sigma$  in the noted interval [145]. The quantum yield  $\eta$ , which is controlled by the supramolecular structure [16] (destroyed by introducing chromophore molecules [145]), in contrast, decreases with increasing  $\sigma$  (Fig. 17b, curve 2).

Concerning the practical application of photosensitive polymers, we should note that the photosensitivity in the visible spectral range of commercially produced (up to 1988) organic photothermoplastic materials was  $10^6 \text{ cm}^2/\text{J}$ , which is only an order of magnitude lower than the sensitivity of the most sensitive inorganic materials based on amorphous Si. Some laboratory samples based on polyimide compositions sensitized by dyes made it possible to obtain a photosensitivity comparable to that of Si.

## 4. CONCLUSIONS

The structural regularities of the change in the quantum yield of the photoeffect found for polymer semiconductors and their molecular complexes showed, first of all, that the classes of photosensitive materials known to date are distinguished by the character of (i) ionic and covalent interaction (interaction energy  $E > 1$  eV [17]) in dye and polymer molecules, (ii) donor–acceptor interaction ( $E = 0.05–1$  eV) upon formation of molecular complexes from polymers with low-molecular impurities, and (iii) hydrogen interaction ( $E = 0.04–0.2$  eV) upon formation of supramolecular structures.

The regularities ascertained made it possible to formulate the requirements for the structure of molecules of complexes with high quantum yields of photoprocesses: donor fragments or molecules must have low ionization potentials (lower than 7.4 eV) and acceptors fragments must have high electron affinities (higher than 1.0 eV). To obtain a high quantum yield of photogeneration, along with the above requirements, the following conditions should be satisfied: either (i) the donor molecule with the ionization potentials of aromatic fragments in the noted range (or the acceptor molecule with the electron affinity in the noted range) should be polymeric and have no less than five fragments periodically located at a distance of 0.7 to 1.5 nm between neighboring ones, or (ii) the donor and acceptor molecules forming a complex should have the ability of forming a polymer with a monomeric unit limited in size to the thermalization length (1.5–3.5 nm).

These requirements make it possible to predict the ultimate quantum yields of photoprocesses and deliberately choose and synthesize photosensitive components of molecular complexes.

The ultimate values of the quantum yields of photoprocesses in molecular complexes and the photosensitivity of recording media on their basis are estimated. It is shown that, at  $\eta = 1$  and the transmittance  $T = 50–70\%$ , the ultimate electrophotographic sensitivity of the molecular media is about  $10^8$  cm<sup>2</sup>/J.

## REFERENCES

- I. A. Akimov, Yu. A. Cherkasov, and M. I. Cherkashin, *Sensitized Photoelectric Effect* (Nauka, Moscow, 1980) [in Russian].
- Yu. A. Cherkasov, in *Photothermoplastic Process. Non-silver Photographic Processes*, Ed. by A. L. Kartuzhanskii (Khimiya, Leningrad, 1984), p. 45 [in Russian].
- E. L. Aleksandrova and Yu. A. Cherkasov, *Opt. Spektrosk.* **64**, 1047 (1988) [*Opt. Spectrosc.* **64**, 624 (1988)].
- J. Simon and J.-J. Andre, *Molecular Semiconductors* (Springer, Berlin, 1985; Mir, Moscow, 1988).
- V. S. Myl'nikov, *Photoconductivity of Polymers* (Nauka, Leningrad, 1990), p. 158 [in Russian].
- B. Wang and M. R. Wasilevski, *J. Am. Chem. Soc.* **119**, 12 (1997).
- A. A. Farach and J. G. Veinot, *Pure Appl. Chem. A* **37**, 1507 (2000).
- K. Meerholz, V. Volodin, and K. Kippelen, *Nature* **371**, 497 (1994).
- J. Bolton and T. A. Moore, *Nature* **289**, 254 (1980); *J. Am. Chem. Soc.* **105**, 7771 (1988).
- A. S. Davydov, *Solitons in Molecular Systems*, 2nd ed. (Naukova Dumka, Kiev, 1984; Kluwer, Dordrecht, 1991).
- Yu. A. Cherkasov and E. L. Aleksandrova, *Opt. Spektrosk.* **84**, 455 (1998) [*Opt. Spectrosc.* **84**, 396 (1998)].
- E. L. Aleksandrova and Yu. A. Cherkasov, *Zh. Nauchn. Prikl. Fotogr.* **43** (2), 63 (1998).
- Yu. A. Cherkasov, E. L. Aleksandrova, P. A. Burov, et al., in *Properties of Photosensitive Materials for Holography* (Nauka, Leningrad, 1987), pp. 18–35 [in Russian].
- E. A. Aleksandrova and Yu. A. Cherkasov, *Zh. Nauchn. Prikl. Fotogr.* **40** (3), 45 (1995).
- J.-M. Lehn, *Supramolecular Chemistry: Concepts and Perspectives* (VCH, Weinheim, 1995; Nauka, Novosibirsk, 1998).
- E. L. Aleksandrova, M. M. Dudkina, and A. V. Ten'kovtsev, *Fiz. Tekh. Poluprovodn. (St. Petersburg)* **37**, 282 (2003) [*Semiconductors* **37**, 266 (2003)].
- M. V. Kurik, É. A. Silin'sh, and V. Chapek, *Electronic Processes in Organic Molecular Crystals* (Zinatne, Riga, 1988) [in Russian].
- A. V. Vannikov and A. D. Grishina, *Photochemistry of Polymer Donor–Acceptor Complexes* (Nauka, Moscow, 1984) [in Russian].
- E. N. Gur'yanova, I. P. Romm, and I. P. Gol'dshtein, *Donor–Acceptor Bond* (Khimiya, Moscow, 1973) [in Russian].
- L. Andrews and R. Keefer, *Molecular Complexes in Organic Chemistry* (Holden-Day, San Francisco, 1964; Mir, Moscow, 1967).
- R. Forster, *Organic Charge-Transfer Complexes* (Academic, London, 1969).
- J. A. Barltrop and J. D. Coyle, *Excited States in Organic Chemistry* (Wiley, London, 1975; Mir, Moscow, 1978).
- R. S. Mulliken and W. B. Person, *Molecular Complexes* (Wiley, London, 1967).
- M. Pope and C. E. Swenberg, *Electronic Processes in Organic Crystals* (Clarendon Press, Oxford, 1982; Mir, Moscow, 1985).
- H. Bässler, G. Schonhern, and M. Abkowitz, *Phys. Rev. B* **26**, 3105 (1982).
- V. I. Archipov, V. A. Kolesnikov, and A. I. Rudenko, *J. Phys. D.: Appl. Phys.* **17**, 1241 (1984).
- H. Bässler and G. Schonhern, *Philos. Mag.* **44**, 47 (1981).
- J. Hirsch, *J. Phys. C: Solid State Phys.* **12**, 321 (1979).
- D. W. Gill, *J. Appl. Phys.* **43**, 5033 (1972).
- A. P. Tyutnev, *Khim. Vys. Énerg.* **30** (1), 5 (1996).
- A. P. Tyutnev, D. N. Sadovnichii, and S. G. Boev, *Khim. Fiz.* **13** (8–9), 54 (1994).
- A. P. Tyutnev, V. S. Saenko, and E. D. Pozhidaev, *Vysokomol. Soedin.* **40**, 1062 (1998).



33. Y. Scher and E. W. Montroll, *Phys. Rev. B* **12**, 2455 (1975).
34. M. Silver and H. Bässler, *Phys. Rev. Lett.* **48**, 352 (1982).
35. G. Briegleb, *Elektronen Donator–Acceptor Komplexes* (Springer, Berlin, 1961).
36. M. Borsenberger, H. Bässler, and L. Pautmeier, *J. Chem. Phys.* **94**, 5447 (1991).
37. H. Bässler, *Phys. Status Solidi B* **75**, 15 (1993).
38. P. J. Bounds and W. Siebrand, *Chem. Phys. Lett.* **75**, 414 (1980).
39. L. Sebastian, G. Weiser, B. Peter, and H. Bässler, *Chem. Phys.* **75**, 103 (1983).
40. P. J. Bounds, W. Siebrand, and I. Eisensttin, *Chem. Phys.* **95**, 197 (1985).
41. A. V. Vannikov, V. P. Sichkar', V. K. Matveev, and A. P. Tyutnev, *Radiation Effects in Polymers: Electrical Properties* (Nauka, Moscow, 1983) [in Russian].
42. E. A. Silinsh and A. J. Yurgis, *Chem. Phys.* **94** (12), 77 (1985).
43. V. A. Kolesnikov and É. A. Silin'sh, *Izv. Akad. Nauk Latv. SSR* **5**, 41 (1982).
44. K. M. Hong and J. Noolandy, *J. Chem. Phys.* **68**, 5163 (1978).
45. K. M. Hong, J. Noolandy, and R. Street, *Phys. Rev. B* **23**, 2967 (1981).
46. L. Onsager, *Phys. Rev.* **54**, 554 (1938).
47. P. M. Borsenberger and A. I. Ateya, *J. Appl. Phys.* **49**, 4035 (1978).
48. E. A. Silinsh, V. A. Kolesnikov, and I. J. Muzikante, *Phys. Status Solidi B* **113**, 379 (1982); **116**, 347 (1982).
49. É. A. Silin'sh, V. A. Kolesnikov, and I. Ya. Muzykante, *Izv. Akad. Nauk Latv. SSR* **5**, 14 (1981).
50. J. Noolandy and K. M. Hong, *J. Chem. Phys.* **70**, 3230 (1979).
51. A. Mozumder, *J. Chem. Phys.* **60**, 4300 (1974); *J. Chem. Phys.* **61**, 780 (1974).
52. M. Scher and S. Racovsky, *J. Chem. Phys.* **81**, 1994 (1984).
53. B. Ries, *Philos. Mag. B* **48**, 87 (1983).
54. B. Ries, H. Bässler, and M. Silver, *Philos. Mag. B* **49**, 27 (1984).
55. J. Frenkel, *Phys. Rev. B* **54**, 647 (1938).
56. V. I. Gaïdylis, *Litov. Fiz. Sb.* **20** (8), 47 (1980).
57. V. I. Gaïdylis, *Litov. Fiz. Sb.* **25** (1), 87 (1985).
58. N. G. Kushvinskiĭ, I. M. Mostovoĭ, N. G. Nakhodkin, *et al.*, in *Fundamentals of Optical Memory and Medium* (Vishcha Shkola, Kiev, 1984), p. 77 [in Russian].
59. V. M. Komko, N. G. Kuvshinskiĭ, and N. G. Nakhodkin, *Ukr. Fiz. Zh.* **30**, 441 (1985).
60. P. M. Borsenberger, L. E. Contois, and D. S. Hoesterey, *Chem. Phys. Lett.* **56**, 574 (1978).
61. Sh. Shhimokishara and M. Jokoyama, *Denshi Shashin Gakkai-shi* **20**, 18 (1981).
62. Sh. Shimokishara, M. Jokoyama, and M. Mikawa, *Denshi Shashin Gakkai-shi* **21**, 25 (1982).
63. M. Jokoyama and M. Mikawa, *Denshi Shashin Gakkai-shi* **22**, 169 (1983).
64. M. Jokoyama and M. Mikawa, *Denshi Shashin Gakkai-shi* **19**, 3 (1980).
65. M. Jokoyama, J. Endo, and M. Mikawa, *Bull. Chem. Soc. Jpn.* **49**, 1539 (1976).
66. K. Okamoto and A. Itaya, *Bull. Chem. Soc. Jpn.* **57**, 1626 (1984).
67. M. Jokoyama and M. Mikawa, *Photograph. Sci. Eng.* **26** (3), 143 (1982).
68. M. Jokoyama, J. Endo, and M. Mikawa, *J. Chem. Phys.* **75**, 3006 (1981).
69. E. I. Balabanov, Yu. I. Bukin, L. A. Mel' nichuk, *et al.*, in *Fundamentals of Optical Memory and Medium* (Vishcha Shkola, Kiev, 1980), p. 97 [in Russian].
70. B. M. Rumyantsev, E. I. Balabanov, and E. L. Frankevich, *Usp. Nauchn. Fotogr.* **22**, 161 (1984).
71. V. Ya. Pochinok, V. P. Naïdenov, and E. D. Korotkaya, in *Fundamentals of Optical Memory and Medium* (Vishcha Shkola, Kiev, 1983), p. 32 [in Russian].
72. P. J. Bounds, B. Peter, and W. Siebrand, *Chem. Phys.* **61**, 303 (1981).
73. P. J. Bounds and W. Siebrand, *Chem. Phys. Lett.* **89**, 1 (1982).
74. G. N. Kurov, V. I. Smirnov, V. A. Babushkin, *et al.*, *Zh. Nauchn. Prikl. Fotogr. Kinematogr.* **32**, 64 (1987).
75. D. Kadyrov, B. Rumyantsev, and E. Frankevich, *Polym. Photochem.* **2** (3), 243 (1982).
76. E. L. Frankevich, *Khim. Fiz.* **3**, 964 (1984).
77. E. L. Aleksandrova and Yu. A. Cherkasov, *Zh. Nauchn. Prikl. Fotogr. Kinematogr.* **31**, 61 (1986).
78. Yu. A. Cherkasov, E. L. Aleksandrova, and Yu. P. Piryatinskiĭ, *Opt. Spektrosk.* **60**, 436 (1986) [*Opt. Spectrosc.* **60**, 267 (1986)]; *Opt. Spektrosk.* **67**, 351 (1989) [*Opt. Spectrosc.* **67**, 203 (1989)].
79. F. Garnier, in *Photonics and Optoelectronics*, Ed. by S. A. Jenekhe and K. J. Wynne (Am. Chem. Soc., New York, 1997), p. 420.
80. A. Ch. Saidov, A. Yu. Kryukov, and A. V. Vannikov, *Zh. Nauchn. Prikl. Fotogr. Kinematogr.* **37**, 377 (1992).
81. U. Scherf and K. Muller, in *Photonics and Optoelectronics*, Ed. by S. A. Jenekhe and K. J. Wynne (Am. Chem. Soc., New York, 1997), p. 358.
82. K. Mecher, H. Horhold, and K. Meerholz, *Phys. Chem. Phys.* **1**, 1749 (1999).
83. T. Wada, L. Wang, and D. Fichou, in *Photonics and Optoelectronics*, Ed. by S. A. Jenekhe and K. J. Wynne (Am. Chem. Soc., New York, 1997), p. 149.
84. C. Li, R. Gervini, and A. Holmes, in *Photonics and Optoelectronics*, Ed. by S. A. Jenekhe and K. J. Wynne (Am. Chem. Soc., New York, 1997), p. 322.
85. Yu. P. Getmanchuk and I. D. Laznikova, *Zh. Nauchn. Prikl. Fotogr. Kinematogr.* **38**, 42 (1993).
86. M. A. Abkowich, *Philos. Mag. B* **65**, 817 (1992).
87. *Polyimides as a Class of Heat-Resistant Polymers*, Ed. by M. M. Koton (Nauka, Leningrad, 1973), p. 28 [in Russian].
88. B. V. Kotov, N. A. Vasilenko, G. I. Rybalko, *et al.*, in *Abstracts of III All-Union Conference on Nonsilver and Unusual Photographic Processes* (Vilnius, 1980), p. 59.

89. B. V. Kotov, N. A. Vasilenko, V. I. Berendyaev, *et al.*, *Vysokomol. Soedin., Ser. A* **39**, 720 (1997); *Dokl. Akad. Nauk* **367**, 81 (1990).
90. E. L. Aleksandrova, *Opt. Zh.* **67** (3), 43 (2000) [*J. Opt. Technol.* **67**, 1034 (2000)]; *Opt. Zh.* **68** (10), 9 (2001) [*J. Opt. Technol.* **68**, 732 (2001)]; *Opt. Zh.* **70** (2), 50 (2003) [*J. Opt. Technol.* **70**, 109 (2003)].
91. E. L. Aleksandrova, *Opt. Spektrosk.* **93**, 17 (2002) [*Opt. Spectrosc.* **93**, 118 (2002)].
92. E. L. Aleksandrova, G. I. Nosova, V. V. Kudryavtsev, *et al.*, *Opt. Zh.* **69** (10), 10 (2002) [*J. Opt. Technol.* **69**, 706 (2002)].
93. E. L. Aleksandrova, G. I. Nosova, V. V. Kudryavtsev, *et al.*, in *Abstracts of All-Russia Conference on Amorphous and Microcrystalline Semiconductors* (St. Petersburg, 2002), p. 103.
94. G. I. Nosova, E. L. Aleksandrova, and V. V. Kudryavtsev, in *Abstracts of All-Russia Conference on Amorphous and Microcrystalline Semiconductors* (St. Petersburg, 2002), p. 106.
95. L. V. Gurevich, G. V. Karachevtsev, V. N. Kondrat'ev, Yu. A. Lebedev, V. A. Medvedev, V. K. Potapov, and Yu. S. Khodeev, *Bond-Breaking Energies. Chemical Ionization Potentials* (Nauka, Moscow, 1974) [in Russian].
96. Yu. A. Cherkasov, E. L. Aleksandrova, and Yu. P. Piryatinskiĭ, *Opt. Spektrosk.* **69**, 1046 (1990) [*Opt. Spectrosc.* **69**, 620 (1990)]; *Opt. Spektrosk.* **71**, 111 (1991) [*Opt. Spectrosc.* **71**, 65 (1991)]; *Opt. Spektrosk.* **73**, 931 (1992) [*Opt. Spectrosc.* **73**, 558 (1992)].
97. Yu. A. Cherkasov, V. I. Smirnov, E. L. Aleksandrova, *et al.*, in *Fundamentals of Optical Memory and Medium* (Vishcha Shkola, Kiev, 1987) [in Russian].
98. E. V. Mikubaeva, N. S. Kobotaeva, and E. E. Sirotkina, *Zh. Nauchn. Prikl. Fotogr.* **39** (6), 28 (1994).
99. E. E. Sirotkina, I. A. Gaĭbel', and V. I. Malkova, *Zh. Obshch. Khim.* **50**, 1589 (1980).
100. Yu. A. Cherkasov, E. L. Aleksandrova, and N. B. Zakharova, *Opt. Zh.* **66** (1), 32 (1999) [*J. Opt. Technol.* **66**, 27 (1999)].
101. I. F. Perepichka, D. D. Mysyk, and N. I. Sokolov, in *Abstracts of International Conference on Electrography-91* (Gamma, Moscow, 1991).
102. E. L. Aleksandrova and Yu. A. Cherkasov, *Opt. Spektrosk.* **87**, 943 (1999) [*Opt. Spectrosc.* **87**, 859 (1999)].
103. N. A. Davidenko, A. A. Golub, and N. G. Kuvshinskiĭ, in *Abstracts of III All-Union Conference on Nonsilver and Unusual Photographic Processes* (Vilnius, 1980), p. 151.
104. V. É. Kampar, *Usp. Khim.* **51** (27), 185 (1982).
105. V. P. Naĭdenov, E. D. Korotkaya, and V. Ya. Pochinok, in *Fundamentals of Optical Memory and Medium* (Vishcha Shkola, Kiev, 1980) [in Russian].
106. E. L. Aleksandrova, N. B. Sokolova, and N. A. Vasilenko, *Opt. Zh.* **67** (6), 61 (2000) [*J. Opt. Technol.* **67**, 551 (2000)].
107. E. E. Sirotkina and N. S. Kobotaeva, in *Abstracts of IV All-Union Conference on Nonsilver and Unusual Photographic Processes* (Suzdal, Russia, 1984).
108. K.-Y. Law and I. Tarnowsky, *J. Imaging Sci. Technol.* **38** (2), 118 (1994).
109. E. L. Aleksandrova, *Opt. Zh.* **68**, 12 (2001) [*J. Opt. Technol.* **68**, 508 (2001)].
110. R. O. Loufty and A. M. Hor, *J. Imaging Sci.* **33** (5), 151 (1989).
111. P. Kazmaker, R. Burt, and Di Paolo-Baranyl, *J. Imaging Sci.* **32** (1), 1 (1988).
112. B. V. Kotov, G. I. Rybalko, and V. I. Gaĭdylis, in *Abstracts of III All-Union Conference on Nonsilver and Unusual Photographic Processes* (Vilnius, 1980), p. 103.
113. E. L. Aleksandrova, N. V. Kamanina, Yu. A. Cherkasov, *et al.*, *Opt. Zh.* **65** (8), 87 (1998) [*J. Opt. Technol.* **65**, 676 (1998)].
114. M. Ya. Goĭkhman, E. L. Aleksandrova, and V. V. Kudryavtsev, *Opt. Zh.* **68** (11), 15 (2001) [*J. Opt. Technol.* **68**, 849 (2001)].
115. M. Ya. Goĭkhman, E. L. Aleksandrova, and V. V. Kudryavtsev, *Vysokomol. Soedin., Ser. A* **45**, 1045 (2003).
116. M. Ya. Goĭkhman, E. L. Aleksandrova, and V. V. Kudryavtsev, *Fiz. Tekh. Poluprovodn. (St. Petersburg)* **37** (7), 846 (2003) [*Semiconductors* **37**, 818 (2003)].
117. T. Enokida and M. Hirihashi, *J. Imaging Sci.* **35**, 235 (1991); *J. Imaging Sci. Technol.* **36**, 135 (1992).
118. Z. Khirokhashi and T. Kasai, *Denshi Shashin Gakkaishi* **25** (1), 24 (1986).
119. M. Khashimoto, *Denshi Shashin Gakkaishi* **25** (3), 10 (1986).
120. V. L. Kustov and S. N. Mazurenko, *Élektron. Prom-st, No. 2*, 31 (1997).
121. G. Kotowich, *J. Phys. Lett.* **69**, 2231 (1996).
122. E. A. Lebedev and T. Dittrich, *Appl. Phys. Lett.* **71**, 2686 (1997).
123. M. Estermatian, Z. D. Popovich, and G. Xu, *J. Phys. Chem.* **100**, 3716 (1996).
124. K. S. Nagayan and K. V. Geetha, *J. Phys. Chem.* **105**, 7671 (2001).
125. S. C. Yu and X. Cong, *Macromolecules* **31**, 5639 (1998).
126. K. Yoshino, X. N. Yin, and T. Akishi, *Mol. Cryst.* **255**, 197 (1994).
127. A. Itaya and I. Suzuki, *J. Phys. Chem. B* **101**, 5118 (1997).
128. A. V. Vannikov, V. I. Berendyaev, and A. R. Tameev, *Zh. Nauchn. Prikl. Fotogr.* **42** (2), 38 (1997).
129. L. P. Kazakova and E. L. Aleksandrova, *Fiz. Tekh. Poluprovodn. (St. Petersburg)* **35**, 695 (2001) [*Semiconductors* **35**, 666 (2001)].
130. R. C. Penwell and B. N. Ganguly, *J. Polym. Sci., Part D: Macromol. Rev.* **13**, 63 (1978).
131. E. L. Aleksandrova and Yu. A. Cherkasov, *Opt. Spektrosk.* **68**, 359 (1990) [*Opt. Spectrosc.* **68**, 210 (1990)]; *Opt. Spektrosk.* **68**, 1073 (1990) [*Opt. Spectrosc.* **68**, 626 (1990)].
132. M. R. Boon, *J. Non-Cryst. Solids* **2**, 177 (1972).



133. V. Gaĩdyalis, L. Elenskis, and Yu. Kalade, *Litov. Fiz. Sb.* **24** (4), 70 (1984); **29** (6), 96 (1989).
134. E. L. Aleksandrova, *Fiz. Tekh. Poluprovodn. (St. Petersburg)* **36**, 1384 (2002) [*Semiconductors* **36**, 1299 (2002)].
135. Yu. A. Cherkasov and N. V. D'yachenko, *Zh. Nauchn. Prikl. Fotogr.* **36**, 435 (1991); **37**, 1 (1992).
136. Y. Wang and A. Suna, *J. Phys. Chem.* **101**, 5627 (1997).
137. A. Rusekas and A. Undzenas, *J. Phys. Chem. B* **102**, 7365 (1998).
138. Z.-K. Xu and B.-K. Zhu, *Chem. Mater.* **10**, 1350 (1998).
139. E. M. Giroto, W. A. Gazotti, and M.-A. Paoly, *J. Phys. Chem. B* **104**, 6124 (2000).
140. C. Bubeck, in *Organic Materials for Photonics: Science and Technology*, Ed. by G. Zerbi (North-Holland, Amsterdam, 1993), p. 449.
141. A. V. Vannikov, A. D. Gishina, and R. V. Rikhval'skiĩ, *Usp. Khim.* **67**, 507 (1998).
142. L. Dai, *J. Macromol. Sci. Rev. Macromol. Chem. C* **39**, 273 (1993).
143. L. I. Subbotina, E. L. Aleksandrova, M. Ya. Goĩkhman, *et al.*, *Fiz. Tekh. Poluprovodn. (St. Petersburg)* **37**, 849 (2003) [*Semiconductors* **37**, 821 (2003)].
144. G. K. Lebedeva, V. A. Lukoshkin, V. V. Kudryavtsev, *et al.*, *Fiz. Tverd. Tela (St. Petersburg)* **43**, 750 (2001) [*Phys. Solid State* **43**, 783 (2001)].
145. A. V. Ten'kovtsev, V. A. Lukoshkin, and M. M. Dudkina, *Zh. Prikl. Khim. (St.-Peterburg)* **74**, 1147 (2001).

*Translated by Yu. Sin'kov*

## ATOMIC STRUCTURE AND NONELECTRONIC PROPERTIES OF SEMICONDUCTORS

# Determination of the Oxygen Diffusion Profile in Polycrystalline Lead Selenide Layers Using Nuclear Microanalysis

A. E. Gamarts<sup>\*^</sup>, V. M. Lebedev<sup>\*\*</sup>, V. A. Moshnikov<sup>\*</sup>, and D. B. Chesnokova<sup>\*</sup>

<sup>\*</sup>*St. Petersburg State Electrotechnical University, St. Petersburg, 197376 Russia*

<sup>^</sup>*e-mail: gamarts@mail.ru*

<sup>\*\*</sup>*Konstantinov St. Petersburg Institute of Nuclear Physics, Russian Academy of Sciences, Gatchina, Leningrad oblast, 188300 Russia*

Submitted March 16, 2004; accepted for publication March 24, 2004

**Abstract**—Rutherford backscattering and nuclear reactions are used to study the concentration profiles of elements in oxidized samples of lead selenide (PbSe). An interpretation of experimental data in the context of the theory of diffusion over the grain boundaries is suggested. © 2004 MAIK “Nauka/Interperiodica”.

Polycrystalline layers of lead chalcogenides are widely used as optical-radiation detectors in designing IR-absorption gas analyzers. The use of devices of this type is most promising to solve problems related to the measurement of gas concentrations at various industrial enterprises. This circumstance is associated with the possibility of using the above photodetectors in the design of small-size, inexpensive, and low-power IR-absorption gas analyzers that operate in the wavelength range 2–5  $\mu\text{m}$ , which includes the resonance-absorption lines of the main gases released by a fuel and power facility (hydrocarbons and carbon oxides).

Polycrystalline layers are subjected to sensitizing annealing in the course of fabrication of photoresistors based on PbSe. As a result, potential barriers are formed at the grain boundaries that separate efficiently the charge carriers and, thus, allow these photoresistors to operate at room temperature.

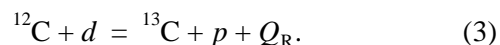
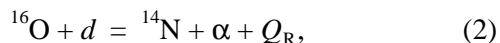
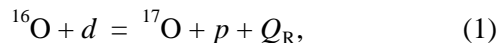
Analyzing mechanisms of oxidation in polycrystalline PbSe layers with a thickness of 0.5–1  $\mu\text{m}$  is a very difficult problem since oxygen can diffuse over grain boundaries and into a grain and can also be involved in chemical reactions that result in the formation of various compounds. The relation between the components of the oxidation process listed above depends on temperature, since these components have different activation energies (as the temperature increases, the rate of diffusion into the grain bulk increases). In addition, the diffusion front can be nonuniform over the depth.

The complexity of the problem requires the use of a method that makes it possible to determine the oxygen concentration in a matrix containing elements with a large atomic number (lead). In order to study the interaction of PbSe film with both atmospheric air and a substrate that contains oxygen, we have to obtain data on the distribution of the relevant elements over the depth of a submicrometer film with a step of tens of nanometers.

The sample under study was formed on a glass substrate using vacuum thermal evaporative deposition; a PbSe charge was used as the source. The film thickness was  $\sim 0.5 \mu\text{m}$ . In order to perform oxygen diffusion into the layer bulk, we annealed the sample in atmospheric air at a temperature of 673 K.

The composition of the PbSe film and concentration profiles of oxygen in this film were studied using non-destructive nuclear-physics methods of elemental analysis: the spectrometry of the Rutherford backscattering (RBS) and nuclear reactions (NRs) with deuterons [1, 2]. Combining the RBS and NR methods in the same experiment makes it possible to determine the ratio between the concentrations of the heavy and light elements in the oxidized PbSe samples to a high accuracy.

In order to determine the concentrations of oxygen and carbon, we can use the following reactions with deuterons:



These nuclear reactions are exothermic (reaction energy  $Q_R > 0$ ); therefore, the energies of protons and  $\alpha$  particles formed in the reactions are higher than those of deuterons scattered from the sample. Since the nuclear reactions of deuterons with heavy nuclei contained in the film and the substrate are prohibited by the Coulomb barrier at low energies, the peaks of secondary particles generated in nuclear reactions are observed against an almost zero background. This circumstance makes it possible to determine the concentrations of the aforementioned elements with a high sensitivity and a high accuracy.

The possibility of determining the concentration profiles of elements in the film using RBS and NR methods is based on the fact that incident ions are slowed down as they penetrate a material. Both the scattered deuterons and the ions generated in nuclear reactions and formed within the film under study at various depths have different energies as they leave the sample because these particles slow down when they traverse the sample. Incident deuterons also lose energy in the sample. Consequently, the larger the depth where the interaction event (scattering or nuclear reaction) occurs, the smaller the energy of the particle escaping from the target. The particles escaping from the surface of the sample have the highest energy, which is controlled by the process kinematics. For a film with a thickness no larger than 1  $\mu\text{m}$ , the energy of a detected particle  $E(x)$  and the depth  $x$  at which this particle is generated are related by the expression [1, 2]

$$E(x) = E(0) - gx, \quad (4)$$

where  $g$  is the total energy losses (per unit length) of the incident and emitted particles and  $E(0)$  is the energy of particles escaping from the surface of the sample. The values of quantities in this formula are determined by the interaction in the course of scattering or nuclear reaction, the elemental composition of the sample, the geometrical characteristics of the experiment, and the stopping power of the target material for deuterons, protons, and  $\alpha$  particles [1, 2].

Thus, the energy of a detected particle provides information about the depth of the layer where scattering or a nuclear reaction occur, while the number of these particles provides data on the content of the relevant element in this layer.

The structure of the film PbSe + O was determined using an analytical facility for studying materials by nuclear microanalysis based on the electrostatic accelerator at the St. Petersburg Institute of Nuclear Physics (Russian Academy of Sciences) [3]. The sample under study was installed in a vacuum chamber and was irradiated with deuterons with energy  $E_d = 0.9$  MeV. The deuteron-beam current at the sample was no higher than 100 nA, and the beam diameter was 0.3 cm. Secondary particles were detected using a planar Si detector with energy resolution  $\Delta E = 10$  keV for  $E_\alpha = 2.7$  MeV. The detector was installed at angle  $\varphi = 135^\circ$  with respect to the beam direction.

In Fig. 1 we show the experimental energy spectrum of the particles. An intense peak of deuterons scattered by the lead and selenium atoms and a continuous spectrum related to the particles scattered by the glass substrate are observed at energies lower than 0.9 MeV. The portion of the spectrum related directly to the PbSe film is shown in more detail in Fig. 2a. Arrows indicate the high-energy edges of the spectrum that correspond to deuterons scattered by the surface selenium and lead atoms.

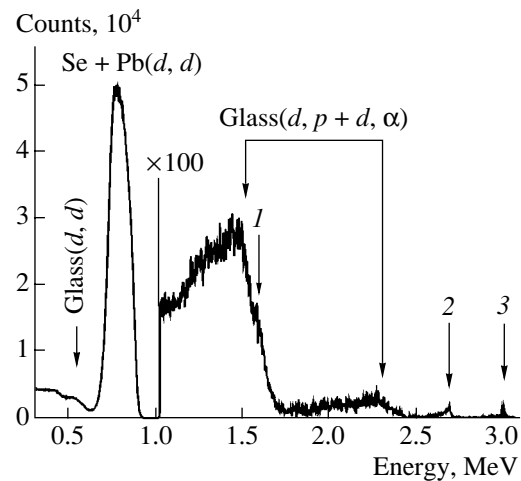


**Fig. 1.** Energy spectrum of the particles formed as a result of irradiation of a PbSe film on a glass substrate with deuterons with energy  $E_d = 0.9$  MeV. Peaks related to the reactions (1)  $^{16}\text{O}_f(d, p)^{17}\text{O}$ , (2)  $^{16}\text{O}_f(d, p)^{14}\text{N}$ , and (3)  $^{12}\text{C}_f(d, p)^{13}\text{C}$  are indicated.

The portion of the spectrum at energies higher than 0.9 MeV is related to the products of nuclear reactions of deuterons with oxygen and carbon. Broad peaks at energies from 1 to  $\sim 2.4$  MeV are due to protons and  $\alpha$  particles that are generated in reactions of deuterons with oxygen contained in the glass substrate. We failed to identify the protons that result from the reaction with oxygen contained in the film (the corresponding peak at an energy of  $\sim 1.6$  MeV is indicated by an arrow in Fig. 1) against the background of these broad peaks. Therefore, we used reaction (2) with the generation of  $\alpha$  particles in order to determine the concentration profile and oxygen content.

The  $\alpha$ -particle peak at an energy of 2.7 MeV is related to oxygen contained in the PbSe film. This portion of the spectrum is shown in Fig. 2b in more detail. Taking into account that the cross section of the nuclear reaction  $^{16}\text{O}(d, \alpha)^{14}\text{N}$  in the deuteron energy range under consideration is nearly constant [2], the steep high-energy falloff and the gently sloping low-energy tail indicate that the oxygen concentration decreases from the surface of the film to its bulk. This peak does not join the broad peak in the low-energy region. Consequently, we may state that only the surface region of the PbSe film (rather than the entire film) is oxidized.

An appreciable concentration of oxygen in the surface layer of the film under study is also indicated by the absence of pronounced flat portions related to lead and selenium in the spectrum and by a gradual transition from lead to selenium in the spectrum of scattered deuterons in Fig. 2a.

Protons with energy  $E_p \approx 3.0$  MeV (Fig. 1) were formed in the nuclear reaction of deuterons with carbon contained in the film. The presence of carbon in the film may be caused by contamination of the sample with the

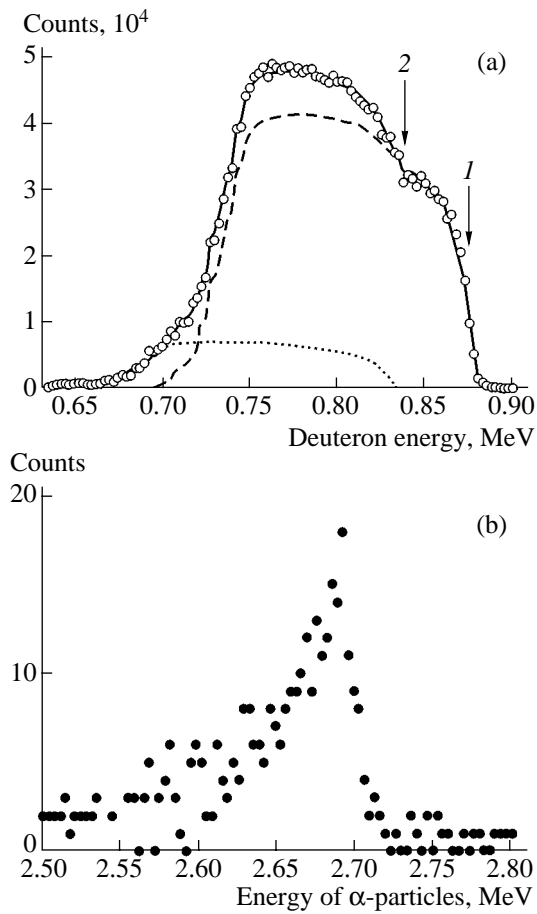


**Fig. 2.** (a) Fragment of an experimental spectrum related to the scattering of deuterons at the PbSe film (circles: (1) Pb, (2) Se) and the calculated simulation spectra: (dotted line) scattering by lead, (dashed line) scattering by selenium, and (solid line) the sum of these contributions. (b) Spectrum of  $\alpha$  particles (products of the  $^{16}\text{O}(d, p)^{14}\text{N}$  reaction with oxygen contained in the PbSe:O film).

products of decomposition of oil (in the vacuum pumps) in the course of the experiment.

Concentration profiles of elements in the film were calculated using the DVBS software package (Dubna), which is intended to be used to analyze spectra of elastically scattered ions [4]. The sample is divided into thin layers with a thickness of  $\sim 50$  nm. The element concentration is then specified in each layer; finally, a simulated spectrum is formed and is compared with experimental data. In fitting the spectra, we varied only the total content of selenium and lead with respect to the oxygen concentration that was obtained from the data on the nuclear reaction (Fig. 2b). The atomic fractions of lead and selenium were assumed to be equal over the entire thickness of the film. The cross section of scattering of 0.9-MeV deuterons by the lead and selenium atoms is equal to  $\sigma_S = 14.7 \times 10^{-24}$  cm<sup>2</sup> and  $\sigma_S = 2.53 \times 10^{-24}$  cm<sup>2</sup>, respectively. The cross section of the nuclear reaction  $^{16}\text{O}(d, \alpha)^{14}\text{N}$  is  $\sigma_R = 5.0 \times 10^{-27}$  cm<sup>2</sup> [2].

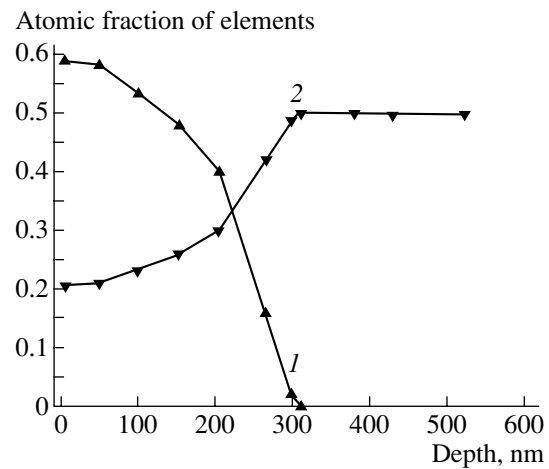


**Fig. 3.** Concentration profiles of (1) oxygen and (2) lead and selenium in the film of lead chalcogenide.

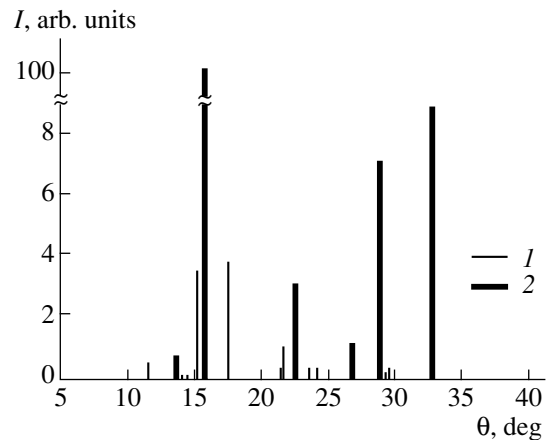


**Fig. 4.** Results of an X-ray analysis of an oxidized PbSe film: (1) PbSeO<sub>3</sub> and (2) PbSe.

In Fig. 2a we show the simulation spectra calculated in this way: contributions of scattering by lead (dotted line) and selenium (dashed line) and the sum of these partial spectra (solid line). It can be seen that there is satisfactory agreement between the simulation spectrum and experimental data (circles). It is still premature to state that oxygen is present in the deeper layers of the PbSe film because of the high oxygen concentration in the substrate and the insufficient thickness of the film itself.

In Fig. 3 we show the concentration profiles of elements in the film. The PbSe film with a thickness of  $\sim 0.52$   $\mu\text{m}$  was oxidized to a depth of  $\sim 0.25$   $\mu\text{m}$ . The greatest degree of oxidation occurs at the surface where the elemental composition corresponding to PbSeO<sub>3</sub> is observed. These data are consistent with the results of the X-ray phase analysis (Fig. 4) [5].

The diffusion profile of oxygen obtained (Fig. 3) can be interpreted in the following way. A gradual decrease

in the oxygen concentration with depth in the film can be accounted for by the prevalent diffusion of oxygen over the grain boundaries according to the Harrison model [6]. It is important that the continuous oxide is present only in the surface layer; the oxide is concentrated at the grain boundaries as the distance from the surface increases. The largest depth of penetration of oxygen atoms into the film can be determined from extrapolation of the concentration profile and is equal to ~300 nm in the case under consideration.

Thus, the nuclear physics methods used make it possible to study special features of diffusion for various durations and temperatures of annealing and determine the relation between the coefficients of diffusion over the grain boundaries and in the film bulk.

#### ACKNOWLEDGMENTS

We thank N.V. Golubchenko for his help in preparing the samples and V.A. Smolin and Yu.G. Luk'yanov for their help in studying the samples using the accelerator.

This study was supported by the Russian Foundation for Basic Research, project no. 04-02-17134a.

#### REFERENCES

1. G. Gavrilov, A. Krivchitch, and V. Lebedev, *Nucl. Instrum. Methods Phys. Res. A* **515**, 108 (2003).
2. A. N. Dyumin, V. K. Eremin, S. G. Konnikov, *et al.*, *Zh. Tekh. Fiz.* **63** (9), 166 (1993) [*Tech. Phys.* **38**, 821 (1993)].
3. V. M. Lebedev, Yu. G. Luk'yanov, and V. A. Smolin, in *Proceedings of XIII International Conference on Electrostatic Accelerators, Obninsk, Russia, 1999* (Obninsk, 2001), p. 60.
4. D. M. Shirokov and V. Bonas, *Nucl. Instrum. Methods Phys. Res. B* **84**, 497 (1993).
5. N. V. Golubchenko, V. A. Moshnikov, A. N. Rippinen, and D. B. Chesnokova, in *Russian High Technologies* (Moscow, 2003), p. 115 [in Russian].
6. L. G. Harrison, *Trans. Faraday Soc.* **57**, 1191 (1961).

*Translated by A. Spitsyn*

## ELECTRONIC AND OPTICAL PROPERTIES OF SEMICONDUCTORS

# Electronic and Structural Transitions in $\text{Pb}_{1-x}\text{Ge}_x\text{Te:Ga}$ Alloys under Pressure

E. P. Skipetrov<sup>1</sup>, E. A. Zvereva<sup>1</sup>, O. S. Volkova<sup>2</sup>, A. V. Golubev<sup>2</sup>,  
A. Yu. Mollaev<sup>3</sup>, R. K. Arslanov<sup>3</sup>, and V. E. Slyn'ko<sup>4</sup>

<sup>1</sup>Faculty of Physics, Moscow State University, Vorob'evy gory, Moscow, 119899 Russia

<sup>^</sup>e-mail: skip@mig.phys.msu.su

<sup>2</sup>Faculty of Materials Science, Moscow State University, Vorob'evy gory, Moscow, 119899 Russia

<sup>3</sup>Institute of Physics, Dagestan Scientific Center, Russian Academy of Sciences, ul. 26 Bakinskikh Komissarov 94, Makhachkala, 367003 Dagestan, Russia

<sup>4</sup>Institute of Materials Sciences (Chernovtsy Branch), National Academy of Sciences of Ukraine, ul. Zhovtneva 5, Chernovtsy, 274001 Ukraine

Submitted February 24, 2004; accepted for publication February 26, 2004

**Abstract**—The effect of pressure on electrical properties of Ga-doped  $n\text{-Pb}_{1-x}\text{Ge}_x\text{Te}$  alloys ( $x = 0.06, 0.08$ ) is studied. The pressure dependence of the activation energy of a deep Ga impurity center is obtained. It is shown that the position of the Ga level with respect to the bottom of the conduction band is virtually unchanged under pressure. Anomalies are found in the temperature and pressure dependences of the resistivity; these anomalies are apparently associated with structural phase transitions from the cubic to the rhombohedral and orthorhombic phases, respectively. The results obtained are used to construct a diagram of the modification of the energy spectrum of charge carriers in the cubic phase of the alloys investigated under pressure. © 2004 MAIK “Nauka/Interperiodica”.

It is known that doping PbTe and PbTe-based alloys with Ga leads to the formation of deep  $E_{\text{Ga1}}$  and  $E_{\text{Ga}}$  donor levels in the energy spectrum of charge carriers. In PbTe, the  $E_{\text{Ga1}}$  level lies in the band gap 65–70 meV below the bottom of the conduction band [1], and the level  $E_{\text{Ga}}$  lies in the region of allowed states in the conduction band 45 meV above the band's bottom [2, 3]. The character of variation in the position of these levels with composition of PbTe-based alloys is currently known with sufficient accuracy only for the  $E_{\text{Ga}}$  level and only for  $\text{Pb}_{1-x}\text{Ge}_x\text{Te}$  alloys. In these alloys, the impurity level shifts in parallel with the top of the valence band as the Ge content increases:  $E_{\text{Ga}} - L_6^- \approx (45 - 1980x)$  meV [2, 3].

There are even fewer data on the shift of Ga impurity levels under pressure, and their interpretation is ambiguous and contradictory [4, 5]. On the one hand, it has been found that the activation energy of the  $E_{\text{Ga1}}$  impurity level in the  $n\text{-PbTe:Ga}$  crystals decreases, which indicates that the level shifts in parallel with the top of the valence band under pressure. On the other hand, the free-hole density under a pressure of  $P > 15$  kbar increases rapidly, which indicates that the impurity level moves from the band gap into the valence band. Therefore, the main purpose of this study was to gain insight into the galvanomagnetic effects in  $\text{Pb}_{1-x}\text{Ge}_x\text{Te:Ga}$  alloys under conditions of hydrostatic compression in order to determine the character of the

shift of the  $E_{\text{Ga}}$  impurity level relative to the edges of the allowed bands and to construct a diagram of the modification of the energy spectrum of charge carriers in Ga-doped alloys under pressure.

Single-crystalline  $n\text{-Pb}_{1-x}\text{Ge}_x\text{Te:Ga}$  samples ( $x = 0.06, 0.08$ ) with Ga concentration  $C_{\text{Ga}} \approx 1.5\text{--}2$  mol % were synthesized by sublimation from the vapor phase. The Ge content in the samples was monitored by X-ray diffractometry, and the impurity content was determined from the Ga content in the charge making allowance for the impurity distribution over the length of the ingot [6]. We measured the temperature dependences of the resistivity and the Hall coefficient in the temperature range  $4.2 \leq T \leq 300$  K and magnetic fields  $B \leq 0.1$  T under a hydrostatic pressure of  $P < 7$  kbar ( $x = 0.06$ ) and the pressure dependence of the resistivity up to 90 kbar at  $T = 300$  K ( $x = 0.08$ ). Hydrostatic pressures as high as 7 kbar were attained in a chamber made of thermally treated beryllium bronze. As a pressure-transferring medium, a kerosene–oil–pentane mixture was used. Hydrostatic pressures as high as 90 kbar were attained in a chamber of the type that has a plane anvil with a hole. The sample was placed in a Teflon capsule filled with an ethanol–methanol mixture.

We found that, in the entire temperature range investigated, the temperature dependences of the resistivity  $\rho(T)$  (Fig. 1) and the Hall coefficient  $R_H(T)$  for  $\text{Pb}_{1-x}\text{Ge}_x\text{Te:Ga}$  alloys are typical of a semiconductor. The clearly pronounced activation portion in the

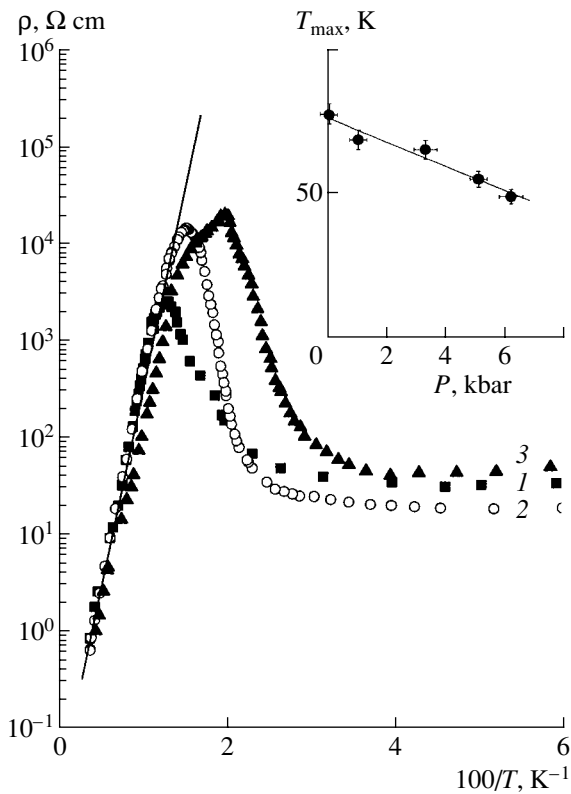


**Fig. 1.** Temperature dependence of the resistivity of the  $\text{Pb}_{0.94}\text{Ge}_{0.06}\text{Te:Ga}$  alloy under hydrostatic compression.  $P = (1)$  0, (2) 3.3, and (3) 6.2 kbar. The pressure dependence of the peak temperature is shown in the inset.

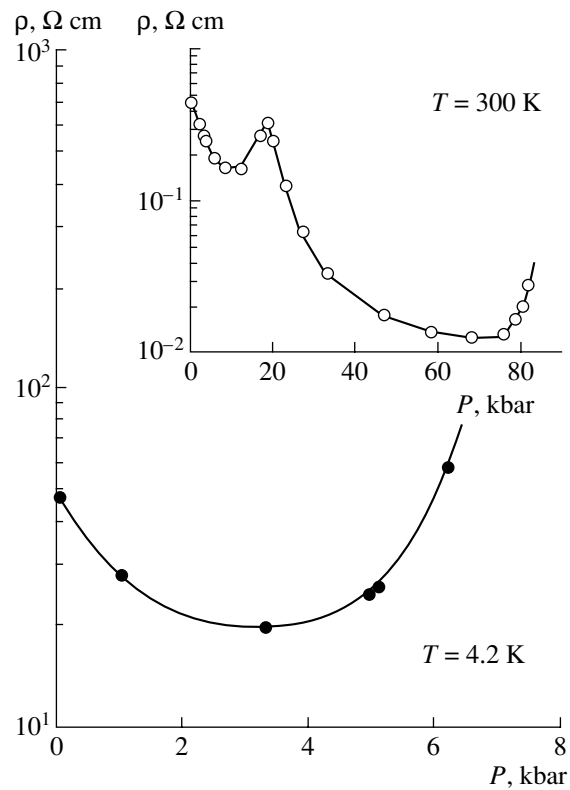


**Fig. 2.** Pressure dependence of the resistivity of the  $\text{Pb}_{1-x}\text{Ge}_x\text{Te:Ga}$  alloy ( $x = 0.06$ ) at  $T = 4.2$  K. The same dependence for the sample with  $x = 0.08$  at 300 K is shown in the inset.

high-temperature region indicates the presence of a deep impurity level in the band gap. The slope of the activation portion remains virtually unchanged as the pressure increases.

Anomalous peaks were observed in the temperature dependence of the resistivity in the range  $T = 50\text{--}80$  K. Previously, similar peaks were observed in the temperature dependence of the resistivity of doped  $\text{Pb}_{1-x}\text{Ge}_x\text{Te}$  alloys under atmospheric pressure [7]. It was shown by X-ray diffraction analysis that a structural phase transition from the cubic phase to the rhombohedral phase occurs at the same temperature [8]. Therefore, it was assumed later that the position of the characteristic peak  $T_{\text{max}}$  in the  $\rho(T)$  dependence for doped alloys also corresponds to the temperature of the structural phase transition  $T_{\text{ph}}$  [9, 10]. A considerable (as large as 70 K) shift in the peak position for Ga-doped crystals was attributed to a decrease in the phase-transition temperature as a result of doping, which was found experimentally, for example, in  $\text{Pb}_{1-x}\text{Ge}_x\text{Te}$  alloys with nonisoelectronic impurities [10].

The pressure dependence of the temperature of the anomalous peak  $T_{\text{max}}$  is shown in the inset to Fig. 1. It turned out that the peak temperature  $T_{\text{max}}$  decreases virtually linearly as the pressure increases. This phenomenon is qualitatively consistent with the behavior of the

phase transition temperature under pressure in undoped alloys. The rate of variation in the peak temperature with pressure was  $dT_{\text{max}}/dP \approx -4$  K/kbar, whereas the pressure coefficient of variation in the phase transition temperature  $dT_{\text{ph}}/dP$ , which was experimentally determined for undoped  $\text{Pb}_{1-x}\text{Ge}_x\text{Te}$  alloys ( $x = 0.01\text{--}0.05$ ), varied in the range from  $-5$  to  $-12$  K/kbar [11, 12]. Therefore, the anomalous peak in the temperature dependences of the resistivity for undoped alloys can indeed be attributed to the structural phase transition to the rhombohedral phase.

Under pressure, the resistivity at liquid-helium temperature decreases, passes through a minimum at  $P \approx 3$  kbar, and then increases (Fig. 2). Such a behavior of the resistivity cannot be accounted for by the reconstruction of the electronic structure under pressure since the activation energy of the impurity level of Ga is virtually unchanged in the pressure range investigated, whereas the zero-gap state in the  $\text{Pb}_{1-x}\text{Ge}_x\text{Te}$  alloy ( $x = 0.06$ ), according to our estimates, can be attained at a pressure of  $P \approx 40$  kbar only.

The pressure dependence of the resistivity at room temperature, which is shown in the inset to Fig. 2, is more complicated, with a local peak at  $P \approx 20$  kbar and a broad valley at  $P \approx 70$  kbar. The valley in the pressure dependence of the resistivity at  $P \approx 70$  kbar apparently

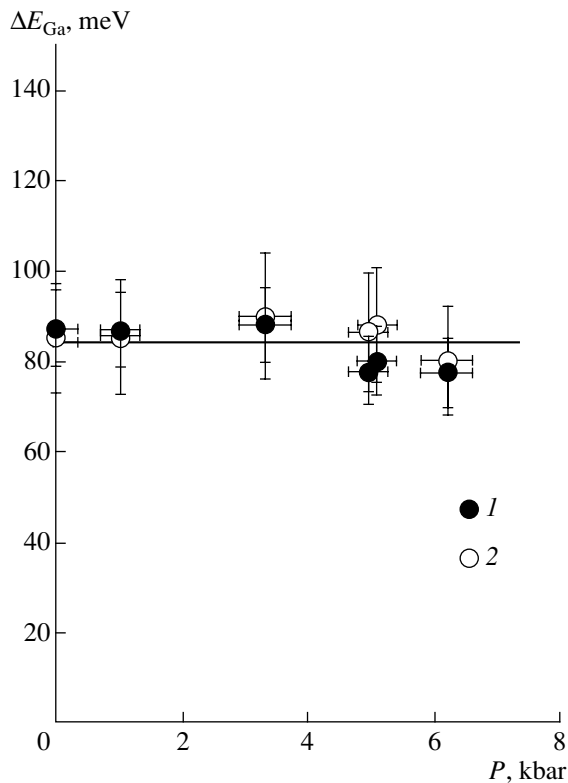


**Fig. 3.** Pressure dependence of the activation energy of the gallium impurity level for the  $\text{Pb}_{0.94}\text{Ge}_{0.06}\text{Te}:\text{Ga}$  alloy. The activation energy was determined from temperature dependences of (1) the resistivity and (2) the Hall coefficient.

corresponds to the point of inversion of the energy bands in the  $\text{Pb}_{1-x}\text{Ge}_x\text{Te}$  alloy ( $x = 0.08$ ) under pressure. Such a behavior of the resistivity with an increase in pressure is typical of the alloys based on lead chalcogenides with a normal spectrum [13, 14] and is usually attributed to a decrease in the effective mass and, consequently, to an increase in the mobility of charge carriers with the transition through the zero-gap state under pressure.

The anomalous peak in the pressure dependence of the resistivity at  $P \approx 20$  kbar has not been previously observed. It is known that a similar peak in the  $\rho(P)$  dependence for  $\text{PbTe}$ , which is located at  $P \approx 60$  kbar, is associated with the phase transition from the cubic lattice of the NaCl type to the orthorhombic lattice of the GeS type [15, 16]. Therefore, we may assume that the peak in the  $\rho(P)$  dependence at  $T = 300$  K and the sharp increase in resistivity at  $T = 4.2$  K under pressure, which were found by us, are also associated with the structural phase transition from the cubic lattice to the orthorhombic lattice. In this case, we can reasonably explain the shift of the critical pressure of the phase transition to lower pressures as the alloy composition varies and the temperature decreases from room temperature to liquid-helium temperature. This shift corresponds qualitatively to the known experimental data on

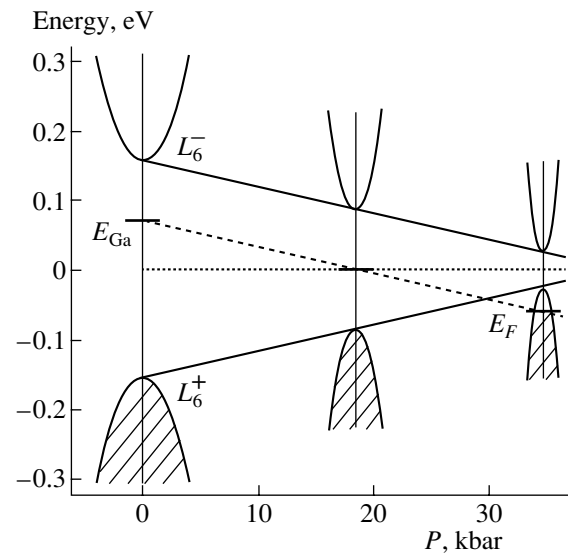


**Fig. 4.** Model of reconstruction of the energy spectrum of charge carriers in the  $\text{Pb}_{0.94}\text{Ge}_{0.06}\text{Te}:\text{Ga}$  alloy under pressure at  $T = 4.2$  K.

the pressure-induced phase transition in  $\text{Pb}_{1-x}\text{Sn}_x\text{Se}$  alloys [17].

We determined the activation energy of the deep gallium level  $\Delta E_{\text{Ga}}$  and constructed its pressure dependence (Fig. 3) from the slope of the activation portion in dependences  $\rho(1/T)$  and  $R_H(1/T)$ . At atmospheric pressure, the activation energy is  $\Delta E_{\text{Ga}} \approx 86$  meV, which is consistent with the data [2, 3] within the experimental accuracy. As the pressure increases, the activation energy of the impurity level is virtually unchanged (straight line in Fig. 3). Therefore, we may conclude that, as the pressure increases, the position of the Ga impurity level relative to the bottom of the conduction band does not change.

Based on the experimental data obtained, we can suggest a diagram of the reconstruction of the energy spectrum of the  $\text{Pb}_{1-x}\text{Ge}_x\text{Te}:\text{Ga}$  alloy under pressure (Fig. 4). As the pressure increases, the band gap decreases, whereas the position of the impurity level relative to the bottom of the conduction band remains unchanged. Therefore, at certain critical pressures, the Ga level that stabilizes the Fermi level  $E_F$  should sequentially intersect the midgap and the top of the valence band, thus inducing  $n$ - $p$  conversion of the conductivity type and an insulator–metal transition under pressure, respectively. In this case, the activation energy of the Ga level should remain constant up to the point of the  $n$ - $p$  conversion. As the pressure further increases, the electrons are thermally activated from the valence band to the Ga level, and the activation energy of the impurity level decreases to zero according to the linear law with the rate  $d(\Delta E_{\text{Ga}})/dP = dE_g/dP \approx 7.4$  meV/kbar [18].

Such a behavior of electrical parameters and the activation energy of the  $E_{\text{Ga}1}$  gallium-impurity level



under pressure was apparently observed previously for  $n$ -PbTe:Ga single crystals [4, 5]. In that case, a decrease in the activation energy of the level caused the conversion of the conductivity type and an sharp increase in the concentration of free holes. Therefore, we may assume that the deep  $E_{\text{Ga1}}$  level also shifts in parallel with the bottom of the conduction band under pressure.

#### ACKNOWLEDGMENTS

This study was supported by the Russian Foundation for Basic Research (project nos. 01-02-17446 and 02-02-17888), a grant from the President of the Russian Federation (no. NSh 1786.2003.2), and the scientific program "Universities of Russia."

#### REFERENCES

1. B. A. Volkov, L. I. Ryabova, and D. R. Khokhlov, *Usp. Fiz. Nauk* **172**, 875 (2002) [*Phys. Usp.* **45**, 819 (2002)].
2. E. P. Skipetrov, E. A. Zvereva, L. A. Skipetrova, *et al.*, *J. Cryst. Growth* **210**, 292 (2000).
3. E. P. Skipetrov, E. A. Zvereva, V. V. Belousov, *et al.*, *Fiz. Tekh. Poluprovodn. (St. Petersburg)* **34**, 932 (2000) [*Semiconductors* **34**, 894 (2000)].
4. B. A. Akimov, N. B. Brandt, A. M. Gas'kov, *et al.*, *Fiz. Tekh. Poluprovodn. (Leningrad)* **17**, 87 (1983) [*Sov. Phys. Semicond.* **17**, 53 (1983)].
5. B. A. Akimov, A. V. Albul, E. V. Bogdanov, and V. Yu. Il'in, *Fiz. Tekh. Poluprovodn. (St. Petersburg)* **28**, 232 (1994) [*Semiconductors* **28**, 140 (1994)].
6. V. E. Slyn'ko, *Vestn. L'vov. Gos. Univ.* **34**, 291 (2001).
7. S. Takaoka and K. Murase, *Phys. Rev. B* **20**, 2823 (1979).
8. D. C. Hohnke, H. Holloway, and S. Kaiser, *J. Phys. Chem. Solids* **33**, 2053 (1972).
9. B. A. Akimov, A. V. Albul, I. I. Ivanchik, *et al.*, *Fiz. Tekh. Poluprovodn. (St. Petersburg)* **27**, 351 (1993) [*Semiconductors* **27**, 194 (1993)].
10. A. I. Lebedev and I. A. Sluchinskaya, *Fiz. Tverd. Tela (St. Petersburg)* **35**, 629 (1993) [*Phys. Solid State* **35**, 321 (1993)].
11. V. V. Maslov, S. V. Baryshnikov, V. V. Kazakov, and I. A. Drabkin, in *Elementary Excitations in Ferroelectrics* (Leningrad, 1983), p. 30 [in Russian].
12. T. Suski, S. Takaoka, K. Ishii, and K. Murase, *J. Phys. C* **17**, 2181 (1984).
13. J. Melngailis, J. A. Kafalas, and T. C. Harman, *J. Phys. Chem. Solids Suppl.* **32**, 407 (1971).
14. J. Melngailis, T. C. Harman, and J. A. Kafalas, in *Physics of IV-VI Semiconductors*, Ed. by S. Rabi (Gordon and Breach, New York, 1974), p. 59.
15. Y. Fujii, K. Kitamura, A. Onodera, and Y. Yamada, *Solid State Commun.* **49**, 135 (1984).
16. T. Chattopadhyay, A. Werner, and H. G. von Schnering, *Rev. Phys. Appl.* **19**, 807 (1984).
17. N. B. Brandt, Ya. G. Ponomarev, E. P. Skipetrov, *et al.*, *Fiz. Tekh. Poluprovodn. (Leningrad)* **17**, 645 (1983) [*Sov. Phys. Semicond.* **17**, 403 (1983)].
18. G. Nimtz and B. Schlicht, in *Narrow-Gap Semiconductors*, Ed. by R. Dornhaus, G. Nimtz, and B. Schlicht (Springer, Berlin, 1983), p. 1.

*Translated by N. Korovin*

## ELECTRONIC AND OPTICAL PROPERTIES OF SEMICONDUCTORS

# Magnetic-Field Dependences of the Conductivity and Hall Factor in MBE-Grown $\text{Cd}_x\text{Hg}_{1-x}\text{Te}$ Layers

P. A. Bakhtin, S. A. Dvoretiskii, V. S. Varavin<sup>^</sup>, A. P. Korobkin,  
N. N. Mikhailov, and Yu. G. Sidorov

*Institute of Semiconductor Physics, Siberian Division, Russian Academy of Sciences, Novosibirsk, 630090 Russia*

<sup>^</sup>e-mail: varavin@isp.nsc.ru

Submitted January 8, 2004; accepted for publication March 4, 2004

**Abstract**—Dependences of conductivity and the Hall factor on magnetic field in  $\text{Cd}_x\text{Hg}_{1-x}\text{Te}$  (mercury cadmium telluride, MCT) have been studied at 77 K. Films of  $n$ -type conduction with  $X = 0.21$ – $0.23$  were grown on (013) GaAs substrates by MBE. As the magnetic field increases from 0 to 1 T, conductivity and the Hall factor decrease by a factor of 3–5. These dependences are well described in terms of a two-layer model with high and low mobility of electrons in the layers. The analysis of data obtained with layer-by-layer etching has shown that an MCT film can be described as a two-layer structure. In this case, a thin layer with high density and low mobility of electrons is located near the interface with a CdTe buffer. A high density and low mobility of electrons can be attributed to the high defectiveness of this layer. Studies by transmission electron microscopy have demonstrated the presence of a network of dislocations in MCT film near the interface with the buffer layer. © 2004 MAIK “Nauka/Interperiodica”.

### 1. INTRODUCTION

To derive IR photodetectors based on  $\text{Cd}_x\text{Hg}_{1-x}\text{Te}$  (mercury cadmium telluride, MCT)—both photovoltaic and photoconductive—information on the density and mobility of carriers and their distribution across the thickness of a structure is required. To characterize the properties of carriers, all the producers of MCT use measurements of conductivity  $\sigma$  and the Hall factor  $R_H$ . However, estimates based on conventional measurements with a given magnetic field can lead to incorrect conclusions, because several types of carriers can coexist in MCT. It is generally recognized that much more information can be obtained from studies of conductivity and the Hall factor dependences on magnetic field and by analyzing hybrid conduction [1–4]. In this case, the density and mobility of different types of carriers in a sample can be determined.

In this study, we investigate  $\sigma$  and  $R_H$  dependences on magnetic field in MBE-grown MCT films with the aim of determining the parameters of carriers (their density and mobility) and their distribution across the thickness of the film.

### 2. EXPERIMENTAL RESULTS AND DISCUSSION

We studied MCT films ( $X = 0.21$ – $0.23$ ) 8–14  $\mu\text{m}$  thick grown by MBE on (013) GaAs substrates [5] with a CdTe buffer layer of about 6  $\mu\text{m}$  in thickness. All the MCT films were grown in similar conditions. They contained a working layer of homogeneous composition and graded-composition layers at the interfaces with the buffer layer and near the free surface, where  $X$

increased to  $X \approx 0.5$  toward the interfaces (Fig. 1). The thickness of the graded-composition layer was 1–1.5  $\mu\text{m}$  at the interface with the buffer and 0.4–0.8  $\mu\text{m}$  near the free surface.

As-grown films had  $n$ -type conduction, and with weak magnetic fields (below 0.05 T) the effective carrier density  $1/|qR_H|$ , where  $q$  is the elementary charge) was  $(2$ – $5) \times 10^{14} \text{ cm}^{-3}$ , and the effective mobility ( $\mu_H = |\sigma R_H|$ ) was  $4 \times 10^4$ – $1.3 \times 10^5 \text{ cm}^2/(\text{V s})$  at 77 K. As the magnetic field increases to 1 T, conductivity and the Hall factor decrease significantly (severalfold). We

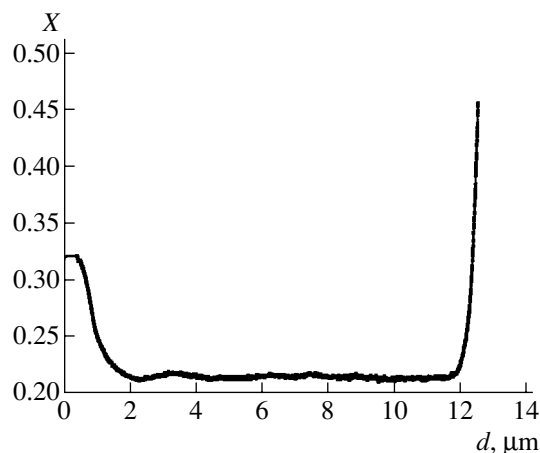


**Fig. 1.** Distribution of composition ( $X$ ) across the thickness of the MCT film, measured with an automated ellipsometer during film growth. The thickness is counted from the interface with the CdTe buffer layer.

measured conductivity and the Hall factor in the magnetic field range 0–1 T, including studies with layer-by-layer etching of MCT films.

Figure 2 shows typical experimental and simulated dependences of the Hall factor and conductivity on the magnetic field.

The calculation of these dependences was done under the assumption that several types of carriers exist in a film [4]:

$$\sigma(B) = \frac{\left[ \sum_i \sigma_{xx}^i(B) \right]^2 + \left[ \sum_i \sigma_{xy}^i(B) \right]^2}{\sum_i \sigma_{xx}^i(B)}, \quad (1)$$

$$R_H(B) = \frac{1}{B} \frac{\sum \sigma_{xy}^i(B)}{\left[ \sum_i \sigma_{xx}^i(B) \right]^2 + \left[ \sum_i \sigma_{xy}^i(B) \right]^2}, \quad (2)$$

where  $\sigma_{xx}^i(B)$  and  $\sigma_{xy}^i(B)$  are components of the conductivity tensor in the magnetic field, which have the form

$$\sigma_{xx}^i(B) = \frac{qn_i\mu_i}{1 + \mu_i^2 B^2}, \quad (3)$$

$$\sigma_{xy}^i(B) = \frac{qn_i\mu_i^2 B}{1 + \mu_i^2 B^2}. \quad (4)$$

The index  $i$  indicates different types of carriers.

Graded band-gap layers were located on the interfaces of MCT films; therefore, we carried out the initial calculations considering these layers. Since  $X$  in graded-gap layers is larger than in the working layer, the electron mobility in these layers is lower. The calculation taking into account the electron mobility dependence on MCT composition in graded-gap layers has shown that, in the case of equal densities in the working and graded-gap layers, the dependences of conductivity and the Hall factor will be considerably weaker (Fig. 2, curves  $I''$ ,  $2''$ ) than those observed in the experiment. The assumption of equal carrier densities in the working and graded-gap layers is based on the fact that, when  $X$  increases from 0.2 to 0.4 in MCT films grown in similar conditions, the electron density decreases only slightly. Therefore, the observed dependences on magnetic field cannot be accounted for only by the presence of graded-gap layers.

The best correlation between the calculated and experimental dependences can be obtained if we assume that electrons with low mobility exist in an MCT film. In this case, the experimental dependences can be described quite well if we consider two types of electrons (Fig. 2, curves  $I'$ ,  $2'$ ). The fitting of calculated

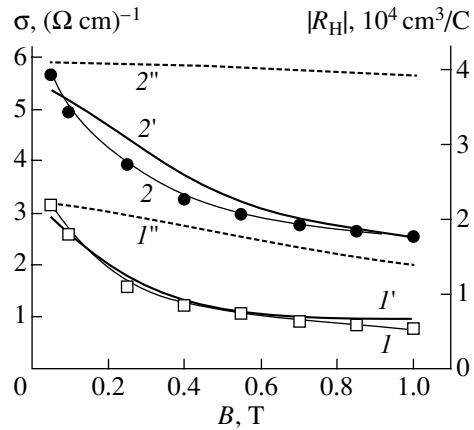


**Fig. 2.** Dependences of the Hall factor and conductivity on magnetic field. The thickness of the MCT film  $d = 13.4 \mu\text{m}$ ,  $X = 0.215$ . ( $I$ ,  $I'$ ,  $I''$ )  $\sigma(B)$  and ( $2$ ,  $2'$ ,  $2''$ )  $R_H(B)$ . ( $I$ ,  $2$ ) Experiment and ( $I'$ ,  $2'$ ) calculation taking into account two types of electrons; ( $I''$ ,  $2''$ ) calculation taking into account only the graded-gap layers.

curves to experimental data was done with fitting parameters  $n_i$  and  $\mu_i$ , so as to obtain the best coincidence for both  $\sigma(B)$  and  $R_H(B)$  dependences simultaneously. For the curves shown in Fig. 1, the best-fit parameters were  $\mu_1 = 130000 \text{ cm}^2/(\text{V s})$ ,  $n_1 = 1.3 \times 10^{14} \text{ cm}^{-3}$ ,  $\mu_2 = 9000 \text{ cm}^2/(\text{V s})$ , and  $n_2 = 3.0 \times 10^{14} \text{ cm}^{-3}$ .

For different films, calculated  $n_1$  and  $\mu_1$  for high-mobility electrons are  $(1-3) \times 10^{14} \text{ cm}^{-3}$  and  $(100000-160000) \text{ cm}^2/(\text{V s})$ , respectively; for low-mobility electrons,  $(2-5) \times 10^{14} \text{ cm}^{-3}$  and  $2000-12000 \text{ cm}^2/(\text{V s})$ . To investigate the distribution of electrons across the thickness of MCT film, experiments with layer-by-layer etching of the film in a 1% solution of Br in HBr were performed. The time of each etching was the same, and the thickness of a single removed layer was assumed to be equal to the total thickness of the removed part divided by the number of etchings. The conductivity, Hall factor, mobility, and carrier density in the removed layers in a magnetic field of 0.5 T were determined by the differential method, using the relations of the two-layer Petritz model [6]:

$$\mu = |R_H| \sigma,$$

$$N = \frac{1}{q|R_H|},$$

where

$$\sigma = \frac{\sigma_{n+1}d_{n+1} - \sigma_n d_n}{d_{n+1} - d_n}, \quad (5)$$

$$R_H = \frac{\sigma_{n+1}^2 |R_{Hn+1}| d_{n+1} - \sigma_n^2 |R_{Hn}| d_n}{(\sigma_{n+1} d_{n+1} - \sigma_n d_n)^2} (d_{n+1} - d_n). \quad (6)$$

In Eqs. (5) and (6), indices  $n$  and  $n + 1$  denote the  $n$ th and  $(n + 1)$ th etchings, and  $d_n$  and  $d_{n+1}$  are the film thicknesses after the  $n$ th and  $(n + 1)$ th etchings, respectively.

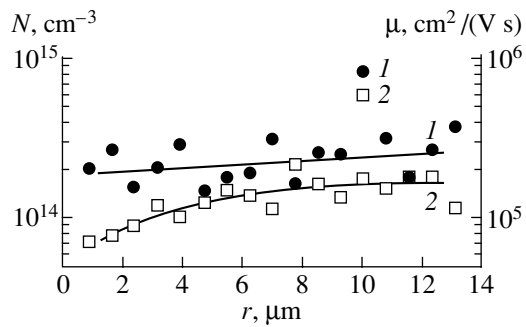


**Fig. 3.** Electron density and mobility in layers removed by etching;  $r$  is the distance from the heterointerface to the middle of the removed layer. The thickness of the MCT film  $d = 13.4 \mu\text{m}$ ,  $X = 0.215$ . Points (calculated): (1) density and (2) mobility; solid lines, the respective smoothed distributions across the film thickness.

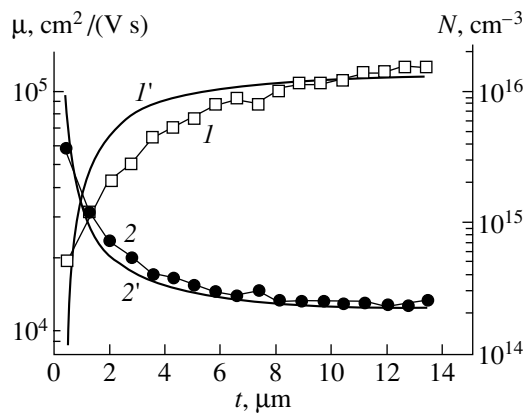


**Fig. 4.** Mobility ( $\mu$ ) and electron density ( $N$ ) in the remaining layer vs. its thickness ( $t$ ). The thickness of MCT film  $d = 13.4 \mu\text{m}$ ,  $X = 0.215$ . (1, 1') density and (2, 2') mobility. (1, 2) Experiment and (1', 2') calculation in terms of the two-layer model.

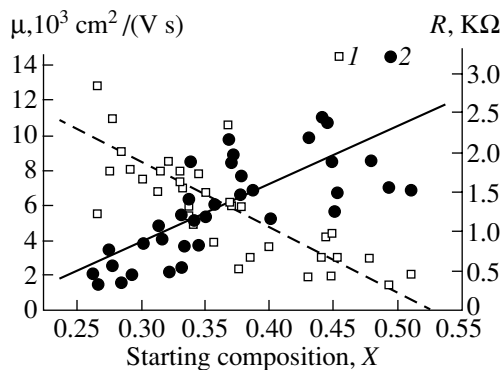


**Fig. 5.** (1) Mobility of slow electrons ( $\mu$ ) and (2) shunting resistance ( $R$ ) for a square photosensitive element as functions of the initial composition of the graded-gap layer on the interface with the CdTe buffer layer.

Figure 3 shows the mobility and electron density in the removed layers. As can be seen, the electron density in the removed layers is nearly constant, and the mobil-

ity slightly decreases as one approaches the heterointerface. Note that, in different samples, the mobility in the removed layers can exceed the initial effective mobility by a factor of 1.5–3. It can be seen from Fig. 3 that, as the remaining part of the film becomes thinner, the mobility in this part sharply decreases, and the density increases. These dependences can be attributed to the inhomogeneity of the layer, so we considered a two-layer model. In this model, the film comprises the basic layer, which contains electrons of high mobility and low density, and a thin ( $\sim 0.5 \mu\text{m}$ ) layer near the heterointerface, which contains electrons of high density and low mobility. Calculations of the density and mobility in the remaining part of the film, which were carried out in terms of the two-layer model, demonstrate a very good qualitative and quantitative agreement with the experimental data (Fig. 4). The obtained best-fit values of mobility and density for two types of electrons

$$d_1 = 12.9 \mu\text{m}, \quad n_1 = 1.8 \times 10^{14} \text{ cm}^{-3},$$

$$\mu_1 = 130000 \text{ cm}^2/(\text{V s}); \quad d_2 = 0.5 \mu\text{m},$$

$$n_2 = 9.0 \times 10^{15} \text{ cm}^{-3}, \quad \mu_2 = 9000 \text{ cm}^2/(\text{V s})$$

also agree well with the values obtained in fitting the dependences on magnetic field for the initial sample. The high density of electrons with low mobility in this layer may be related to the high defectiveness of this layer. Transmission electron microscopy has shown a network of mismatch dislocations at a distance of about  $0.1 \mu\text{m}$  from the interface with the buffer layer. According to [6, 7], a high density of dislocations in MCT can induce an increase in the electron density and a decrease in mobility.

Since the layer with high electron density near the heterointerface is a shunting layer in fabricating the photoresistors, it is necessary to minimize its contribution to the total conductance of a film. In the films under study, this contribution can reach a value of 0.05–0.5. We have studied MCT films with various initial compositions of the graded-gap layer at the interface with the CdTe buffer layer. The mobility and density of low-mobility electrons and the shunting resistance  $R$  for a square photosensitive element were determined from the analysis of dependences on magnetic field. Figure 5 shows the dependences of mobility and shunting resistance on the initial composition of the graded-gap layer. It can be seen that, as  $X$  increases, the mobility of the low-mobility electrons decreases, and  $R$  steadily increases because of the decrease in mobility. Twofold scatter is observed in the density of low-mobility electrons, its value in terms of the surface concentration is  $(7\text{--}15) \times 10^{11} \text{ cm}^{-2}$ , and no dependence on the initial composition is observed.

Therefore, the contribution of low-mobility electrons to total conductance of an MCT film can be reduced by the formation of a graded-gap layer with high initial  $X$  on the interface with the buffer.

## 3. CONCLUSIONS

In MBE-grown  $n$ -type MCT films, conductivity and the Hall factor decrease severalfold as the magnetic field increases. The dependences on magnetic field are well described in terms of the conduction model with two types of carriers: electrons with high and low mobility.

The analysis of data obtained by means of layer-by-layer etching has shown that in an MCT film, near the interface with the buffer layer, a thin layer exists with a high density of low-mobility electrons, which can be attributed to the high defectiveness of this layer. This layer can significantly reduce the effective mobility and raise the effective carrier density in MCT films; it may also have a shunting effect on photoresistors. The contribution of low-mobility electrons to the total conductance of an MCT film can be reduced by the formation of a graded-band-gap layer with high initial  $X$  on the interface with the buffer.

## ACKNOWLEDGMENTS

The authors are grateful to I.I. Izhnin for valuable discussions and to A.K. Gutakovskii for TEM studies of interface layers in MCT films.

## REFERENCES

1. M. B. Reine, K. R. Maschhoff, S. P. Tobin, *et al.*, *Semicond. Sci. Technol.* **8**, 788 (1993).
2. J. R. Meyer, C. A. Hoffman, F. J. Bartoli, *et al.*, *Semicond. Sci. Technol.* **8**, 805 (1993).
3. E. Finkman and Y. Nemirovsky, *J. Appl. Phys.* **53**, 1052 (1982).
4. L. F. Lou and W. H. Frye, *J. Appl. Phys.* **56**, 2253 (1984).
5. Yu. G. Sidorov, S. A. Dvoret'skiĭ, V. S. Varavin, *et al.*, *Fiz. Tekh. Poluprovodn. (St. Petersburg)* **35**, 1092 (2001) [*Semiconductors* **35**, 1045 (2001)].
6. R. L. Petritz, *Phys. Rev.* **110**, 1254 (1958).
7. S. G. Gasan-zade, S. V. Staryĭ, M. V. Strikha, and G. A. Shepel'skiĭ, *Fiz. Tekh. Poluprovodn. (St. Petersburg)* **37**, 8 (2003) [*Semiconductors* **37**, 6 (2003)].

*Translated by D. Mashovets*

## ELECTRONIC AND OPTICAL PROPERTIES OF SEMICONDUCTORS

# Effect of Low-Temperature Annealing on Electrical Properties of $n$ -HgCdTe

P. A. Bakhtin, S. A. Dvoretiskii, V. S. Varavin\*, A. P. Korobkin,  
N. N. Mikhailov, I. V. Sabinina, and Yu. G. Sidorov

*Institute of Semiconductor Physics, Siberian Division, Russian Academy of Sciences, Novosibirsk, 630090 Russia*

\*e-mail: varavin@isp.nsc.ru

Submitted January 8, 2004; accepted for publication March 4, 2004

**Abstract**—The effect of low-temperature isothermal annealing on electrical properties of  $\text{Cd}_x\text{Hg}_{1-x}\text{Te}$  (mercury cadmium telluride, MCT) films is investigated. Films of  $n$ -type conduction with  $x = 0.21$ – $0.23$  were grown on GaAs substrates by MBE. Annealings of 1–1000 h duration were carried out at 90–230°C. The changes in conductivity, the Hall factor, and the lifetime of minority carriers after annealing are explained by the formation of mercury vacancies and egress of Hg atoms from the sample. The effect of various surface coatings on the rate of variation of MCT film electrical properties was investigated. An anodic oxide appeared to be the most efficient coating to stabilize the parameters of  $n$ -type films. The analysis of the magnetic-field dependences of the Hall factor and conductivity has shown that the observed modification of parameters upon annealing can be described in terms of a two-layer model with two types of electrons—high and low mobility. © 2004 MAIK “Nauka/Interperiodica”.

## 1. INTRODUCTION

The solid solution  $\text{Cd}_x\text{Hg}_{1-x}\text{Te}$  (mercury cadmium telluride, MCT), whose band gap can be varied in a wide range by composition modification, is the leading material in the production of IR photodetectors for the 3–5 and 8–12  $\mu\text{m}$  wavelength ranges. The development of fabrication technology for narrow-gap semiconductors and the elaboration of a whole range of photoresistor and photodiode designs has led to the creation of high quality devices. Therefore, along with further improvement of the device parameters, the problems of current interest are reproducibility and stability. It is well known that the electrical parameters of MCT, primarily, the density of carriers and the conduction type, are modified under various thermal treatments. These modifications are related to the evaporation of mercury from the surface of the sample, which causes the formation of vacancies that diffuse into the sample bulk. In addition, oxidation processes strongly affect the electrical properties of the surface layers of a semiconductor, which leads to a deterioration in the parameters of finished devices. Intensive efforts have therefore been applied to develop insulator coatings to protect the surface of narrow-gap semiconductors. To protect devices based on MCT, ZnS [1], CdTe [2], and anodic oxide [3] are widely used.

The goal of this study was to investigate the variation of electrical parameters of  $n$ -type MBE-grown MCT (MBE MCT) films with the time and temperature of annealing and to clarify the effect of protective coatings on the rate of variation of these parameters under low-temperature annealing.

## 2. RESULTS AND DISCUSSION

We studied MCT films grown on GaAs substrates by MBE [4]. First, a CdTe buffer layer 5–7  $\mu\text{m}$  thick was grown on a substrate, followed by an MCT film comprising a working layer 8–10  $\mu\text{m}$  thick with  $x = 0.21$ – $0.23$  and a thin (0.15–1.5  $\mu\text{m}$ ) graded-composition layer, with  $x$  increasing to 0.5 at the surface of the film. As-grown films had  $n$ -type conduction. Several samples were covered with protective layers of anodic oxide (0.025–0.1  $\mu\text{m}$  thick), CdTe (0.1–0.3  $\mu\text{m}$ ), and an insulator (0.3  $\mu\text{m}$ ). The insulator was a multilayer coating including layers of ZnS and CdTe deposited by vacuum evaporation. The anodic oxide was deposited using the electrochemical technique from a KOH-based electrolyte. Thin CdTe layers were grown in a single process at the final stage of MCT growth.

Annealings at temperatures  $T_{\text{ann}} = 120$ – $230^\circ\text{C}$  were performed in a He atmosphere, and the annealing at  $90^\circ\text{C}$  was done either in He or in air, which did not affect the results. Conductivity  $\sigma$  and the Hall factor  $R_H$  were measured by the van der Pauw method at 77 K in the magnetic field range 0–1 T in samples about  $1 \times 1 \text{ cm}^2$  in size.

Figures 1–4 show typical variations of the film parameters with the annealing time for  $T_{\text{ann}} = 90^\circ\text{C}$ . The effective carrier density ( $1/|qR_H|$ ), where  $q$  is the elementary charge, and mobility ( $|\sigma R_H|$ ) were determined for the magnetic field  $B = 0.05 \text{ T}$ . Samples 1–3 were cut from an epitaxial structure no. 1; sample 4, from structure no. 2.

It can be seen that, as the annealing time increases, conductivity and effective mobility decrease signifi-

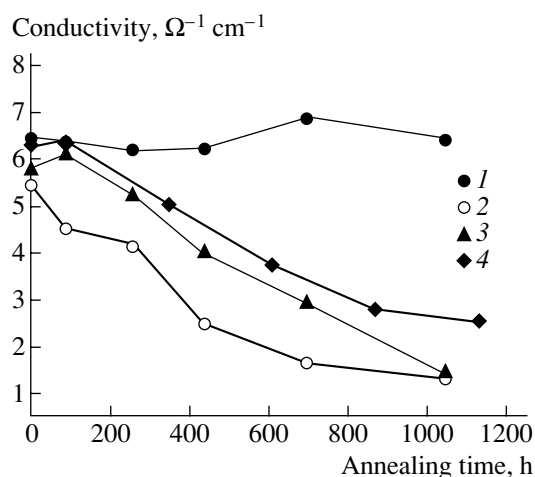


**Fig. 1.** Conductivity vs. annealing time for samples: (1) with anodic oxide, (2) without a coating, (3) with an insulator, and (4) with CdTe. Samples 1–3 were cut from epitaxial structure no. 1; sample 4, from structure no. 2.  $T_{\text{ann}} = 90^\circ\text{C}$ .

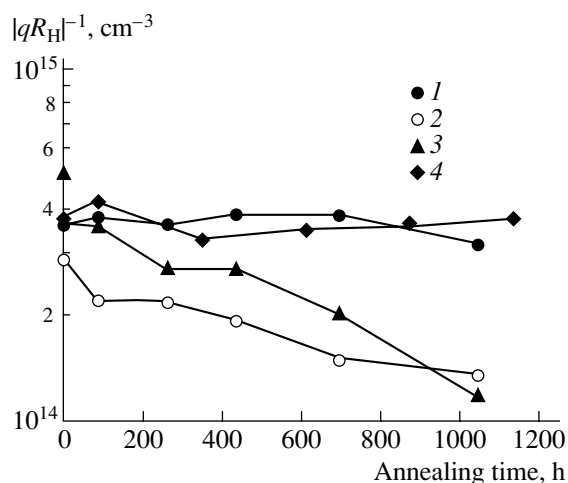


**Fig. 2.** Carrier density ( $1/qR_H$ ) vs. annealing time. Curve designations as in Fig. 1.

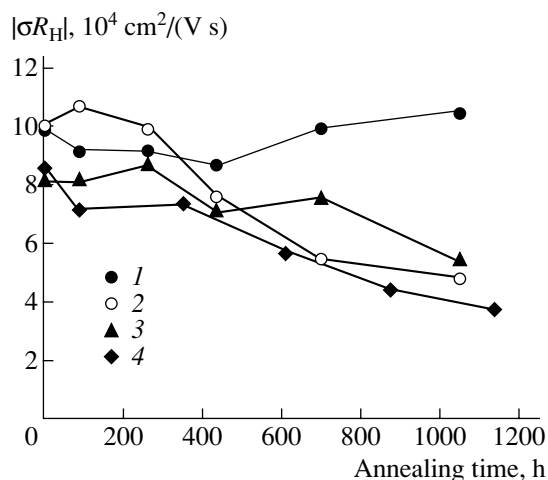


**Fig. 3.** Hall mobility ( $|\sigma R_H|$ ) vs. annealing time. Curve designations as in Fig. 1.

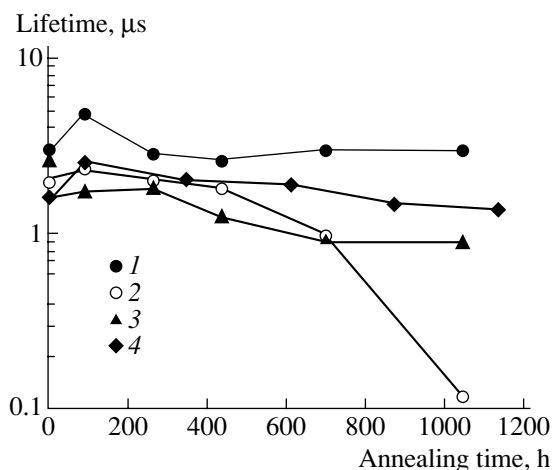


**Fig. 4.** Lifetime of minority carriers vs. annealing time. Curve designations as in Fig. 1.

cantly in all the samples, except the sample with the anodic oxide coating. The strongest decrease in conductivity is observed in the uncoated sample; the decrease in samples with the insulator and CdTe is weaker. Furthermore, the effective density slightly decreases in samples without a coating and with an insulator (Fig. 2). The weakest variation of parameters is observed with samples coated with an anodic oxide.

To establish the reason for the variations observed in the parameters, we analyzed the dependences of conductivity and the Hall factor on magnetic field, taking several types of carriers into consideration, as in [5–7]. It was found that, in *n*-type MBE-MCT films, the dependences on magnetic field can be explained by the presence of two types of electrons—high and low mobility ( $\sim 10^5$  and  $\sim 10^4 \text{ cm}^2/(\text{V s})$ , respectively) [8].

Analysis of data obtained under layer-by-layer etching has shown that the low-mobility electrons are localized in a thin (0.1–0.2  $\mu\text{m}$ ) layer in MCT near the heterointerface. The dependences on magnetic field, recorded before and after the annealing of samples, were analyzed in terms of this model, and the parameters of the two types of electrons, which are typical of samples without protection layers, are listed in the table. The fitting of the model parameters to experimental data was performed so as to obtain the best fit for both dependences,  $\sigma(B)$  and  $R_H(B)$ , simultaneously.

As can be seen from the table, the annealing does not change the mobility of high-mobility electrons, whereas their density decreases severalfold. The parameters of low-mobility electrons change only slightly during annealing in the conditions used. As a

**Table**

Parameters of electrons	Before annealing	After annealing
$n_1, \text{cm}^{-3}$	$2.2 \times 10^{14}$	$7.0 \times 10^{13}$
$n_2, \text{cm}^{-3}$	$4.2 \times 10^{14}$	$3.0 \times 10^{14}$
$\mu_1, \text{cm}^2 \text{V}^{-1} \text{s}^{-1}$	120000	120000
$\mu_2, \text{cm}^2 \text{V}^{-1} \text{s}^{-1}$	8000	6000

Note:  $n_1$  and  $n_2$  are the densities of electrons with high ( $\mu_1$ ) and low ( $\mu_2$ ) mobility;  $T_{\text{ann}} = 90^\circ\text{C}$ .

result, the effective mobility and conductivity of samples decrease as the annealing time increases.

The decrease in density of high-mobility electrons in the working layer of MCT film during annealing is related to the formation of vacancies, which compensate part of the donors in the film. It is well known that Hg vacancies are acceptors; they are generated at elevated temperature due to the egress of Hg atoms from the sample. According to published data, Hg vacancies are also responsible for recombination centers, which reduce the lifetime of minority carriers in *p*-MCT obtained by the introduction of vacancies. The annealing in Hg vapor results in the filling of vacancies.

We annealed samples at temperatures 200–230°C in an inert atmosphere and in the presence of Hg vapor. It was established that annealing in an inert atmosphere for 24 h at a temperature of about 220°C converts samples to *p*-type conduction, with a hole density of about  $(8\text{--}20) \times 10^{15} \text{cm}^{-3}$ . Subsequent annealing in the same mode, but in Hg vapor, again yields (in a reversible way) *n*-type conduction. This behavior, as well as the observed decrease in conductivity and lifetime of minority carriers during 90°C annealing, are related to

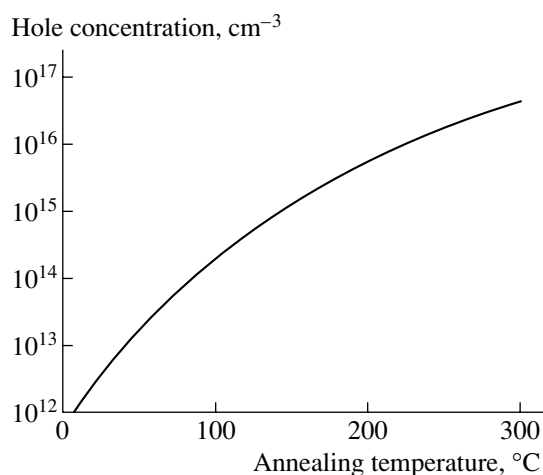


**Fig. 5.** Calculated equilibrium hole density vs. annealing temperature [9], extrapolated to low temperatures.

the formation of Hg vacancies. Figure 5 shows the calculated dependence of the equilibrium density of holes (produced by Hg vacancies) on the annealing temperature, extrapolated to room temperature with the use of data from [9]. The measured hole density in our samples without protective coating, annealed at 220°C, agree well with the calculated data. The variation observed in the parameters presented in Figs. 1–3 and in the table (annealing at 90°C) can be explained in terms of a two-layer model, assuming that the hole density related to Hg vacancies is about  $1.5 \times 10^{14} \text{cm}^{-3}$ . This value is close to the calculated value ( $\sim 10^{14} \text{cm}^{-3}$ ). Similar values were also obtained in calculations [10]. As can be seen in Fig. 5, at room temperature the equilibrium hole density related to the formation of vacancies is low (about  $3 \times 10^{13} \text{cm}^{-3}$ ), which cannot induce a significant modification of parameters of the MCT films under study.

As stated above, an anodic oxide on the surface of the sample stabilizes its electrical parameters under low-temperature (90°C) annealing. Annealing at temperatures in the range 140–160°C have demonstrated that the time necessary for the onset of variation in the parameters is proportional to the thickness of the anodic oxide, whereas the rate of variation in the parameters is independent of thickness. We explain this effect of the anodic oxide as follows: this oxide can serve as a mercury reservoir from which Hg atoms diffuse into the sample bulk and fill vacancies formed during the annealing, whereas thin layers of CdTe or an insulator reduce the egress of Hg atoms from the sample only to a certain extent.

### 3. CONCLUSIONS

The modification of parameters of *n*-type MBE MCT films under low-temperature annealing is related to a decrease in the density of high-mobility electrons in the basic layer of the film and to the presence of a surface layer near the interface with the CdTe buffer layer. The surface layer is characterized by a high density of low-mobility electrons, and these parameters change insignificantly under low-temperature (90°C) annealing. The decrease in the density of high-mobility electrons in the basic layer of the film occurs due to the compensation of donors by Hg vacancies, which are formed during annealing because of the egress of Hg atoms from the sample. At room temperature, this process does not modify the electrical parameters of the material.

An anodic oxide is the most efficient protective coating to stabilize the electrical parameters of *n*-type MCT films at elevated temperatures, as compared to thin CdTe or insulator layers.



## REFERENCES

1. W. Sang, J. Ju, W. Shi, and Y. Qian, *J. Cryst. Growth* **214–215**, 265 (2000).
2. I. Virt, M. Bilyk, I. Stefaniuk, and M. Kuzma, *Solid-State Electron.* **45**, 1743 (2001).
3. O. P. Agnohotri, C. A. Musca, and L. Faraone, *Semicond. Sci. Technol.* **13**, 839 (1998).
4. Yu. G. Sidorov, S. A. Dvoretiskii, V. S. Varavin, *et al.*, *Fiz. Tekh. Poluprovodn. (St. Petersburg)* **35**, 1092 (2001) [*Semiconductors* **35**, 1045 (2001)].
5. E. Finkman and Y. Nemirovsky, *J. Appl. Phys.* **53**, 1052 (1982).
6. M. B. Reine, K. R. Maschhoff, S. P. Tobin, *et al.*, *Semicond. Sci. Technol.* **8**, 788 (1993).
7. J. R. Meyer, C. A. Hoffman, F. J. Bartoli, *et al.*, *Semicond. Sci. Technol.* **8**, 805 (1993).
8. P. A. Bakhtin, A. K. Gutakovskii, S. A. Dvoretiskii, *et al.*, in *Abstracts of Conference: Photonics 2003* (Novosibirsk, 2003), p. 56.
9. G. L. Destafanis, *J. Cryst. Growth* **86**, 700 (1988).
10. V. V. Bogoboyashchyy, *Proc. SPIE* **5065**, 209 (2003).

*Translated by D. Mashovets*

## ELECTRONIC AND OPTICAL PROPERTIES OF SEMICONDUCTORS

# Formation and Study of Buried SiC Layers with a High Content of Radiation Defects

E. V. Bogdanova\*, V. V. Kozlovski\*\*, D. S. Rumyantsev\*\*, A. A. Volkova\*, and A. A. Lebedev\*

\*Ioffe Physicotechnical Institute, Russian Academy of Sciences, Politekhnikeskaya ul. 26, St. Petersburg, 194021 Russia

\*\*St. Petersburg Polytechnical University, ul. Politekhnikeskaya 29, St. Petersburg, 195251 Russia

Submitted March 1, 2004; accepted for publication March 4, 2004

**Abstract**—Protons with energy  $E = 100$  keV were implanted with doses ranging from  $2 \times 10^{17}$  to  $4 \times 10^{17}$  cm $^{-2}$  into 6H- and 4H-SiC n-type samples at room temperature. The samples were subjected to various types of postimplantation heat treatment in the temperature range 550–1500°C. The parameters of the samples were studied by measuring the capacitance–voltage and current–voltage characteristics and by analyzing the photoluminescence spectra. Blistering on the surface of the sample is observed after annealing the samples at a temperature of 800°C only after implantation of protons with a dose of  $\leq 3 \times 10^{17}$  cm $^{-2}$ . A decrease in the resistivity of the compensated layer sets in after annealing at a temperature of  $\sim 1200^\circ\text{C}$  and is completed after annealing at a temperature of  $\sim 1500^\circ\text{C}$ . A drastic decrease in the photoluminescence intensity is observed after implantation for all types of samples. Recovery of the photoluminescence intensity sets in after annealing at temperatures  $\geq 800^\circ\text{C}$  and is complete after annealing at a temperature of 1500°C. © 2004 MAIK “Nauka/Interperiodica”.

### 1. INTRODUCTION

It is well known that the depth distribution of stopping energy losses for protons in a material is quite specific. As a result, radiation defects are produced by protons in a semiconductor predominantly at depths that are close to the protons' projected range  $R_p$ . It is important that the radiation-defect generation rate directly at the surface is almost an order of magnitude lower than that at depths close to  $R_p$ . At the same time, radiation defects are not produced at all at depths that far exceed  $R_p$  [1]. Thus, irradiation with protons can be used to form layers that are highly localized at a certain depth (buried layers) and have a high concentration of radiation defects. As a result, irradiation with high doses of low-energy protons is widely used in the technology of various semiconductors, for example, to form high-resistivity buried layers (SOI technology) or to detach thin films of material after annealing of irradiated samples (so-called Smart Cut technology) [1]. The use of irradiation with protons in SiC technology may be of particular interest in the context of a recent report that it is possible to form an amorphous SiC layer as a result of exposure to proton radiation [2]. As is well known, the phenomenon of amorphization under the effect of irradiation with protons is typically not observed for other semiconductors [1].

The aim of this study was to form buried SiC layers with a high concentration of radiation defects and to study the properties of these layers.

### 2. EXPERIMENTAL

We used 6H- and 4H-SiC wafers with n-type conductivity as the samples. The concentration of uncompensated donors  $N_d - N_a$  was  $\sim 1.6 \times 10^{18}$  cm $^{-3}$  in

6H-SiC and  $3.8 \times 10^{18}$  cm $^{-3}$  in 4H-SiC. The samples were irradiated with protons using the accelerator of an NG-200U neutron generator at room temperature. We used protons with energy  $E = 100$  keV and with doses ranging from  $2 \times 10^{17}$  to  $4 \times 10^{17}$  cm $^{-2}$ . The value of  $R_p$  for 100-keV protons is equal to  $\sim 0.65$   $\mu\text{m}$  in SiC [1]. The samples were subjected to postirradiation isochronous annealing at temperatures in the range 500–1500°C in an argon atmosphere. The parameters of the samples before and after irradiation and after annealing at various temperatures were determined from measurements of the capacitance–voltage ( $C$ – $V$ ) and current–voltage ( $I$ – $V$ ) characteristics, as well as from an analysis of photoluminescence (PL) spectra. The  $C$ – $V$  characteristics were measured using a mercury probe in a capacitance bridge with a parallel equivalent circuit and with a sinusoidal-signal frequency of 10 kHz. The PL spectra were measured under excitation with pulsed radiation from a nitrogen laser (wavelength  $\lambda = 337$  nm, light-spot diameter 400  $\mu\text{m}$ ) at a temperature of 77 K.

### 3. RESULTS

A band peaked at a wavelength of  $\lambda_{\text{max}} \approx 465$ –470 nm was observed in the PL spectra of unirradiated 6H-SiC samples (Fig. 1). This band is caused by radiative recombination at the Al–N donor–acceptor pairs. A PL band peaked at  $\lambda_{\text{max}} \approx 420$  nm was also observed in the PL spectrum of unirradiated 4H-SiC crystals; this band is related to radiative recombination involving the Al acceptor center. In addition, a band peaked at  $\lambda_{\text{max}} \approx 560$  nm and related to the B impurity in SiC crystals [3] was observed in the long-wavelength portion of the 4H-SiC PL spectrum. The PL almost disappeared in all types of samples immediately after irradiation. Previ-

ously [4–6], the quenching of PL related to the atoms of the Al impurity was studied in SiC samples treated in a hydrogen plasma. This quenching was presumably [4–6] caused by the ability of hydrogen atoms to passivate the B and Al acceptor centers in SiC, i.e., the ability of hydrogen to form electrically inactive complexes with the Al and B atoms. These complexes do not exhibit a high thermal stability and decompose at temperatures  $>200^{\circ}\text{C}$ ; simultaneously, diffusion of hydrogen from the semiconductor bulk is observed [6]. Koshka and Mazzola [4] observed the complete recovery of the initial PL intensity after annealing samples at temperatures  $\sim 750^{\circ}\text{C}$ . In our case, an appreciable recovery of the PL intensity sets in at higher temperatures ( $\sim 800^{\circ}\text{C}$ ) (Figs. 1, 2), which is apparently related to the much higher hydrogen concentration in our samples than in the samples studied by Hulsen *et al.* [6]. It is worth noting that this temperature ( $\sim 800^{\circ}\text{C}$ ) is close to the temperature for the onset of annealing of radiation defects in SiC [7, 8]. The PL intensity in the samples under study reverted to the initial (preirradiation) value after annealing at  $1500^{\circ}\text{C}$ .

Studies of the surface of irradiated samples showed that morphological parameters remained unchanged after irradiation with protons in the entire range of doses used. A variation in the surface morphology sets in after annealing of irradiated samples. It is worth noting that, in contrast to silicon [2], the annealing temperatures required are quite high ( $\sim 880^{\circ}\text{C}$ ).

Blistering and detachment of flakes of the material were observed for all the samples irradiated with a dose  $<3 \times 10^{17} \text{ cm}^{-2}$  of protons and then annealed at temperatures  $\geq 800^{\circ}\text{C}$  [2]. Blistering of the surface was not observed for the samples irradiated with a dose  $\geq 3 \times 10^{17} \text{ cm}^{-2}$  of protons and then annealed in the temperature range  $800\text{--}1500^{\circ}\text{C}$  (Fig. 3b). In our opinion, the observed suppression of blistering is caused by amorphization of the implanted layer. Kozlov *et al.* [2] used atomic-force microscopy to detect the presence of an amorphous phase in silicon carbide irradiated with low-energy protons with a dose of  $3 \times 10^{17} \text{ cm}^{-2}$  and comparatively low proton-beam currents ( $<5 \mu\text{A cm}^{-2}$ ). Apparently, this observation is indicative of specific features of separation of primary radiation defects in silicon carbide, which may lead to the accumulation of a concentration of multivacancy complexes that is sufficient for amorphization of the semiconductor. Amorphization suppresses the formation of flat two-dimensional vacancy–hydrogen defects that are observed only in the crystalline material and represent the main factor in the development of microcracks in the plane of buried defect-rich layers, which gives rise to blistering.

In Figs. 3a and 3b, we show optical micrographs of surfaces of 4H-SiC samples annealed after irradiation with different doses of protons. A similar pattern was observed for 6H-SiC.

A shift of the  $C$ – $V$  characteristics upward along the vertical axis with the initial slope (the initial value of  $N_d - N_a$ ) retained was observed after irradiation of the surface-barrier structures under study. In addition, a

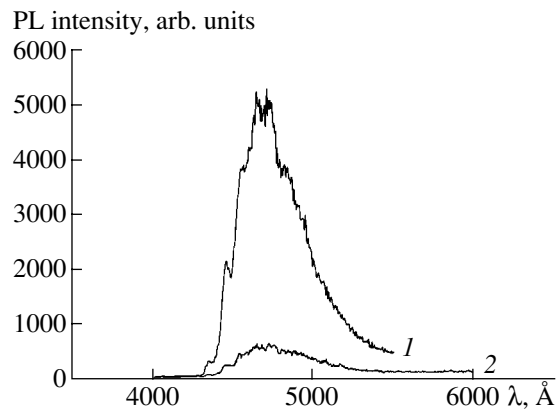


**Fig. 1.** Photoluminescence (PL) spectra of a 6H-SiC sample (1) before irradiation and (2) after irradiation and subsequent annealing at  $800^{\circ}\text{C}$ . Radiation dose:  $4 \times 10^{17} \text{ cm}^{-2}$ .

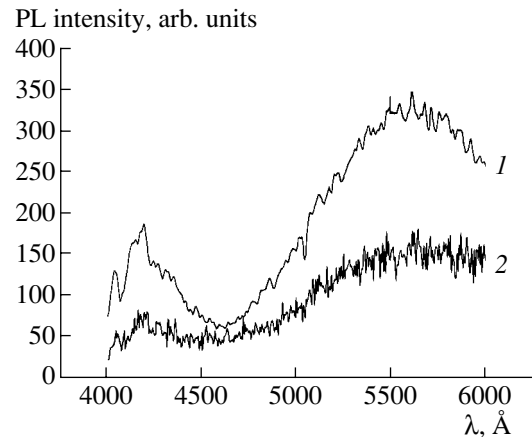


**Fig. 2.** Photoluminescence (PL) spectra of a 4H-SiC sample (1) before irradiation and (2) after irradiation and subsequent annealing at  $800^{\circ}\text{C}$ . Radiation dose:  $4 \times 10^{17} \text{ cm}^{-2}$ .

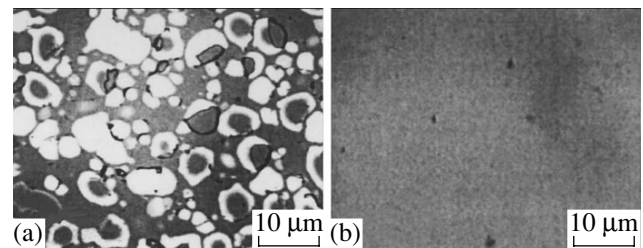


**Fig. 3.** Optical photographs of the surface of 4H-SiC samples after irradiation and subsequent annealing at  $800^{\circ}\text{C}$ . Radiation doses: (a)  $2 \times 10^{17}$  and (b)  $4 \times 10^{17} \text{ cm}^{-2}$ .

dependence of the measured capacitance  $C$  on the frequency used in the measurements ( $f$ ) was observed:  $C$  increased as  $f$  decreased. The value of  $C$  coincided with that for an unirradiated diode at frequencies  $\sim 100 \text{ Hz}$ . This feature of the  $C$ – $V$  characteristic [9] indicates that the ohmic resistance of the diode increases significantly as

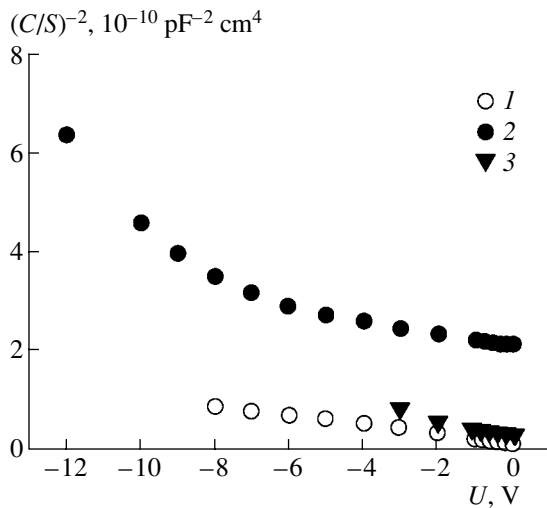


**Fig. 4.** Capacitance–voltage characteristics of the 6H-SiC samples (1) before irradiation, (2) immediately after irradiation, and (3) after irradiation and subsequent annealing at 1500°C; radiation dose:  $4 \times 10^{17} \text{ cm}^{-2}$ .  $S$  denotes the surface area of the sample.

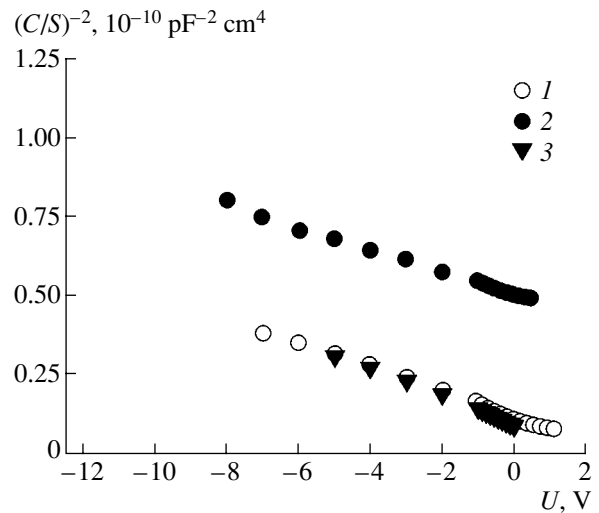


**Fig. 5.** Capacitance–voltage characteristics of the 4H-SiC samples (1) before irradiation, (2) immediately after irradiation, and (3) after irradiation and subsequent annealing at 1500°C. Radiation dose:  $4 \times 10^{17} \text{ cm}^{-2}$ .  $S$  denotes the surface area of the sample.

a result of irradiation. In addition, a nonlinear dependence  $C^{-2}(U)$  was observed for 6H-SiC samples at reverse-bias voltages  $>8 \text{ V}$  (thickness of the space-charge layer  $>0.1 \mu\text{m}$ ); this observation indicated that the difference concentration  $N_d - N_a$  decreased with increasing depth. This effect is much less pronounced for the 4H-SiC samples, which is evidently related to the higher initial (before irradiation) concentration  $N_d - N_a$  in the samples of this polytype (thickness of the space-charge layer is  $\sim 0.06 \mu\text{m}$  at the highest reverse-bias voltages). Thus, according to the capacitance measurements, irradiation led to the formation of a compensated layer at depths  $>0.1 \mu\text{m}$ ; at the same time, the concentration at the surface of the sample did not change.

The capacitance–voltage characteristics of irradiated structures coincided completely with those of unirradiated structures after postirradiation annealing at 1500°C (Figs. 4, 5).

#### 4. CONCLUSIONS

We studied the effects of irradiation with low-energy protons and subsequent annealing on the properties of SiC samples. It is shown that for SiC the applicability of irradiation with protons to various technological processes depends on the proton dose. A dose of  $\sim 3 \times 10^{17} \text{ cm}^{-2}$  is the critical dose for 100-keV protons. Irradiation with doses  $<3 \times 10^{17} \text{ cm}^{-2}$  leads to the development of blistering during annealing and can be used in Smart Cut technology. This blistering phenomenon is found to be suppressed at doses  $>3 \times 10^{17} \text{ cm}^{-2}$ , most likely because of the developing amorphization of the irradiated layer. The thickness of this layer can be varied by varying the proton energy. Thus, irradiation with protons with doses  $>3 \times 10^{17} \text{ cm}^{-2}$  may turn out to be promising for the formation of SOI structures based on

SiC. It is worth noting that the cross section for the defect production usually decreases as the proton energy increases; as a result, the concentration of defects in the buried layer decreases. Therefore, we may expect that an increase in the proton energy will lead to an increase in the critical value of the radiation dose.

#### ACKNOWLEDGMENTS

This study was supported by INTAS (grant no. 01-603), NATO (grant no. SfP-978011), and the Russian Foundation for Basic Research (project no. 03-02-16054).

#### REFERENCES

1. V. V. Kozlovskii, *Modification of Semiconductors by Proton Beams* (Nauka, St. Petersburg, 2003) [in Russian].
2. V. A. Kozlov, V. V. Kozlovskii, A. N. Titkov, *et al.*, *Fiz. Tekh. Poluprovodn.* (St. Petersburg) **36**, 1310 (2002) [*Semiconductors* **36**, 1227 (2002)].
3. A. A. Lebedev, *Fiz. Tekh. Poluprovodn.* (St. Petersburg) **33**, 129 (1999) [*Semiconductors* **33**, 107 (1999)].
4. Y. Koshka and M. Mazzola, *Appl. Phys. Lett.* **79**, 752 (2001).
5. Y. Koshka and M. Mazzola, *Mater. Sci. Forum* **389–393**, 609 (2002).
6. C. Hulsen, N. Achtziger, U. Reinlohner, and W. Witthuhn, *Mater. Sci. Forum* **338–342**, 929 (2000).
7. T. Dalibor, G. Pensl, T. Kimoto, *et al.*, *Phys. Status Solidi A* **162**, 199 (1997).
8. A. A. Lebedev, A. I. Veinger, D. V. Davydov, *et al.*, *J. Appl. Phys.* **88**, 6265 (2000).
9. A. A. Lebedev and N. A. Sobolev, *Fiz. Tekh. Poluprovodn.* (Leningrad) **16**, 1874 (1982) [*Sov. Phys. Semicond.* **16**, 1207 (1982)].

*Translated by A. Spitsyn*

---

## ELECTRONIC AND OPTICAL PROPERTIES OF SEMICONDUCTORS

---

# A Model of Electrical Isolation in GaN and ZnO Bombarded with Light Ions

A. I. Titov<sup>\*^</sup>, P. A. Karasev<sup>\*</sup>, and S. O. Kucheyev<sup>\*\*</sup>

<sup>\*</sup>St. Petersburg State Polytechnical University, St. Petersburg, 195021 Russia

<sup>^</sup>e-mail: titov@phtf.stu.neva.ru

<sup>\*\*</sup>Research School of Physical Sciences and Engineering, The Australian National University, Canberra, ACT 0200, Australia

Submitted January 30, 2004; accepted for publication March 20, 2004

**Abstract**—A model of a decrease in electrical conductivity of GaN and ZnO under the effect of irradiation with fast ions is suggested. The formation of complexes composed of a doping-impurity atom and the simplest defect formed by the ion beam is considered as the main process that leads to a decrease in the free-carrier concentration and an increase in the resistivity. A comparison of the model-based results and experimental data on the origination of isolation that were obtained for *n*-GaN and ZnO shows that the model can be used to describe satisfactorily the processes that occur. © 2004 MAIK “Nauka/Interperiodica”.

### 1. INTRODUCTION

The great interest in wide-gap semiconductors is stimulated by the potential possibilities for applying them in, for example, optoelectronics and high-power electronics [1, 2]. Since ion implantation is one of the most convenient tools in the commercial production of semiconductor devices, great efforts have been made to study the interaction of accelerated ions with the crystals of wide-gap semiconductors.

The formation of insulating layers that isolate active devices on a wafer is one of technological uses of the beams of accelerated ions. For example, it was experimentally found that the structural defects formed in the course of ion bombardment of gallium nitride may induce an increase in the sheet resistance of the samples by more than ten orders of magnitude [1–6]. The high sheet resistance is retained after annealing at fairly high temperatures.

Such a drastic increase in sheet resistance may be caused by several factors. The first factor is the appearance of deep levels in the band gap, which can efficiently capture the free charge carriers. The second factor is the decrease in mobility; however, the effect of mobility on resistivity should be less pronounced since the range of variation in mobility is much less than ten orders of magnitude. This inference is confirmed by direct experiments. For example, Kucheyev *et al.* [5] reported the results of Hall measurements of the mobility and concentration of free charge carriers and data on the sheet resistance of *n*-GaN in relation to the dose of irradiation with 0.6-MeV H<sup>+</sup> ions. The data obtained indicate that a decrease in the conductivity in GaN crystals by approximately five orders of magnitude as a result of irradiation with fast ions is accompanied by a decrease in the mobility by less than an order of magnitude.

It is difficult to construct a model that adequately describes the variation in the sheet resistance as a result of irradiation since data on the origin of defects that introduce deep levels in the band gap are lacking. These defects can be (i) isolated point defects (such as vacancies, interstitial atoms, antisite defects) and their clusters; (ii) complexes composed of point defects and impurities that were introduced unintentionally into the crystal during its growth; and (iii) complexes composed of point radiation defects and doping impurities (shallow-level donors for *n*-type crystals and shallow acceptors for *p*-type crystals).

The kinetics of the increase in the sheet resistance with increasing dose is usually complicated and nonlinear [1–11]. Until recently, only one model had been suggested for gallium nitride [6]; this model is based on the assumption that GaN is polycrystalline. The variation in the conductivity was treated in the context of the approximation of electron transport in a polycrystal, the intercrystallite-barrier height in which depends linearly on the number of defects introduced (the dependence of this number on the radiation dose is also assumed to be linear). However, the available experimental data [7, 8] show that single-crystal GaN does not transform into a polycrystal; rather, an increase in the resistivity is related to a decrease in the concentration of charge carriers due to their capture by deep-level traps formed as a result of irradiation. Consequently, the aforementioned model [6] is not adequate.

Another model of the formation of defects that reduce the electrical conductivity in gallium nitride has been suggested recently [9]. This model describes satisfactorily the kinetics of the process under consideration and is based on the assumption that the shallow levels of doping impurities are transformed into deep levels as a result of the formation of complexes com-

posed of a defect and a doping-impurity atom. A comparison of the results of simulation [9] with experiment was restricted mainly to the data obtained for irradiation of GaN with protons. Below, we show that such a comparatively simple model [9] may well be used to describe the experimental data on the variation in the sheet resistance of single-crystal GaN samples as a result of irradiation with various high-energy light ions; this model may also be applied with good results to ZnO.

## 2. MODEL

Various simplest point defects are produced when an accelerated light ion moves in a two-component single crystal; these defects include vacancies in both sublattices, interstitial atoms of both components, and antisite defects. However, at present it is not clear which of these defects or complexes introduce deep levels into the band gap. It is assumed in the model under consideration that only a single type of defect plays a significant role in the formation of insulating layers. The origin of this particular defect is unknown and is not discussed owing to the lack of information. It is also believed that defects of this type can effectively form complexes with atoms of a doping impurity; as a result, shallow levels are transformed into deep levels. It is also assumed that each of the complexes formed captures a charge carrier either from the valence band (for a *p*-type semiconductor) or from the conduction band (for an *n*-type semiconductor) and thus reduces the charge-carrier concentration. Therefore, an irradiation-induced increase in the sheet resistance is mainly caused by a decrease in the concentration of charge carriers due to their capture by the deep levels formed.

This approach seems to be quite realistic. Indeed, the majority of the doping-impurity atoms are naturally always in a charged state at room temperature. If the point defects under consideration (these defects are assumed to be unstable) are charged as a result of capturing the majority charge carriers, the charge of these defects turns out to be opposite to the charge of doping impurities; as a result, an efficient interaction of the defects and impurities should occur.

In the experiments whose results are to be compared with the model, the electrical-conductivity degradation was studied for epitaxial conducting films with a fairly uniform distribution of the doping impurity. The energy of primary ions (~1 MeV) was such that generation of the simplest defects was almost uniform over the entire depth of these films [4, 10, 11]. These circumstances make it possible to disregard the diffusion-related redistribution of the concentration of the defects under consideration. In addition, the large range of primary ions makes it possible to disregard the chemical interaction of implanted ions with the target atoms within the conducting layer and disregard the effect of hopping conductivity at a depth that is close to the range of the ions.

Thus, we consider (i) the formation of the simplest point defects of a single type; (ii) the recombination of these defects at unsaturable sinks with a characteristic relaxation time  $\tau$ ; and (iii) the interaction of the defects with the doping impurity, which is characterized by the rate constant  $\alpha$  of quasi-chemical reaction. Since the typical duration of irradiation of the sample ( $t > 10$  s) far exceeds the average lifetime of the defects under consideration  $\tau$ , the concentration  $n$  of these defects depends on time only slightly (the quasi-equilibrium approximation); i.e.,  $dn/dt \approx 0$  at each instant of time.

Taking into account the above, we obtain the following system of equations:

$$\begin{cases} gF - n/\tau - \alpha n_i n(1 - n_d/n_i) = 0 \\ dn_d/d\Phi = \alpha n_i n F^{-1} (1 - n_d/n_i). \end{cases} \quad (1)$$

Here,  $g$  is the average density of generation of defects produced by each ion,  $F$  is the ion flux,  $n_d$  is the concentration of the produced complexes composed of a defect and a doping-impurity atom,  $n_i$  is the doping-impurity concentration (equal to the initial charge-carrier concentration in the sample), and  $\Phi = Ft$  is the dose of ions. In the first equation in (1), the first term describes the point-defect generation, the second term describes the recombination of these defects at unsaturable sinks, and the third term describes the interaction of the defects with the doping-impurity atoms. The second equation in (1) describes the variation in the concentration of complexes that form the deep-level traps.

A solution of system (1) with the evident boundary condition  $n_d = 0$  at  $\Phi = 0$  yields the following nonlinear equation that relates the concentration of complexes to the radiation dose:

$$\ln(1 - n_d/n_i) = \alpha \tau n_d (1 - g\Phi/n_d), \quad (2)$$

which can be used to determine  $n_d(\Phi)$ . The concentration of free charge carriers  $n_c$  and the surface concentration  $N_s$  of charge carriers are determined from the following expressions:

$$n_c = n_i - n_d = n_i(1 - n_d/n_i); \quad N_s = (n_c + n_{th})h. \quad (3)$$

Here,  $h$  is the thickness of the conducting layer and  $n_{th}$  is the residual concentration of charge carriers at very high radiation doses, when all the doping-impurity atoms have already formed complexes with defects. The latter concentration is many orders of magnitude lower than the initial charge-carrier concentration  $n_i$  and, consequently, makes an appreciable contribution to the sheet resistance only at large doses. Finally, the sheet resistance  $R_s$  can be found from the expression

$$R_s = [e\mu N_s]^{-1} = [e\mu h(n_c + n_{th})]^{-1}, \quad (4)$$

where  $e$  is the elementary charge and  $\mu$  is the effective mobility of charge carriers.

Not only the dependence of the charge-carrier concentration on the radiation dose but also a decrease in

Model parameters calculated for GaN in the approximations of varying and constant charge-carrier mobility and for ZnO in the approximation of constant mobility

Target	Ion	Energy, MeV	$\alpha\tau$ , cm <sup>3</sup>	$g$ , cm <sup>-1</sup>	$g$ TRIM, cm <sup>-1</sup>
GaN, $h = 1.5 \mu\text{m}$ , $\mu = f(\Phi)$	<sup>1</sup> H	0.6	$4.112 \times 10^{-17}$	2164	2521
	<sup>7</sup> Li	3.0	$4.288 \times 10^{-17}$	22334	38724
	<sup>12</sup> C	6.6	$4.292 \times 10^{-17}$	82595	130285
	<sup>16</sup> O	6.6	$4.289 \times 10^{-17}$	183830	313010
GaN, $h = 1.5 \mu\text{m}$ , $\mu = 570 \text{ cm}^2 \text{ V}^{-1} \text{ s}^{-1}$	<sup>1</sup> H	0.6	$2.793 \times 10^{-17}$	3008	2521
	<sup>7</sup> Li	3.0	$3.144 \times 10^{-17}$	30606	38724
	<sup>12</sup> C	6.6	$3.759 \times 10^{-17}$	101020	130285
	<sup>16</sup> O	6.6	$3.255 \times 10^{-17}$	247520	313010
ZnO, $h = 0.6 \mu\text{m}$ , $\mu = 80 \text{ cm}^2 \text{ V}^{-1} \text{ s}^{-1}$	<sup>7</sup> Li	0.7	$1.539 \times 10^{-18}$	16579	132276
	<sup>16</sup> O	2.0	$3.131 \times 10^{-18}$	43046	734133
	<sup>28</sup> Si	3.5	$2.876 \times 10^{-18}$	107530	1886521

the charge-carrier mobility contribute to the variation in the sheet resistance. At this stage, the dependence of mobility on the radiation dose is disregarded in the model since this dependence represents a separate complicated problem, the majority of starting data for which are unknown. The reason for disregarding the mobility effect was discussed above: variation in the mobility plays a relatively minor role in the kinetics of  $R_s(\Phi)$ . Note that, in calculating the kinetics of electrical isolation in GaN, we took into account the dependence  $\mu(\Phi)$  estimated on the basis of the available experimental data (see below for more detail).

We now consider two particular cases: low and high doses of radiation. At low doses, the concentration of complexes composed of a defect and a doping-impurity atom is also low; as a result, we have  $n_d/n_i \ll 1$ . Substitution of  $1 - n_d/n_i = 1$  into the first equation of system (1) makes it possible to obtain an analytical solution for the surface charge-carrier concentration as

$$n_c = n_i \exp[-\alpha\tau g\Phi / (1 + \alpha\tau n_i)]. \quad (5)$$

In the case of high doses, we have  $n_d/n_i \approx 1$ ; therefore, Eq. (2) can be rewritten as  $\ln(1 - n_d/n_i) = -\alpha\tau g\Phi[1 - (n_d/n_i)(n_i/g\Phi)] = -\alpha\tau g\Phi + \alpha\tau n_i$ , which yields the following expression for the charge-carrier concentration:

$$n_c = n_i(1 - n_d/n_i) = n_i \exp[\alpha\tau n_i] \exp[-\alpha\tau g\Phi]. \quad (6)$$

It can be seen from formulas (5) and (6) that, in both cases, the dose dependence of the charge-carrier concentration is linear if plotted on the semilogarithmic scale. This circumstance is important since it makes it possible to determine the parameters of Eq. (2) using experimental data.

### 3. COMPARISON WITH EXPERIMENT FOR GaN

In order to compare the results of the simulation with experiment, we used the data in [4] on irradiation of an epitaxial  $n$ -GaN layer that was grown by

MOCVD on a 0.5- $\mu\text{m}$ -thick undoped GaN buffer layer formed on a sapphire substrate, had a wurtzite structure, and included a 1.5- $\mu\text{m}$ -thick conducting layer. The crystal was cut into equal rectangular resistors. The initial charge-carrier concentration in the samples was  $3 \times 10^{17} \text{ cm}^{-3}$ , and the sheet resistance was  $218 \Omega/\square$ . The type and energy of ions used for bombardment are listed in the table; the ion-current density was  $\sim 6.4 \times 10^{10} \text{ cm}^{-2} \text{ s}^{-1}$ . The sheet resistance was measured *in situ* after each stage of irradiation.

The previous [9] comparative analysis of experimental data [5] on the variation in the GaN conductivity as a result of irradiation with high-energy light ions and the results of calculations based on the model under consideration showed good agreement between the theory and experiment. At the same time, calculations of the kinetics of the increase in the sheet resistance were performed for irradiation with protons [5]; consequently, it is also interesting to simulate the dose dependences of the sheet resistance for the other ions used by Boudinov *et al.* [4].

#### 3.1. Normalization Procedures for the Dose Dependences of the Sheet Resistance

As already mentioned above, it follows from the model under consideration that, both for low and high doses of radiation, the dependences of reciprocal surface charge-carrier concentration  $n_c$  plotted in semilogarithmic coordinates should be represented by portions of straight lines [see expressions (5) and (6)]. In Fig. 1 we show one of these dependences that represents the variation in the charge-carrier concentration in a GaN sample as a result of irradiation with 0.6-MeV protons [5] (the method for transforming the dependence  $R_s(\Phi)$  into  $n_c(\Phi)$  is considered below). Two linear portions are distinct in the curve in Fig. 1; one portion corresponds to low doses ( $\Phi < 1 \times 10^{14} \text{ cm}^{-2}$ ) and the other portion corresponds to higher doses ( $\sim 2.0 \times 10^{14} < \Phi < 2.5 \times$

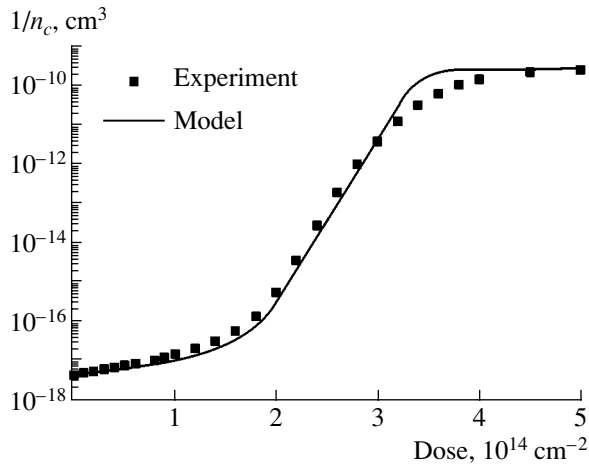


**Fig. 1.** Experimental [5] (squares) and calculated (solid line) dependences of reciprocal charge-carrier concentration in GaN on the dose of irradiation with 0.6-MeV protons.

$10^{14} \text{ cm}^{-2}$ ). If GaN is irradiated with other ions (Li, C, O), the surface concentration of charge carriers varies with the dose in the same way; i.e., the corresponding dependences exhibit the same two characteristic portions. However, the curves are shifted to lower doses by one to two orders of magnitude. Thus, the assumption that the variation in the reciprocal surface concentration of charge carriers is linear at low and high doses of irradiation is confirmed by experimental data.

If the variation in the sheet resistance of the samples is considered in the context of the above model, it follows from Eq. (2) and expressions (5) and (6) that the concentration ( $n_d$ ) of the complexes composed of a defect and a doping-impurity atom and, consequently, the charge-carrier concentration ( $n_c$ ) are governed by the product  $g\Phi$ . The latter is equivalent to the total concentration of defects introduced by radiation into the surface layer. The dose dependences of the sheet resistance for identical samples irradiated with different ions should then coincide if these dependences are plotted as  $R_s(g\Phi)$ . In order to verify this assumption, we must know the density of the defect generation by a single ion ( $g$ ). This density can be estimated on the basis of the results of ballistic calculations; for example, the standard TRIM software package can be used [12]. However, an accurate determination of the value of  $g$  is made difficult by two factors. First, we do not know the data on the threshold energy for atomic displacements in different sublattices. Second, it is not known which defects effectively form the complexes with impurities. When calculating the value of  $g$  using the TRIM software package (version SRIM-2003.17), we assumed that the threshold displacement was equal to 25 eV for both the gallium and nitrogen sublattices. In the right-most column of the table, we list (for definiteness) the number of vacancies in the nitrogen sublattice of GaN. We used these values in plotting the dependences

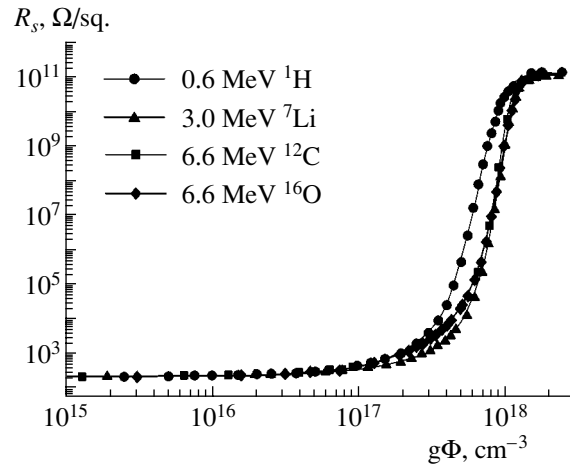


**Fig. 2.** Sheet resistance of identical GaN samples irradiated with various ions [4] in relation to the total number of atomic displacements.

$R_s(g\Phi)$  shown in Fig. 2 (experimental values are taken from [4] and are shown in Fig. 3).

It is clearly seen that, in contrast to the initial dependences  $R_s(\Phi)$  that are shifted with respect to each other by about two orders of magnitude in doses (Fig. 3), the curves for the lithium, carbon, and oxygen ions in Fig. 2 coincide within the measurement accuracy, whereas the curve for protons is shifted with respect to the above curves by a factor of only  $\sim 1.5$ . Note that both the agreement between curves and the value of the shift remain unchanged if we identify  $g$  with the displacement generation density in the gallium (rather than nitrogen) sublattice. This shift can be caused by several factors, for example, the roughness of approximations of the model under consideration, the limitations of the

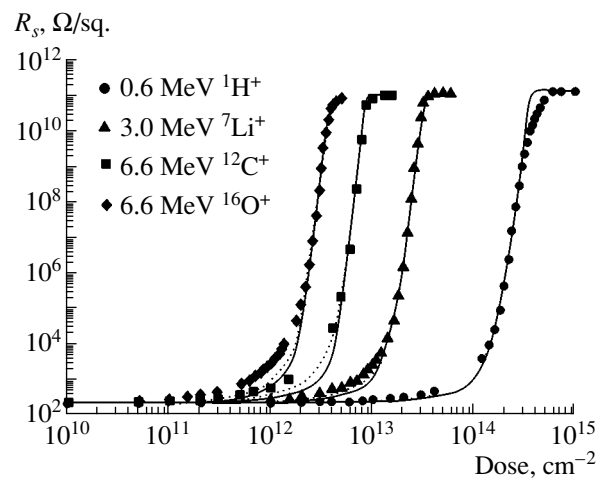


**Fig. 3.** Experimental [4] (squares, triangles, circles) and calculated dependences of the sheet resistance of GaN on the dose of irradiation with various ions taking into account (dotted lines) and disregarding (solid lines) the variations in the charge-carrier mobility.



TRIM software package for protons, the dependence of the exit of the Frenkel pairs from the displacement cascade on the cascade density, and so on. These factors call for further analysis. However, if we disregard the aforementioned deviation, we may state in general that another assumption of the model is confirmed satisfactorily by experimental data.

3.2. *Dependence of the Threshold Dose for the Formation of the Insulating Layer on the Initial Charge-Carrier Concentration and the Number of Atomic Displacements*

An analysis of the variation in the sheet resistance with increasing ion dose shows that there is a threshold dose of radiation  $\Phi_{th}$ , i.e., the dose that gives rise to a trapping-center concentration that is close to the initial concentration of free charge carriers; as a result, the curve  $R_s(\Phi)$  levels off. The dependence of the threshold dose on the initial charge-carrier concentration in GaN doped with silicon is linear ( $\Phi_{th} \propto n_i$ ) [4]. At the same time, the threshold dose is found to be inversely proportional to the number of atomic displacements produced by ions ( $\Phi_{th} \propto g^{-1}$ ).

In the context of the model we suggested, the charge-carrier concentration  $n_{th}$  corresponding to the threshold radiation dose can be determined from formula (6) as

$$\begin{aligned} n_{th} &= n_i(1 - n_d(\Phi_{th})/n_i) \\ &= n_i \exp[\alpha\tau n_i] \exp[-\alpha\tau g \Phi_{th}], \end{aligned} \quad (7)$$

which describes the threshold concentration for various materials, the different initial charge-carrier concentrations  $n_i$ , and the different bombarding ions. It follows from formula (7) that

$$\Phi_{th} = [\alpha\tau n_i + \ln(n_i/n_{th})](\alpha\tau g)^{-1}. \quad (8)$$

Taking into account the values of  $\alpha\tau = 4.29 \times 10^{-17} \text{ cm}^3$ ,  $n_{th} = 6.55 \times 10^9 \text{ cm}^{-3}$ , and  $n_i = 0.3\text{--}5.6 \times 10^{18} \text{ cm}^{-3}$ , which correspond to irradiation of GaN with carbon ions [4], it is easy to verify that the deviation from linearity amounts to less than 1%. Thus, both facts observed experimentally are described satisfactorily by expression (8), so that  $\Phi_{th} \propto n_i g^{-1}$ .

3.3. *Variation in the Sheet Resistance with Increasing Dose*

It is very interesting to use the model under consideration to describe the dependence of the sheet resistance on the radiation dose. We can derive this dependence using Eq. (2), from which follows the variation in the concentration of the defect-impurity complexes  $n_d(\Phi)$  as the dose increases, and expressions (3) and (4) that relate the concentration of complexes to the charge-carrier concentration and the sheet resistance. However, we should preliminarily determine the rate constants of quasi-chemical reactions ( $\alpha$ ,  $\tau$ ) and the

average number of defects that are generated by a single ion per unit path length ( $g$ ); these quantities are parameters in Eq. (2). The rate constants appear in all intermediate equations in terms of the product  $\alpha\tau$ ; therefore, the combination of these constants can be considered as a single parameter. The average number of defects  $g$  should be determined on the basis of experimental data for the reasons outlined above.

Both parameters can be determined using any two of the following relations: (i) according to formula (5), in the limit of low doses, the dependence of the logarithm of the reciprocal charge-carrier concentration  $\ln(n_c^{-1})$  on the dose is linear and has a slope given by  $k_S = \alpha\tau g(1 + \alpha\tau n_i)$ ; (ii) similarly, in the limit of high doses, expression (6) yields the slope of the linear portion of the same curve as  $k_L = \alpha\tau g$ ; and (iii) the dose at which the straight lines defined by expressions (5) and (6) intersect is equal to  $\Phi_I = (1 + \alpha\tau n_i)/\alpha\tau g$ .

In order to determine the dependence of the surface charge-carrier concentration  $N_s(\Phi)$  from the available experimental dependence of the sheet resistance  $R_s(\Phi)$ , we should know the dose dependence of the charge-carrier mobility because, in accordance with expression (6), we have  $N_s^{-1}(\Phi) = e\mu(\Phi)R_s(\Phi)$ . Direct experimental data are lacking; therefore, we used the results of isochronous annealing of GaN irradiated with 0.6-MeV protons at a dose of  $2 \times 10^{14} \text{ cm}^{-2}$  [5]. We used these data to estimate the correlation of the mobility with the sheet resistance, which made it possible to determine  $N_s(\Phi)$  and, consequently, the parameters in Eq. (2). Using the estimate obtained for  $\mu(R_s)$  and expression (4), we can also easily obtain the dependence of mobility on the concentration of complexes  $\mu(n_d)$ , which was used in calculating the dependence  $R_s(\Phi)$  on the basis of the solutions to Eq. (2). Undeniably, this estimate of mobility is rather crude since, for the same value of sheet resistance, the concentration and the properties of scattering centers (which control the value of the charge-carrier mobility) in the sample after irradiation can differ from those after subsequent isochronous annealing. At the same time, deviations of the mobility from the true value should not significantly affect the shape of the dependence  $R_s(\Phi)$ , since the variation in the sheet resistance as a result of irradiation turns out to be several orders of magnitude larger than the effect of mobility.

The main results of processing the experimental data are listed in the table. The four upper rows list the values of parameters calculated for the case of irradiation of identical GaN samples taking into account the variation in the mobility as the dose increases. The remaining rows give the corresponding parameters for the same ion-target combinations but for a constant mobility equated numerically to the value of the charge-carrier mobility in initial samples. It can be seen from the table that the parameter  $\alpha\tau$  is found to be

nearly constant if the dose dependence of mobility is taken into account. This behavior of  $\alpha\tau$  should be expected since this parameter characterizes the efficiency of interaction between the simplest defects and the doping-impurity atoms and the disappearance of these defects at unsaturable sinks. These sinks should clearly be the same in a series of experiments with identical samples cut from the same wafer. If the dose dependence of mobility is disregarded, the spread in the parameters increases somewhat. Note that the result  $\alpha\tau = 7.405 \times 10^{-17} \text{ cm}^3$  obtained by Titov and Kucheyev [9] exceeds the value listed in the table for the case of varying mobility by approximately a factor of 2; however, the value of  $\alpha\tau$  reported in [9] was obtained for samples from another series. The average density of defect generation by a single ion calculated using the TRIM software package practically coincides with that obtained from experimental curves of the reciprocal surface concentration of charge carriers; this circumstance also counts in favor of the suggested model.

In Fig. 3 we show the experimental dependences  $R_s(\Phi)$  and the dependences calculated taking into account and disregarding the dose dependence of mobility (in the latter case, it was assumed that the mobility was invariably equal to the value before irradiation). It can be seen that, with the dependence  $\mu(\Phi)$  taken into account, better agreement with experimental data is attained; the calculated and experimental curves nearly coincide for the lightest ions. An increase in the ion mass leads to a deviation of the results of calculations from experimental data in the region of the transition from low to high doses. The origin of this deviation calls for further analysis. Apparently, the difference between the theory and experiment is related to an increase in the defect-generation density as the ion mass increases. Indeed, Kucheyev *et al.* [5] noted that an increase in the defect-generation density as a result of an increase in the ion-flux density  $F$  (rather than  $g$ ) was accompanied by changes in the shape of the  $R_s(\Phi)$  curve for relatively large values of  $F$ . This observation indicates that nonlinear terms should be present in the system of Eqs. (2). In order to simplify the consideration, these nonlinear processes were disregarded in [9] and in this study; the model is expected to be more realistic for comparatively light ions and low ion-current densities.

In addition, it can be seen from Fig. 3 that allowing for the dose dependence of mobility does not significantly affect the shape of calculated dependences  $R_s(\Phi)$ . This circumstance means that we can expect the dose dependences of the sheet resistance to be described satisfactorily for materials for which data on the variation in mobility are lacking.

Recently, an interesting publication [13] appeared that dealt with Hall measurements of nominally undoped  $n$ -GaN films grown by MOCVD and irradiated with comparatively low doses of 0.9-MeV electrons at room temperature; in this case, the level of GaN

damage was low compared to irradiation with ions [4, 5]. It was found experimentally [13] that the concentration and mobility of electrons in the conduction band decreased at low temperatures as a result of irradiation, whereas these parameters remained unchanged at room temperature. In this case, the radiation defects introduced were unstable at  $T > 200^\circ\text{C}$  and were completely annealed out at  $T = 400^\circ\text{C}$ . Based on these data, it was concluded [13] that Si atoms introduced unintentionally during the MOCVD process did not interact with defects produced by incident electrons. Apparently, this conclusion contradicts the suggested model of ion-induced increase in the sheet resistance of  $n$ -GaN.

However, we should note that the experimental conditions and the behavior of defects in the experiments [4, 5] we simulate are very different from those in [13]. Indeed, the electron concentration in the samples [4, 5] was one to two orders of magnitude higher than in [13]; accordingly, the positions of the Fermi level differed as well. For measurements at room temperature in [4, 5], where  $n$ -GaN was intentionally doped with silicon, electrical conductivity decreased by no less than ten orders of magnitude, the charge-carrier mobility decreased by at least an order of magnitude, and the defects responsible for the compensation of donors were completely annealed out only at  $T > 600^\circ\text{C}$  even for comparatively low doses of radiation. If we assume that the donor levels of Si atoms are compensated as a result of the introduction of acceptor levels that correspond to defects of unknown origin and are not related in any way to the complexes involving Si atoms (as was assumed in [13]), the kinetics of isolation due to irradiation with ions should differ considerably from the experimental data [4, 5]. In principle, this difference in the results can be related to the fact that, even in high-quality GaN films grown by MOCVD, there always exist atoms of impurities that are introduced unintentionally, such as H, C, and O, with concentrations that exceed  $10^{16} \text{ cm}^{-3}$  [1], which makes the interpretation of the results more difficult. Thus, at present one cannot state that the model considered here contradicts the results reported in [13]. Further research is required to gain insight into the special features of the behavior of defects in GaN at low levels of radiation damage.

#### 4. COMPARISON WITH EXPERIMENT FOR ZnO

The dependence of the sheet resistance of zinc oxide irradiated with Li, O, and Si ions on the radiation dose has a shape that is very similar to that of gallium nitride and exhibits pronounced linear portions on the semilogarithmic scale at low and high doses, with leveling off at very high doses [10, 11]. The kinetics of the origination of isolating properties in unintentionally doped  $n$ -ZnO epitaxial layers 0.6  $\mu\text{m}$  thick that are grown by MBE on a sapphire substrate was described in [10, 11]. The sample was cut into identical resistors with an area of  $3.5 \times 3.5 \text{ mm}^2$ . The initial surface concentration of charge carriers in the resistors was  $N_c \approx 10^{17} \text{ cm}^{-3}$ , the

effective Hall mobility  $\mu \approx 80 \text{ cm}^2 \text{ V}^{-1} \text{ s}^{-1}$ , and the sheet resistance  $R_s \approx 1 \text{ k}\Omega/\square$ . The identical resistors obtained were irradiated with ions at room temperature. The type and the energy of ions are listed in the table; the ion-current density was  $(1.0\text{--}1.9) \times 10^{11} \text{ cm}^{-2} \text{ s}^{-1}$ . The ion energy was chosen so that the maximum of the atomic displacements was located deep in the sapphire substrate. The sheet resistance was measured in situ after each step in dose. Since these conditions of irradiation of ZnO are consistent with approximations of the model, it is interesting to use this model to describe the degradation of electrical conductivity in another wide-gap semiconductor. Despite the fact that the origin of a donor impurity in ZnO has not yet been definitively clarified, all the main model hypotheses concerning the defects responsible for the introduction of deep levels remain the same. Specifically, the origination of these deep levels is caused by the attachment of a mobile point defect generated by an incident ion to a doping immobile defect (an extraneous atom or an intrinsic crystal defect).

As mentioned above, it follows from the suggested model that the charge-carrier concentration  $n_c$  is controlled by the total concentration of defects  $g\Phi$  produced in the conducting layer during irradiation. As a result, the curves that represent an increase in the sheet resistance of identical samples irradiated with different ions and are plotted as  $R_s(g\Phi)$  should coincide. In order to verify this assumption, we used the TRIM software package to calculate the defect-generation density  $g$  in the zinc sublattice of ZnO irradiated with lithium, oxygen, and silicon ions (see table). The threshold energies for atomic displacements were assumed to be equal to 57 eV for both sublattices, in accordance with the data reported previously [14, 15]. In Fig. 4, we show the corresponding set of rearranged experimental dependences reported by Kucheyev *et al.* [10]. It can be seen that these dependences coincide for lithium and oxygen, whereas the curve for the heavier silicon ions is slightly shifted to higher doses.

Calculations of the ZnO sheet resistance is complicated by the fact that data on the dependence of the charge-carrier mobility on dose  $\mu(\Phi)$  are lacking. At the same time, it was substantiated above that a constant value of mobility may be used as the first approximation (in our case, the charge-carrier mobility is assumed to be equal to its value before irradiation). The experimental dependences of charge-carrier concentration on dose  $N_s^{-1}(\Phi)$  obtained from the dependences  $R_s(\Phi)$  and plotted on the semilogarithmic scale also exhibit two characteristic (predicted by the model) linear portions at low and high doses of ions.

In order to describe quantitatively the kinetics of increase in the sheet resistance  $R_s$  with dose  $\Phi$  in ZnO using Eq. (2) and expressions (3) and (4), we should determine the parameters  $\alpha\tau$  and  $g$ . The obtained values of these parameters are listed in the three lower rows of the table. As can be seen, the values of  $\alpha\tau$  for all the

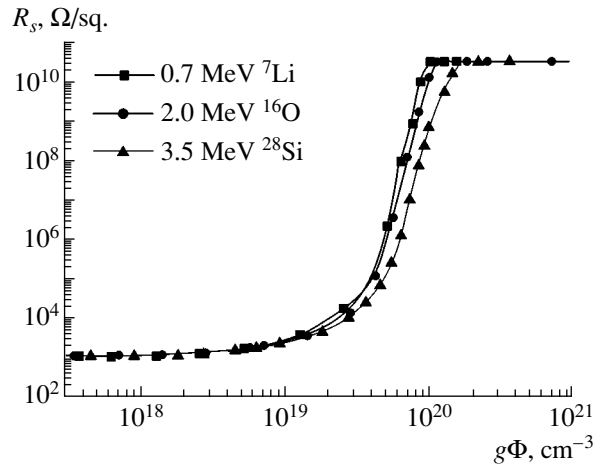


Fig. 4. Sheet resistance of identical ZnO samples irradiated with different ions as a function of the total number of atomic displacements.

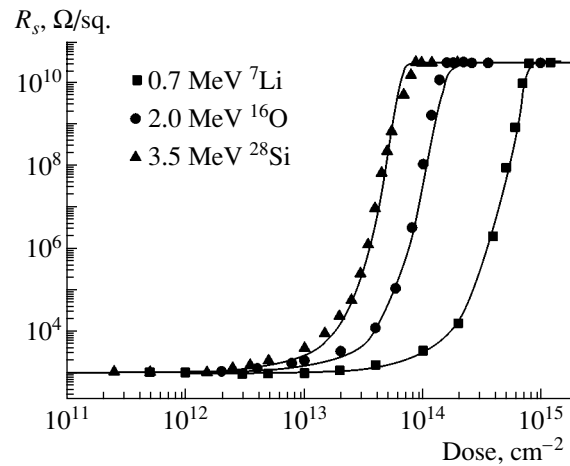


Fig. 5. Experimental (triangles, circles, and squares) and calculated (solid lines) dependences of the sheet resistance of ZnO on the dose of irradiation with different ions.

samples are almost the same, although the spread in these values is somewhat larger than that for gallium nitride. In principle, this behavior may be attributed to the lower degree of development of the methods for producing ZnO epitaxial layers compared to those for GaN. At the same time, the average densities of the defect generation  $g$  calculated using the TRIM software package exceed the experimental data by a factor of 8–18. This effect may be related to the active interaction of the simplest point defects with each other in zinc oxide, even during the development of a primary displacement cascade. In this case, the effective number of simplest defects that leave the cascade and are involved in a quasi-chemical reaction with impurity atoms (as obtained by processing the experimental data) would be smaller than the total number of produced defects calculated using the TRIM software.

The results of calculating the variations in the sheet resistance of ZnO as a result of irradiation with Li, O, and Si ions in the context of the suggested model are shown in Fig. 5. As can be seen, there is good agreement between the calculated curves and the experimental data. Discrepancies between the theory and experiment are again observed mainly in the regions of transition from low doses of ions ( $n_d/n_i \ll 1$ ) to high doses ( $n_d/n_i \approx 1$ ) and transition to the stable state with low conductivity in the region of high doses. Clearly, one of the causes of these discrepancies is the independence of the mobility of the radiation dose, as was assumed in the calculations. However, in general we may state that the model satisfactorily describes the kinetics of degradation of electrical conductivity in ZnO. Apparently, better agreement between theoretical and experimental results for both ZnO and GaN can be attained if the following is included in the calculation: (i) a more realistic dependence of the charge-carrier mobility on the radiation dose, (ii) nonuniform generation of mobile point defects over the depth in the sample, and (iii) nonlinear effects related to the formation of additional types of defect-containing complexes. Nonlinear effects related to the ion-current density should also be taken into account.

## 5. CONCLUSIONS

We considered a model of the variation in electrical conductivity of wide-gap semiconductors as a result of irradiation with fast light ions. The mechanism of increase in the sheet resistance is mainly related to the formation complexes that capture efficiently the charge carriers. The formation of these complexes is caused by the interaction of primary radiation defects with doping-impurity atoms. The analysis shows that the suggested model satisfactorily describes the processes that occur at low ion-current densities. In particular, the model describes the dependences of the sheet resistance on the ion dose and the number of atomic displacements produced by ions. In addition, the model accounts for the form of the dependences of the threshold dose for the formation of the insulating layer on the

initial charge-carrier concentration and the number of atomic displacements.

## ACKNOWLEDGMENTS

We thank V.S. Belyakov and V.V. Emtsev for a number of useful comments. We are grateful to the Ministry of Education and the Ministry of Science and Technology of the Russian Federation for their support of this study.

## REFERENCES

1. S. J. Pearton, J. C. Zolper, R. J. Shul, and F. Ren, *J. Appl. Phys.* **86**, 1 (1999).
2. D. C. Look, *Mater. Sci. Eng. B* **80**, 383 (2001).
3. S. J. Pearton, R. G. Wilson, J. M. Zavada, *et al.*, *Appl. Phys. Lett.* **73**, 1877 (1998).
4. H. Boudinov, S. O. Kucheyev, J. S. Williams, *et al.*, *Appl. Phys. Lett.* **78**, 943 (2001).
5. S. O. Kucheyev, H. Boudinov, J. S. Williams, *et al.*, *J. Appl. Phys.* **91**, 4117 (2002).
6. C. Uzan-Saguy, J. Salzman, R. Kalish, *et al.*, *Appl. Phys. Lett.* **74**, 2441 (1999).
7. S. J. Pearton, *Mater. Sci. Rep.* **4**, 313 (1990).
8. S. O. Kucheyev, J. S. Williams, and S. J. Pearton, *Mater. Sci. Eng. R* **33**, 51 (2001).
9. A. I. Titov and S. O. Kucheyev, *J. Appl. Phys.* **92**, 5740 (2002).
10. S. O. Kucheyev, P. N. K. Deenapanray, C. Jagadish, *et al.*, *Appl. Phys. Lett.* **81**, 3350 (2002).
11. S. O. Kucheyev, C. Jagadish, J. S. Williams, *et al.*, *J. Appl. Phys.* **93**, 2972 (2003).
12. J. P. Biersack and L. G. Haggmark, *Nucl. Instrum. Methods* **174**, 257 (1980).
13. V. V. Emtsev, V. Yu. Davydov, K. V. Emtsev, *et al.*, *Phys. Status Solidi C* **0**, 601 (2003).
14. J. M. Meese and D. R. Locker, *Solid State Commun.* **11**, 1547 (1972).
15. D. R. Locker and J. M. Meese, *IEEE Trans. Nucl. Sci.* **19**, 237 (1972).

*Translated by A. Spitsyn*

---

---

**ELECTRONIC AND OPTICAL PROPERTIES  
OF SEMICONDUCTORS**

---

---

## **Optical and Electrical Properties of 4H-SiC Irradiated with Fast Neutrons and High-Energy Heavy Ions**

**E. V. Kalinina<sup>1</sup>, G. F. Kholuyanov<sup>1</sup>, G. A. Onushkin<sup>1</sup>, D. V. Davydov<sup>1</sup>, A. M. Strel'chuk<sup>1</sup>,  
A. O. Konstantinov<sup>2</sup>, A. Hallén<sup>3</sup>, A. Yu. Nikiforov<sup>4</sup>, V. A. Skuratov<sup>5</sup>, and K. Havancsak<sup>6</sup>**

<sup>1</sup>*Ioffe Physicotechnical Institute, Russian Academy of Sciences, St. Petersburg, 194021 Russia*

<sup>^</sup>*e-mail: evk@pop.ioffe.rssi.ru*

<sup>2</sup>*ACREO AB, Electrum 236, SE 16440 Kista, Sweden*

<sup>3</sup>*Royal Institute of Technology (Department of Electronics), Electrum 229, SE 16440 Kista, Sweden*

<sup>4</sup>*Specialized Electronic Systems, Moscow, 115409 Russia*

<sup>5</sup>*Joint Institute for Nuclear Research, Dubna, 141980 Russia*

<sup>6</sup>*Eötvös University, Pázmány P. sétány 1/A, H-1117 Budapest, Hungary*

Submitted March 1, 2004; accepted for publication March 23, 2004

**Abstract**—Photoluminescence and deep-level transient spectroscopy are used to study the effect of irradiation with fast neutrons and high-energy Kr (235 MeV) and Bi (710 MeV) ions on the optical and electrical properties of high-resistivity high-purity *n*-type 4H-SiC epitaxial layers grown by chemical vapor deposition. Electrical characteristics were studied using the barrier structures based on these epitaxial layers: Schottky barriers with Al and Cr contacts and  $p^+n$  diodes fabricated by Al ion implantation. According to the experimental data obtained, neutrons and high-energy ions give rise to the same defect-related centers. The results show that, even for the extremely high ionization density (34 keV/nm) characteristic of Bi ions, the formation of the defect structure in SiC single crystals is governed by energy losses of particles due to elastic collisions. © 2004 MAIK “Nauka/Interperiodica”.

### 1. INTRODUCTION

The ability of devices based on SiC to operate under extreme conditions (under high levels of radiation, at temperatures higher than 600°C, and in chemically active media) makes these devices useful in solving problems related to space research, keeping record and control of nuclear materials and nuclear waste, and detecting high-energy nuclear particles. Taking into account the possible wide range of applications of SiC-based devices, there is a need to study in more detail the effect of various types of radiation on the processes of radiation-defect production in SiC. Such studies will make it possible to affect the processes of controlled production or removal of various defect- and impurity-related centers in SiC in order to improve or intentionally vary the electrical properties of this material, as well as gain information about the radiation resistance of SiC. The data obtained in studying the effect of irradiation with  $\alpha$  particles, neutrons, electrons, and protons on the nature of defects in SiC made it possible to clarify certain special features of defect production in this material [1–4]. At the same time, study of the special features of defect production during irradiation of SiC with heavy high-energy ions (under conditions of a high level of ionization-related energy losses and a high rate of radiation-defect generation) has begun only recently [5–8].

In this paper, we report the results of comparative research into the effect of irradiation with fast neutrons and with 245-MeV Kr and 710-MeV Bi ions on defect production in lightly doped 4H-SiC epitaxial layers that had *n*-type conductivity and were grown by chemical vapor deposition (CVD).

### 2. EXPERIMENTAL

We studied diode structures fabricated on the basis of 4H-SiC epitaxial layers that were grown by CVD and had a concentration of uncompensated donors of  $N_d - N_a = (5-8) \times 10^{15} \text{ cm}^{-3}$ . The 26- $\mu\text{m}$ -thick epitaxial layers were grown on commercial  $n^+$ -4H-SiC substrates with  $N_d - N_a = 1 \times 10^{19} \text{ cm}^{-3}$ . The  $p^+n$  structures of the diode were formed using the implantation of 150-keV Al ions with a dose of  $5 \times 10^{16} \text{ cm}^{-2}$  with subsequent activation annealing for 15 s at 1700°C in an Ar atmosphere [9]. Ohmic contacts were formed using thermal vacuum sputtering–deposition of Al and Cr/Al onto the  $p^+$ - and  $n^+$ -type regions of the diode structures, respectively. In addition, we studied Schottky barriers with Al and Cr contact layers, which were also deposited thermally onto the epitaxial layers. Diode mesa structures with the Schottky barriers and  $p^+n$  junctions with an area of  $1 \times 10^{-3} \text{ cm}^2$  and a height of 30  $\mu\text{m}$  were formed using ion–plasma etching. The diode structures were subjected to various doses of irradiation with

**Table 1.** Parameters of irradiation of the 4H-SiC samples

Particle	Energy, MeV	Dose, cm <sup>-2</sup>
Neutrons	1	1.2 × 10 <sup>14</sup>
		3.1 × 10 <sup>14</sup>
		6.24 × 10 <sup>14</sup>
Kr	245	1 × 10 <sup>10</sup> 5 × 10 <sup>10</sup>
Bi	710	1.42 × 10 <sup>9</sup>
		1 × 10 <sup>10</sup>
		5 × 10 <sup>10</sup>

1-MeV neutrons and Kr and Bi ions with energies of 245 and 710 MeV, respectively. The irradiation parameters are listed in Table 1.

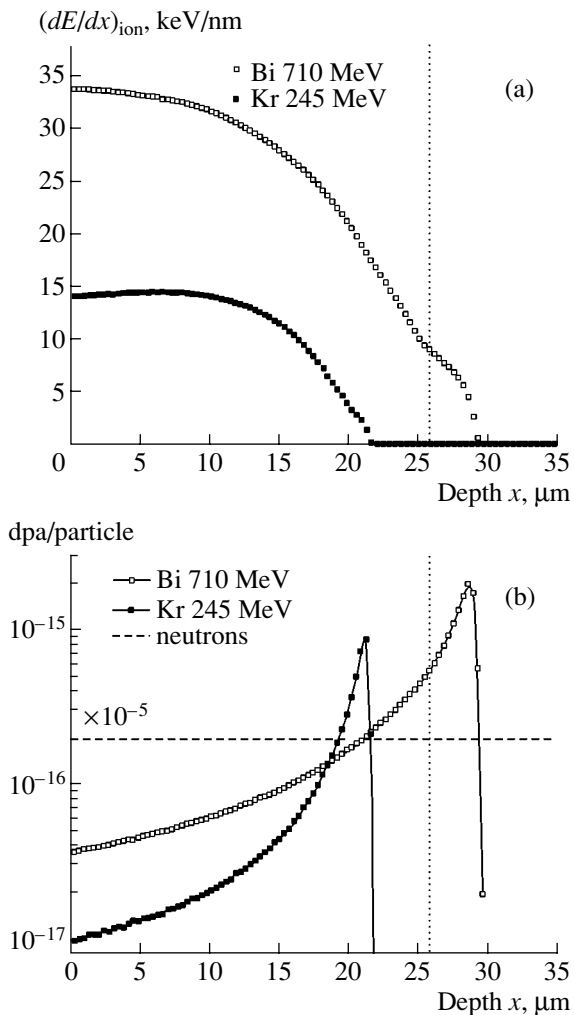


**Fig. 1.** Calculated profiles of (a) energy losses by ionization and (b) primary radiation defects in 4H-SiC irradiated with neutrons, 245-MeV Kr ions, and 710-MeV Bi ions. The dotted vertical line indicates the boundary of the epitaxial layer.

The structure of defect-related centers was studied by analyzing the photoluminescence (PL) spectra. The PL was excited using radiation from a helium-cadmium gas-discharge laser with a power of 20 mW and a wavelength of 325 nm, which was selected using a UFS-1 filter. The spectra were recorded with the samples at temperature  $T = 80$  K. The concentration profiles of electrically active impurities in the CVD layers near the Schottky barrier and the region of  $p^+n$  junctions were determined from the capacitance-voltage ( $C-V$ ) characteristics measured at frequencies of 0.1, 1, and 10 kHz and at temperatures of 80 and 293 K. The presence and the number of deep-level centers in 4H-SiC epitaxial layers were estimated using the data of capacitance spectroscopy ( $C$ -DLTS) at a frequency of 10 kHz in the temperature range  $T = 80-400$  K for the Schottky barriers and  $T = 80-700$  K for the  $p^+n-n^+$  structures. The current-voltage ( $I-V$ ) characteristics of the Schottky barriers and  $p^+n-n^+$  structures were measured at a constant current at temperatures of 293–650 K.

### 3. RESULTS AND DISCUSSION

In Fig. 1 we show the profiles of ionization-related energy losses  $(dE/dx)_{\text{ion}}$  and the profiles of the number of primary radiation defects in the dpa (displacement per atom) units along the track of the Kr and Bi ions in SiC; these profiles were obtained using the TRIM2000 software package. The threshold energies for the production of displacements in the silicon and carbon sublattices were assumed to be equal to 35 and 20 eV, respectively [10]. According to calculations, the ranges of Kr and Bi ions were equal to 21.2 and 28.8  $\mu\text{m}$ , respectively. Taking into account that the thickness of the epitaxial layer was equal to 26  $\mu\text{m}$  (the vertical dotted line in Fig. 1), we may state that the results obtained in the case of irradiation with ions are representative of the processes that occur in the epitaxial layers. In order to estimate the number of defects produced by neutrons, we used data on the cross sections of defect production as reported by Avramenko *et al.* [11]. In Fig. 1b we show the estimated number of defects in SiC for the used conditions of irradiation with neutrons (horizontal dashed line).

In Fig. 2 we show the PL spectra measured for the starting samples (curve 1) and the samples irradiated with Bi and Kr ions (curves 2 and 3, respectively) with doses no higher than  $1 \times 10^{10}$  cm<sup>-2</sup>. An intense band peaked at  $h\nu = 3.169$  eV was observed in the PL spectra of starting (unirradiated) samples; this band is caused by recombination of free excitons [12]. In addition, a broad defect-related band peaked at  $h\nu = 2.35$  eV was observed in the spectra, which is typical of SiC and is caused by the presence of deep levels in the band gap [13, 14]. Emission related to free excitons was no longer observed after irradiation of the samples with high-energy particles, although the PL spectrum still included the defect-related band. Furthermore, irradiation gave rise to a new broad PL band peaked at  $\sim 2.6$  eV

(the so-called  $D_1$  spectrum) [15]. The large breadth of the  $D_1$  spectrum indicates that various defects with different energy levels are produced by radiation. Similar luminescence spectra were also observed previously in the case of irradiation of SiC with neutrons, electrons, and light ions [2, 16, 17]. As an illustration, the cathodoluminescence spectrum for 6H-SiC crystals grown by the Lely method and irradiated with neutrons at a dose of  $10^{18} \text{ cm}^{-2}$  is also shown in Fig. 2 (curve 4).

According to the measurements of the  $C$ - $V$  characteristics, the space-charge capacitance was independent of temperature and used a frequency within the aforementioned range of these parameters for the starting diode structures of both types (Schottky barriers and  $p^+-n$  junctions). However, a decrease in the difference concentration  $N_d - N_a$  (to the point of complete compensation of conductivity) was characteristic of all types of radiation as the dose of particles increased. Furthermore, the  $C$ - $V$  characteristics measured at different temperatures and frequencies had the same features for the samples irradiated with either neutrons or ions. An increase in the temperature of the sample during measurements led to an increase in the concentration  $N_d - N_a$ , probably because of partial annealing of the compensating centers produced as a result of irradiation. An increase in the measurement frequency within the aforementioned range led to an insignificant decrease in the value of  $N_d - N_a$ . It is most probable that the centers produced during irradiation have no time to recharge as the frequency increases. The values of limiting doses for different types of radiation (the doses leading to the attainment of voltage-independent values of capacitance for the diode structures) were different and decreased as the mass and energy of incident particles increased. It is noteworthy that the voltage-independent values of capacitance corresponded to an insulator layer with a thickness of 26–30  $\mu\text{m}$ , which was comparable to the thickness of the high-resistivity epitaxial layer.

The DLTS measurements performed for the starting CVD layers showed that there is a single type of deep levels with an ionization energy of 0.63–0.68 eV in the band gap. The corresponding centers are referred to as  $Z_1$  centers in 4H-SiC (Fig. 3, curve 1) [1]. As a result of irradiation of the diode structures with neutrons and heavy ions, the  $Z_1$ -center concentration increased; in addition, the levels with ionization energies of 0.37–0.43 eV (radiation-defect centers  $NI_1$ ), 0.74 eV ( $NI_2$ ), 0.92 eV ( $NI_3$ ), and 1.47–1.56 eV ( $NI_4$ ) were detected in the upper half of the band gap, irrespective of the type of radiation. In Fig. 3 we show the DLTS spectra measured for initial samples (curve 1) and the samples irradiated with Kr ions (curve 2), neutrons (curve 3), and Bi ions (curve 4). Some of the radiation-defect centers ( $NI_1$ ,  $NI_2$ ) were annealed out as a result of heating the sample to 700 K. Similar irradiation-induced centers were observed in 4H-SiC irradiated with electrons, protons, and other light particles [18–20]. The ionization energies  $E_c - E_0$  and the cross sections for electron cap-

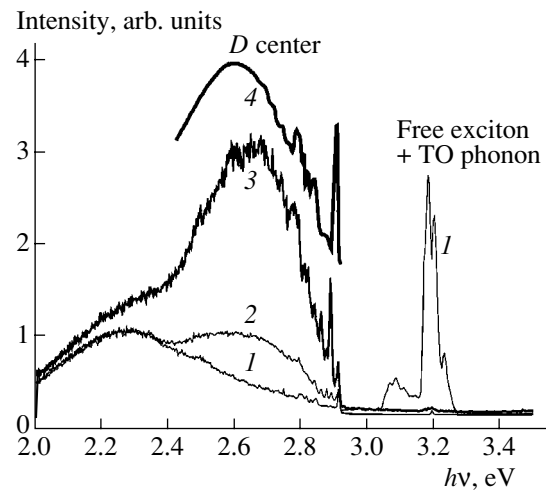


Fig. 2. Photoluminescence spectra of 4H-SiC epitaxial layers (1) before and (2, 3) after irradiation with the (2) Bi and (3) Kr ions. Curve 4 represents the cathodoluminescence spectrum of 6H-SiC crystal irradiated with neutrons [9].

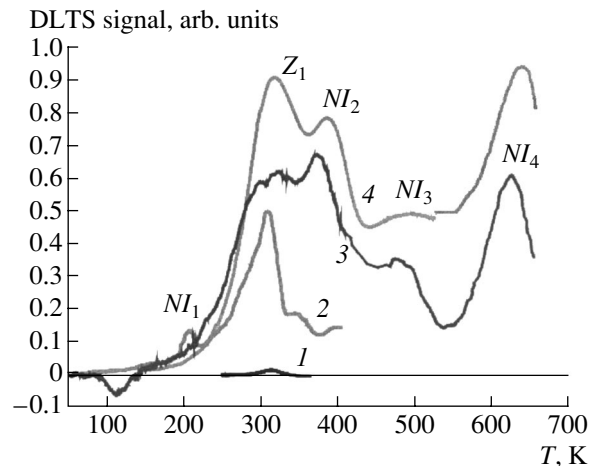


Fig. 3. DLTS spectra of 4H-SiC epitaxial layers for (1) the initial sample and (2, 3, 4) after irradiation of the sample with (2) Kr ions, (3) neutrons, and (4) Bi ions. Curves 1 and 2 correspond to the Schottky barriers (measurements at temperatures no higher than 400 K), and curves 3 and 4 correspond to the  $p^+-n$  junctions (measurements at temperatures as high as 700 K).

ture  $\sigma_n$  for various deep levels were determined from the Arrhenius equations. These parameters and the concentrations  $N$  of all the deep-level centers observed for the initial and irradiated samples are listed in Table 2.

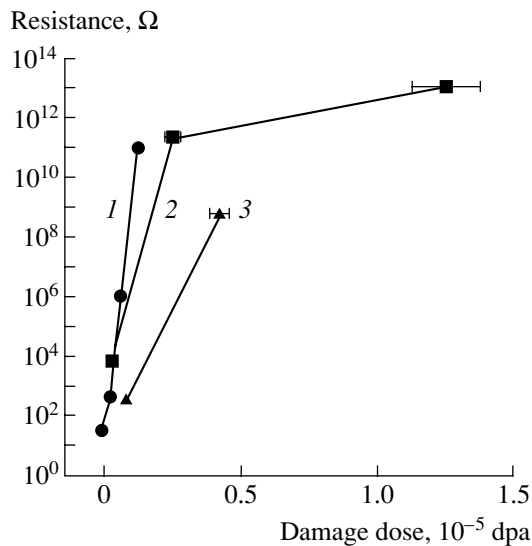
It was noted previously that the shape of the  $I$ - $V$  characteristics of similar diode structures irradiated with neutrons is controlled by the variation in the resistance of epitaxial layers due to the introduction of radiation defects [21]. As mentioned above, the range of heavy ions was smaller than or equal to the thickness of the epitaxial layer. This circumstance makes it possible to state that, in the case of irradiation with heavy ions,

**Table 2.** Parameters of deep levels detected in 4H-SiC epitaxial layers after irradiation with neutrons and with Kr and Bi ions

Particles	Type of centers	$E_c - E_0$ , eV	$\sigma_n$ , cm <sup>2</sup>	$N$ , cm <sup>-3</sup>
Initial CVD layer	$Z_1$	$0.63 \pm 0.01$	$1 \times 10^{-14}$	$2 \times 10^{13}$
Neutrons, dose $3.1 \times 10^{14}$ cm <sup>-2</sup>	$NI_1$	$0.37 \pm 0.01$	$1 \times 10^{-16}$	$5.5 \times 10^{13}$
	$Z_1$	$0.69 \pm 0.01$	$1 \times 10^{-14}$	$5.5 \times 10^{13}$
	$NI_2$	$0.74 \pm 0.03$	$5 \times 10^{-15}$	$5.8 \times 10^{13}$
	$NI_3$	$0.92 \pm 0.10$	$5 \times 10^{-15}$	$\sim 2 \times 10^{14}$
	$NI_4$	$1.56 \pm 0.02$	$5 \times 10^{-13}$	$8 \times 10^{14}$
Kr, dose $1 \times 10^{10}$ cm <sup>-2</sup>	$NI_1$	$0.43 \pm 0.01$	$4 \times 10^{-15}$	$5 \times 10^{13}$
	$Z_1$	$0.66 \pm 0.02$	$1 \times 10^{-14}$	$2.5 \times 10^{14}$
Bi, dose $1.4 \times 10^9$ cm <sup>-2</sup>	$Z_1$	$0.68 \pm 0.01$	$1 \times 10^{-14}$	$5.3 \times 10^{14}$
	$NI_2$	$0.74 \pm 0.03$	$1 \times 10^{-14}$	$2.8 \times 10^{14}$
	$NI_3$	$0.92 \pm 0.10$	$5 \times 10^{-15}$	$\sim 1 \times 10^{14}$
	$NI_4$	$1.47 \pm 0.04$	$5 \times 10^{-13}$	$4 \times 10^{14}$

the main contribution to the variation in the resistance of the diode structures is also made by the variation in the resistance of the epitaxial layer. In Fig. 4 we show the dependences of the resistance of the 4H-SiC epitaxial layers on the damage dose for all the high-energy incident particles used in our experiments. The data reported here do not allow us to conclude that there are any significant differences in the form of these dependences for neutrons and ions.

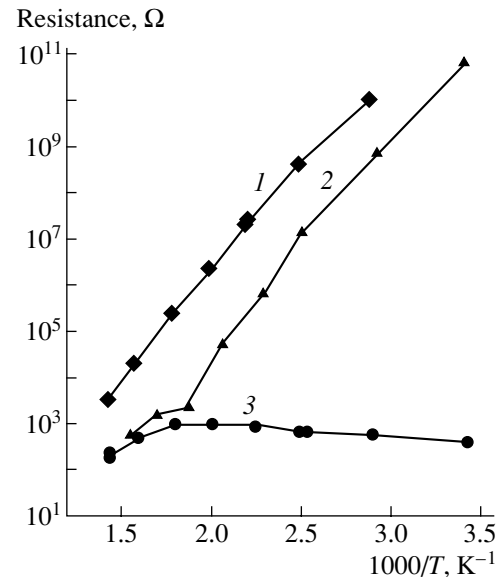
Heating the samples after irradiation led to various changes in the resistance of epitaxial layers, depending

**Fig. 4.** Resistance of 4H-SiC epitaxial layers irradiated with (1) neutrons and (2, 3) high-energy ions of (2) Bi and (3) Kr as a function of the damage dose.

on the type of radiation and the dose of the bombarding particles. In Fig. 5 we show the temperature dependences of the resistance of epitaxial layers irradiated with Bi ions and neutrons (curves 1 and 2, respectively) with the doses that correspond to the formation (according to the measurements of the C-V characteristics) of an insulating layer whose thickness is comparable to that of the lightly doped epitaxial layer (26 μm). Similar temperature dependences of the resistance have been previously observed for SiC samples irradiated with protons and electrons [22, 23]. It was assumed that this type of variation in the resistance of irradiated SiC samples may be attributed to the annealing of radiation defects formed in the cascades of atomic collisions [23]. In the case of irradiation of SiC with Kr heavy ions at low doses, a portion corresponding to so-called reverse annealing was observed in the temperature dependence of resistance (curve 3) [8]. The presence of a similar portion in the corresponding dependence for SiC samples annealed after irradiation with high doses of ions and neutrons was previously attributed to the formation of thermally unstable vacancy-containing clusters. The sizes, concentration, and thermal stability of these clusters depend on the type and dose of radiation, as well as on the doping level and purity of the starting material [23].

#### 4. CONCLUSIONS

We established that irradiation of high-resistivity high-purity 4H-SiC epitaxial CVD layers of n-type conductivity with 245-MeV Kr ions and 710-MeV Bi ions led to the formation of radiation defects that had the same parameters as those produced by irradiation with electrons, neutrons, and light ions. Thus, the for-

**Fig. 5.** Temperature dependences of the resistance of 4H-SiC epitaxial layers irradiated with (1) Bi ions, (2) neutrons, and (3) Kr ions.



mation of the defect structure in SiC is independent of the processes related to the relaxation of energy losses by ionization in the tracks of high-energy ions up to a level of 34 keV/nm and is controlled by radiation damage produced as a result of elastic-collision events.

#### ACKNOWLEDGMENTS

We thank G.N. Violina for useful comments.

This study was supported in part by the Russian Foundation for Basic Research (project no. 01-02-17911) and the Hungarian Academy of Sciences.

#### REFERENCES

1. T. Dalibor, G. Pensl, H. Matsunami, *et al.*, Phys. Status Solidi A **162**, 199 (1997).
2. V. V. Makarov, Fiz. Tverd. Tela (Leningrad) **13**, 2357 (1971) [Sov. Phys. Solid State **13**, 1974 (1971)].
3. V. S. Balandovich and G. N. Violina, Cryst. Lattice Defects Amorphous Mater. **13**, 189 (1987).
4. A. M. Strel'chuk, V. V. Kozlovskii, N. S. Savkina, *et al.*, Mater. Sci. Eng. **61–62**, 441 (1999).
5. M. Levalois, I. Lhermitte-Sebire, P. Marie, *et al.*, Nucl. Instrum. Methods Phys. Res. B **107**, 239 (1996).
6. L. Liskay, K. Havancsak, M.-F. Barthe, *et al.*, Mater. Sci. Forum **363**, 123 (2001).
7. S. J. Zinkle, J. W. Jones, and V. A. Skuratov, Mater. Res. Soc. Symp. Proc. **650**, R3.19.1 (2001).
8. E. Kalinina, G. Kholujanov, G. Onushkin, *et al.*, Mater. Sci. Forum **433–436**, 467 (2003).
9. E. Kalinina, G. Kholujanov, V. Solov'ev, *et al.*, Appl. Phys. Lett. **77**, 3051 (2000).
10. W. J. Weber, F. Gao, R. Devanathan, *et al.*, Nucl. Instrum. Methods Phys. Res. B **216**, 25 (2004).
11. V. I. Avramenko, Yu. V. Konobeev, and A. M. Strokova, At. Energ. **56** (3), 139 (1984).
12. M. Ikeda and H. Matsunami, Phys. Status Solidi A **58**, 657 (1980).
13. Yu. M. Suleimanov, A. M. Grekhov, and V. M. Grekhov, Fiz. Tverd. Tela (Leningrad) **25**, 1840 (1983) [Sov. Phys. Solid State **25**, 1060 (1983)].
14. Yu. A. Vodakov, G. A. Lomakina, E. N. Mokhov, *et al.*, Fiz. Tekh. Poluprovodn. (Leningrad) **20**, 2153 (1986) [Sov. Phys. Semicond. **20**, 1347 (1986)].
15. L. Patrick and W. J. Choyke, Phys. Rev. B **5**, 3253 (1972).
16. V. V. Makarov and N. N. Petrov, Fiz. Tverd. Tela (Leningrad) **8**, 1602 (1966) [Sov. Phys. Solid State **8**, 1272 (1966)].
17. N. V. Kodra and V. V. Makarov, Fiz. Tekh. Poluprovodn. (Leningrad) **15**, 1408 (1981) [Sov. Phys. Semicond. **15**, 813 (1981)].
18. C. Hemmingsson, N. T. Son, O. Kordina, *et al.*, J. Appl. Phys. **81**, 6155 (1997).
19. V. S. Balandovich, Fiz. Tekh. Poluprovodn. (St. Petersburg) **33**, 1314 (1999) [Semiconductors **33**, 1188 (1999)].
20. A. A. Lebedev, A. M. Ivanov, and N. B. Strokan, Fiz. Tekh. Poluprovodn. (St. Petersburg) **38**, 129 (2004) [Semiconductors **38**, 125 (2004)].
21. E. V. Kalinina, G. F. Kholuyanov, D. V. Davydov, *et al.*, Fiz. Tekh. Poluprovodn. (St. Petersburg) **37**, 1260 (2003) [Semiconductors **37**, 1229 (2003)].
22. A. A. Lebedev, A. I. Veinge, D. V. Davydov, *et al.*, Fiz. Tekh. Poluprovodn. (St. Petersburg) **34**, 1058 (2000) [Semiconductors **34**, 1016 (2000)].
23. A. I. Girka, A. D. Mokrushin, E. N. Mokhov, *et al.*, Zh. Éksp. Teor. Fiz. **97**, 578 (1990) [Sov. Phys. JETP **70**, 322 (1990)].

*Translated by A. Spitsyn*

---

---

**SEMICONDUCTOR STRUCTURES, INTERFACES,  
AND SURFACES**

---

---

## **Fabrication and Photosensitivity of Heterojunctions Based on $\text{CuIn}_3\text{Se}_5$ Crystals**

**I. V. Bodnar<sup>2</sup>, S. E. Nikitin<sup>1</sup>, G. A. Il'chuk<sup>1</sup>, V. Yu. Rud<sup>3</sup>, Yu. V. Rud<sup>1</sup>, and M. V. Yakushev**

<sup>1</sup>*Ioffe Physicotechnical Institute, Russian Academy of Sciences, Politekhnikeskaya ul. 26, St. Petersburg, 194021 Russia*

<sup>^</sup>*e-mail: rudvas@spbstu.ru*

<sup>2</sup>*Belarussian State University of Information Science and Radioengineering, Minsk, 220030 Belarus*

<sup>3</sup>*St. Petersburg State Technical University, Politekhnikeskaya ul. 29, St. Petersburg, 195251 Russia*

Submitted December 22, 2003; accepted for publication December 25, 2003

**Abstract**—Heterojunctions based on  $p\text{-CuIn}_3\text{Se}_5$  crystals are fabricated by magnetron sputtering of an  $n\text{-ZnO:Al}$  target and by putting naturally cleaved  $n\text{-GaSe}$  thin wafers onto polished surfaces of  $p\text{-CuIn}_3\text{Se}_5$  wafers. The current–voltage characteristics and mechanisms of current flow in the diodes under study are analyzed. The photovoltaic effect revealed in the fabricated structures is discussed. It is shown that the fabricated photosensitive heterojunctions are promising for the development of selective analyzers of linearly polarized radiation. © 2004 MAIK “Nauka/Interperiodica”.

### 1. INTRODUCTION

I–III–VI<sub>2</sub> semiconductors and their solid solutions have been widely investigated with the aim of developing highly efficient radiation-resistance thin-film solar cells [1–3]. At present, the efficiency of photoconversion in ZnO/CdS/CuInGaSe<sub>2</sub> heterostructures is as high as 19%, which is considered a record for thin-film photoconverters [2]. The optimization of the properties of thin Cu–III–VI<sub>2</sub> films is traditionally provided using solid solutions, for example,  $\text{CuIn}_x\text{Ga}_{1-x}\text{Se}_2\text{S}_{2-2x}$ . Research into the phase interaction in I–III–VI systems revealed a new possibility for controlling the fundamental properties of such semiconductors. On the one hand, many positionally ordered I–III <sub>$n+2$</sub> –VI <sub>$2n+3$</sub>  phases ( $n = 1, 2, 3, \dots$ ) have been found, which are formed in I<sub>2</sub>VI–III<sub>2</sub>VI<sub>3</sub> quasi-binary joins. These phases make it possible to vary discretely the fundamental properties of substances within their regions of stability [6–9]. This circumstance raises the problem of finding the correlation of the physical properties of new phases with their atomic composition. On the other hand, new grounds have appeared to expect that the conditions favorable for the formation of precipitates of the I–III <sub>$n+2$</sub> –VI <sub>$2n+3$</sub>  type in the mother phase are reproduced under various conditions for growing I–III–VI<sub>2</sub> ternary compounds. Therefore, the investigation of these phases in the form of bulk homogeneous crystals is of prime importance for determining the effect of variation in the composition and appearance of spatially restricted precipitates of various atomic composition and scale. This study belongs to this promising area of research and is devoted to studying the photosensitivity of the first heterostructures based on bulk  $\text{CuIn}_3\text{Se}_5$  crystals.

### 2. EXPERIMENTAL

The  $\text{CuIn}_3\text{Se}_5$  crystals used to fabricate heterojunctions were grown by planar crystallization (the Bridgman method) in a vertical single-zone furnace. The starting substances were Cu, In, and Se of 99.9999% purity. The elements taken in a stoichiometric ratio with a total weight of 25 g were charged into double quartz cells with a cone-shaped bottom. After charging, the cells were evacuated, sealed, and placed in a growth furnace. The furnace temperature was increased at a rate of ~50 K/h to 1260–1270 K. The cells were kept at ~1270 K for 2 h with vibrational stirring of the melt. After the vibrator was switched off, planar crystallization of the melt was performed. To homogenize the fabricated ingots, we carried out vacuum thermal treatment at ~1070 K for 150 h. The crystals grown were 12 mm in diameter and 40 mm in length.

The composition of the crystals was determined by X-ray microprobe analysis using a Cameca-SX100 microprobe. The content of elements in the grown crystals (Cu : In : Se = 11.4 : 32.9 : 55.7 at %) is in satisfactory agreement with the specified content in the starting charge (Cu : In : Se = 11.18 : 33.31 : 55.51 at %).

The structure and parameters of the unit cell of the crystal lattice was determined by X-ray diffraction analysis. The X-ray diffraction patterns taken from different parts of the ingot corresponded to the defect chalcopyrite structure. The unit-cell parameters calculated by the least-squares method from the lines with  $2\theta > 60^\circ$  are  $a = 5.766 \pm 0.001 \text{ \AA}$  and  $c = 11.499 \pm 0.005 \text{ \AA}$ , which is in agreement with the data of [9]. The high resolution of high-angle lines in the X-ray diffraction patterns indicates the homogeneity of the crystals grown.

To fabricate photosensitive structures, the ingots were cut into wafers 0.2–0.3 mm thick, which were mechanically ground and polished with subsequent

treatment in a polishing etchant. According to the thermovoltage sign, the  $\text{CuIn}_3\text{Se}_5$  crystals had  $p$ -type conductivity.

### 3. RESULTS AND DISCUSSION

The physical and technological research conducted showed that photosensitive heterojunctions can be fabricated by depositing thin  $\text{ZnO:Al}$  films ( $d \approx 1 \mu\text{m}$ ) onto the polished surfaces of  $\text{CuIn}_3\text{Se}_5$  wafers. The  $\text{ZnO:Al}$  films were fabricated by magnetron sputtering of a pressed  $\text{ZnO}$  target in argon with the addition of pure Al with a content of  $\sim 2.5$  at %. The argon pressure was kept at about 0.5 Pa during deposition of the film and the substrate temperature was  $40\text{--}50^\circ\text{C}$ . The  $\text{ZnO:Al}$  films had an electron density of  $\sim 5 \times 10^{20} \text{ cm}^{-3}$  and a Hall mobility of  $\sim 5 \text{ cm}^2/(\text{V s})$  at  $T = 300 \text{ K}$  and showed good adhesion to the substrate surface.

The measurements of the steady-state current–voltage ( $I$ – $U$ ) characteristics showed that the new  $n\text{-ZnO:Al}/p\text{-CuIn}_3\text{Se}_5$  heterojunctions have typical diode characteristics. Figure 1a shows the  $I$ – $U$  characteristic of such a structure at  $T = 300 \text{ K}$ . It turned out that the forward direction for all fabricated heterojunctions is always realized with a negative bias on the  $\text{ZnO:Al}$  film, which agrees with an approximated energy-band model of the heterostructure under study. The rectification coefficients for the best structures at  $|U| = 1\text{--}3 \text{ V}$  were  $K = 15\text{--}20$  (Fig. 1b, curves 1, 2). In our opinion, the values of  $K$  obtained are restricted by the rather poor quality of the heterojunctions.

At forward biases  $U < 0.35 \text{ V}$  (Fig. 1b, curve 1), the current increases by the exponential law

$$I = I_s \exp\left(\frac{eU}{\beta kT}\right), \quad (1)$$

where the saturation current  $I_s$  of the heterojunctions is in the range  $3 \times 10^{-7}\text{--}7 \times 10^{-8} \text{ A}$ , while the diode factor  $\beta = 3\text{--}4$  at  $T = 300 \text{ K}$ . This dependence suggests a tunneling–recombination mechanism of current transport.

At bias voltages in the range  $0.3 \text{ V} < U < 5 \text{ V}$ , the power dependence of the forward current  $I \propto U^m$  is clearly pronounced (Fig. 2, curve 1). The exponent  $m$  is generally in the range 1.6–2.1 for various structures and bias ranges, which indicates possible competition of the contributions of the currents restricted by the space charge in the velocity-saturation mode [10, 11]

$$I = \frac{2\varepsilon\varepsilon_0 v_s A}{L^2} U \quad (2)$$

and in the mobility mode (the trapless quadratic law) [12, 10]

$$I = \frac{8\varepsilon\varepsilon_0 \mu_p A}{L^3} U^2, \quad (3)$$

where  $\varepsilon$  is the permittivity of  $\text{CuIn}_3\text{Se}_5$ ,  $\varepsilon_0$  is the permittivity of free space,  $v_s$  is the saturation velocity,  $\mu_p$  is the

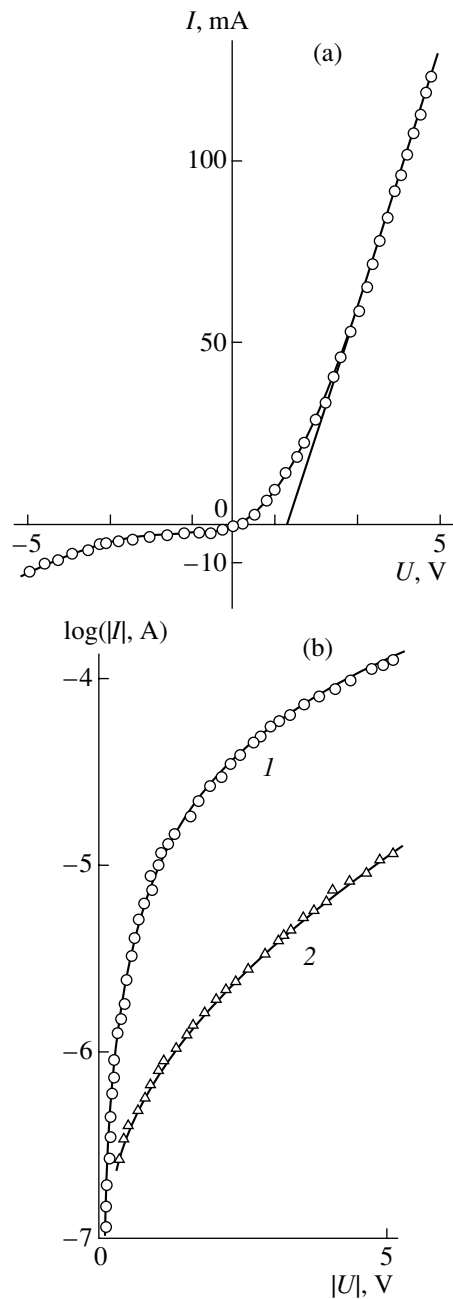


**Fig. 1.** Steady-state current–voltage characteristic of an  $n\text{-ZnO:Al}/p\text{-CuIn}_3\text{Se}_5$  heterojunction in the coordinates (a)  $I$ – $U$  and (b)  $\log I$ – $U$ . Curves 1 and 2 correspond to the forward and reverse portions, respectively, at  $T = 300 \text{ K}$ ; sample 2-1. The forward direction corresponds to a positive polarity of the  $\text{CuIn}_3\text{Se}_5$  substrate.

hole mobility,  $A$  is the interface area, and  $L$  is the thickness of the  $\text{CuIn}_3\text{Se}_5$  substrate.

At  $U > 3 \text{ V}$  (Fig. 1a, curve 1), the forward portion of the  $I$ – $U$  characteristics of the  $n\text{-ZnO:Al}/p\text{-CuIn}_3\text{Se}_5$  heterojunctions follows the linear law

$$U = U_0 - IR_0, \quad (4)$$

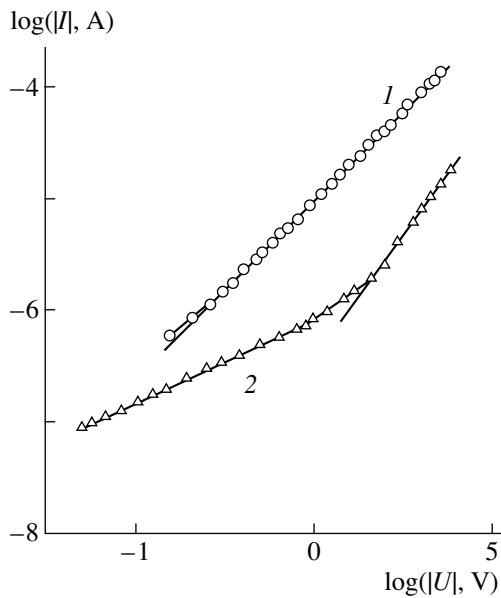


**Fig. 2.** (1) Forward and (2) reverse portions of the current–voltage characteristic of an  $n\text{-ZnO:Al/p-CuIn}_3\text{Se}_5$  heterojunction in a double logarithmic scale at  $T = 300$  K; sample 2-1.

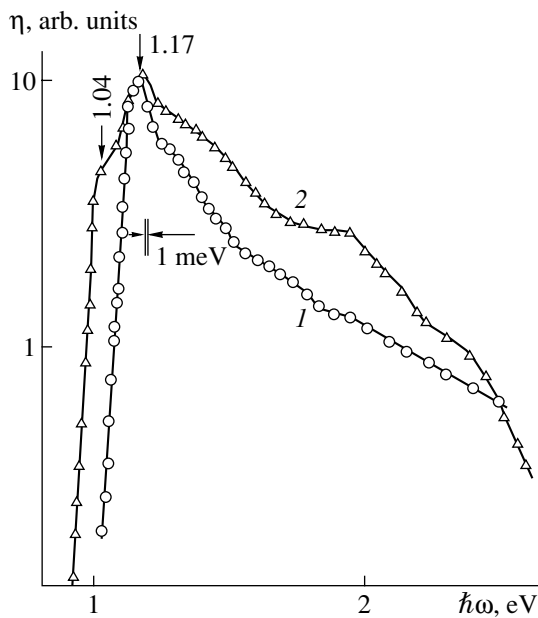


**Fig. 3.** Spectral dependences of the quantum efficiency of photoconversion for  $n\text{-ZnO:Al/p-CuIn}_3\text{Se}_5$  heterojunctions at  $T = 300$  K. Curves 1 and 2 correspond to samples 22 and 1-2, respectively. Exposure to unpolarized light from the  $n\text{-ZnO:Al}$  side.

where the cutoff voltage  $U_0 \approx 1.3$  V and  $R_0$  is the resistance of the heterojunction base, which varies from  $2.5 \times 10^2$ – $4 \times 10^7$   $\Omega$  at 300 K. Such a wide range of  $R$  is due to variations in the growth conditions for  $\text{CuIn}_3\text{Se}_5$  crystals.

It can be seen from Fig. 2 (curve 2) that reverse currents through the  $n\text{-ZnO:Al/p-CuIn}_3\text{Se}_5$  heterojunctions

also follow the power law  $I \propto U^m$  in the entire range of bias voltages used. At reverse voltages  $|U| < 1$  V, the dependence  $I \propto U^{0.74}$  is observed, which is similar to the power law. This circumstance gives grounds to attribute the current-flow mechanism to either tunneling or the restriction of carrier velocity by the space charge in the saturation mode (see relationship (2)). With a further increase in the reverse bias in the range  $1 \text{ V} < |U| < 10$  V, the exponent increases to  $m \approx 2$ , which corresponds to relationship (3). In this context, the observed quadratic dependence can be attributed to current restriction by the space charge in the mobility mode [10, 11].

When  $n\text{-ZnO:Al/p-CuIn}_3\text{Se}_5$  heterojunctions are illuminated, the photovoltaic effect becomes well defined. The photosensitivity of the heterojunctions is highest when they are illuminated from the side of the  $\text{ZnO:Al}$  film. When nonpolarized radiation of an incandescence lamp with power  $P \approx 10$   $\text{mW/cm}^2$  was used, the open-circuit voltage was as high as  $U_{oc} \approx 0.45$  V for the best structures and the short-circuit current was  $I_{sc} \approx 50$   $\mu\text{A}$  at  $T = 300$  K. The signs of the photovoltage and short-circuit photocurrent were independent of the photon energy and the point of incidence of a light probe on the heterostructure surface and corresponded to the forward direction. This fact suggests that the photosensitivity is related to the only active region formed by the heterocontact of the  $\text{CuIn}_3\text{Se}_5$  crystal with the  $n\text{-ZnO}$  film. For the best  $n\text{-ZnO:Al/p-CuIn}_3\text{Se}_5$  heterojunctions, the highest photovoltaic sensitivity is  $\sim 50$  V/W, and the current photosensitivity is  $\sim 50$  mA/W at 300 K.

Typical spectral dependences of the relative quantum efficiency of photoconversion  $\eta$  of the fabricated  $n\text{-ZnO:Al/p-CuIn}_3\text{Se}_5$  heterojunctions under illumination from the side of the wide-gap component  $n\text{-ZnO}$  are shown in Fig. 3. The characteristic features of the spectra of  $\eta$  are the presence of a peak near the photon energy  $\hbar\omega^m = 1.17$ – $1.18$  eV for different structures and a more pronounced (compared with the surface-barrier  $\text{In/p-CuIn}_3\text{Se}_5$  structures [8]) short-wavelength falloff of the photosensitivity.

We observed long-wavelength edges of two types in the spectra of  $\eta$  of the  $n\text{-ZnO:Al/p-CuIn}_3\text{Se}_5$  heterojunctions (Fig. 3, curves 1, 2). In the coordinates  $(\eta\hbar\omega)^2 - \hbar\omega$ , the long-wavelength edge of the spectrum of  $\eta$  straightens out. According to theoretical analysis of the edge absorption of semiconductors [13], this circumstance allows us to attribute this edge to direct interband optical transitions. The energy of the direct interband transitions in  $\text{CuIn}_3\text{Se}_5$ , which was determined from the energy position of the cutoff point by the extrapolation  $(\eta\hbar\omega)^2 \rightarrow 0$ , is  $E_g \approx 1.09$  eV at 300 K. A similar result was obtained by the same treatment of the long-wavelength edge of the spectra of  $\eta$  for Schottky barriers based on  $\text{CuIn}_3\text{Se}_5$  crystals [7].

Among the studied spectra of  $\eta$  of the  $n\text{-ZnO:Al/p-CuIn}_3\text{Se}_5$  heterojunctions, we observed spectra with a pronounced inflection point in the vicinity of  $\hbar\omega^m \approx 1.04$  eV at energies  $\hbar\omega < \hbar\omega^m$  (Fig. 3, curve 2). A sim-

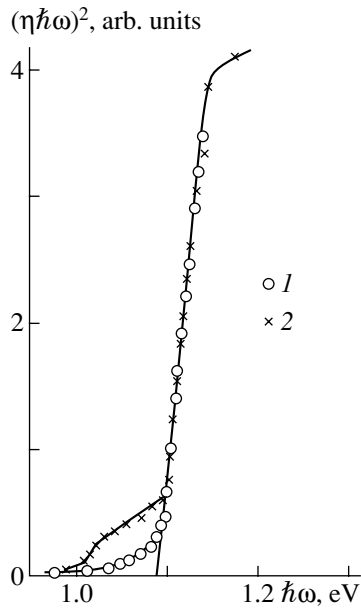


**Fig. 4.** Long-wavelength edge of the spectral dependences  $(\eta\hbar\omega)^2$  for  $n\text{-ZnO:Al}/p\text{-CuIn}_3\text{Se}_5$  heterojunctions at  $T = 300$  K. Curves 1 and 2 correspond to samples 22 and 1-2, respectively. Exposure to unpolarized light from the  $n\text{-ZnO:Al}$  side.

ilar feature was found previously in the photosensitivity spectra of  $\text{In}/p\text{-CuIn}_3\text{Se}_5$  Schottky barriers [7]. This feature was attributed to photoactive absorption by the lattice-defect levels. This explanation can also be given based on the reported spectra of long-wavelength photosensitivity for  $n\text{-ZnO:Al}/p\text{-CuIn}_3\text{Se}_5$  heterojunctions (Fig. 3, curve 2). However, taking into account that the value of  $\hbar\omega^m$  is similar to the band gap of  $\text{CuInSe}_2$  [14], the specific feature in question apparently can also be attributed to the presence of  $\text{CuInSe}_2$  precipitates in  $\text{CuIn}_3\text{Se}_5$ . In order to resolve this uncertainty definitively, it is evidently necessary to carry out additional microscopic studies to search for spatially confined  $\text{CuInSe}_2$  inclusions in  $\text{CuIn}_3\text{Se}_5$ .

Along with the structures considered above, we also attempted to fabricate heterojunctions by putting thin ( $\sim 50$   $\mu\text{m}$ ) cleaved  $n\text{-GaSe}$  wafers with free-electron density  $n \approx 10^{14}$   $\text{cm}^{-3}$  ( $T = 300$  K) into a direct optical contact with a polished surface of  $p\text{-CuIn}_3\text{Se}_5$  [15]. The fabricated  $n\text{-GaSe}/p\text{-CuIn}_3\text{Se}_5$  contacts also showed rectification ( $K \approx 5$  at  $U \approx 40$  V) and a photovoltaic effect ( $S_u \approx 40$  V/W at 300 K).

Figure 5a shows a typical spectrum of  $\eta$  for a heterojunction at 300 K under illumination from the GaSe side. The photosensitivity of these heterojunctions is observed in a wide spectral range from 1 to 2 eV. The photosensitivity dominates in the fundamental-absorption region of GaSe [15, 16], which is associated with the preferred location of the active region in the wide-gap component of this heterojunction. The reason for this is that the resistivity of  $n\text{-GaSe}$  is four to five orders

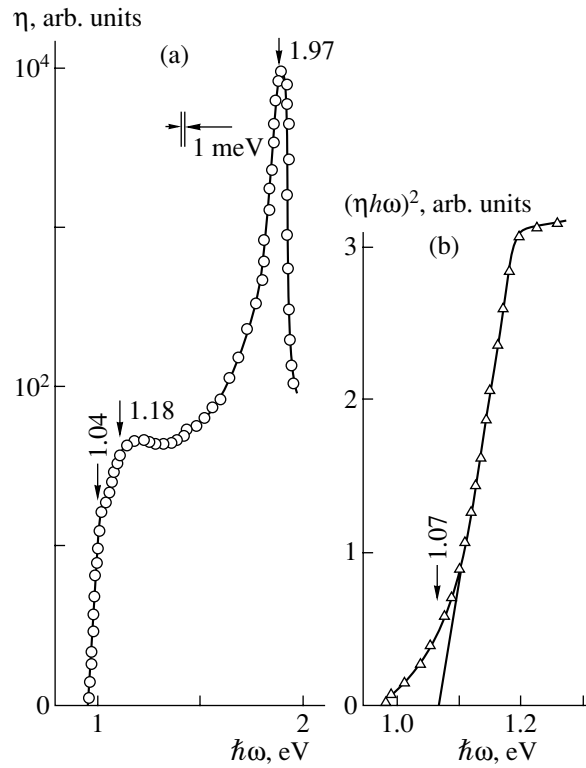


**Fig. 5.** (a) Spectral dependence of the relative quantum efficiency of photoconversion of a  $n\text{-GaSe}/p\text{-CuIn}_3\text{Se}_5$  heterojunction (sample 1-6) at  $T = 300$  K. (b) The long-wavelength edge of the spectral dependence. Illumination from the side of the  $n\text{-GaSe}$  wafer of thickness  $d \approx 50$   $\mu\text{m}$ . Arrows show the energy positions of spectral features.

of magnitude higher than the resistivity of  $p\text{-CuIn}_3\text{Se}_5$ . It should be noted that the structure and energy position of the long-wavelength edge in the spectrum of  $\eta$  of the  $n\text{-GaSe}/p\text{-CuIn}_3\text{Se}_5$  heterojunctions (Fig. 5a) are very close to those observed for the  $n\text{-ZnO:Al}/p\text{-CuIn}_3\text{Se}_5$  heterojunctions [9]. This circumstance suggests that the long-wavelength edge of photosensitivity of the  $n\text{-GaSe}/p\text{-CuIn}_3\text{Se}_5$  heterojunctions is controlled by the interband absorption in the ternary compound  $\text{CuIn}_3\text{Se}_5$ . The straightening of the long-wavelength edge of photosensitivity of the  $n\text{-GaSe}/p\text{-CuIn}_3\text{Se}_5$  heterojunctions, as well as similar values of the cutoff energy obtained by the extrapolation  $(\eta\hbar\omega)^2 \rightarrow 0$  for the heterojunctions fabricated by bringing them into optical contact (Fig. 5b), is also in favor of direct interband transitions in  $\text{CuIn}_3\text{Se}_5$  crystals ( $E_g \approx 1.08$  eV at 300 K).

It should be noted that, in the case of  $n\text{-GaSe}/p\text{-CuIn}_3\text{Se}_5$  heterojunctions, we observed no short-wavelength falloff of photosensitivity deep in the fundamental absorption region of  $\text{CuIn}_3\text{Se}_5$  at  $\hbar\omega > 1.18$  eV, which is characteristic of Schottky barriers [7] and  $n\text{-ZnO:Al}/p\text{-CuIn}_3\text{Se}_5$  structures (Fig. 3). Hence, there is almost no recombination of photogenerated carriers at interfacial states, which indicates the high quality of

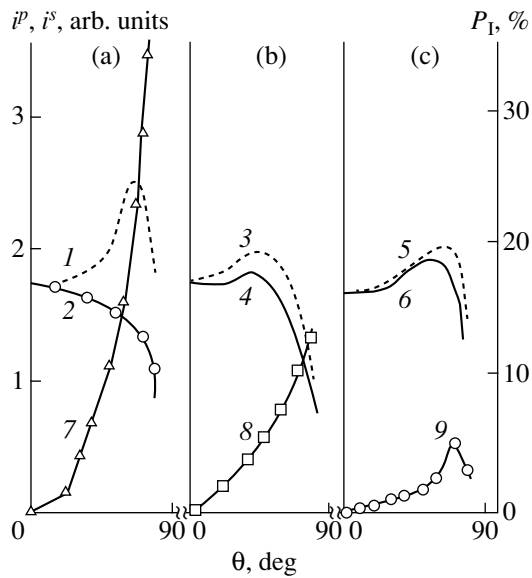


**Fig. 6.** Dependences of the photocurrents (1, 3, 5)  $i^p$  and (2, 4, 6)  $i^s$  and (7–9) the coefficient of induced photopoleochroism on the angle of incidence of linearly polarized radiation on the photodetecting  $n$ -Zn:Al plane of an  $n$ -ZnO:Al/ $p$ -CuIn<sub>3</sub>Se<sub>5</sub> heterojunction at  $T = 300$  K (sample 22) at the wavelengths of incident radiation  $\lambda =$  (1, 2, 7) 1.15, (3, 4, 8) 1.05, and (5, 6, 9) 0.86  $\mu\text{m}$ .

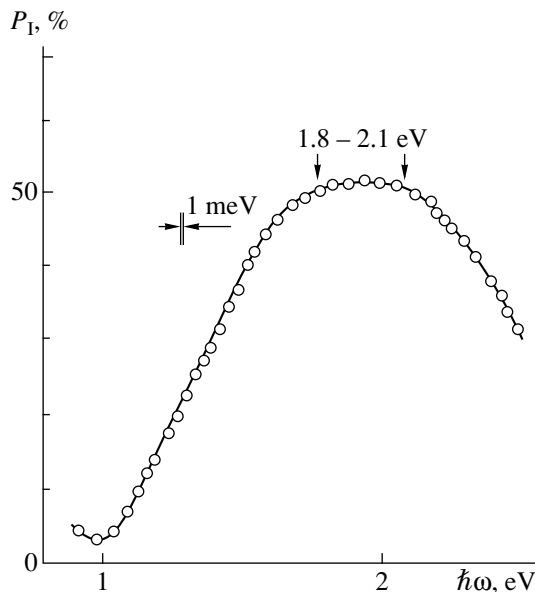


**Fig. 7.** Spectral dependences of the coefficient of induced photopoleochroism of an  $n$ -ZnO:Al/ $p$ -CuIn<sub>3</sub>Se<sub>5</sub> heterojunction at  $T = 300$  K (sample 22). Illumination from the side of the  $n$ -ZnO:Al layer.  $\Theta = 85^\circ$ .

the interface with respect to the recombination processes.

We investigated the photosensitivity of the  $n$ -ZnO:Al/ $p$ -CuIn<sub>3</sub>Se<sub>5</sub> heterojunctions using linearly polarized radiation. These investigations showed that

polarization photosensitivity occurs only under conditions of oblique incidence of radiation onto the photo-detecting  $n$ -ZnO:Al plane. Indeed, as can be seen from Fig. 6, when linearly polarized radiation is incident normally to the ZnO plane (the angle of incidence  $\Theta = 0$ ), the photocurrents are equal in magnitude, whereas the coefficient of induced photopoleochroism [17]

$$P_I = \frac{(i^p - i^s)}{(i^p + i^s)} \equiv 0, \quad (5)$$

where  $i^p$  and  $i^s$  are the photocurrents for the vector of the electric field  $\mathbf{E}$  of the incident light wave directed parallel and normally to the plane of incidence, respectively. We found that identity (5) is satisfied. This fact means that the natural photopoleochroism [18] is absent in the heterojunctions under study due to the polycrystalline structure of CuIn<sub>3</sub>Se<sub>5</sub> crystals used as substrates and the low natural tetragonal distortion of the crystal lattice of this compound [14].

It can be seen from Fig. 6 that, when the angle of incidence  $\Theta$  differs from zero, the photocurrents differ from each other ( $i^p > i^s$ ) in the photosensitivity region of the heterojunction. This effect is accompanied by the appearance of photopoleochroism induced by the obliquely incident linearly polarized radiation [17]:

$$P_I > 0. \quad (6)$$

In this case, as can be seen from Fig. 6, the angular dependences  $i^p(\Theta)$  and  $i^s(\Theta)$ , as well as  $P_I(\Theta)$ , vary over the spectrum, whereas the coefficient of induced photopoleochroism follows the quadratic law known from the theory [17]:  $P_I \propto \Theta^2$ .

Figure 7 shows the spectral dependence of the coefficient of induced photopoleochroism for a fixed angle of incidence of linearly polarized radiation  $\Theta = 85^\circ$ . This dependence is typical of the heterojunctions under study. As can be seen from Fig. 7, in contrast to the coefficient of induced photopoleochroism that is almost independent of the photon energy, which is expected for optically homogeneous media [17], the coefficient  $P_I$  of the fabricated heterojunctions depends heavily on the photon energy. The highest value of  $P_I$  (about 50%) is similar to that expected from the theory [19] for the air/ZnO interface only in the peak of the experimental spectrum of  $P_I$  at  $\Theta = \text{const}$ . An abrupt decrease in  $P_I$  to 4–5% near  $\hbar\omega \approx 1$  eV is due to the decrease in the difference between the photocurrents  $i^s$  and  $i^p$ , as a result of which the equality  $P_I \approx 0$  becomes valid at  $\Theta \neq 0$ . The disappearance of induced photopoleochroism [17] is attributed to the interference clearing in the  $n$ -ZnO:Al/ $p$ -CuIn<sub>3</sub>Se<sub>5</sub> heterojunctions, which occurs at  $P_I \rightarrow 0$ . With an increase in  $\hbar\omega > 1$  eV (as follows from Fig. 7), the coefficient of induced photopoleochroism increases and attains its maximum value  $P_I \approx 50\%$  at  $\Theta = 85^\circ$  in the range 1.8–2.1 eV. With a further increase in the photon energy to  $\hbar\omega > 2.1$  eV,  $P_I$  decreases again. One may suggest that the dependence  $P_I(\hbar\omega)$  shown in Fig. 7 is the result of oscillations

of the coefficient of induced photopleochroism in the  $n$ -ZnO:Al/ $p$ -CuIn<sub>3</sub>Se<sub>5</sub> heterojunctions [17]. It is evident that the quantum efficiency of photoconversion in such structures should meet the condition  $P_I \approx 0$  in the entire spectral range of incident radiation. For the heterojunctions under study, this condition is not satisfied in the case of a single-layer ZnO:Al coating. Hence, it is necessary to search for and develop multilayer interference coatings to satisfy the condition  $P_I \approx 0$  in the entire (wide) spectral range. Rapid monitoring of clearing can be performed by measuring the dependence  $P_I(\hbar\omega)$  at  $\Theta > 0$ .

#### 4. CONCLUSIONS

Thus, we fabricated for the first time new photosensitive  $n$ -ZnO:Al/ $p$ -CuIn<sub>3</sub>Se<sub>5</sub> and  $n$ -GaSe/ $p$ -CuIn<sub>3</sub>Se<sub>5</sub> heterojunctions that can be used as selective photoconverters of natural and linearly polarized radiation. It is shown that polarization photoelectric spectroscopy can be used for rapid monitoring of as-prepared photoconverters, which opens up new possibilities for the effective search for process conditions to optimize ZnO–CuIn<sub>3</sub>Se<sub>5</sub> structures.

#### ACKNOWLEDGMENTS

This study was supported by programs of the Department of Physical Sciences, Russian Academy of Sciences (“New Principles of Energy Conversion in Semiconductor Structures”) and INTAS (project no. 2001-283).

#### REFERENCES

1. H. W. Schock and A. Shah, in *Proceedings of 14th European Photovoltaic Solar Energy Conference* (Barcelona, Spain, 1997).
2. O. Lundberg, M. Edoff, and L. Stolt, in *Abstract Book of Solar World Congress, ISES-2003* (Göteborg, Sweden, 2003), p. 57.
3. T. M. Razykov, *Abstract Book of Solar World Congress, ISES-2003* (Göteborg, Sweden, 2003), p. 61.
4. S. D. Tsang, S. H. Wei, A. Zunger, and H. Katayama-Yoshida, *Phys. Rev. B* **57**, 9642 (1998).
5. S. H. Wei, S. D. Tsang, and A. Zunger, *Appl. Phys. Lett.* **72**, 3199 (1998).
6. I. V. Bodnar', V. F. Gremenok, V. Yu. Rud', and Yu. V. Rud', *Fiz. Tekh. Poluprovodn. (St. Petersburg)* **33**, 805 (1999) [*Semiconductors* **33**, 740 (1999)].
7. I. V. Bodnar', T. L. Kushner, V. Yu. Rud', and Yu. V. Rud', *Zh. Prikl. Spektrosk.* **69**, 519 (2002).
8. G. Marin, R. Marques, and R. Guevara, *Jpn. J. Appl. Phys., Part 1* **39**, 44 (2000).
9. I. V. Bodnar', V. Yu. Rud', Yu. V. Rud', and M. V. Yakushev, *Fiz. Tekh. Poluprovodn. (St. Petersburg)* **36**, 1211 (2002) [*Semiconductors* **36**, 1132 (2002)].
10. E. Hernandez, *Cryst. Res. Technol.* **33**, 285 (1998).
11. M. A. Lampert and P. Mark, *Current Injection in Solids* (Academic, New York, 1970; Mir, Moscow, 1973).
12. S. E. Nikitin, Yu. A. Nikolaev, I. K. Polushina, *et al.*, *Fiz. Tekh. Poluprovodn. (St. Petersburg)* **37**, 1329 (2003) [*Semiconductors* **37**, 1291 (2003)].
13. Yu. A. Ukhanov, *Optical Properties of Semiconductors* (Nauka, Moscow, 1977) [in Russian].
14. *Physicochemical Properties of Semiconductors: Handbook* (Nauka, Moscow, 1979) [in Russian].
15. I. V. Bodnar, V. Yu. Rud', and Yu. V. Rud', *Cryst. Res. Technol.* **31**, 261 (1996).
16. N. M. Mekhtiev, Yu. V. Rud', and É. Yu. Salaev, *Fiz. Tekh. Poluprovodn. (Leningrad)* **12**, 1566 (1978) [*Sov. Phys. Semicond.* **12**, 924 (1978)].
17. F. P. Kesamanly, V. Yu. Rud', and Yu. V. Rud', *Fiz. Tekh. Poluprovodn. (St. Petersburg)* **30**, 1921 (1996) [*Semiconductors* **30**, 1001 (1996)].
18. Yu. V. Rud', *Izv. Vyssh. Uchebn. Zaved., Fiz.* **29**, 68 (1986).
19. G. A. Medvedkin and Yu. V. Rud', *Phys. Status Solidi A* **67**, 333 (1981).

*Translated by N. Korovin*

## SEMICONDUCTOR STRUCTURES, INTERFACES, AND SURFACES

# Influence of Hydrogen Sulfide on Electrical and Photoelectric Properties of Al-*p*-Si-SnO<sub>2</sub>:Cu-Ag Heterostructures

S. V. Slobodchikov<sup>†</sup>, E. V. Russu, É. V. Ivanov, Yu. G. Malinin, and Kh. M. Salikhov

*Ioffe Physicotechnical Institute, Russian Academy of Sciences, Politekhnikeskaya ul. 26, St. Petersburg, 194021 Russia*

Submitted December 30, 2003; accepted for publication March 15, 2004

**Abstract**—*I-V* characteristics, spectral photosensitivity, and the dependence of the photocurrent on bias, as well as the effect of a 1% -H<sub>2</sub>S/N<sub>2</sub> gas mixture, were studied for an Al-*p*-Si-SnO<sub>2</sub>:Cu-Ag heterostructure. The charge transport for carriers in the dark and under illumination was found to obey the law  $J \propto U^2$ . Exposure to hydrogen sulfide results in a spectral shift of the photovoltage curve to shorter wavelengths. The kinetics of the decrease in photocurrent in a hydrogen sulfide medium is characterized by long relaxation times. © 2004 MAIK "Nauka/Interperiodica".

### 1. INTRODUCTION

Tin dioxide SnO<sub>2</sub> is widely used to produce sensors of various gases: hydrogen sulfide H<sub>2</sub>S, methane CH<sub>4</sub>, and carbon oxide CO, among other gases [1, 2]. The operation of such sensors is based on a change in the conductivity of the SnO<sub>2</sub> layer in the atmosphere of the detected gas.

Despite a number of important advantages, including high sensitivity and simple design, these sensors also have significant disadvantages. One of them is the need to heat a sensitive element to 300–400°C, which in turn requires significant power. Moreover, the selectivity of SnO<sub>2</sub>-based sensors to some gases is not high enough.

Meanwhile, specific technical requirements are of primary importance in most applications of gas analyzers. Specifically, the device should be made in a portable (or even hand-held) modification. This device should have low energy consumption, the required sensitivity and selectivity, and be able to operate efficiently under specific industrial conditions.

Therefore, it is of interest to study the properties of tin dioxide as applied to the problem of detecting various gases using physical effects that differ from those employed in conventional SnO<sub>2</sub>-based gas analyzers.

Many studies [3–5] have shown that the sensitivity of conventional gas sensor based on a change in the conductivity of an operating element can be significantly improved by doping tin dioxide with copper. These structures have obviously attracted the most attention.

In this paper, we report some experimental results related to the development of SnO<sub>2</sub>:Cu-based heterostructures, their electrical and photoelectric characteristics, and the influence of hydrogen sulfide on these parameters.

### 2. TECHNOLOGY OF HETEROSTRUCTURES

*p*-Si wafers with crystallographic orientation (100) were used as substrates. Thin SnO<sub>2</sub>:Cu layers were deposited by spraying in a horizontal reactor in an oxygen medium at a substrate temperature of 300–400°C. The oxygen flow rate was 0.7 l/min. The solution spraying duration was 90–220 s. The deposition was carried out through circular windows such that the heterostructure diameter was 1 mm.

The solution for spraying was prepared by tin chloride dissolution in ethanol until a viscosity of 0.04 P was attained. Doping with copper was carried out from a 0.1M SnCl<sub>2</sub> · 2H<sub>2</sub>O + 0.01M CuCl<sub>2</sub> · 2H<sub>2</sub>O solution in ethanol.

### 3. RESULTS AND DISCUSSION

The heterostructure samples prepared were used to measure the current–voltage (*I-V*) and capacitance–voltage (*C-V*) characteristics, photovoltage spectral curves, and the dependences of the photocurrent on bias.

To study the influence of hydrogen sulfide on these characteristics, the samples were placed for a time into a cell filled with a mixture of nitrogen and hydrogen sulfide. The volume concentration of hydrogen sulfide in the cell was 1%.

All the measurements were carried out at room temperature (20°–25°C).

#### 3.1. Electrical Characteristics of Heterostructures

The *I-V* characteristics of one of the typical samples with forward biases (positive voltage at *p*-Si) are shown in Fig. 1. The curves were measured before the sample was exposed to a 1% -H<sub>2</sub>S/N<sub>2</sub> atmosphere (curve 1), as well as after exposure to this gas mixture for 5–10 min followed by exposure to air for 24 h (curve 2).

<sup>†</sup>Deceased.



We can see in Fig. 1 that the dependences of the forward current on voltage are almost identical in both cases, but there are some quantitative differences. Both curves contain two regions: the ohmic ( $J \propto U$ ) and quadratic ( $J \propto U^2$ ) regions. These regions seem to be caused by features in the electrical and energy-band characteristics of the heterostructure.

The thickness of the layer with relatively high resistivity was estimated using capacitance measurements and was found to be 1.0–1.5  $\mu\text{m}$ . The electron density calculated from the dependence  $C^{-2} = f(U)$  was  $n_0 \leq 10^{12} \text{ cm}^{-3}$ . This high-resistivity region may have formed due to the compensation of donors in  $n\text{-SnO}_2$  by a copper impurity. A possible energy-band diagram of the heterostructure is shown in Fig. 2.

Hence, the observed features of the forward portion of the  $I$ - $V$  characteristic are accounted for by the double injection of carriers: holes from  $p\text{-Si}$  (current  $J_p$ ) and electrons from the metal into  $n\text{-SnO}_2\text{:Cu}$  (current  $J_n$ ) with different injection factors  $J_p/J$  and  $J_n/J$  (where  $J$  is the total current).

It should be noted that the reverse portion of the  $I$ - $V$  characteristic does not exhibit the double injection mechanism (i.e.,  $J_n/J$  and  $J_p/J \ll 1$ ) and features the current saturation region characteristic of an ordinary diode structure.

Let us consider the features of double injection as applied to the heterostructure under consideration. Transforming the equation of conservation of the number of particles, we can write (see [6])

$$(n_0 - p_0)dE/dx + (2kT/q)d^2n/dx^2 \approx (b + 1)(n - n_0)/(\mu_n \tau), \quad (1)$$

where  $b = \mu_n/\mu_p$ ,  $E$  is the electric field strength, and the other designations are conventional. When deriving Eq. (1), we assumed that the effect of plasma injected into an insulator can be disregarded.

If the first term of Eq. (1) is dominant for most of the  $\text{SnO}_2\text{:Cu}$  layer (region I in Fig. 2), we have

$$J \approx q(n_0 - p_0)\mu_n\mu_p\tau U^2/L^3, \quad (2)$$

where  $L$  is the length of region I. This is the charge transport mechanism that is observed in the heterostructure.

Since this mechanism should be dominant at  $L/L_A \gg 1$ , where  $L_A = [(2kT/q)\mu_n\tau/(b + 1)]^{1/2}$  is the ambipolar diffusion length, and region I is rather short, it can be concluded that the diffusive displacement is small; hence, the carrier lifetime is short.

This result is not surprising, if we take into account the features of the microstructure of the  $\text{SnO}_2\text{:Cu}$  layer. Indeed, there is no sharp increase in the current (which is caused by filling of the main trapping level and which controls the recombination rate) in the region of high biases beyond the  $I$ - $V$  characteristic region described by expression (2). This fact may indicate the involve-

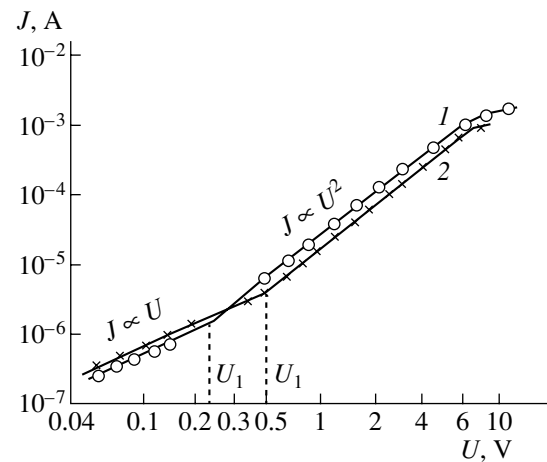


Fig. 1.  $I$ - $V$  characteristics of the Al- $p$ -Si- $\text{SnO}_2\text{:Cu}$ -Ag heterostructure under forward bias (1) before and (2) after exposure to a 1%- $\text{H}_2\text{S}/\text{N}_2$  gas mixture.

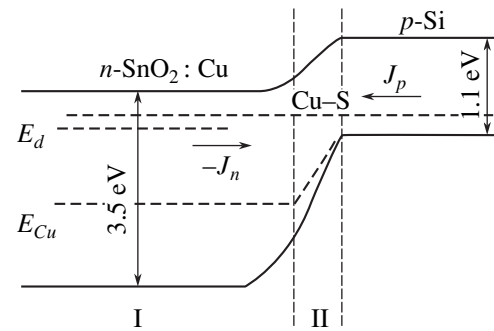


Fig. 2. Energy-band diagram of the Al- $p$ -Si- $\text{SnO}_2\text{:Cu}$ -Ag heterostructure.

ment of several trapping centers that are associated not only with a chemical impurity, but also with structure defects under exposure to light.

The voltage  $U_1$  corresponding to the intersection point of the ohmic and quadratic portions of the  $I$ - $V$  characteristic (see Fig. 1) may be written as

$$U_1 = U_{1,n}(1 + bn_0/p_0)/(1 - n_0/p_0),$$

where

$$U_{1,n} = L^2/(\mu_p \tau). \quad (3)$$

Before exposure of the sample to a 1%- $\text{H}_2\text{S}/\text{N}_2$  gas mixture, this voltage was  $U_1 \approx 0.22 \text{ V}$ . After exposure of the heterostructure to this mixture, followed by exposure to air,  $U_1 \approx 0.5 \text{ V}$ .

As noted above, after exposure to hydrogen sulfide, the current-voltage dependence remained unchanged. At the same time, the current in the region of double injection was reduced by factor of approximately 1.5 compared to the current before exposure, while the current in the ohmic region increased by 20–30%.

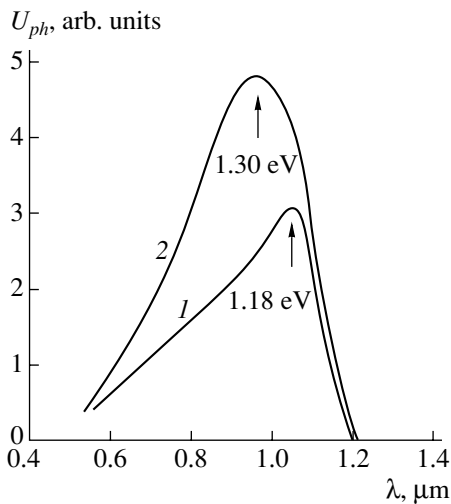


**Fig. 3.** Spectral photosensitivity of the Al-*p*-Si-SnO<sub>2</sub>:Cu-Ag structure (1) before and (2) after exposure to a 1%-H<sub>2</sub>S/N<sub>2</sub> gas mixture.

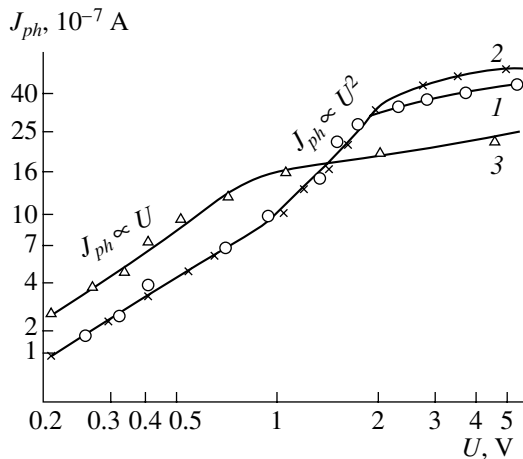


**Fig. 4.** Dependences of the photocurrent on the applied bias (1, 3) before exposure to a 1%-H<sub>2</sub>S/N<sub>2</sub> gas mixture under forward and reverse bias, respectively, and (2) after exposure under forward bias.

This current change in the ohmic region is caused by an increase in the concentration of equilibrium carriers, rather than by an increase in their mobility, since the bias has to be increased to neutralize the injected plasma. This conclusion is confirmed by the increase in  $U_1$  observed in Fig. 1.

The decrease in the current of the double injection in the quadratic region of the  $I$ - $V$  characteristic after exposure to hydrogen sulfide may be associated with a decrease in the hole injection factor from the side of the SnO<sub>2</sub>:Cu-*p*-Si interface. This effect is rather pronounced, but the interface plays a more significant role in research on the photovoltage and photocurrent.

### 3.2. Photoelectric Characteristics of Heterostructures

Figure 3 shows two dependences of the spectral photosensitivity, measured before (curve 1) exposure to

hydrogen sulfide and after exposure with further exposure to air (curve 2). These dependences were measured under conditions of open-circuit photovoltage.

First, it follows from Fig. 3 that the spectral photosensitivity of the heterostructures under study is controlled by the component with the narrowest band gap, i.e., *p*-Si.

Then, as a result of exposure to hydrogen sulfide, the photovoltage magnitude (curve 2) increased by a factor of 1.5 compared to its initial values (curve 1). The peak of this dependence shifted to shorter wavelengths by 0.12 eV.

Figure 4 shows the dependence of the photocurrent on the forward and reverse bias voltages. In curves 1 and 2 (measured under forward bias before and after exposure to hydrogen sulfide, respectively), the linear portion ( $J \propto U$ ) is followed by the quadratic portion ( $J \propto U^2$ ) at  $U > 1$  V. In curve 3 measured under reverse bias before exposure to the 1%-H<sub>2</sub>S/N<sub>2</sub> mixture, the linear region gradually transforms into a region of leveling off.

In all the curves, the increase in the photocurrent in the linear region is mainly caused by a change in the heterostructure resistivity of region I under the condition that the concentration of equilibrium carriers is  $n_0 \geq \Delta n, \Delta p$ .

As the bias further increases, the concentration of excess photogenerated carriers exceeds  $n_0$ , and the mode of double injection of carriers arises under illumination. This mode corresponds to the quadratic portion of the curve; i.e., photocurrent amplification takes place. However, this mode is largely controlled by the trapping and recombination of excess carriers in both region I and region II at the heterointerface.

When testing the effect of external unmodulated illumination, we detected a decrease in the photocurrent with increasing radiation intensity, which indicated that the corresponding trapping levels were recharged. Assuming that the copper level in SnO<sub>2</sub> is an acceptor, region I may be considered heavily compensated. Therefore, pronounced trapping of excess electrons is observed under injection of photogenerated carriers (as for carriers in the previous case in the absence of illumination). These processes are reflected in the run of the  $I$ - $V$  characteristic: the quadratic region is followed by a region of leveling off.

According to Eq. (1), in the absence of trapping (i.e., at constant  $\tau$ ) one should expect a contribution from the second term  $(2kT/q)d^2n/dx^2$  to carrier transport. This effect results from the accumulation of electrons near the SnO<sub>2</sub>:Cu-*p*-Si interface. An accumulation of electrons and holes would lead to a decrease in the electric-field strength, as well as to the prevalence of the diffusion term effect. In this case, the exponent at  $U$  in formula (2) should be larger than two. In the case under consideration, such an accumulation does not take place due to electron trapping. As a result, the electric-field strength increases toward the heterointerface and attains a certain finite maximum near it.

Figure 5 shows the experimental curve of the photocurrent as a function of the time the heterostructure is exposed to the 1%-H<sub>2</sub>S/N<sub>2</sub> gas mixture (region I) with further exposure to air (region II). As hydrogen sulfide is introduced into the cell with the sample, the photocurrent drops almost without delay to 77% of its initial value. A further 8-min exposure of the sample to the H<sub>2</sub>S mixture results in a decrease in the photocurrent to 34% of its initial value. After discharging the 1%-H<sub>2</sub>S/N<sub>2</sub> gas mixture from the cell and during further exposure to air, the photocurrent gradually increases. Eventually, the values of the photocurrent under forward bias, measured before and after exposure to hydrogen sulfide, turn out to be almost identical, including those under conditions of double injection (Fig. 4, curves 1, 2).

One possible explanation for the influence of hydrogen sulfide on the photoelectric characteristics of the structures studied is associated with the role of the SnO<sub>2</sub>:Cu-*p*-Si interface. Since the photovoltage arises due to the presence of a heterobarrier, the variation in this voltage should be related to the change in the height of the barrier. The technology used for deposition of the SnO<sub>2</sub>:Cu layer necessarily causes a high concentration of large through pores in these layers, which allows gases to rapidly penetrate the heterointerface from the surrounding medium. The reversibility of the influence of gases on the photoelectric properties of heterostructures most likely indicates physical sorption-desorption of gases (which changes the charge state of the heterointerface), rather than the chemical mechanism of the effect. In this case, the height of the energy barrier and, consequently, the photocurrent may change. The shift of the photovoltage curve to shorter wavelengths, apart from other causes, may result from a decrease in the recombination rate near the heterointerface (in regions of highest copper content in the SnO<sub>2</sub> layer) during the adsorption of hydrogen sulfide molecules at this interface.

Furthermore,  $U_{ph} \approx J_{ph}R_0$  at small signals ( $R_0$  is the resistance at zero bias). In the case of generation-recombination, the latter example is represented by

$$R_0A = (\tau_0/n_i)(U_{bi}N_a)^{1/2}/(2\varepsilon\varepsilon_0q)^{1/2}, \quad (4)$$

where  $A$  is the active area of the structure,  $U_{bi}$  is the contact potential,  $\tau_0$  is the carrier lifetime,  $n_i$  is the intrinsic carrier concentration, and the other designations are conventional. Since  $\tau_0$  increases near the heterointerface, the value of  $R_0A$  also increases. In turn, this should cause an increase in the photovoltage, which is precisely what takes place in the experiment.

In the context of the above, the previously indicated identity of the bias dependences of the photocurrent

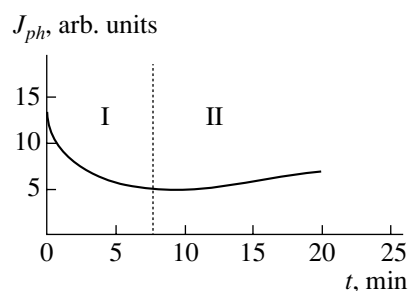


Fig. 5. Kinetics of photocurrent variation during exposure of the heterostructure to a 1%-H<sub>2</sub>S/N<sub>2</sub> gas mixture (region I) and further exposure to air (region II).

(see Fig. 4) measured before and after exposure to hydrogen sulfide becomes clear, since these curves were measured under excitation radiation with a wavelength of 1  $\mu$ m.

#### 4. CONCLUSIONS

The results obtained show that it is possible in principle to use SnO<sub>2</sub>-based heterostructures to detect hydrogen sulfide using the new physical effect, i.e., the change in the photosensitivity of the heterostructure in the atmosphere of a detected gas. For practical purposes, it is especially important that the processes observed are reversible and take place even at room temperature.

Further studies planned in this line of research should provide additional information on the properties of the heterostructures under consideration as applied to the problem of developing corresponding systems for gas analysis.

#### REFERENCES

1. W. Gopel, *Prog. Surf. Sci.* **20**, 9 (1985).
2. *Solid State Gas Sensors*, Ed. by P. T. Moseley and B. C. Tofield (Hilger, Bristol, 1987), p. 51.
3. T. Maekawa, J. Tamaki, N. Miura, and N. Jamazoe, *Chem. Lett.* **4**, 575 (1991).
4. J. Tamaki, T. Maekawa, N. Miura, and N. Jamazoe, *Sens. Actuators* **9**, 197 (1992).
5. A. M. Gas'kov, L. I. Ryabova, M. Labo, *et al.*, *Neorg. Khim.* **41**, 989 (1996).
6. M. A. Lampert and P. Mark, *Current Injection in Solids* (Academic, New York, 1970; Mir, Moscow, 1973).
7. B. A. Akimov, A. V. Albul, A. M. Gas'kov, *et al.*, *Fiz. Tekh. Poluprovodn. (St. Petersburg)* **31**, 400 (1997) [*Semiconductors* **31**, 335 (1997)].

Translated by A. Kazantsev

---

---

LOW-DIMENSIONAL  
SYSTEMS

---

---

# Suppression of Dome-Shaped Clusters During Molecular Beam Epitaxy of Ge on Si(100)

A. A. Tonkikh<sup>1,2\*</sup>, G. E. Cirilin<sup>1,2</sup>, V. G. Dubrovskii<sup>2</sup>, V. M. Ustinov<sup>2</sup>, and P. Werner<sup>3</sup>

<sup>1</sup>*Institute of Analytical Instrument Making, Russian Academy of Sciences, St. Petersburg, 198103 Russia*

<sup>\*</sup>*e-mail: alex234@newmail.ru*

<sup>2</sup>*Ioffe Physicotechnical Institute, Russian Academy of Sciences, St. Petersburg, 194021 Russia*

<sup>3</sup>*Max Planck Institute for Microstructure Physics, Halle/Saale, Weinberg 2, D-06120 Germany*

Submitted February 11, 2004; accepted for publication February 16, 2004

**Abstract**—Morphological properties of Ge nanoscale island arrays formed on the Si(100) surface during molecular beam epitaxy are studied using reflection high-energy electron diffraction and atomic-force microscopy. It is shown that codeposition of Sb and Ge significantly increases the density of final island arrays and suppresses the formation of dome-shaped clusters at substrate temperatures of 550–600°C. The results are discussed in the context of the kinetic model of formation of elastically strained islands in heteroepitaxial systems with a lattice mismatch. © 2004 MAIK “Nauka/Interperiodica”.

## 1. INTRODUCTION

At present, silicon is a base material for the industry of semiconductor devices. Silicon-based planar technology of integrated circuits has achieved significant successes and is constantly improving. However, up to now, fabrication of effective silicon-based light-emitting devices has not been successful. Much effort in this direction is actually being made by many teams using different approaches [1–6]. We believe that the approach based on the use of Si/Ge heterostructures is one of the most promising. For the last 20 years, numerous theoretical and experimental studies have been devoted to this problem. In some theoretical studies [7, 8], the possibility of realizing direct optical transitions in such systems was predicted for structures with small-size germanium clusters embedded into the silicon matrix. Epitaxial technologies, in particular, molecular beam epitaxy (MBE), make it possible to realize such conditions in experiment. When Ge is deposited on the surface of single-crystalline silicon in an ultrahigh vacuum, nanometer islands are formed at the initial stage of the deposition. After these islands are covered with silicon, they can localize charge carriers (holes) in the quantum wells formed by the band offsets at the Si/Ge/Si interfaces. Since the Si/Ge heterojunction is a type-II heterojunction, the electrons can be localized in silicon at the heterointerface [9]. It has previously been established that, when Ge is deposited on the Si(100) surface, islands of two types can be formed: so-called hut-shaped clusters with {105} faces and dome-shaped clusters that are polyhedral islands with {113} faces. The germanium islands have the form of hut clusters for substrate temperatures lower than 600°C; dome-shaped clusters are formed at temperatures above 550°C [10]. In the temperature range 550–

600°C, both phases are observed, hut- and dome-shaped clusters. Classification of the shapes of Ge islands is described in sufficient detail in the review [11].

In addition to the basic problem of attaining direct optical transitions, fabrication of light-emitting devices on the basis of Si/Ge heterostructures requires the preparation of epitaxial layers of high crystallographic quality; namely, it is necessary to avoid the formation of misfit dislocations and to ensure the lowest possible level of background doping. The growth of epitaxial layers at high substrate temperatures (>550°C) makes it possible to lower the background doping to an acceptable level. However, Ge deposition at high substrate temperatures results in formation of large-size dome-shaped islands, so that the carrier localization in such islands is substantially suppressed. In addition, after being covered with silicon, dome-shaped islands can become sources of misfit dislocations [12]. We also note that, in the temperature range of 550–600°C, the scatter in the Ge-island size in the hut-cluster phase and also in the island size of all Ge islands is large due to the coexistence of the hut and dome phases [11].

In this study, we suggest approaches that make it possible to avoid formation of dome-shaped clusters for Ge deposition on the Si(100) surface at substrate temperatures of 550–600°C. Furthermore, the implemented approaches increase the size uniformity of Ge island arrays and also, in some cases, produce their spatial ordering.

## 2. EXPERIMENTAL

Growth experiments were performed using an MBE Riber Siva-45 installation. Electron beam evaporators served as sources of atomic Si and Ge fluxes. The latter

were monitored by two quadrupole mass spectrometers tuned to the masses 28 (Si) and 74 (Ge). Pregrowth chemical preparation of the silicon surface was performed by the RCA method [13]. The protective oxide layer was removed directly in the growth chamber and before the deposition of the silicon buffer layer with thickness of 100 nm. A Ge layer of equivalent thickness of 0.85 nm was deposited on the silicon buffer layer. Several samples were grown at substrate temperatures in the range from 500 to 600°C, and, in some of the samples under study, germanium deposition was accompanied by exposure of the substrate surface to the Sb flux; for other samples, only Ge was deposited on the Si surface. Observation of patterns of reflection high-energy electron diffraction (RHEED) showed that Ge islands are formed in all samples. After the termination of growth, the samples were cooled to room temperature as rapidly as possible and were removed from the vacuum chamber. Then they were studied by atomic force microscopy (AFM) in a contactless mode using a Digital Instruments atmospheric microscope (USA).

### 3. RESULTS AND DISCUSSION

Direct in situ observations of the variation in RHEED patterns in heteroepitaxial systems with lattice-parameter mismatch make it possible to obtain quantitative information on the instant of transition from the two-dimensional to the three-dimensional growth mechanism [14, 15]. In [14], the dynamics of the RHEED pattern variation for the Ge/Si system over a wide temperature range was analyzed in detail. Applying a method similar to that used in [14] to the Ge/Si and (Ge + Sb)/Si systems, we measured the critical thickness of the germanium wetting layer on silicon in the presence of antimony. Figure 1a shows a typical RHEED pattern in the [011] direction from the Si(100) surface at the instant corresponding to an effective thickness of the Ge layer of 0.7 nm. The substrate temperature was 550°C. In this case, bright reflection spots were indicative of the formation of three-dimensional (3D) islands on the substrate surface. To obtain exact information on the instant of transition from two-dimensional (2D) to 3D growth, we monitored the intensity dynamics of the (01) reflections [14] in the cross section  $A-A'$  indicated in Fig. 1a. In Fig. 1b, we plotted the intensity distribution in the cross section  $A-A'$  of the diffraction pattern at different instants of time. According to the preliminary calibration of the Ge growth rate which was performed by using the transmission electron microscopy of thick (~200 nm) Ge layers, we established that an effective thickness of the Ge layer of 0.66 nm corresponds to time  $t_1$  (curve 1 in Fig. 1b), 0.68 nm to time  $t_2$  (curve 2), and 0.70 nm to time  $t_3$  (curve 3). We note that, in the time interval between  $t_1$  and  $t_3$ , the intensity spectrum for the diffraction pattern in the cross section  $A-A'$  is transformed, indicating the formation of Ge islands on the surface of the wetting Ge layer. Thus, for the Ge/Si system with a substrate

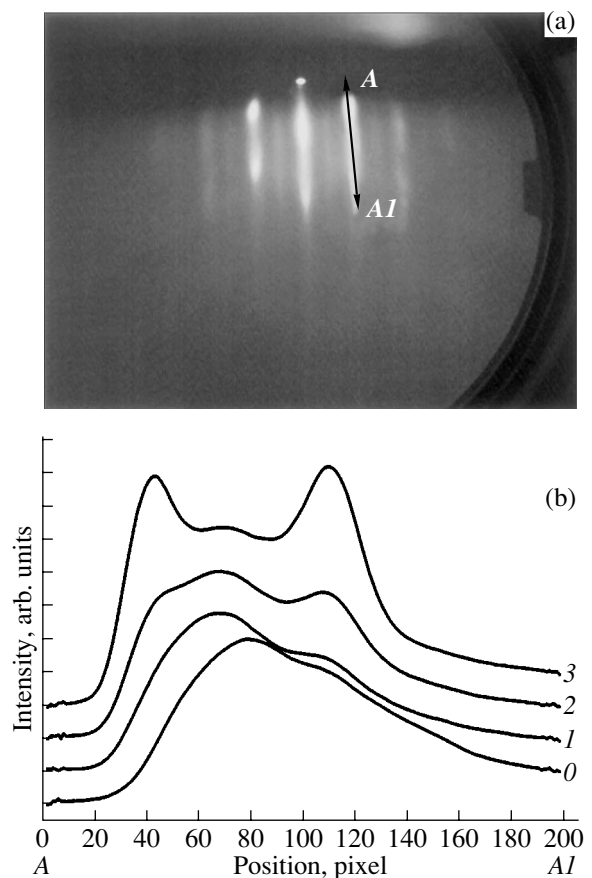


**Fig. 1.** (a) The RHEED image of the Si surface covered with a 0.7-nm Ge layer and (b) the intensity distribution in the RHEED pattern at different points in time in the  $A-A'$  cross section (see Fig. 1a) for an effective Ge thickness of (0) 0, (1) 0.66, (2) 0.68, and (3) 0.70 nm.

temperature of 550°C and Ge growth rate of 0.02 nm/s, the critical thickness of transition from 2D to 3D growth was determined with an accuracy of  $\pm 0.02$  nm, i.e., 0.14 monolayers (ML). A similar approach was applied to the measurement of the critical thickness in the (Ge + Sb)/Si system for two Ge growth rates. For a growth rate of 0.02 nm/s, the transition was observed at an effective Ge thickness of 0.60 nm, and for a rate of 0.002 nm/s, it was observed at an effective thickness of 0.51 nm. Thus, we established that, in the presence of Sb, Ge islands are formed earlier, all other factors being the same. We note that, for the Si(111) orientation and under certain conditions of growth and surface exposition to the Sb flux, no formation of Ge islands on the surface was observed and the stress relaxation was due to the generation of dislocations [16, 17].

Figure 2a shows an AFM image of the Si(100) surface with Ge islands. Germanium was deposited on the Si substrate at a rate of 0.02 nm/s at a temperature of 550°C. The islands have rectangular and square bases. The average island height is 1.8 nm. These islands are typical hut-shaped clusters [11]. Figure 2b shows the

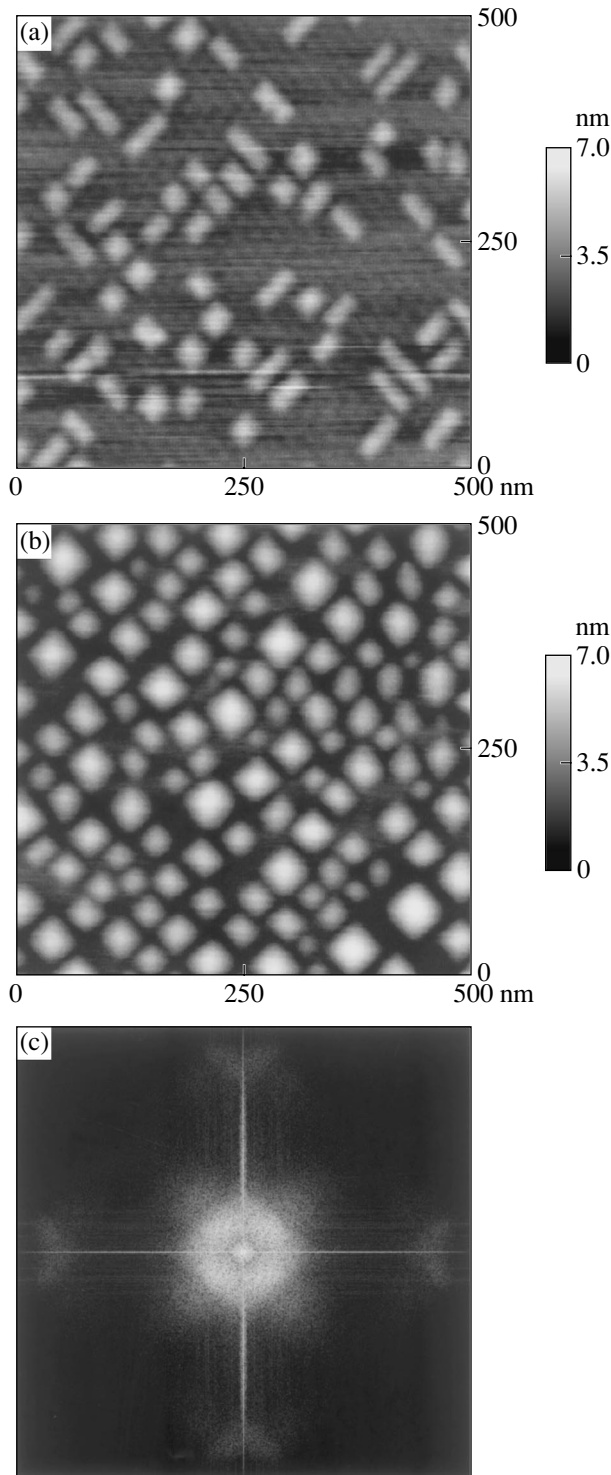


**Fig. 2.** AFM images of a 0.85-nm Ge layer on the Si surface. (a) Ge deposited at a substrate temperature of 550°C at a rate of 0.02 nm/s, (b) Ge codeposited with Sb at a substrate temperature of 550°C at a rate of 0.02 nm/s, and (c) the Fourier transform of the AFM image (b).

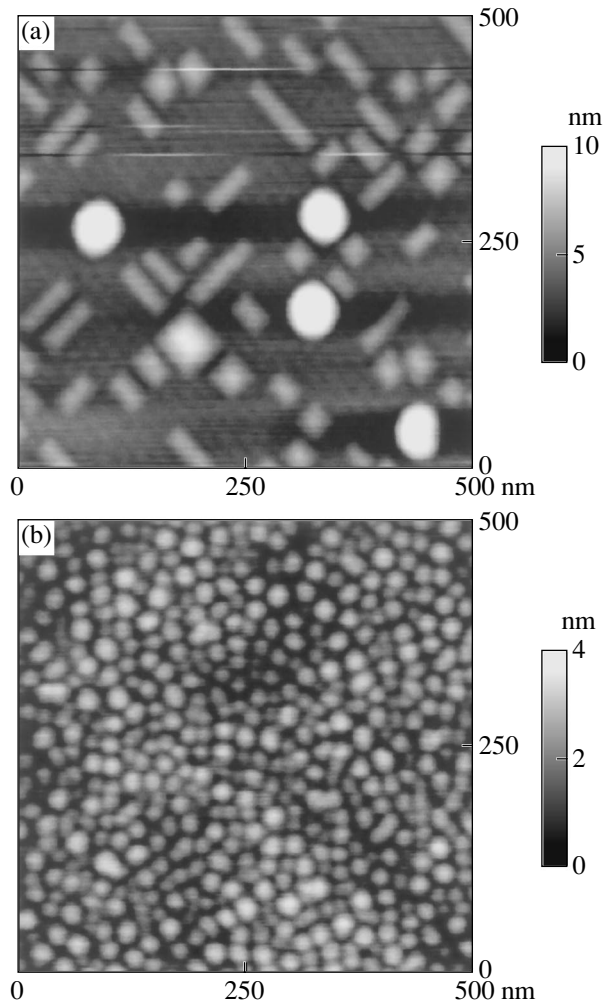
AFM image of the Si surface covered with Ge islands, which also have been formed at a substrate temperature of 550°C and a deposition rate of 0.02 nm/s; however,

during germanium deposition, the substrate surface was exposed to an antimony flux. The temperature of the Sb source was 450°C, which corresponded to an effective deposition rate of 0.2 ML/s (1 ML contains  $6.8 \times 10^{14} \text{ cm}^{-2}$  atoms [18]). Preliminary observations of RHEED patterns during direct prolonged deposition of Sb on the Si(100) surface heated to 550°C showed that there were no changes in the shape and position of RHEED reflections, which was indicative of desorption of Sb atoms/molecules. Nevertheless, in [18, 19], it is shown that antimony is present on the silicon surface. It has been established [18] that the Sb adhesion factor on the silicon surface in a temperature range of 550–600°C is unity for covering layer thicknesses  $<0.7$  ML. With increasing thickness of the covering layer, the adhesion factor rapidly decreases and vanishes at a thickness of 1 ML [18, 19].

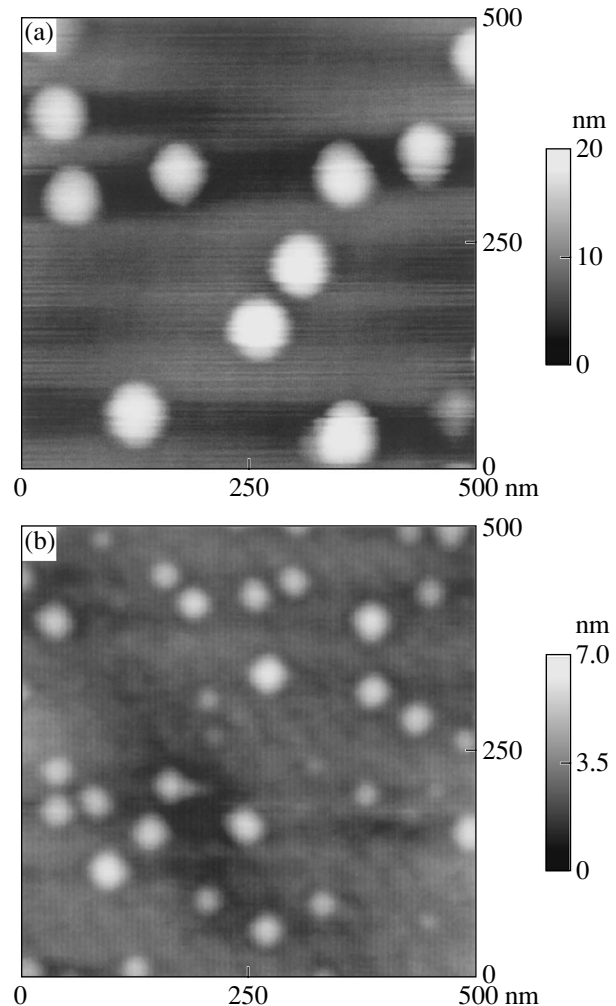
Comparing Figs. 2a and 2b, we note that the morphologies of the arrays of Ge islands are substantially different. First, in the presence of Sb, the hut phase of Ge islands completely disappears from the surface. Second, the average island size increases: the side of the pyramid base attains 40 nm and the pyramid height becomes 3 nm. Thus, the faces of the pyramids have indices  $\{106\}$ . We cannot consider such islands as dome phase, since we have not observed the multifaceted structure of the pyramid faces in the RHEED patterns. Furthermore, in Fig. 2c, we show the Fourier transform of the AFM image (Fig. 2b) of the Si surfaces with Ge islands codeposited with Sb. Figure 2c indicates that the objects of square shape (in our case, the Ge islands) are ordered in real space in the crystallographic  $\langle 010 \rangle$  directions.

Figure 3a shows the AFM image of the Si(100) surface with Ge deposited at a temperature of 550°C and a rate of 0.002 nm/s. We see in the figure that the hut and dome phases coexist on the surface. The observed shape and size distribution is typical of the given temperature range [11]. The situation becomes radically different if Sb is added to the Ge/Si system. Figure 3b shows the Si surface on which Ge was codeposited with Sb. In this case, the islands have the following dimensions: the side of the pyramid base is 24.0 nm and the pyramid height is 2.6 nm. The density of the island array is high and equal to  $1.4 \times 10^{11} \text{ cm}^{-2}$ . It is important to note that, if Sb is present on the Si surface, the island dimensions are relatively small and the shape of all islands in the array is pyramidal.

In Fig. 4a, the AFM image of the Si(100) surface with Ge deposited at 600°C at a rate of 0.02 nm/s is shown. We note that, in this case, there is only the dome phase on the surface and the density of the island array is lower compared to the sample deposited under the same conditions but at 550°C. Figure 4b shows the surface of a structure whose difference from the previous one consists in the presence of Sb on the substrate surface during Ge deposition. We note that, in the latter case, the dome phase is not observed. The spread in the



**Fig. 3.** AFM images of a 0.85-nm Ge layer on the Si surface. (a) Ge deposited at a substrate temperature of 550°C at a rate of 0.002 nm/s and (b) Ge codeposited with Sb at a substrate temperature of 550°C at a rate of 0.002 nm/s.



**Fig. 4.** AFM images of a 0.85-nm Ge layer on the Si surface. (a) Ge deposited at a substrate temperature of 600°C at a rate of 0.02 nm/s and (b) Ge codeposited with Sb at a substrate temperature of 600°C at a rate of 0.002 nm/s.

island sizes is appreciable, the lateral island size does not exceed 40.0 nm, and the height is smaller than 2.5 nm.

We note that, in all cases where Ge deposition was accompanied by exposition of the substrate surface to Sb, the density of the Ge island array was higher than that in the corresponding samples that were grown in the absence of Sb by no less than 60%. Our experimental results show that the increase in the rate of Ge deposition and the codeposition of Sb and Ge suppress the formation of dome-shaped clusters on the Si surface and also generate a dense ensemble of clusters with almost the same sizes. In the case of deposition of pure Ge, hut-shaped clusters with {105} sides are formed. If Sb impurity is added, the cluster faces are oriented in the {106} directions. In both cases, the characteristic lateral cluster size is at least two times smaller than the characteristic size of dome-shaped clusters formed for the same values of the effective thickness and surface temperature for low Ge deposition rates in the absence of Sb.

The above results can be interpreted in the context of the kinetic model of formation of elastically strained islands in a heteroepitaxial systems with lattice mismatch [20–22]. The kinetic model predicts the increase in the surface island density and decrease in their size with increasing material deposition rate for the same surface temperature and effective thickness of the deposited layer. In the system under study, the increase in the growth rate produces an increase in the density of cluster nucleation centers of fluctuation origin; at the same time, the characteristic size to which clusters have time to grow before the Ge source is switched off remains quite small and no dome-shaped clusters appear. An addition of Sb impurity changes both the energy and the kinetic properties of the system [23]. First, the diffusion length for atoms on the surface decreases, thus decreasing the growth rate of clusters compared to the case of pure Ge deposition. Second, the activation barrier for cluster nucleation decreases,



thus increasing (with other factors being the same) their number, decreasing the average size, and decreasing the critical thickness for island formation, in agreement with experimental observations. A detailed analysis of the dependence of the scatter in size and degree of ordering of the nanoisland ensemble under study on the Ge growth rate and on the Sb concentration will be published in a separate communication.

#### 4. CONCLUSIONS

We can make the following conclusions from the analysis of the above results. The system of Ge (Sb) islands on the Si surface is a new phase of the heteroepitaxial Ge/Si system, whose most important properties are ordering of the island shapes (on the Si surface, there are only pyramidal islands with square bases and there is no multifaceted face structure) and a substantial increase in the surface density. In some cases, island ordering in the  $\langle 010 \rangle$  crystallographic directions with the resulting formation of a two-dimensional lattice on the surface of the wetting Ge layer is observed. The suggested methods for depositing an array of islands of the same shape can form a basis for the development of optoelectronic devices and silicon-based multispikes cathodes.

#### ACKNOWLEDGMENTS

We thank V.É. Ptitsyn for useful discussions of the results. This study was supported by the scientific programs of the Ministry of Industry, Science, and Technology of the Russian Federation and the Russian Foundation for Basic Research. G.E. Cirlin also thanks the Alexander von Humboldt Stiftung.

#### REFERENCES

1. V. G. Shengurov, S. P. Svetlov, V. Yu. Chalkov, *et al.*, *Fiz. Tekh. Poluprovodn. (St. Petersburg)* **36**, 662 (2002) [*Semiconductors* **36**, 625 (2002)].
2. M. Stoffel, U. Denker, and O. G. Schmidt, *Appl. Phys. Lett.* **82**, 3236 (2003).
3. V. G. Talalaev, G. E. Cirlin, A. A. Tonkikh, *et al.*, *Phys. Status Solidi A* **198**, R4 (2003).
4. L. X. Yi, J. Heitmann, R. Scholz, and M. Zacharias, *Appl. Phys. Lett.* **81**, 4248 (2002).
5. K. K. Linder, J. Phillips, O. Qasimeh, *et al.*, *Appl. Phys. Lett.* **74**, 1355 (1999).
6. G. Dehlinger, L. Diehl, U. Gennser, *et al.*, *Science* **290**, 2277 (2000).
7. T. Takagahara and K. Takeda, *Phys. Rev. B* **46**, 15578 (1992).
8. S. Y. Ren, *Solid State Commun.* **102**, 479 (1997).
9. A. V. Dvurechenskii and A. I. Yakimov, *Fiz. Tekh. Poluprovodn. (St. Petersburg)* **35**, 1143 (2001) [*Semiconductors* **35**, 1095 (2001)].
10. N. V. Vostokov, Z. F. Krasil'nik, D. N. Lobanov, *et al.*, *Fiz. Tverd. Tela (St. Petersburg)* **46**, 63 (2004) [*Phys. Solid State* **46**, 60 (2004)].
11. O. P. Pchelyakov, Yu. B. Bolkhovityanov, A. V. Dvurechenskii, *et al.*, *Fiz. Tekh. Poluprovodn. (St. Petersburg)* **34**, 1281 (2000) [*Semiconductors* **34**, 1229 (2000)].
12. C. J. Huang, Y. H. Zuo, D. Z. Li, *et al.*, *Appl. Phys. Lett.* **78**, 3881 (2001).
13. G. E. Cirlin, P. Werner, G. Gösele, *et al.*, *Pis'ma Zh. Tekh. Fiz.* **27**, 31 (2001) [*Tech. Phys. Lett.* **27**, 14 (2001)].
14. V. Cimalla and K. Zekentes, *Appl. Phys. Lett.* **77**, 1452 (2000).
15. G. E. Cirlin, N. P. Korneeva, V. N. Demidov, *et al.*, *Fiz. Tekh. Poluprovodn. (St. Petersburg)* **31**, 1230 (1997) [*Semiconductors* **31**, 1057 (1997)].
16. D. Reinking, M. Kammler, M. Horn-von Hoegen, and K. R. Hofmann, *Appl. Phys. Lett.* **71**, 924 (1997).
17. A. Janzen, I. Dumkow, and M. Horn-von Hoegen, *Appl. Phys. Lett.* **79**, 2387 (2001).
18. S. A. Barnett, H. F. Winters, and J. E. Green, *Surf. Sci.* **165**, 303 (1986).
19. K.-S. Kim, Y. Takakuwa, T. Abukawa, and S. Kono, *J. Cryst. Growth* **186**, 95 (1998).
20. V. G. Dubrovskii, G. E. Cirlin, and V. M. Ustinov, *Phys. Rev. B* **68**, 075409 (2003).
21. A. A. Tonkikh, V. G. Dubrovskii, G. E. Cirlin, *et al.*, *Phys. Status Solidi B* **236**, R1 (2003).
22. V. G. Dubrovskii, Yu. G. Musikhin, G. E. Cirlin, *et al.*, *Fiz. Tekh. Poluprovodn. (St. Petersburg)* **38**, 342 (2004) [*Semiconductors* **38**, 329 (2004)].
23. C. S. Peng, Q. Huang, W. Q. Cheng, *et al.*, *Appl. Phys. Lett.* **72**, 2541 (1998).

*Translated by I. Zvyagin*



---

---

LOW-DIMENSIONAL  
SYSTEMS

---

---

## Effect of Nonradiative Recombination Centers on Photoluminescence Efficiency in Quantum Dot Structures

M. V. Maksimov\*<sup>^</sup>, D. S. Sizov\*, A. G. Makarov\*, I. N. Kayander\*, L. V. Asryan\*, A. E. Zhukov\*,  
V. M. Ustinov\*, N. A. Cherkashin\*, N. A. Bert\*, N. N. Ledentsov\*\*, and D. Bimberg\*\*

\*Ioffe Physicotechnical Institute, Russian Academy of Sciences, St. Petersburg, 194021 Russia

<sup>^</sup>e-mail: maximov@beam.ioffe.ru

\*\*Technische Universität Berlin, Berlin D-10623, Germany

Submitted February 20, 2004; accepted for publication February 26, 2004

**Abstract**—The influence of dislocations on photoluminescence (PL) intensity in structures with InAs–GaAs quantum dots (QD) has been studied. The structural characteristics of samples were studied by transmission electron microscopy in bright-field and weak-beam dark-field diffraction conditions. At temperatures below room temperature and for moderate excitation density, the PL intensity in a structure containing large clusters with dislocations was about the same as in a structure with a significantly lower density of clusters. In contrast, the measurement of PL intensity at elevated temperatures and high excitation densities allows an accurate estimation of the structural perfection of QD structures. The overgrowth of QDs with a thin (1–2 nm) GaAs layer with subsequent annealing reduces the density of clusters with dislocations and significantly improves the temperature stability of the PL intensity. © 2004 MAIK “Nauka/Interperiodica”.

### 1. INTRODUCTION

Light-emitting devices with self-organized quantum dots (QD) is a thriving area of semiconductor physics. QD lasers demonstrate unique characteristics that were earlier predicted by theory: a low threshold current density and high differential efficiency and temperature stability (for review, see [1]). One of the specific properties of QDs compared to quantum well (QW) structures is the possibility of attaining longer emission wavelengths in a given material system, for example, InGaAs–GaAs. To increase the emission wavelength, special growth techniques are used, such as the formation of vertically coupled QDs [2] or an activated decomposition of solid solution [3]. At the same time, the growing of large QDs can be followed by the formation of isolated dislocations in QDs and large clusters with dislocations, which gives rise to nonradiative recombination. These entities significantly impair the characteristics of QD devices. Note that, despite the fact that optical properties of QDs have been extensively studied (see, e.g., [4, 5]), only a small number of publications have been devoted to studying nonradiative processes. In this study, we performed a systematic investigation of the effect of nonradiative recombination centers on the optical properties of QD structures. It is shown that studies at high excitation densities and elevated temperatures are necessary for an adequate estimation of the defect density in these structures.

### 2. EXPERIMENT

The structures for study were grown by MBE on (100) GaAs semi-insulating substrates. After the removal of oxide from the substrate surface, a GaAs buffer layer was grown at 600°C. To prevent the diffusion of nonequilibrium carriers to the substrate, a six-period GaAs(20 Å)/Al<sub>0.25</sub>Ga<sub>0.75</sub>As(20 Å) superlattice was grown on top of the buffer layer. A 0.1-μm-thick GaAs layer was then grown, the substrate temperature was reduced to 480°C, and InAs QDs were deposited and overgrown with a 10-nm-thick GaAs layer at the same temperature. After this, the substrate temperature was increased to 600°C, and a GaAs layer 400 Å thick, a superlattice similar to the lower one, and a thin GaAs capping layer were grown successively.

Quantum dots were grown using the stimulated decomposition of InGaAs solid solution [3]. In this growth mode, the initial QDs, produced by deposition of  $D_{IS}$  InAs monolayers (ML), are overgrown with an In<sub>x</sub>Ga<sub>1-x</sub>As layer with average thickness  $H$  (as a rule,  $D_{IS} = 1.7–3.5$  ML InAs,  $x = 0–0.3$ ,  $H = 0–6$  nm). In the course of overgrowing, it is energetically favorable for In atoms to diffuse toward QDs, whose lattice parameter is closer to that of InAs, whereas it is favorable for Ga atoms to diffuse to regions between QDs, where the lattice parameter is closer to that in a GaAs lattice. This process results in the effective enlargement of the initial QDs and, accordingly, to the red shift of the photoluminescence (PL) line. The fact that QDs are overgrown by an InGaAs layer makes an additional contribution to the red shift of the PL line, due to the decrease in the

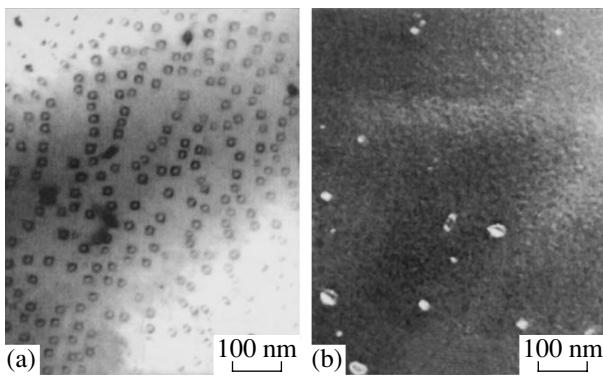


**Fig. 1.** TEM images of structure B: (a) bright-field diffraction conditions and (b) weak-beam dark-field diffraction conditions. The two images show different parts of the sample.

matrix band gap and the redistribution of stress fields within the QDs. The existence of several growth parameters ( $D_{IS}$ ,  $x$ ,  $H$ ) allows us to effectively control the parameters of QD arrays. Specifically, it is possible to obtain an emission wavelength of 1.3  $\mu\text{m}$ , while the structural and optical quality of samples is maintained at a high level [3, 6].

The PL was excited with an Ar-ion laser (wavelength  $\lambda = 514.5$  nm, incident power density  $500$  W  $\text{cm}^{-2}$ ) and recorded using an MDR23 monochromator and North Coast E0/817R Ge  $p$ - $i$ - $n$  photodiode. A Philips EM 420 microscope with 100-kV acceleration voltage was used for transmission electron microscopy (TEM). The samples in planar (001) and transverse (110) and (010) configuration were prepared by the standard technology, i.e., grinding, polishing, and finishing sputtering of the material with  $\text{Ar}^+$  ions at grazing angles to the surface ( $\sim 12^\circ$ – $14^\circ$ ), with an acceleration voltage of 4 keV.

### 3. INFLUENCE OF EXCITATION INTENSITY AND TEMPERATURE ON PHOTOLUMINESCENCE OF STRUCTURES WITH QUANTUM DOTS CONTAINING DEFECTS

The parameters of structures A and B, which were used in the study of the influence of dislocations on the optical properties of QD structures, were (A)  $D_{IS} = 2.6$  ML,  $x = 0.15$ , and  $H = 45$  Å; (B)  $D_{IS} = 3$  ML,  $x = 0.15$ , and  $H = 50$  Å. Thus, the initial QDs used for stimulated decomposition of InGaAs were larger in sample B. The increase in size of initial islands, which stimulates the decomposition of InGaAs, results in an increase in QD size. According to TEM data, the lateral size of dots increased from  $(14.9 \pm 1.5)$  nm in structure A to  $(16.4 \pm 1.6)$  nm in structure B. The density of QDs in structures A and B was  $6.2 \times 10^{10}$  and  $5.5 \times 10^{10}$   $\text{cm}^{-2}$ , respectively.

In addition to QDs, bright-field TEM images demonstrate clusters that are larger than QDs. In these clusters, stress relaxation occurs via plastic deformation, i.e., owing to the formation of dislocations. To deter-

mine more accurately the density of clusters with dislocations, we studied structures A and B in the weak-beam dark-field diffraction conditions corresponding to  $(\mathbf{g}; +2\mathbf{g})$ , where the diffraction vector  $\mathbf{g} = (220)$ . Figures 1a and 1b show a comparison of TEM images of structure B obtained in bright-field and weak-beam dark-field diffraction conditions, respectively (these images show different parts of the sample). The weak-beam study of dislocations in a crystal structure is a standard method of electron microscopy that has several advantages over bright-field diffraction conditions. When the image is obtained in weak-beam dark-field diffraction conditions, a sample strongly deviates from the exact Bragg position, so an error in the excitation of the diffracted beam is rather large. However, near the dislocation core the Bragg conditions are satisfied owing to the bending of crystal planes, which results in a strong reflection of the diffracted beam. A dislocation is pictured as a bright line on the dark background of the other part of the sample. Therefore, dark-field images in the weak-beam mode allow better visualization of dislocations compared with images obtained in bright-field diffraction conditions. The regions with dislocations can be seen in Fig. 1b as bright regions, which is typical of dislocation loops. The density of dislocations in structures A and B was  $1.3 \times 10^9$  and  $2.2 \times 10^9$   $\text{cm}^{-2}$ , respectively. Note that the dislocation loops in sample A were significantly smaller than those in sample B.

Owing to the larger size of QDs, the wavelength of the PL spectral peak reached in sample B is longer than that in sample A (the red shift of the PL line is  $\sim 30$  meV). At the same time, in the given growth conditions the increased size of the initial QDs and the corresponding red shift are accompanied by the formation of large clusters with dislocations, as mentioned above, and an increase in the dislocation density per QD sheet, i.e., by considerable degradation of the crystal perfection. It is interesting to note that, as the amount of deposited In (the values of  $D_{IS}$  and  $x$ ) increases further, the red shift is saturated, whereas the density of dislocations continues to increase. This effect has been observed and studied in detail in [3, 6].

At room temperature and an excitation density of  $100$  W  $\text{cm}^{-2}$ , both structures demonstrate nearly the same PL intensity (Fig. 2a), despite the worse crystal perfection of structure B. Figure 2b shows PL spectra of the samples under study for an excitation density of  $5000$  W  $\text{cm}^{-2}$ . In these conditions, the PL intensity in structure A is much higher than that in structure B. Owing to the high excitation density, the intensity of the PL line of the QD ground state in structure A is saturated, and the spectral line of the first excited state becomes dominant. In contrast, in structure B the intensity of the PL line of the ground state is not saturated. This fact can be explained by the difference in “effective” intensities of optical excitation for structures A and B. In structure B, some of the excited carriers are lost in nonradiative processes, and the number of carriers that can be trapped by QDs is reduced.

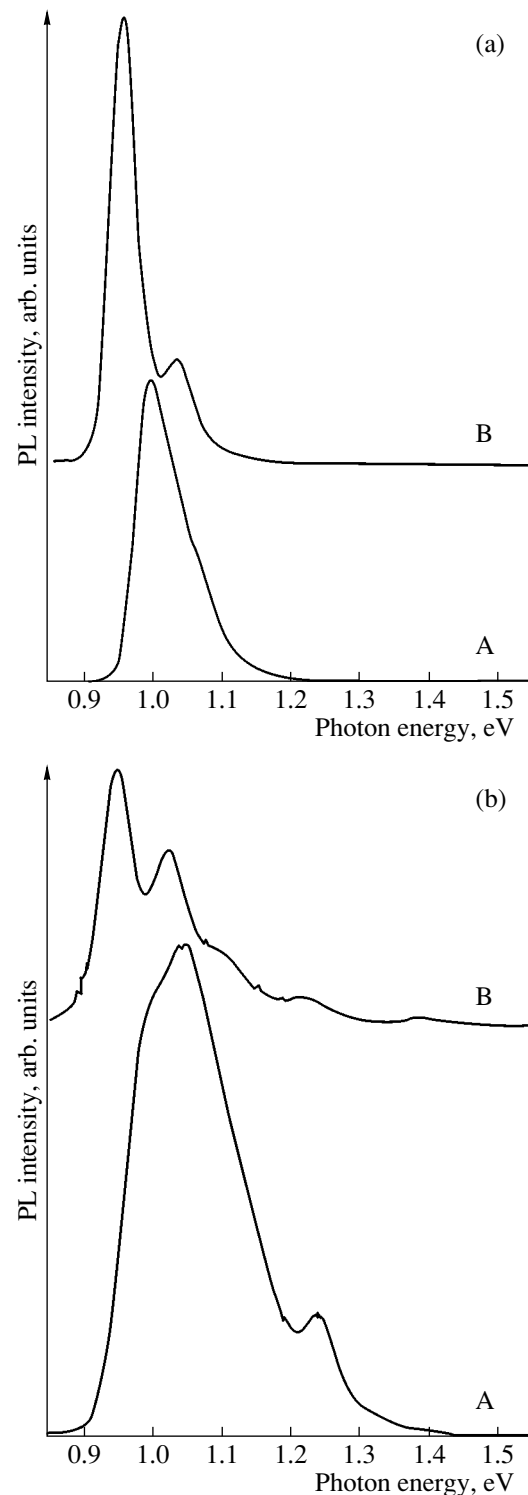
We also studied the structural and optical quality of samples C and D, which were grown under conditions that were optimized compared to those for structures A and B (growth rate, As pressure). The parameters used at the deposition of both structures, C and D, were  $D_{IS} = 3.0$  ML,  $x = 0.13$ , and  $H = 50$  Å. To reduce the density of clusters with dislocations, the QDs in structure D were specially annealed in the course of growth: QDs were overgrown by a thin (1 nm) GaAs layer at  $480^\circ\text{C}$ , and then the substrate temperature was increased to  $600^\circ\text{C}$ . In this case, large clusters that are not completely covered by GaAs evaporate, and the structure is annealed [7]. During annealing, the shape and size of coherent (elastically stressed) QDs remain virtually unchanged. A TEM study of structures C and D was performed only in bright-field diffraction conditions. The density of dislocations in sample C, which was grown in optimized mode, was lower than that in sample A. In structure D, which was grown with annealing during the course of growth, no entities with dislocations were found in the study under bright-field diffraction conditions.

Figure 3a shows PL spectra of structures C and D. In the same figure, we present the PL spectrum of structure E with QDs produced by the deposition of 2.2 ML GaAs (without overgrowing by an InGaAs layer). Since the size of the QDs in structure E is significantly smaller than in structures A–D, it can be assumed that isolated dislocations in QDs and large clusters with dislocations are absent in this structure. At room temperature and an excitation density of  $5000\text{ W cm}^{-2}$ , the integral PL intensity in structure C is smaller than that in structure D by a factor of  $\sim 1.5$ , which correlates with the TEM data and can be attributed to the greater number of QD sheets in structure D.

At the same time, to obtain a more objective estimation of the defect and dislocation density in QD structures from optical studies, it is desirable to create experimental conditions in which the difference between the intensities in samples of different crystal perfection will be as large as possible. This is especially important for samples grown in different series, because a small difference in the PL intensity can be related to incidental factors, such as the purity of materials in the MBE installation. Figure 3b shows PL spectra of structures C, D, and E recorded at  $140^\circ\text{C}$ . At this temperature, the difference between the integral PL intensities of structures increases to the factor of 11. As can be seen in Fig. 4, the difference in integral PL intensities steadily increases as temperature increases. It is noteworthy that in structure E, which is free of dislocations, there is practically no decrease in integral intensity as the temperature increases.

#### 4. DISCUSSION

According to our data, the presence of dislocations with density  $<(2-3) \times 10^9\text{ cm}^{-2}$  in a QD structure does not cause a significant decrease in the integral PL intensity at moderate excitation density ( $0.1-500\text{ W cm}^{-2}$ )



**Fig. 2.** PL spectra of structures A and B recorded at room temperature at an excitation density of (a) 100 and (b)  $5000\text{ W cm}^{-2}$ .

and relatively low temperatures ( $<300\text{ K}$ ). This fact was published in [8], where the authors studied the luminescence of QDs grown on a commercial GaAs substrate and on a Si substrate with a deposited GaAs layer. Due

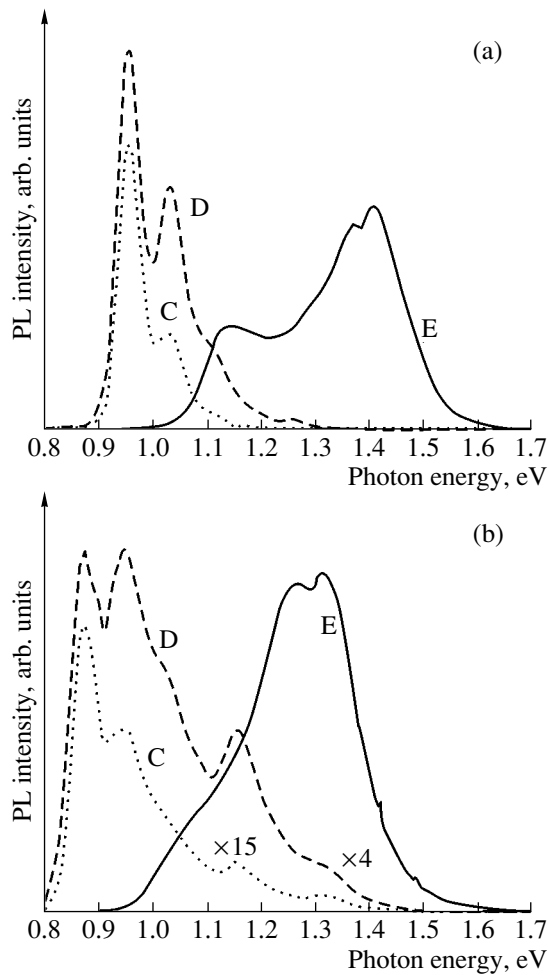


**Fig. 3.** PL spectra of structures C, D, and E at temperatures of (a) 20 and (b) 140°C. Excitation density, 5000 W cm<sup>-2</sup>.

to lattice mismatch between GaAs and Si, the density of dislocations in the GaAs buffer layer on Si exceeded  $1 \times 10^7$  cm<sup>-2</sup> (in this case, the density of dislocations was determined by chemical etching of the sample). It was shown that the PL intensity in both structures was nearly the same at quite low temperatures and excitation densities. At the same time, the PL intensity from an InGaAs QW grown on a Si substrate was significantly smaller than that from a QW grown on a GaAs substrate. Note that the lasing in a QD laser grown on a Si substrate was observed only at liquid nitrogen temperature, and the threshold current density was very high (3.8 kA cm<sup>-2</sup>) [9]. Thus, the high PL efficiency at moderate excitation density and relatively low temperatures is not a sufficient condition for obtaining low threshold current density in a laser based on such QDs.

The conventional qualitative explanation for the low sensitivity of the PL efficiency in QD structures to the presence of dislocations is as follows: the capture of carriers in a QD is a very fast process [10], and their localization with respect to the wetting layer and GaAs matrix is very effective (especially in large QDs). At

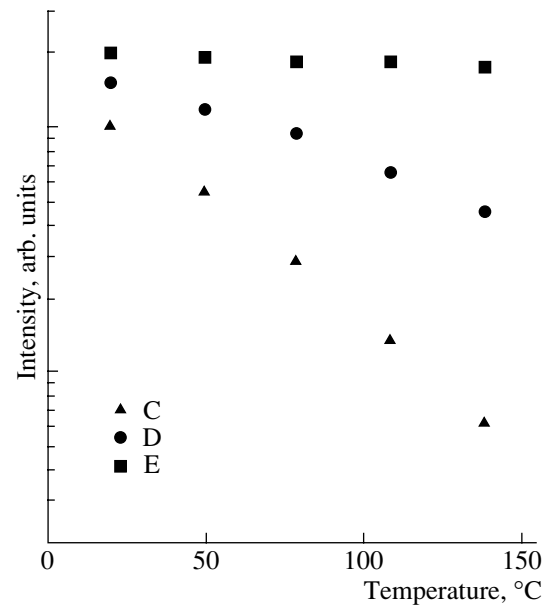


**Fig. 4.** Temperature dependences of integral PL intensity for samples C, D, and E. Excitation density, 5000 W cm<sup>-2</sup>.

moderate excitation densities and relatively low temperatures, the density of carriers in the wetting layer and GaAs matrix, which could diffuse to dislocations, is quite low. Therefore, carriers within QDs “do not feel” dislocations, and standard experimental conditions give no way of estimating the perfection of a crystal structure. To provide higher occupancy in the wetting layer and GaAs matrix and, accordingly, to enhance the lateral transport toward defects and dislocations, it is necessary to apply high excitation densities and/or high temperatures, which is confirmed by our experimental data. At the same time, the argumentation given above is too general; to optimize QD structures, it is desirable to have a more precise quantitative description of nonradiative recombination that would allow the simulation of PL spectra dependences on temperature and excitation.

The data obtained in TEM and optical studies suggest that at least two types of nonradiative recombination centers exist in QD structures.

The first type is clusters with dislocations, which are seen in TEM images (Fig. 1). In general case, the rate of nonradiative recombination integrated over spectrum can be represented as

$$R_{nr}^{\text{cluster}} = \frac{N_t f_t}{\tau_t}, \quad (1)$$

where  $N_t$  is the surface (2D) density of centers;  $\tau_t$ , the characteristic time of recombination via a center; and  $f_t$ , the occupancy of these centers. At a high density of optical excitation,  $f_t$  tends to unity, and, accordingly, the rate of nonradiative recombination tends to  $N_t/\tau_t$ . In other words, at a sufficiently high excitation density in a structure with a lower dislocation density, the rate of

nonradiative recombination is saturated and, accordingly, the PL intensity increases faster, which is observed experimentally. If a structure is in thermal equilibrium (i.e., a quasi-Fermi level defined by the excitation density exists) and the energy level related to the centers is known,  $f_i$  is described by the Fermi function. The dependence of the quasi-Fermi level on the excitation density can be calculated in terms of the model [11], and the density of defects can be determined from the TEM data. Therefore, the value of  $\tau_i$  can in principle be determined from the experimentally measured saturated rate of nonradiative recombination.

The second type of centers is the defects located in the vicinity of QDs in the wetting layer and/or in GaAs. In general, the rate of nonradiative recombination via defects in the 2D wetting layer and in the bulk of GaAs has the form

$$R_{nr}^{2D} = \frac{n^{2D}}{\tau_{nr}^{2D}}, \quad (2)$$

$$R_{nr}^{3D} = b \frac{n}{\tau_{nr}^{3D}}, \quad (3)$$

where  $n^{2D}$  is the 2D density of carriers in the wetting layer;  $n$ , the density of carriers in the bulk of GaAs;  $\tau_{nr}^{2D}$ , the characteristic time of nonradiative recombination via centers in the wetting layer;  $\tau_{nr}^{3D}$ , the characteristic time of nonradiative recombination via centers in GaAs; and  $b$ , the thickness of the GaAs layer. As temperature increases, the carrier densities in the wetting layer and GaAs increase, which results in an increase in the rate of nonradiative recombination. At the same time, note that if defects in the structure existed only in the wetting layer and GaAs, the rate of nonradiative recombination would not be saturated when the excitation density increased. The difference in the PL intensities of structures that differ in crystal perfection should be especially marked at very low, rather than at very high, excitation densities. In our experiments, the minimum density of excitation was limited by the sensitivity of the recording system. Preliminary experiments with relatively low ( $\sim 0.5 \text{ W cm}^{-2}$ ) excitation density were not informative for estimating the crystal perfection of the samples. We are currently preparing studies with lower ( $< 0.05 \text{ W cm}^{-2}$ ) excitation densities at elevated temperatures, which may broaden our understanding of nonradiative recombination processes in QD structures.

The presence of several channels of nonradiative recombination complicates the interpretation of the results of optical experiments considerably. To obtain an adequate description of the PL dependences on temperature and excitation in QD structures, we are planning to independently determine the nature and density of dislocations and their energy spectrum by electron microscopy, capacitance spectroscopy, and DLTS. Theoretical modeling is very important in order to understand the optical properties of QD laser structures. The

theoretical description of radiative processes in QD structures has now been rather well developed [4, 11]. It was shown that, taking into account nonradiative recombination in QD lasers even in terms of a very simple model, it is possible to obtain considerably better agreement with the experimental data [12]. A more detailed consideration of nonradiative recombination may significantly improve our understanding of the optical properties of QD structures.

## 5. CONCLUSIONS

The influence of isolated dislocations and large clusters with dislocations on PL intensity in QD structures has been studied. The data obtained suggest that, in the presence of nonradiative recombination channels, the dependences of PL intensity on temperature and excitation are complicated and strongly nonlinear. Specifically, it is shown that, below room temperature and at a moderate excitation density ( $0.5\text{--}500 \text{ W cm}^{-2}$ ), structures with a large difference in the density of clusters with dislocations can exhibit virtually the same PL intensity. In contrast, measurements at a high excitation density ( $5000 \text{ W cm}^{-2}$ ) and at elevated temperatures ( $140^\circ\text{C}$ ) make it possible to estimate the crystal quality of a sample.

## ACKNOWLEDGMENTS

This study was supported by the Russian Foundation for Basic Research, the program "Physics of Solid-State Nanostructures," and INTAS.

## REFERENCES

1. N. N. Ledentsov, IEEE J. Sel. Top. Quantum Electron. **8**, 1015 (2002).
2. N. N. Ledentsov, V. A. Shchukin, M. Grundmann, *et al.*, Phys. Rev. B **54**, 8743 (1996).
3. M. V. Maximov, A. F. Tsatsul'nikov, B. V. Volovik, *et al.*, Phys. Rev. B **62**, 16671 (2000).
4. D. Bimberg, M. Grundman, and N. N. Ledentsov, *Quantum Dot Heterostructures* (Wiley, Chichester, 1999).
5. M. Grundmann, *Nano-Optoelectronics: Concepts, Physics and Devices* (Springer, Berlin, 2002).
6. B. V. Volovik, A. F. Tsatsul'nikov, D. A. Bedarev, *et al.*, Fiz. Tekh. Poluprovodn. (St. Petersburg) **33**, 990 (1999) [*Semiconductors* **33**, 901 (1999)].
7. N. N. Ledentsov, M. V. Maximov, D. Bimberg, *et al.*, Semicond. Sci. Technol. **15**, 604 (2000).
8. J. M. Jerard, O. Cabrol, and B. Sermage, Appl. Phys. Lett. **68**, 3123 (1996).
9. K. K. Linder, J. Phillips, O. Qasaimeh, *et al.*, Appl. Phys. Lett. **74**, 1355 (1999).
10. L. A. Graham, D. L. Huffaker, and D. G. Deppe, Appl. Phys. Lett. **74**, 2408 (1999).
11. L. V. Asryan and R. A. Suris, Semicond. Sci. Technol. **11**, 554 (1996).
12. M. V. Maximov, L. V. Asryan, Yu. M. Shernyakov, *et al.*, IEEE J. Quantum Electron. **37**, 676 (2001).

*Translated by D. Mashovets*

## LOW-DIMENSIONAL SYSTEMS

# Calculation of the Thermoelectric Figure of Merit for Multilayer Structures with Quantum Wells in the Case of Carrier Scattering by Polar Optical Phonons

D. A. Pshenai-Severin\* and Yu. I. Ravich\*\*

\*Ioffe Physicotechnical Institute, Russian Academy of Sciences, St. Petersburg, 194021 Russia

\*\*St. Petersburg State Technical University, St. Petersburg, 195251 Russia

Submitted January 21, 2004; accepted for publication March 3, 2004

**Abstract**—The increase in the thermoelectric figure of merit in layered structures with quantum wells is calculated for the case of polar charge-carrier scattering by optical phonons. On the basis of previous and new calculations, it is concluded that the quantum confinement effect can give rise to the increase in the figure of merit only if the probability of carrier scattering decreases with increasing wave vector transfer. © 2004 MAIK “Nauka/Interperiodica”.

### 1. INTRODUCTION

The study of thermoelectric properties of structures with quantum confinement was initiated by Hicks and Dresselhaus [1–3], who performed calculations and estimates of the thermoelectric figure of merit  $Z$  of a layered structure with quantum wells (QWs). They have shown that the increase in the density of states due to quantum confinement produces an increase in the figure of merit of such structures by a factor of 2–3 compared to the bulk value provided that the carrier mobility does not change when we pass from a bulk sample to a sample with QWs.

At the same, it has been shown time in a number of studies [4–8] that an increase in the density of states in the structures with quantum confinement, which is the main cause of the increase in the thermoelectric figure of merit, can simultaneously result in the decrease in charge carrier mobility. In particular, in the case of scattering by acoustic phonons and by a short-range impurity potential in the elementary model with a standard carrier dispersion law, our analytical calculations [8] have shown that the expressions for the thermoelectric figure of merit in a bulk sample and in a sample with QWs coincide exactly. The values of the thermoelectric figures of merit in both cases are equal if we choose chemical potentials from the maximization condition for the figure of merit.

If the charge carriers are scattered by acoustic phonons and a short-range impurity potential, the matrix element is independent of the difference of wave vectors of electrons in the final and initial states; however, for scattering by polar optical lattice vibrations, such a dependence exists. In [8], when calculating the relaxation time in a sample with QWs for this scattering mechanism, the accuracy of treating the effect of the dependence of the matrix element on the transferred

momentum in the integrand was insufficient. Therefore, in the case of polar scattering, the result of [8] is correct only for rather large QW widths, and for small QW widths, it should be corrected. In this study, we use the model [8] that is based on the assumption of an isotropic parabolic spectrum of charge carriers and takes polar scattering of charge carriers by optical phonons of the bulk type into account and describe the effect of quantum confinement on the relaxation time and thermoelectric figure of merit in layered structures with QWs more accurately. In addition, we compare the dependence of the figure of merit on the QW width in the case under consideration with that obtained by using the assumption [1] of the invariance of the relaxation time with respect to the bulk value.

### 2. RELAXATION TIME

Above the Debye temperature, the scattering by optical phonons is elastic, and the relaxation time in a structure with QWs  $\tau_{2D}$  is given by the following expression:

$$\tau_{2D}^{-1} = \sum_q \frac{2\pi}{\hbar} |M_{\mathbf{k}_\parallel, \mathbf{k}_\parallel + \mathbf{q}_\parallel}|^2 \frac{\mathbf{k}_\parallel \mathbf{q}_\parallel}{k_\parallel^2} \delta(\varepsilon(\mathbf{k}_\parallel + \mathbf{q}_\parallel) - \varepsilon(\mathbf{k}_\parallel)) - \sum_q \frac{2\pi}{\hbar} |M_{\mathbf{k}_\parallel, \mathbf{k}_\parallel - \mathbf{q}_\parallel}|^2 \frac{\mathbf{k}_\parallel \mathbf{q}_\parallel}{k_\parallel^2} \delta(\varepsilon(\mathbf{k}_\parallel - \mathbf{q}_\parallel) - \varepsilon(\mathbf{k}_\parallel)). \quad (1)$$

Here,  $\hbar$  is Planck's constant,  $\mathbf{q}$  is the phonon wave vector,  $\mathbf{q}_\parallel$  is the component of the phonon wave vector in the layer plane,  $M_{\mathbf{k}_\parallel, \mathbf{k}_\parallel \pm \mathbf{q}_\parallel}$  is the matrix element for electron scattering from the state with wave vector  $\mathbf{k}_\parallel$  in the layer plane to the state with wave vector  $\mathbf{k}_\parallel \pm \mathbf{q}_\parallel$  accompanied by phonon absorption or emission,

$\delta$  function takes into account the energy conservation for elastic scattering, and  $\epsilon(\mathbf{k}_{\parallel})$  is the electron energy related to the motion in the layer plane and measured from the edge of the confinement subband. In this case, the scattering matrix element is given by [8]

$$M_{\mathbf{k}_{\parallel}, \mathbf{k}_{\parallel} + \mathbf{q}_{\parallel}} = M(q)Y^{\pm}(q_z^*), \quad (2)$$

where  $M(q)$  is the well-known matrix element for polar scattering in a bulk sample and the factor  $Y^{\pm}(q_z^*)$  appears in the calculation of the matrix element when integrating with respect to the coordinate  $z$  directed normally to the layer plane,

$$Y^{\pm}(q_z^*) = \frac{\exp(\pm i\pi q_z^*) \sin \pi q_z^*}{\pi q_z^* (1 - q_z^{*2})}. \quad (3)$$

Here, the dimensionless quantity  $q_z^*$  is proportional to the component of the phonon wave vector  $q_z$  normal to the layer plane,

$$q_z^* = \frac{aq_z}{2\pi}. \quad (4)$$

In expression (1), we pass from summation to integration in the cylindrical system of coordinates, with the cylindrical axis directed along the  $z$  axis and the azimuthal angle  $\phi$  measured from the direction of the wave vector  $\mathbf{k}_{\parallel}$ . Then, writing out explicitly the dependence of the bulk matrix element on the phonon wave vector,  $M^2(q) = M^2(k_{\parallel})k_{\parallel}^2/q^2$ , we obtain

$$\begin{aligned} \tau_{2D}^{-1} &= \frac{2\pi M^2(k_{\parallel})Vm^*}{\hbar 8\pi^3 \hbar^2} \int_{-\infty}^{\infty} dq_z \int_0^{2k_{\parallel}} q_{\parallel} dq_{\parallel} \\ &\times \int_0^{2\pi} d\phi \left[ \frac{\cos \phi}{q^2} \left\{ |Y^+(q_z^*)|^2 \delta\left(\frac{q_{\parallel}}{2k_{\parallel}} + \cos \phi\right) \right. \right. \\ &\quad \left. \left. - |Y^-(q_z^*)|^2 \delta\left(\frac{q_{\parallel}}{2k_{\parallel}} - \cos \phi\right) \right\} \right], \end{aligned} \quad (5)$$

where  $V = Sa$  is the volume of the layer corresponding to a QW for electrons, and  $m^*$  is the electron effective mass.

Integrating first with respect to the angle  $\phi$  (using  $\delta$  functions) and then with respect to  $q_{\parallel}$ , we obtain the expression for the inverse relaxation time,

$$\begin{aligned} \tau_{2D}^{-1} &= \frac{2\pi M^2(k_{\parallel})Vm^*}{\hbar 8\pi^3 \hbar^2} \\ &\times \int_{-\infty}^{\infty} Y^2(q_z^*) \left( 1 - \frac{|q_z^*|}{\sqrt{q_z^{*2} + u^2}} \right) dq_z^*, \end{aligned} \quad (6)$$

where  $Y^2(q_z^*) = |Y^{\pm}(q_z^*)|^2$  and  $u = ak_{\parallel}/\pi$ . This expression is consistent with the result reported previously [7].

Denoting the integral in (6) by  $3I(u)/2$ , we obtain

$$\tau_{2D}^{-1} = \frac{2\pi}{\hbar} M^2(k_{\parallel}) V \frac{g_{2D}^3}{a} I(u), \quad (7)$$

where  $g_{2D} = m^*/2\pi\hbar^2$  is the two-dimensional density of electron states disregarding the spin degeneracy and

$$I(u) = \frac{2}{3} \int_{-\infty}^{\infty} Y^2(q_z^*) \left( 1 - \frac{|q_z^*|}{\sqrt{q_z^{*2} + u^2}} \right) dq_z^*. \quad (8)$$

In a bulk sample, the relaxation time can be written as [9]

$$\tau_{3D}^{-1} = \frac{2\pi}{\hbar} M^2(k) V g_{3D}, \quad (9)$$

where  $g_{3D} = m^*k/2\pi^2\hbar^2$  is the density of electron states per unit volume disregarding the spin degeneracy. Using this expression, we find the ratio between the relaxation times in a sample with QWs and in a bulk sample

$$\frac{\tau_{2D}}{\tau_{3D}} = \frac{2ak}{3\pi} \Gamma^{-1}(u). \quad (10)$$

The integral  $I(u)$  tends to unity for large values of  $u$  and is approximately equal to  $I(u) \approx \frac{4}{3}u$  for small  $u$ .

Therefore, for large thicknesses  $a$  of the confining layers, the ratio of relaxation times coincides with that obtained in [8]. For small QW widths, this ratio appears to be independent of  $a$ , so that the relaxation time in a sample with QWs tends to  $\tau_{3D}/2$ .

Thus, for scattering by polar optical phonons at relatively large QW widths, the conclusions of [8] remain valid; i.e., the expressions for electrical conductivity, thermoelectric power, electronic heat conductivity, and the figure of merit coincide with the corresponding expressions for a bulk sample. If the QW widths are relatively small, the relaxation time becomes independent of  $a$ , and the assumptions of Hicks and Dresselhaus [1] are valid, taking into account the fact that  $\tau_{2D}$  is two times smaller than  $\tau_{3D}$ . In this case, the figure of merit begins to increase with decreasing thickness of the quantum-confinement layer due to the increase in the density of states in QWs, as predicted in [1].

### 3. KINETIC COEFFICIENTS AND THE THERMOELECTRIC FIGURE OF MERIT

Using the obtained expression for the relaxation time in a sample with QWs, we can easily find the electrical conductivity, thermoelectric power, and electronic heat conductivity, and then the thermoelectric figure of merit in such structures.

For example, for the electrical conductivity, we have

$$\sigma_{2D} = \frac{2e^2}{m^*} \int_0^\infty \left( -\frac{\partial f_0(\varepsilon, \mu)}{\partial \varepsilon} \right) \tau_{2D} \frac{g_{2D}}{a} \varepsilon d\varepsilon, \quad (11)$$

where  $f_0(\varepsilon, \mu)$  is the Fermi distribution function,  $\varepsilon$  is the electron energy related to the motion in the layer plane, and  $\mu$  is the chemical potential; we measure the energy from the bottom of the quantum-confinement subband.

For convenience, we explicitly write the energy dependence and rewrite the relaxation time in the case of scattering by polar optical phonons in a bulk sample as

$$\tau_{3D} = \tau_0 x^{1/2}, \quad (12)$$

where  $x = \varepsilon/k_0T$ ,  $k_0$  is the Boltzmann constant, and  $T$  is the absolute temperature. Then, according to (10), the relaxation time in a sample with QWs is given by

$$\tau_{2D} = \frac{2}{3} \tau_0 \frac{wx}{I(w\sqrt{x})}, \quad (13)$$

where  $w = a\sqrt{2m^*k_0T}/\pi\hbar$ .

Taking into account (13), we can rewrite expression (11) as

$$\sigma_{2D} = \frac{2\sqrt{2}e^2\sqrt{m^*}(k_0T)^{3/2}\tau_0}{3\pi^2\hbar^3} I_2^{(2D)}(\mu^*, w), \quad (14)$$

where  $\mu^* = \mu/k_0T$  is the dimensionless chemical potential and

$$I_n^{(2D)}(\mu^*, w) = \int_0^\infty \left( -\frac{\partial f_0(x, \mu^*)}{\partial x} \right) \frac{x^n}{I(w\sqrt{x})} dx. \quad (15)$$

We can obtain the expression for the electrical conductivity in a bulk sample simply by replacing the integral  $I_n^{(2D)}(\mu^*, w)$  with the integral  $I_n^{(3D)}(\mu^*)$  given by

$$I_n^{(3D)}(\mu^*) = \int_0^\infty \left( -\frac{\partial f_0(x, \mu^*)}{\partial x} \right) x^n dx. \quad (16)$$

Likewise, we can obtain the expressions for the thermoelectric power

$$\alpha_{2D} = -\frac{k_0}{e} \left( \frac{I_3^{(2D)}(\mu^*, w)}{I_2^{(2D)}(\mu^*, w)} - \mu^* \right), \quad (17)$$

the electronic heat conductivity

$$\kappa_{2D} = \frac{2\sqrt{2}\sqrt{m^*}k_0/(k_0T)^{5/2}\tau_0}{3\pi^2\hbar^3} \times \left\{ I_4^{(2D)}(\mu^*, w) - \frac{(I_3^{(2D)}(\mu^*, w))^2}{I_2^{(2D)}(\mu^*, w)} \right\}, \quad (18)$$

and the dimensionless thermoelectric figure of merit

$$Z_{2D}T = \frac{(I_3^{(2D)}(\mu^*, w) - \mu^* I_2^{(2D)}(\mu^*, w))^2}{I_2^{(2D)}(\mu^*, w)(1/B + I_4^{(2D)}(\mu^*, w)) - (I_3^{(2D)}(\mu^*, w))^2}. \quad (19)$$

Here, the material parameter  $B$  is defined by the expression

$$B = \frac{2\sqrt{2m^*}k_0(k_0T)^{5/2}\tau_0}{3\pi^2\hbar^3\kappa_{ph}}, \quad (20)$$

where  $\kappa_{ph}$  is the phonon contribution to the heat conductivity.

In a bulk sample, the expression for the dimensionless thermoelectric figure of merit  $Z_{3D}T$  is similar to (19), where we must replace  $I_n^{(2D)}(\mu^*, w)$  with  $I_n^{(3D)}(\mu^*)$ ; then, the expression for the material parameter appears to be the same as for a sample with QWs (20) if we assume that the phonon contribution to the heat conductivity is the same in both cases.

If we assume, like Hicks and Dresselhaus [1], that the relaxation time in a sample with QWs is the same as the bulk relaxation time, then the electrical conductivity  $\sigma_{2D}^*$  can be obtained from (11) by substituting  $\tau_{2D} = \tau_{3D}$ ,

$$\sigma_{2D}^* = \frac{e^2k_0T\tau_0}{\pi\hbar^2a} I_{3/2}^{(3D)}(\mu^*). \quad (21)$$

In this case, we obtain the following expression for the figure of merit:

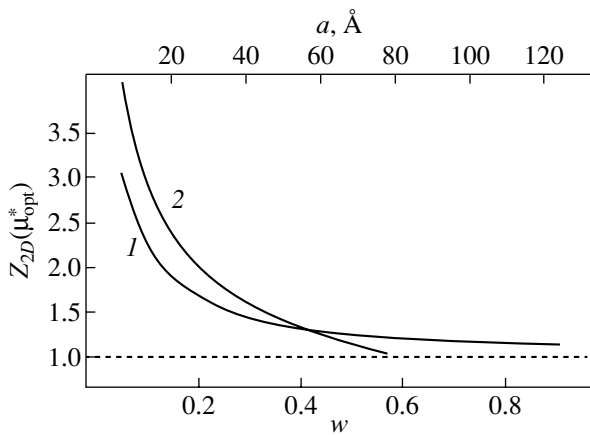
$$Z_{2D}^*T = \frac{(I_{5/2}^{(3D)}(\mu^*) - \mu^* I_{3/2}^{(3D)}(\mu^*))^2}{I_{3/2}^{(3D)}(\mu^*)(1/B^* + I_{7/2}^{(3D)}(\mu^*)) - (I_{5/2}^{(3D)}(\mu^*))^2}. \quad (22)$$

Here, the material parameter  $B^*$  differs from  $B$  by the factor  $3/2w$ ,

$$B^* = B \frac{3}{2w}. \quad (23)$$

Using formulas (19) and (22), we can estimate the variation in the figure of merit if we pass from a bulk sample to a sample with QWs and also compare the values of this variation taking into account the decrease in the relaxation time (19) and disregarding this decrease (22). To this end, we choose the value of the parameter  $B = 0.073$ , which corresponds to the figure of merit  $Z_{3D}(\mu_{opt}^*)T \approx 1$  optimized with respect to the chemical potential. Thus, we can construct plots for the  $w$  dependence of the figures of merit  $Z_{2D}(\mu_{opt}^*)$  and  $Z_{2D}^*(\mu_{opt}^*)$  optimized with respect to the chemical potential and normalized to the bulk value (see figure).





Dependence of the ratio of the thermoelectric figure of merit in a layered structure with quantum wells to the bulk value on the parameter  $w$  proportional to the quantum well width  $a$ . Curve 1 is plotted taking into account the change in the relaxation time for a structure with quantum wells, and curve 2 corresponds to the bulk relaxation time [1].

For numerical estimations, we choose the following parameters: the Debye temperature  $\Theta_D = 150$  K and the average effective mass  $m^* = 0.07m_0$ , which correspond to the parameters of PbTe. Then the condition for scattering elasticity is satisfied at room temperature  $T = 300$  K.

In order to realize the situation in which the lowest subband makes the main contribution to the transport, the energy distance to the second subband, equal to  $3\hbar^2\pi^2/2m^*a^2$ , must be large compared to the thermal energy or to the chemical potential in the degenerate case. The first of these conditions sets an upper bound of  $\sqrt{3}$  for the variation of the parameter  $w$ . Verification of the second of these conditions using the above estimates shows that, for  $w > 0.44$ , where the quantity  $\mu_{opt}^*$  is positive, the optimum values of the chemical potential do not exceed  $k_0T$ . Thus, the contribution from higher subbands can be disregarded.

In the figure, curve 1 corresponds to the thermoelectric figure of merit normalized to the bulk value for structures with QWs with allowance for the variation of the relaxation time and curve 2 represents the figure of merit calculated using the bulk relaxation time [1]. The comparison shows that, in both cases, the thermoelectric figures of merit increase with decreasing width of the QWs; however, if we take into account the change in the relaxation time when passing from a bulk sample to a structure with QWs, then the gain in the figure of merit is somewhat smaller, since in this case the limiting value of the relaxation time in a structure with QWs is two times smaller than that in a bulk sample.

#### 4. CONCLUSIONS

In this study, we theoretically considered the effect of the variation in the relaxation time on the thermo-

electric figure of merit of layered structures with quantum wells in the case of scattering of charge carriers by polar optical phonon scattering. The calculations show that, upon decreasing the QW width  $a$ , the relaxation time in a sample with QWs becomes independent of  $a$  and different from the bulk value only by a numerical factor. This is accounted for by the dependence of the scattering matrix element on the phonon wave vector. Since there is no quasi-momentum conservation law in the direction of the  $z$  axis, the number of phonons with which electrons can interact increases; i.e., the phase volume of such phonons in the wave-vector space expands. This circumstance leads to an increase in the scattering probability and a decrease in the relaxation time if the matrix element is independent of the phonon wave vectors; this situation is realized, for example, in the case of scattering by acoustic phonons. In the case of scattering by optical phonons, the decrease in the bulk matrix element with increasing phonon wave vector balances the increase in scattering probability due to the expansion of the phase volume of the relevant phonons.

The absence of a dependence of the relaxation time on the QW width for small  $a$  produces an increase in the figure of merit compared to the bulk sample. However, the increase in the figure of merit in this case appears to be smaller than that obtained by using the assumption that the relaxation time is the same as for a bulk sample [1]; indeed, for small  $a$ , the relaxation time for a structure with QWs is two times smaller than that for a bulk sample.

It follows from our calculations in this study and in [8] that an increase in  $Z$  due to electron quantum confinement is possible only if the charge-carrier scattering probability decreases with increasing wave vector transferred in a scattering event.

The numerical results of this study make sense only in comparison with the results obtained disregarding the effect of quantum confinement on the mobility. It is known [4–7, 10–13] that more realistic results can be obtained only by taking into account the effect of the layered character of the structure on phonons, electron tunneling through the barriers separating QWs, heat conduction in the barrier layers, and also scattering by nonuniformities in the width of QWs.

#### ACKNOWLEDGMENTS

This study was supported by the Program of Basic Research of the Division of Physical Sciences of the Russian Academy of Sciences.

#### REFERENCES

1. L. D. Hicks and M. S. Dresselhaus, Phys. Rev. B **47**, 12727 (1993).
2. L. D. Hicks and M. S. Dresselhaus, Phys. Rev. B **47**, 16631 (1993).

3. L. D. Hicks, T. C. Harman, and M. S. Dresselhaus, *Appl. Phys. Lett.* **63**, 3230 (1993).
4. D. A. Broido and T. L. Reinecke, *Appl. Phys. Lett.* **67**, 1170 (1995).
5. D. A. Broido and T. L. Reinecke, *Phys. Rev. B* **51**, 13797 (1995).
6. T. L. Reinecke and D. A. Broido, *Mater. Res. Soc. Symp. Proc.* **487**, 161 (1997).
7. I. Sur, A. Casian, A. A. Balandin, *et al.*, in *Proceedings of 21st International Conference on Thermoelectrics* (Long Beach, CA, USA, 2002), p. 288.
8. D. A. Pshenai-Severin and Yu. I. Ravich, *Fiz. Tekh. Poluprovodn. (St. Petersburg)* **36**, 974 (2002) [*Semiconductors* **36**, 908 (2002)].
9. A. I. Anselm, *Introduction to Semiconductor Theory* (Nauka, Moscow, 1978; Prentice Hall, Englewood Cliffs, N.J., 1981).
10. L. Friedman, *Phys. Rev. B* **32**, 955 (1985).
11. T. Koga, O. A. Rabin, and M. S. Dresselhaus, *Phys. Rev. B* **62**, 16703 (2000).
12. A. Balandin, *Phys. Low-Dimens. Semicond. Struct.* **5-6**, 73 (2000).
13. A. Khitun and K. L. Wang, *Phys. Low-Dimens. Semicond. Struct.* **5-6**, 11 (2000).

*Translated by I. Zvyagin*

---

---

LOW-DIMENSIONAL  
SYSTEMS

---

---

# Properties of GaAs Nanowhiskers Grown on a GaAs(111)B Surface Using a Combined Technique

A. A. Tonkikh<sup>1,2\*</sup>, G. E. Cirlin<sup>1,2</sup>, Yu. B. Samsonenko<sup>1,2</sup>, I. P. Soshnikov<sup>2</sup>, and V. M. Ustinov<sup>2</sup>

<sup>1</sup>*Institute for Analytical Instrumentation, Russian Academy of Sciences,  
Rizhskii pr. 26, St. Petersburg, 190103 Russia*

<sup>2</sup>*Ioffe Physicotechnical Institute, Russian Academy of Sciences,  
ul. Politekhnikeskaya 26, St. Petersburg, 194021 Russia*

\*e-mail: alex234@newmail.ru

Submitted March 2, 2004; accepted for publication March 4, 2004

**Abstract**—Arrays of GaAs whiskers on GaAs(111)B substrates were grown using a technique combining vacuum evaporation and molecular-beam epitaxy. The surface structural properties of the samples obtained were studied by scanning electron microscopy. It was found that the areal density of the whiskers amounted to  $(1-2) \times 10^9 \text{ cm}^{-2}$ . The typical dimensions of the whiskers were 30–150 nm (diameter) and 300–800 nm (length). It was shown that the whisker size can be controlled by changing the growth conditions and varying the thickness of the evaporated Au film. © 2004 MAIK “Nauka/Interperiodica”.

## 1. INTRODUCTION

Whisker crystals have been known for quite a long time. According to classical concepts, whiskers are crystalline solids whose length considerably exceeds their diameter. An important property of objects of this kind, which are widely used in modern industrial technology, is their high mechanical strength. The dimensions of such whisker crystals are several micrometers in diameter and several millimeters in length. A mechanism for whisker growth was suggested by Wagner and Ellis in 1964 [1]; this was the beginning of research into artificial whisker crystals, which were subsequently grown on the basis of various crystalline substances. In this country, a considerable contribution to the development of whisker-crystal technology was made by E.I. Givargizov, who in monograph [2] presented a detailed review of the properties, growth techniques, and theories of the formation of whisker crystals known by 1977. The current interest in whisker crystals is caused by the fact that modern technologies make it possible to produce nanowhiskers (NWs), i.e., whisker crystals with a diameter of several tens of nanometers [3]. Such objects may find application in the creation of multiple-tip cathodes and ultrasharp tips for scanning-probe microscopy [4]. NWs made of a semiconductor material (e.g., GaAs) can be viewed as vertical quantum wires. Thus, the range of applications of NWs may be extended into the field of semiconductor microelectronics and optoelectronics. The first nanotransistors based on NWs have already been fabricated [5]. It was suggested that GaAs NWs may be used as visible-light emitters, the concept of which was discussed in [6]. Note that the possibility of forming GaAs/AlAs lateral quantum wires on GaAs substrates

with orientations other than (100) was demonstrated earlier, and possible applications for them were suggested [7]. Quantum wires grown by this technique are often coupled due to electron tunneling, which hinders their study and application as isolated one-dimensional objects. Using NWs, it is possible to synthesize nanowires oriented at an angle to the substrate surface [8] (in particular, at a right angle). In addition, nanowires without electron-tunneling coupling can be grown in this case.

In this study, we suggest a method for synthesizing GaAs NWs on GaAs(111)B substrates using a technique combining vacuum evaporation of gold and epitaxial growth of gallium arsenide in a molecular-beam epitaxy (MBE) chamber.

## 2. EXPERIMENTAL

The growth of whiskers using the molecular beam-liquid–solid mechanism, which is a modification of the vapor–liquid–solid (VLS) method suggested by Wagner and Ellis [1], requires a several-stage process. We used a three-stage technological scheme for the formation of NWs. At the first stage, the surface of GaAs is prepared as described below. At the second stage, a film of Au (catalyst metal) is deposited on the GaAs surface. At the third stage, the formation of GaAsAu droplets and NW growth takes place. According to the VLS mechanism, NWs are expected to grow at the sites on the surface where droplets of GaAsAu, acting as catalyst for the whisker growth, are formed.

It was shown in [8] that GaAs whiskers formed by the VLS mechanism grow predominantly in the [111] crystallographic direction. To obtain NWs oriented normally to the substrate, we chose a (111)B-oriented

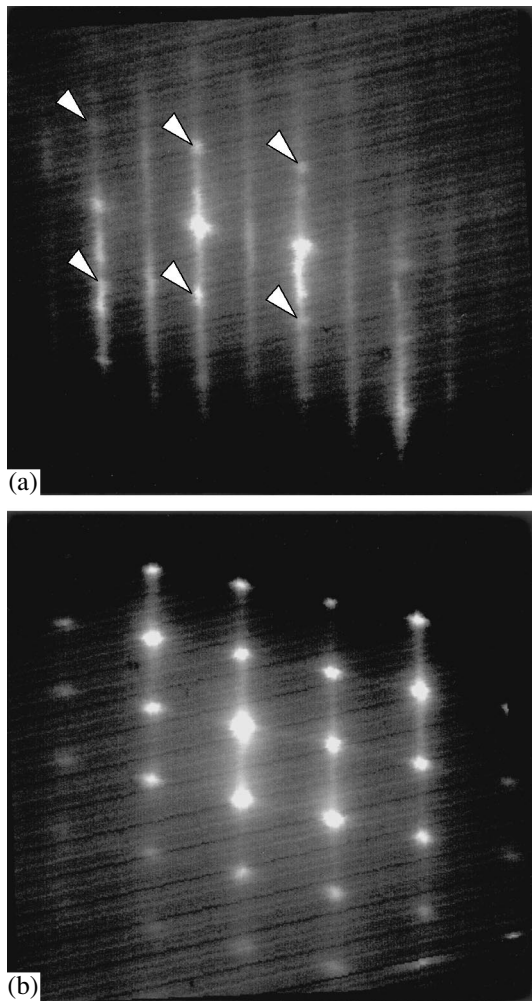


**Fig. 1.** RHEED patterns obtained (a) for a GaAs(111)B surface after the deposition of a GaAs layer with an effective thickness of 24 nm (white arrows indicate additional reflections related to the NW system) and (b) for the system of NWs after the termination of the growth process; the electron-beam energy was 25 keV.

GaAs surface. Preparation of the surface at the first stage was carried out as follows. A GaAs(111)B wafer was loaded into the growth chamber of the ÉP1203 MBE system (NTO, USSR Academy of Sciences), and the oxide layer was removed from its surface by heating at 610°C in a flow of As<sub>4</sub>. After removal of the oxide layer, a 0.25- $\mu\text{m}$ -thick GaAs buffer layer that smoothed out possible roughness of the surface was grown at 550°C. Next, the surface of the sample was coated with an arsenic layer  $\sim 1$  nm thick at a substrate temperature below 200°C in order to prevent the formation of the natural oxide during the transportation of the samples from the MBE chamber to the vacuum sputtering unit (VUP-5, NPO Electron, Sumy, Ukraine) for Au deposition.

At this stage, a film of Au was formed on the GaAs surface using the following procedure. First, the protective As layer was removed by heating the sample to

(250  $\pm$  10)°C. Then, the temperature of the sample was reduced to 110°C and the GaAs(111)B surface was covered with the Au film using vacuum deposition from an electron-impact source. Gold with a purity of at least 99.99% was used as the source material. The thickness of the deposited Au layer was determined from measurements of optical transmission. The measurement accuracy was no lower than  $\sim 0.1\%$ ; for small layer thicknesses, this corresponds to  $\sim 0.2$  nm. Scanning electron microscope (SEM) images of the GaAs(111)B surface covered with the Au layer indicated the smoothness of the surface. After deposition of the Au film, the samples were loaded again into the growth chamber of the MBE system. Patterns of reflection high-energy electron diffraction (RHEED) recorded immediately after loading the samples into the growth chamber indicated that the surface structure was amorphous, which meant that either the deposited Au film was in an amorphous state or an oxide layer was present on the surface.

In the MBE growth chamber, samples were heated in order to remove the oxide layer and initiate the formation of GaAsAu droplets saturated with Ga and As. The highest temperature of heating the sample corresponded to the lower limit required for the removal of the oxide layer from GaAs ( $\sim 610^\circ\text{C}$ ). After heating for 5 min, the sample temperature was lowered to 550°C and GaAs deposition was performed. The effective rate of GaAs growth was one monolayer per second, and the ratio of the Ga and As<sub>4</sub> fluxes was  $\sim 1$ . The process of NW formation was monitored in situ by recording the RHEED patterns [9]. Three samples were investigated. In samples 1 and 2, the thicknesses of the deposited Au films were 2.5 and 1.2 nm, respectively, and the effective thickness of the GaAs layer was 200 nm. In sample 3, the thickness of the Au layer was 1.2 nm and the effective thickness of the GaAs layer was 500 nm.

The surface morphology of the samples was studied using a CamScan S4-90FE scanning electron microscope with a field-emission cathode. The microscope operated in the secondary-electron mode; the electron energy in the probe beam was 20 keV, and the beam was oriented at an angle of 27° to the surface of the GaAs substrate.

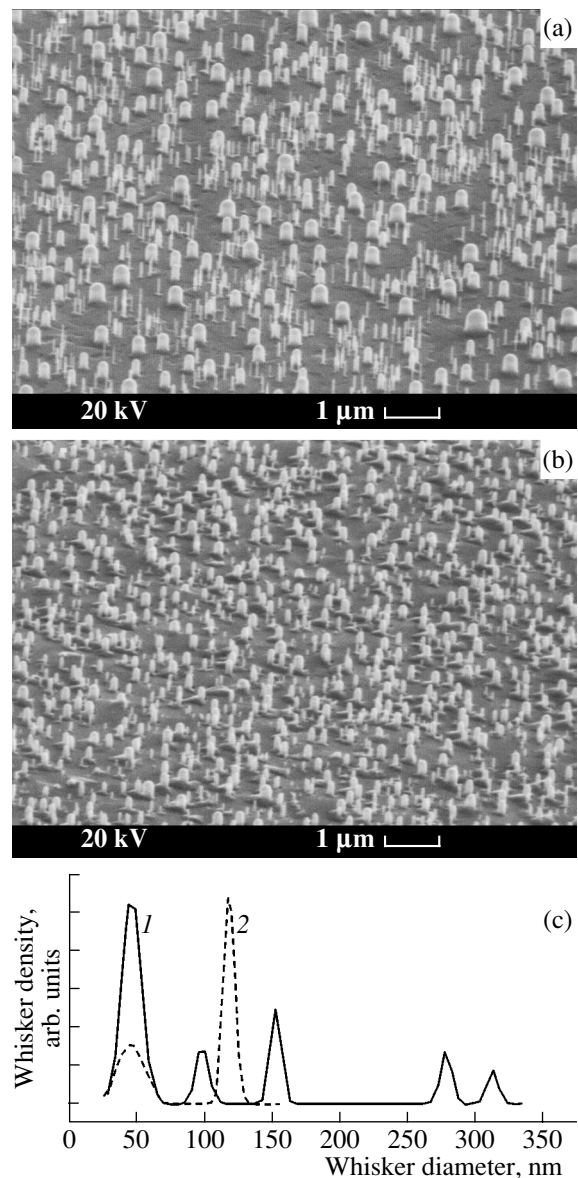
### 3. RESULTS AND DISCUSSION

Figure 1a shows the RHEED pattern obtained from a GaAs(111)B surface at azimuth [110] after the deposition of a GaAs layer with effective thickness equal to 24 nm. In addition to the main reflections originating from the reconstructed GaAs(111)B surface, the diffraction pattern displays point reflections (indicated by white arrows). The appearance of such point reflections gives evidence of the formation of a well-developed surface structure—in this case, NWs. Note that point reflections are arranged in a regular pattern, typical of diffraction from single-crystal systems. In Fig. 1b is shown the RHEED pattern for the sample with a NW system after the growth process has finished. In this

case, only the pattern of diffraction peaks is present; the pattern of stripes related to GaAs(111)B surface is absent. Reconstruction of the GaAs(111)B surface is not observed at any azimuth. Thus, it may be suggested that the pattern shown in Fig. 1b originates from electron diffraction at the NW system. The shape of the pattern in Fig. 1b corresponds to the diffraction from a GaAs single crystal in the direction [110] (see [10, 11]).

An SEM image of the surface of sample 1 with the NW array is shown in Fig. 2a. One can see that the NWs are oriented perpendicularly to the GaAs(111) surface. The density of the NW array is  $2 \times 10^9 \text{ cm}^{-2}$ . Figure 2b represents an image of sample 2, which differs from the previous sample only in the thickness of the initially deposited Au film (1.2 nm). The density of the NW array in sample 2 is close to that in sample 1 and is equal to  $1.8 \times 10^9 \text{ cm}^{-2}$ .

It is important to note that the lengths of the NWs in samples 1 and 2 range from 100 to 400 nm; thus, the length distribution is rather broad. It should be emphasized that the largest NW lengths do not exceed  $2d_{\text{eff}}$ , where  $d_{\text{eff}}$  is the effective thickness of the deposited GaAs layer. Another important parameter characterizing NWs is the diameter. In Fig. 2c, the diameter distribution (approximated by Gaussian functions) is shown for the samples of Figs. 2a and 2b. In sample 1, where the Au film was thicker, the spread in the NW diameter is large. The peaks of the distribution correspond to NWs with  $d \approx 45, 95, 155, 275,$  and  $310 \text{ nm}$ . In sample 2, where the initially deposited Au layer was 1.2 nm thick, the diameter distribution is different; here, the most typical NWs have  $d \approx 35\text{--}50$  and  $120 \text{ nm}$ . Thus, it can be concluded that NWs in sample 2 are more uniform in their diameters. Previously, the relationship between the size of droplets of the melt catalyzing the whisker growth and the diameter of whiskers obtained by gas-phase epitaxy was discussed in a number of papers [3, 12]. It was shown that, in most cases, the whisker diameter equals or slightly exceeds the diameter of the GaAsAu droplet [12]. The latter, in turn, depends on the thickness of the initially deposited Au film. It was shown that a decrease in the thickness of the initial Au film can lead to a decrease in the typical size and size spread of GaAsAu droplets, which brings about the corresponding changes in the system of whiskers [2]. For example, it was shown that a process of InAs NW growth in which the thickness of the initial Au film was 0.2 nm yields whiskers with a diameter of 20 nm in their upper part. Comparing the NW diameter distribution in samples 1 and 2, we find that the spread in NW diameters is indeed reduced as the thickness of the Au film decreases. In sample 2, there are no NWs with diameters exceeding 200 nm, and the distribution peak corresponds to  $d \approx 120 \text{ nm}$ . In addition, NWs with diameters  $\sim 20 \text{ nm}$ , which are absent in sample 1, can be found in sample 2. However, the fraction of such NWs in the array is small, and the main peak in the distribution of small-diameter NWs appears at 30–50 nm (the same range as in sample 1).



**Fig. 2.** (a) SEM image of the surface of sample 1 with an NW array; (b) SEM image of the surface of sample 2 with an NW array; (c) diameter distribution of NWs in samples (1) 1 and (2) 2.

There are two possible explanations for the observed limitation of the minimum diameter. First, it is known that the diameter of whiskers grown by the VLS mechanism cannot be arbitrarily small: there is a certain critical diameter below which whisker formation is impossible [2]. Second, we rely on the method of the formation of GaAsAu droplets based on thermal disintegration of the initially deposited Au film into the array of GaAsAu droplets. Decreasing the temperature at which this process is carried out should favor a reduction in the typical size of droplets and a decrease in the diameter of the crystals [8]. In the case under consideration, the temperature of the formation of

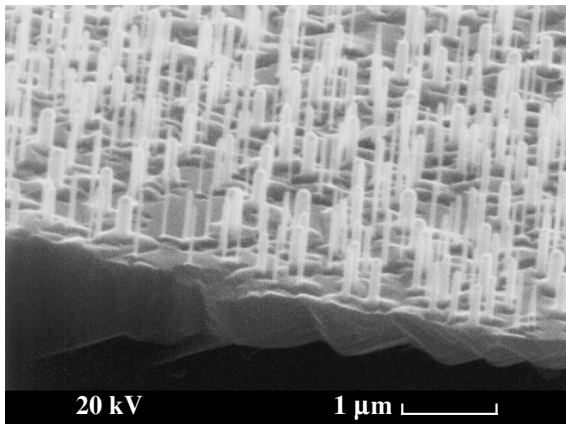


**Fig. 3.** SEM image of the surface of sample 3 with an NW array recorded in the vicinity of a cleaved edge.

GaAsAu droplets was determined by the temperature needed for the removal of the oxide layer from the GaAs surface and could not be lowered in order to obtain smaller droplets for a given thickness of Au film.

For application purposes, an increase in both the length of NWs (to  $\sim 1 \mu\text{m}$  or more) and the length-to-diameter ratio is important. This can be achieved by consistently choosing the distribution of GaAsAu droplets on the GaAs surface from which the NWs are formed and the amount of GaAs deposited. To implement this approach, in sample 3 (whose SEM image is shown in Fig. 3) the amount of GaAs deposited was increased. The distribution of GaAsAu droplets, which determines the diameter distribution of the NWs and the density of the NW array, was chosen to be the same as in sample 2. Thus, a 1.2-nm-thick initial Au film was deposited and identical conditions of the annealing of the surface were used. The effective thickness of the deposited GaAs was 500 nm. Figure 3 shows the image of sample 3 in the vicinity of a cleaved edge (the wafer was cleaved after growth of the NW). Note that no region of damaged NWs, which could appear due to mechanical stress induced during cleaving, appears near the edge, which confirms the high mechanical strength of synthesized GaAs NWs. The NW density ( $2 \times 10^9 \text{ cm}^{-2}$ ) and the diameter distribution in sample 3 are close to those in sample 2. The NW length is 500–800 nm, and the length-to-diameter ratio is as large as 20–25 for some of the NWs. The largest length of the NWs does not exceed  $2d_{\text{eff}}$ , as in the first two samples. An increase in the effective thickness of the GaAs film evidently leads to an increase in the length of GaAs NWs compared to sample 2. Thus, the length of nanowhiskers that can be grown by MBE ranges from 100 nm to several micrometers and is determined mainly by the amount of deposited GaAs. We believe that the NW diameter can be reduced to 20 nm or smaller by decreasing the thickness of the initially deposited Au film and reducing the temperature of the formation of GaAsAu droplets.

#### 4. CONCLUSIONS

An efficient method for the formation of whisker crystals of nanometer dimensions ( $\sim 100 \text{ nm}$  in diameter) is suggested. The arrays of synthesized GaAs nanowhiskers are oriented strictly normally to the (111)B surface of the GaAs substrate and have a high areal density ( $\sim 10^9 \text{ cm}^{-2}$ ). It is shown that a decrease in the thickness of the Au film results in a shift of the NW diameter distribution to lower values. It is found that the length of the NW is limited by a value equal to the doubled effective thickness of the deposited GaAs layer. The arrays of NWs grown can be used in the fabrication of multiple-tip cathodes and, due to their high strength, in separating biological and organic substances. Furthermore, we plan to develop a method for overgrowing NWs with a layer of  $\text{Al}_x\text{Ga}_{1-x}\text{As}$  with high Al content in order to obtain visible-range emission from a GaAs/AlGaAs heterostructure with NWs as quantum wires.

#### ACKNOWLEDGMENTS

We are grateful to V.G. Dubrovskii and V.É. Pitsyn for useful discussions of the results obtained and V.M. Busov and S.I. Troshkov for measurements with the scanning electron microscope. G.É. Cirilin acknowledges support from the Alexander von Humboldt Stiftung.

This study was supported by several programs of the Russian Academy of Sciences.

#### REFERENCES

1. R. S. Wagner and W. C. Ellis, *Appl. Phys. Lett.* **4**, 89 (1964).
2. E. I. Givargizov, *Growth of Whisker and Scaly Crystals from Vapors* (Nauka, Moscow, 1977) [in Russian].
3. B. J. Ohlsson, M. T. Bjork, M. H. Magnusson, *et al.*, *Appl. Phys. Lett.* **79**, 3335 (2001).
4. E. I. Givargizov, *Priroda* (Moscow) **11**, 20 (2003).
5. Y. Cui and C. M. Lieber, *Science* **291**, 851 (2000).
6. K. Haraguchi, T. Katsuyama, K. Hiruma, and K. Ogawa, *Appl. Phys. Lett.* **60**, 745 (1992).
7. Zh. I. Alferov, A. Yu. Egorov, A. E. Zhukov, *et al.*, *Fiz. Tekh. Poluprovodn.* (St. Petersburg) **26**, 1715 (1992) [*Sov. Phys. Semicond.* **26**, 959 (1992)].
8. K. Hiruma, M. Yazawa, T. Kaatsuyama, *et al.*, *J. Appl. Phys.* **77**, 447 (1995).
9. G. M. Gur'yanov, V. N. Demidov, N. P. Korneeva, *et al.*, *Zh. Tekh. Fiz.* **67** (8), 111 (1997) [*Tech. Phys.* **42**, 956 (1997)].
10. F. Bechstedt and R. Enderlein, *Semiconductor Surfaces and Interfaces* (Akademie, Berlin, 1988).
11. J. M. Cowley, *Diffraction Physics* (Elsevier, New York, 1975; Mir, Moscow, 1979).
12. E. I. Givargizov and A. A. Chernov, *Kristallografiya* **18**, 147 (1973) [*Sov. Phys. Crystallogr.* **18**, 89 (1973)].

*Translated by M. Skorikov*

---

**AMORPHOUS, VITREOUS,  
AND POROUS SEMICONDUCTORS**

---

## Distribution of the Density of Electronic States in the Energy Gap of Microcrystalline Hydrogenated Silicon

A. G. Kazanskiĭ\* and K. Yu. Khabarova

*Moscow State University, Moscow, 119992 Russia*

\*e-mail: kazanski@phys.msu.su

Submitted March 1, 2004; accepted for publication March 23, 2004

**Abstract**—Photomodulation spectroscopy was applied to a study of the distribution of the density of electronic states in the energy gap of microcrystalline hydrogenated silicon ( $\mu\text{c-Si:H}$ ) with a varied level of boron doping. The information on the density-of-states distribution was extracted by analyzing temperature dependences of the constant and modulated components of photoconductivity in a sample exposed to modulated light. The distributions of the density of electronic states in the upper and lower halves of the energy gap of  $\mu\text{c-Si:H}$  were determined. The study demonstrated that the tail of the density-of-states distribution near the valence band is less steep than that near the conduction band. © 2004 MAIK “Nauka/Interperiodica”.

Microcrystalline hydrogenated silicon ( $\mu\text{c-Si:H}$ ) has recently attracted the attention of researchers because, since it has more stable photoelectric parameters compared to amorphous hydrogenated silicon ( $a\text{-Si:H}$ ) and good technological compatibility with  $a\text{-Si:H}$ , this material is widely used in optoelectronics and, in particular, in tandem solar cells based on  $\mu\text{c-Si:H}$  and  $a\text{-Si:H}$  [1].

One of the basic characteristics of disordered semiconductors, which include  $\mu\text{c-Si:H}$ , is the density of localized electronic states in the energy gap or the mobility gap. The distribution of the density of electronic states in the energy gap of  $\mu\text{c-Si:H}$  governs its physical characteristics and the processes that occur in the material: optical absorption, conductivity, and photoconductivity.

The distribution of the density of electronic states in  $\mu\text{c-Si:H}$  has been considerably less studied than that in  $a\text{-Si:H}$ . A number of issues associated with the density-of-states distribution in the energy gap of  $\mu\text{c-Si:H}$  remain unclear. It has been established that there is an exponential tail of the density-of-states distribution near the edge of the conduction band ( $E_c$ ) of  $\mu\text{c-Si:H}$  [2–4]. It is assumed that an exponential distribution of localized states must also exist near the edge of the valence band ( $E_v$ ) in  $\mu\text{c-Si:H}$ . However, there are almost no published experimental data on the distribution of localized states near  $E_v$  [5]. At the same time, these states must play an important role in carrier transport and recombination in  $\mu\text{c-Si:H}$  and, in particular, in acceptor-doped  $\mu\text{c-Si:H}$  films. In view of the above, the goal of this study was to examine the distribution of the density of localized states in the upper and lower halves of the energy gap in  $\mu\text{c-Si:H}$ .

The measurements were carried out on  $\mu\text{c-Si:H}$  films lightly doped with boron.  $\mu\text{c-Si:H}$  films 0.6–0.7  $\mu\text{m}$  thick were deposited onto a quartz substrate at a temperature of 220°C in a standard PECVD reactor (University of Marburg) by glow-discharge decomposition of a silane–hydrogen mixture containing 1.5% monosilane ( $\text{SiH}_4$ ). The doping with boron was done by introducing diborane ( $\text{B}_2\text{H}_6$ ) into the reaction chamber. The volume ratio of the gases  $k = [\text{B}_2\text{H}_6]/[\text{SiH}_4]$  was in the range  $2 \times 10^{-6}$ – $10^{-5}$ . According to thermoelectric data, the films obtained at  $k \leq 3 \times 10^{-6}$  had  $n$ -type conduction, and those for which  $k \geq 4 \times 10^{-6}$ ,  $p$ -type conduction. According to electron-microscopic data, the films were composed of columns 30–100 nm in diameter, which contained 3 to 30-nm crystallites. The crystalline component in the Raman spectra of these films constituted 85%.

Magnesium contacts were deposited onto the surface of the films. The measurements were performed in a vacuum at a residual pressure of  $10^{-3}$  Pa. Prior to measurements, the films were annealed in a vacuum at 180°C for 30 min.

For  $a\text{-Si:H}$ , the distribution of states in the mobility gap and, in particular, near the band edges is obtained in most cases by analyzing spectral dependences of the absorption coefficient at energies lower than the optical energy gap [6]. In the case of  $\mu\text{c-Si:H}$ , the considerable contribution to the absorption from interband optical transitions in microcrystals [7] makes it difficult to obtain information on the distribution of localized states in the energy gap by optical techniques. That is why photomodulation spectroscopy [8, 9] was used in the present study.

Conventionally, the method of photomodulation spectroscopy measures the phase shift between the

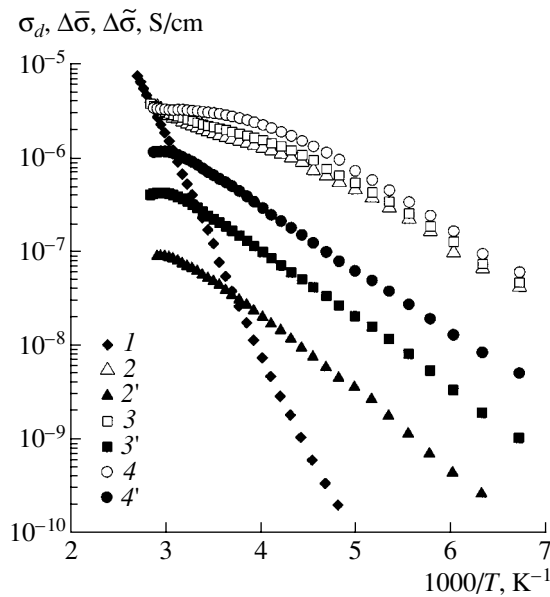


**Fig. 1.** Temperature dependences of (1) dark conductivity  $\sigma_d$ , (2–4) the constant component of photoconductivity ( $\Delta\bar{\sigma}$ ), and (2'–4') the amplitude of the modulated component of photoconductivity ( $\Delta\tilde{\sigma}$ ) at different illumination intensities for a sample fabricated at  $k = 4 \times 10^{-6}$ .  $I_0 = I_1$ : (2, 2')  $10^{15}$ , (3, 3')  $4 \times 10^{15}$ , and (4, 4')  $1.3 \times 10^{16}$   $\text{cm}^{-2} \text{s}^{-1}$ .

exciting light, which is modulated with frequency  $\omega$  and has an intensity of  $I_0 + I_1 \sin(\omega t)$  ( $I_0 \geq I_1$ ), and the modulated photocurrent generated in a sample [8]. Analysis of how the phase shift depends on the modulation frequency makes it possible to determine the energy distribution of localized states,  $N_i(E)$  [2–4, 8]. At the same time, according to [10],  $N_i(E)$  can also be obtained by measuring the constant and modulated components of the photocurrent. In this case,  $N_i(E_f^n) = [G_1/\omega k_B T](\Delta\bar{\sigma}/\Delta\tilde{\sigma})$  for an  $n$ -type material, where  $\Delta\bar{\sigma}$  and  $\Delta\tilde{\sigma}$  are the constant component and the amplitude of the modulated component of photoconductivity, respectively;  $E_f^n$ , the quasi-Fermi energy for electrons;  $G_1$ , the amplitude of the rate of generation of nonequilibrium carriers under modulated excitation;  $T$ , temperature; and  $k_B$ , the Boltzmann constant. Thus, the position of  $E_f^n$  can be changed by varying the temperature or excitation intensity, and, accordingly, the  $N_i(E)$  distribution can be obtained by measuring  $\Delta\bar{\sigma}$  and  $\Delta\tilde{\sigma}$ .

The above expression for  $N_i(E_f^n)$  is valid for modulation frequencies that satisfy the condition  $(1/\tau_n) < \omega < N_c^* v S \exp[-(E_c - E_f^n)/kT]$ , where  $\tau_n$ ,  $N_c^*$ ,  $v$ , and  $S$  are the photoresponse time, effective density of states in the conduction band, thermal velocity of carriers, and cross

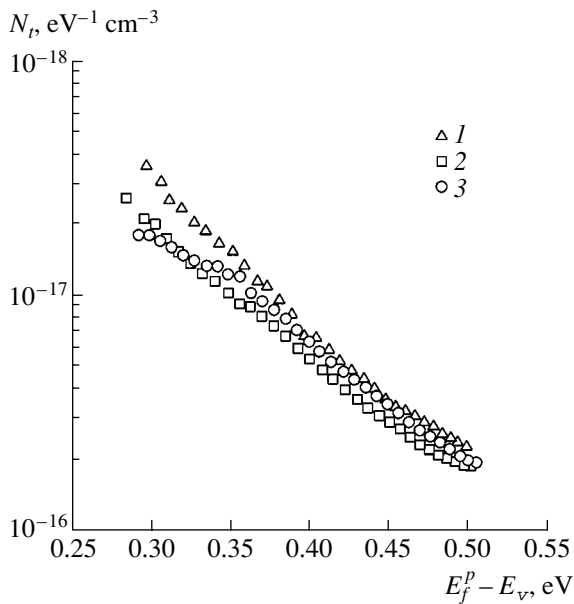
section of their capture by localized states, respectively. The upper bound on  $\omega$  is necessary for a thermodynamic equilibrium to exist under modulated excitation between free carriers and those captured in states near  $E_f^n$ . At the same time, if the lower bound on  $\omega$  is satisfied, the value of  $\Delta\tilde{\sigma}$  must be independent of the carrier lifetime and vary in inverse proportion to  $\omega$ .

In this study, samples were excited with modulated light emitted by an IR LED with a wavelength of  $0.87 \mu\text{m}$  and intensity  $I_0 = I_1 = 10^{15} - 1.5 \times 10^{16} \text{ cm}^{-2} \text{ s}^{-1}$ . Measurements of the frequency dependences of  $\Delta\tilde{\sigma}$  demonstrated that, for all the samples under study, the dependence  $\Delta\tilde{\sigma}(\omega)$  is nearly inversely proportional in the modulation frequency range  $f = \omega/2\pi > 7$  kHz. Therefore, all the measurements described below were carried out at  $f = 8$  kHz.

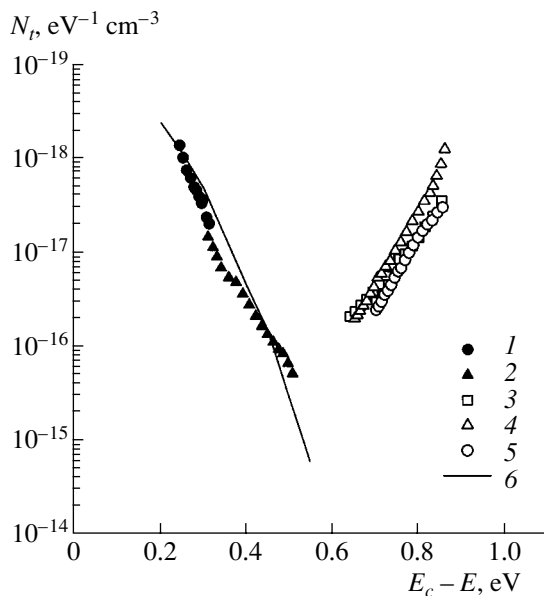
The measurements demonstrated that the temperature dependences of  $\Delta\bar{\sigma}$  and  $\Delta\tilde{\sigma}$  are similar for all the  $\mu\text{c-Si:H}$  films studied. For example, Fig. 1 shows the temperature dependences of  $\Delta\bar{\sigma}$  and  $\Delta\tilde{\sigma}$ , measured at different intensities of modulated light for a  $\mu\text{c-Si:H}$  film doped with boron at  $k = 4 \times 10^{-6}$ . The same figure shows the temperature dependence of the dark conductivity  $\sigma_d$ . It can be seen that, as the illumination intensity increases, the value of  $\Delta\bar{\sigma}$  does not change significantly, whereas  $\Delta\tilde{\sigma}$  grows appreciably. The result obtained confirms that the condition  $(\tau_n)^{-1} < \omega$  is satisfied for the modulation frequency used. Indeed, the slight change in  $\Delta\bar{\sigma}$  on raising the excitation intensity is due to the small value of the exponent  $\gamma$  in the current–light characteristic ( $\Delta\bar{\sigma} \propto I_0^\gamma$ ) [11], which is, in turn, caused by the strong dependence of the carrier lifetime on excitation intensity in  $\mu\text{c-Si:H}$  films. As already mentioned, if the condition  $(\tau_n)^{-1} < \omega$  is satisfied, the value of  $\Delta\tilde{\sigma}$  must be independent of the lifetime and vary in proportion to the excitation intensity, which is actually observed in the experiment.

Figure 2 shows the distribution of density of states near the edge of the valence band, calculated for a sample obtained at  $k = 4 \times 10^{-6}$  from the temperature dependences of  $\Delta\bar{\sigma}$  and  $\Delta\tilde{\sigma}$ , presented above. It was assumed in the calculation that the position of the quasi-Fermi level in  $\mu\text{c-Si:H}$  relative to the edge of the conduction band for  $n$ -type samples,  $(E_c - E_f^n)$ , or to the edge of the valence band for  $p$ -type samples,  $(E_f^p - E_v)$ , is determined by the relation  $|E_{c(v)} - E_f^{n(p)}| = k_B T \ln(\sigma_0/\Delta\bar{\sigma})$ , where  $\sigma_0 = 200 \Omega^{-1} \text{ cm}^{-1}$  [12]. It can be seen in the figure that the density of electron states, determined by the method considered above, is virtually independent of light intensity, as it should be if the





**Fig. 2.** Distribution of the density of localized electron states near the valence band for a sample fabricated at  $k = 4 \times 10^{-6}$ , determined from the results of measurements at different illumination intensities.  $I_0 = I_1$ : (1)  $10^{15}$ , (2)  $4 \times 10^{15}$ , and (3)  $1.3 \times 10^{16} \text{ cm}^{-2} \text{ s}^{-1}$ .



**Fig. 3.** Distribution of the density of localized electron states in the energy gap of  $\mu\text{c-Si:H}$ . (1–5) Results of this study and (6) data of [6].  $k =$  (1)  $2 \times 10^{-6}$ , (2)  $3 \times 10^{-6}$ , (3)  $4 \times 10^{-6}$ , (4)  $5 \times 10^{-6}$ , and (5)  $10^{-5}$ .

necessary conditions for the applicability of the technique described are satisfied.

Figure 3 shows the density-of-states distribution over energy  $E$  in the energy gap of  $\mu\text{c-Si:H}$ , obtained

for all the samples studied by processing the temperature dependences of  $\Delta\bar{\sigma}$  and  $\Delta\tilde{\sigma}$ . The energies for samples with  $p$ -type conduction were calculated for the energy gap of  $\mu\text{c-Si:H}$ , which was obtained from optical measurements as 1.12 eV [7]. For comparison, the figure shows the distributions of density of states near the edge of the conduction band in  $\mu\text{c-Si:H}$ , obtained in [2] by photomodulation spectroscopy from phase-shift measurements. It can be seen from the figure that, for the  $\mu\text{c-Si:H}$  samples studied, the distribution of density of states near the edge of the conduction band is nearly exponential with a characteristic energy  $k_B T_0^c = 0.04$ – $0.06$  eV. This is in an agreement with the results of other studies, which are shown in the figure. For  $p$ -type  $\mu\text{c-Si:H}$  samples, an exponential tail of the distribution of density of states is also observed near the valence band, and the characteristic energy of this tail ( $k_B T_0^v = 0.06$ – $0.07$  eV) somewhat exceeds the energy  $k_B T_0^c$  obtained for the tail of the conduction band. This result confirms the assumptions made in the literature according to which the tail of localized states near the valence band in  $\mu\text{c-Si:H}$  is less steep than that near the conduction band [13].

At present, there are no data on the influence exerted by the doping level and, accordingly, the position of the Fermi level ( $E_f$ ) on the distribution of the density of localized states in the energy gap of  $\mu\text{c-Si:H}$ . If it is assumed that the distribution of the density of localized states is independent of the position of  $E_f$ , then the data presented in the figure reflect the distribution of the density of localized states in the energy gap of  $\mu\text{c-Si:H}$ . If, however, the distribution of the density of localized states depends on the position of  $E_f$  [14] and, accordingly, on the doping level and the type of conduction in the material, then the curves in Fig. 3 characterize the dependences  $N_l(E)$  in the upper half of the energy gap of  $\mu\text{c-Si:H}$  for  $n$ -type samples and in the lower half for  $p$ -type samples.

#### ACKNOWLEDGMENTS

The authors are grateful to Dr. H. Mell for providing the boron-doped  $\mu\text{c-Si:H}$  films.

This study was supported in part by the Russian Foundation for Basic Research, project no. 02-02-39020-GFEN-a.

#### REFERENCES

1. J. Meier, P. Torres, R. Platz, *et al.*, Mater. Res. Soc. Symp. Proc. **420**, 3 (1996).
2. R. Bruggemann, J. P. Kleider, C. Longeaud, and F. House, *Materials for Information Technology in the New Millennium*, Ed. by J. M. Marshall *et al.* (Bookcraft, Bath, UK, 2001), p. 212.

3. W. Bronner, J. P. Kleider, R. Bruggemann, and M. Mehring, *Thin Solid Films* **427**, 51 (2003).
4. T. Unold, R. Bruggemann, J. P. Kleider, and C. Longeaud, *J. Non-Cryst. Solids* **266–269**, 325 (2000).
5. I. Balberg, Y. Dover, R. Naides, *et al.*, *Phys. Rev. B* **69**, 035203 (2004).
6. J. Kocka, *J. Non-Cryst. Solids* **90**, 91 (1987).
7. A. G. Kazanskiĭ, Kh. Mell, E. I. Terukov, and P. A. Forsh, *Fiz. Tekh. Poluprovodn. (St. Petersburg)* **34**, 373 (2000) [*Semiconductors* **34**, 367 (2000)].
8. H. Oheda, *J. Appl. Phys.* **52**, 6693 (1981).
9. R. R. Koropecski, J. A. Smidt, and R. Arce, *J. Appl. Phys.* **91**, 8965 (2002).
10. K. W. Boer and E. A. Niekisch, *Phys. Status Solidi* **1**, 275 (1961).
11. P. A. Forsh, A. G. Kazanskii, H. Mell, and E. I. Terukov, *Thin Solid Films* **383**, 251 (2001).
12. H. Overhof and M. Otte, *Future Directions in Thin Film Science and Technology* (World Sci., Singapore, 1997), p. 23.
13. F. Finger, J. Muller, C. Malten, *et al.*, *J. Non-Cryst. Solids* **266–269**, 511 (2000).
14. P. Altermatt and G. Heiser, *J. Appl. Phys.* **92**, 2561 (2002).

*Translated by M. Tagirdzhanov*

---

PHYSICS OF SEMICONDUCTOR  
DEVICES

---

# Ge/Si Waveguide Photodiodes with Built-In Layers of Ge Quantum Dots for Fiber-Optic Communication Lines

A. I. Yakimov<sup>^</sup>, A. V. Dvurechenskii, V. V. Kirienko, N. P. Stepina,  
A. I. Nikiforov, V. V. Ul'yanov, S. V. Chaikovskii, V. A. Volodin,  
M. D. Efremov, M. S. Seksenbaev, T. S. Shamirzaev, and K. S. Zhuravlev

*Institute of Semiconductor Physics, Siberian Division, Russian Academy of Sciences,  
pr. Akademika Lavrent'eva 13, Novosibirsk, 630090 Russia*

<sup>^</sup>*e-mail: yakimov@isp.nsc.ru*

Submitted February 3, 2004; accepted for publication February 11, 2004

**Abstract**—The results of research aimed at the development of high-efficiency Ge/Si-based photodetectors for fiber-optic communication applications are reported. The photodetectors are designed as vertical  $p-i-n$  diodes on silicon-on-insulator substrates in combination with waveguide lateral geometry and contain Ge quantum-dot layers. The layer density of quantum dots is  $1 \times 10^{12} \text{ cm}^{-2}$ ; the dot size in the plane of growth is  $\sim 8 \text{ nm}$ . Unprecedentedly high quantum efficiency suitable for the range of telecommunication wavelengths is attained; specifically, in the waveguides illuminated from the end side, the efficiency was as high as 21 and 16% at 1.3 and 1.55  $\mu\text{m}$ , respectively. © 2004 MAIK “Nauka/Interperiodica”.

## 1. INTRODUCTION

One of the most important areas in the development of information transfer facilities in television and telephone networks, the Internet, and optical computers is the elaboration of fiber-optic communication lines (FOCLs). FOCLs contain a transmitter and a receiver, commutation elements, and fiber-optic waveguides. In the transmitter, electrical signals pass an electron control circuit and enter a semiconductor radiator (a laser or a light-emitting diode), where they are converted into optical signals that are fed via matching devices into a fiber-optic waveguide and propagate there to a specified point. A photodetector (PD) detects the radiation and performs the optoelectrical conversion and the subsequent amplification of the electrical signals.

Quartz is conventionally employed for optical waveguides incorporated in FOCLs. An absorption spectrum of high purity quartz typically features three windows of transparency in the vicinity of 0.85, 1.3, and 1.55  $\mu\text{m}$ . This region also corresponds to the nearest atmospheric transparency window. It is currently assumed that the near-infrared (IR) range from 1.3 to 1.55  $\mu\text{m}$  is the most appropriate for FOCL applications.

The wide use of FOCLs is hindered by the high cost of optical transmitter–receivers operating in the near-IR spectral region. It is expected that the implementation of a silicon-compatible technology for the production of photonic FOCL elements will significantly reduce the cost of such elements and allow monolithic integration of all components including radio-amplifying and shifting electronics on the basis of a simple, reliable, and easy-to-reproduce optoelectronic integrated circuit [1]. However, silicon itself is transparent for radiation with

a wavelength larger than 1.1  $\mu\text{m}$ . A fairly high sensitivity in the vicinity of the wavelength  $\lambda \approx 1.5 \mu\text{m}$  can be obtained with germanium PDs. This circumstance means that researchers are currently interested in developing Ge/Si heterostructures that are sensitive at room temperature within the telecommunication wavelength range from 1.3 to 1.55  $\mu\text{m}$ .

As for the prospects for incorporating Ge/Si heterostructures into the concept of silicon VLSI, Ge/Si heterostructures with coherently introduced Ge nanoclusters (quantum dots) are the most promising, since these structures offer the possibility of overgrowing the elastically stressed germanium layers with well-structured Si layers, which may serve as a base for the subsequent VLSI elements to be mounted on. Furthermore, such a system has already been employed in light-emitting diodes radiating at room temperature in the range 1.3–1.55  $\mu\text{m}$  with the quantum yield at a level of 0.015% [2].

Initially, Ge/Si photodiodes with Ge quantum dots (QDs) were designed for normal incidence of light on the side of the  $p-n$  junction plane [3, 4]. The quantum efficiency  $\eta$  ranged from 3 to 8% for  $\lambda = 1.3\text{--}1.46 \mu\text{m}$ . One can increase the quantum efficiency by using a waveguide structure that involves the effect of multiple internal reflection from the walls of the waveguide. Since the optical beams should propagate in the plane of the integrated circuit, which includes all the necessary FOCL elements [1], such a design is advantageously suited to end-on illumination of the detector. The fabrication of waveguide photodetectors based on Ge/Si heterostructures with coherently introduced Ge nanoislands was reported in [5, 6]. The highest quantum efficiency attained at the wavelength  $\lambda = 1.3 \mu\text{m}$

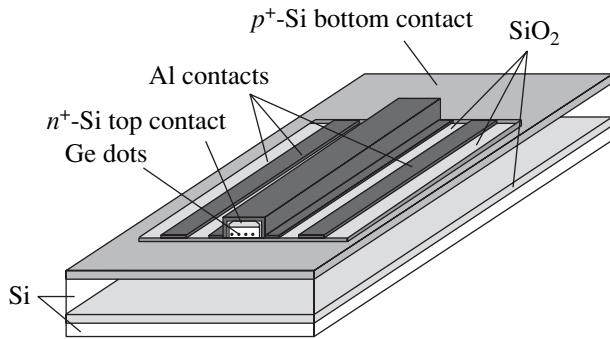


**Fig. 1.** Schematic representation of the photodetector formed on a silicon-on-insulator substrate.

was  $\eta = 5.3$  and  $9.5\%$  for a PD structure in the form of a  $p-i-n$  diode [5] and a bipolar  $n-p-n$  phototransistor [6], respectively. It should be noted that in [5, 6] the layer density of islands was  $1 \times 10^{11} \text{ cm}^{-2}$  or lower. Clearly, one way to further increase the quantum efficiency of photoconversion in such structures is to raise the density of Ge nanoclusters. The aim of this study is to develop a waveguide Ge/Si photodetector containing arrays of Ge QDs with a layer density at  $10^{12} \text{ cm}^{-2}$  and featuring high sensitivity over the telecommunication wavelength range.

## 2. PHOTODETECTOR PRODUCTION TECHNOLOGY

The photodetectors under study were silicon  $p-i-n$  diodes with 36 layers of Ge islands built into the base region that were divided by 30-nm-wide Si layers. Each device combined a vertical photodiode and lateral waveguide (Fig. 1). In order to obtain high-density germanium islands, they were formed by molecular-beam epitaxy (MBE) in the Volmer–Weber growth mode on a preliminarily oxidized silicon surface [7]. In our previous studies, it was shown that this procedure allows one to yield layers of Ge nanoclusters that are coherently matched to Si and have a layer density of up to  $10^{12} \text{ cm}^{-2}$  for sizes no larger than 10 nm [4, 7, 8].

As substrates, we used the silicon-on-insulator (SOI) wafers fabricated by SMART CUT technology (Wafer World, Inc.). The silicon layer cut off from the SOI structure and the buried oxide had thicknesses of 280 nm and 380 nm, respectively. The upper silicon layer was (100)-oriented. Before the MBE process, the silicon layer was thinned to 250 nm by thermal oxidation with subsequent etching of the oxide in a hydrofluoric acid solution. The diffraction pattern obtained from the silicon surface indicated that the SOI-wafer working layer was of high crystal quality and would be suitable for epitaxial growth. In the near-IR region, the difference between the Si and SiO<sub>2</sub> refractive indices is equal to two, which is sufficiently high to allow efficient spatial focusing of a beam propagating in the waveguide over the substrate plane.

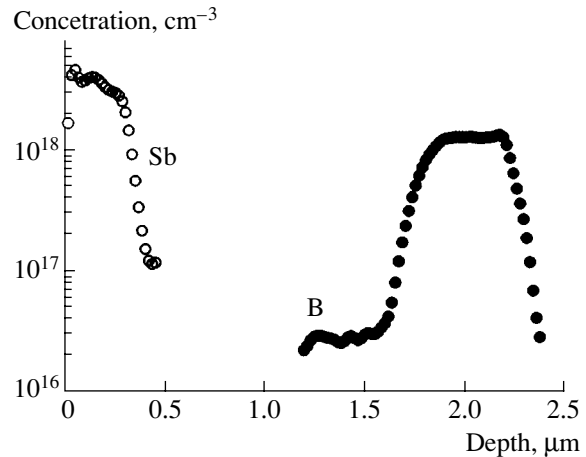


**Fig. 2.** SIMS profiles of boron and antimony concentrations across the epitaxial layer starting from the surface.

Both the Si and Ge layers were grown at  $500^\circ\text{C}$ . The growth rate was maintained at a level of 0.3 and 0.03 nm/s for Si and Ge, respectively. At first, after the conventional cleaning of the SOI surface, a 500-nm-thick  $p^+$ -Si layer doped with boron to a concentration of  $1 \times 10^{18} \text{ cm}^{-3}$  was grown; then, a 100-nm-thick buffer layer of nominally undoped Si was deposited. After that, oxygen was let into the growth chamber and the Si surface was oxidized for 10 min at an oxygen pressure of  $10^{-4} \text{ Pa}$  and a substrate temperature of  $500^\circ\text{C}$ . This procedure resulted in the formation of a SiO<sub>x</sub> layer with a thickness of several angstroms. Oxygen was then pumped out of the chamber so that the pressure decreased to  $10^{-7} \text{ Pa}$  and a 0.5-nm-thick Ge layer was deposited and overgrown with Si to a thickness of 30 nm. The overgrowth was preceded by an increase in the wafer temperature to  $600^\circ\text{C}$  over a short period (2 min). Such annealing was necessary for the subsequent growth of defect-free Ge layers. The last four procedures (oxidation, the deposition of a 0.5-nm-thick Ge layer, annealing for 2 min, and the deposition of a 20-nm-thick Si layer) were successively repeated 36 times. The resulting multilayer Ge/Si structure was covered with a 100-nm-thick Si layer. The background concentration of boron in the nominally undoped Si layers was  $3 \times 10^{16} \text{ cm}^{-3}$ . Finally, the formation of the  $p-i-n$  diode was completed by the growth of a 300-nm-thick  $n^+$ -Si layer (with an Sb concentration of  $4 \times 10^{18} \text{ cm}^{-3}$ ). Figure 2 shows the boron and antimony concentration profiles in the structure according to the data of secondary-ion mass spectrometry.

The state of the grown Ge layer surface was checked using scanning tunneling microscopy (STM). By statistical processing of the surface profiles, the average size of the Ge islands in the growth plane was estimated as  $\sim 8 \text{ nm}$ , and the density of islands,  $\sim 10^{12} \text{ cm}^{-2}$ . Reference specimens on silicon substrate–satellites were grown for Raman scattering (RS) and photoluminescence (PL) measurements. The sequence of layers was

the same as in the SOI wafers, except for the upper  $n^+$ -Si layer, which was absent in the reference structures. Also, the number of Ge layers in the reference structures was only 10 instead of 36.

The fabrication of PDs was continued on a silicon linear array using a specially designed set of photo-masks. The waveguide width was 50  $\mu\text{m}$  and the length varied from 100  $\mu\text{m}$  to 5 mm. The vertical walls were formed by the conventional photolithography method and plasma-chemical etching to a depth of 1.6  $\mu\text{m}$ . The buried  $\text{SiO}_2$  layer was used as a reflective coating on the substrate side, while a 70-nm-thick aluminum foil was used for the same purpose on the lateral walls of the waveguide, where it also served as an electrical contact to the upper  $n^+$ -Si layer. The illuminated end face of the waveguide, like all the other walls, was covered with a 225-nm-thick pyrolytic  $\text{SiO}_2$  layer, which also functioned as an antireflection layer at wavelength of 1.3  $\mu\text{m}$ .

### 3. RAMAN SCATTERING

We analyzed the structure of Ge nanoclusters using the data of Raman scattering (RS) spectroscopy. The RS spectra of the structures under excitation by Ar-laser radiation ( $\lambda = 514.5 \text{ nm}$ ) were detected at room temperature using a computer-controlled setup built around a DFS-52 spectrometer (LOMO, St. Petersburg) in the quasi-backscattering geometry. We used the polarization scattering geometry XY; i.e., the incident radiation was polarized along the crystallographic direction [001] ( $X$  axis) and the scattered radiation was detected in the polarization [010] ( $Y$  axis). This geometry was chosen since it is allowed for scattering by LO phonons in Ge and Si and is forbidden for two-phonon scattering by TA phonons from the silicon substrate. Thus, we avoided the difficulties encountered during the interpretation of RS spectra in [9].

Figure 3 shows the Raman spectra of a sample with Ge islands and a Si substrate in XY geometry and the spectrum obtained from the silicon substrate without the polarization analysis of the scattered light. The latter spectrum shows peaks that correspond to two-phonon RS by TA phonons of silicon and are similar to those observed in [9]. It can be seen that, in XY polarization geometry, these peaks have another shape and have an intensity that is more than one order of magnitude lower (for clarity and ease of comparison, the spectrum in XY geometry from the Si substrate is multiplied by a factor of 10). The spectrum of the sample with Ge nanoclusters contains peaks that correspond to RS by optical vibrations of Ge-Ge and Ge-Si bonds, as well as by optical vibrations of Si-Si bonds (from the substrate). Analysis of the position and intensity of the RS spectrum allowed us to estimate the stoichiometry level and the stresses in the Ge islands.

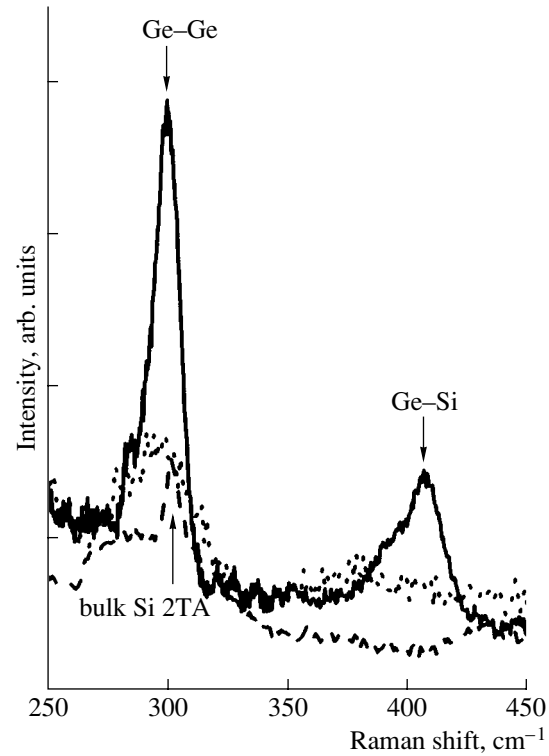


**Fig. 3.** Raman spectra (solid line) in a sample with Ge nanoclusters and (dotted line, with intensity multiplied by a factor of 10) in the Si substrate in XY geometry. The dashed line shows the spectrum from the silicon substrate without polarization analysis of the scattered light.

The integrated intensities of scattering by Ge-Ge and Ge-Si bonds are related as

$$\frac{I_{\text{GeGe}}}{I_{\text{SiGe}}} \approx B \frac{x}{2(1-x)}, \quad (1)$$

where  $B = 3.2$  [10]. Based on these data, we established the relative content of germanium in the islands  $x$  within the range 0.65–0.70.

We analyzed the position of the RS peaks using the approach described in [11, 12]. Since the optical-phonon frequency at the center of the Brillouin zone for bulk germanium equals 302  $\text{cm}^{-1}$ , the frequencies of Si-Si, Ge-Si, and Ge-Ge bonds can be approximated as

$$\begin{aligned} \omega_{\text{SiSi}} &= 520.5 - 62x - 8.15\varepsilon, \\ \omega_{\text{GeSi}} &= 400.5 + 14.2x - 5.75\varepsilon, \\ \omega_{\text{GeGe}} &= 302 - 18(1-x) - 3.85\varepsilon, \end{aligned} \quad (2)$$

where  $x$  is the Ge content in the islands and  $\varepsilon$  is the relative mismatch of the lattice constants. In [12] the values of these frequencies (in  $\text{cm}^{-1}$ ) are presented versus the composition (when  $x$  does not exceed 0.4) and the relative mismatch of the lattice constants in the plane of growth (100)  $\varepsilon$  (in percent). The shift is taken for Ge and is negative in the case of compression. Expressions (2)

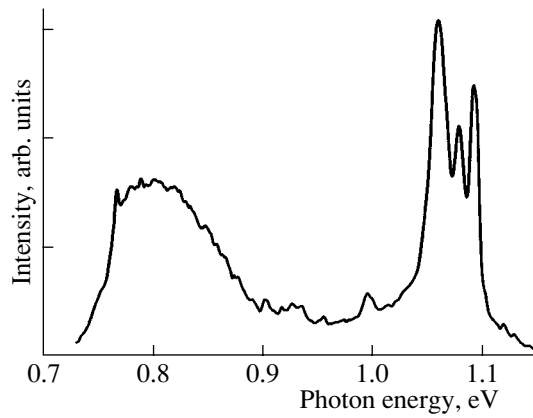


Fig. 4. PL spectrum measured at 4.2 K.

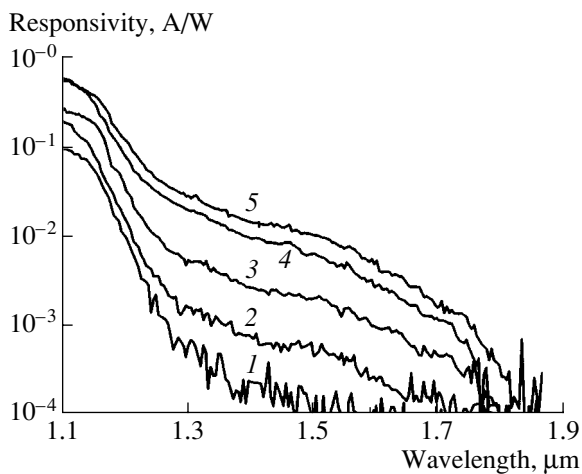


Fig. 5. Sensitivity spectra of the photodetectors with different waveguide length  $L$  in short-circuit mode:  $L = (1)$  0.2, (2) 0.5, (3) 1, (4) 2, and (5) 3 mm; room-temperature measurements.

extrapolate these dependences to the region of nanoclusters with the Ge content  $x$  approaching unity.

The maximum signal from Ge–Ge bonds is observed at  $300\text{ cm}^{-1}$  (Fig. 3). Taking into account that, because of the size-related quantum effect, the peak for 1.4-nm-high islands is shifted to lower frequencies by  $4\text{ cm}^{-1}$ , we can evaluate its position in unstrained  $\text{Ge}_{0.7}\text{Si}_{0.3}$  nanoclusters at  $292.5\text{ cm}^{-1}$ . Thus, the total shift due to stresses equals  $7.5\text{ cm}^{-1}$ . The maximum relative difference between the lattice constants in completely strained nonrelaxed  $\text{Ge}_{0.7}\text{Si}_{0.3}$  islands and the Si matrix is 2.9%. Hence, it follows that the maximal shift of the RS peak due to stress in nonrelaxed islands would equal  $11\text{ cm}^{-1}$ . This result means that the relaxation of stresses in germanium nanoclusters amounts to 30%.

#### 4. PHOTOLUMINESCENCE

The steady-state photoluminescence (PL) spectra were measured using a setup based on an SDL-1 double

monochromator with a 300 groove/mm grating (focal distance, 600 mm). The PL was excited using Ar-laser radiation ( $\lambda = 488\text{ nm}$ ) with a power density of  $25\text{ W/cm}^2$ . Emission was detected using a liquid-nitrogen-cooled germanium  $p$ – $i$ – $n$  photodiode (Edinburgh Instruments). Figure 4 shows the PL spectrum measured at 4.2 K. The spectrum features a set of lines in the range 1.05–1.1 eV that correspond to the exciton recombination in silicon and a broad band in the vicinity of 0.8 eV ( $\lambda = 1.55\text{ }\mu\text{m}$ ) attributed to indirect (in real space) optical recombination between holes localized in Ge islands and electrons at the type-II heteroboundary in Si. The low-energy edge of the PL signal from the islands is defined by the edge of the Ge-detector spectral characteristic. The presence of efficient PL in the wavelength range of interest allows one to hope that waveguide photodetectors will provide highly efficient photoconversion.

#### 5. PHOTOELECTRIC CHARACTERISTICS OF THE PHOTODETECTOR

Typical spectral dependences of the current–power sensitivity of the photodetector in the short-circuit mode (bias  $U = 0$ ) when the waveguide ends are illuminated are shown in Fig. 5. Different curves correspond to different waveguide lengths  $L$ . The photoresponse of the samples was measured at room temperature using an IKS-31 infrared spectrometer and a phase-sensitive nanovoltmeter at a modulation frequency of 560 Hz. The spectral characteristics of illuminance were obtained using a cooled CdHgTe photoresistor. In order to exclude the penetration of light into the substrate, which would lead to an erroneous value of illuminance because of an increase in the area that is illuminated in reality, the light beam was directed onto the detector from above at an angle of  $\sim 5^\circ$  relative to the normal to the detector's end face. As for the photosensitive area, we took the value  $50 \times 400\text{ }\mu\text{m}^2$ , where  $50\text{ }\mu\text{m}$  is the waveguide width and  $400\text{ }\mu\text{m}$  is the total thickness of the structure including the substrate. This procedure disregards the optical coupling of light in the waveguide and yields the lower-bound estimate of the sensitivity and quantum efficiency.

Figure 6 shows the dependences of quantum efficiency  $\eta$  at the wavelengths  $\lambda = 1.3$  and  $1.55\text{ }\mu\text{m}$  on the waveguide length and the reverse bias. The values of  $\eta$  were calculated from the relationship between the sensitivity  $R$ , photon energy  $h\nu$ , and the elementary charge  $e$ :  $R = (eh\nu)\eta$ . It turned out that the maximum quantum efficiency is attained in the structures with waveguide length  $L > 3\text{ mm}$  (Fig. 6a) at reverse bias  $U > 3\text{ V}$  (Fig. 6b) and is as high as 21 and 16% for wavelengths of 1.3 and  $1.55\text{ }\mu\text{m}$ , respectively. The flattening out of  $\eta$  observed in long waveguides apparently indicates that the light that penetrates the face of the edge and propagates over the germanium layers is completely absorbed in this case. We previously observed the flattening of the photoresponse with reverse bias in the

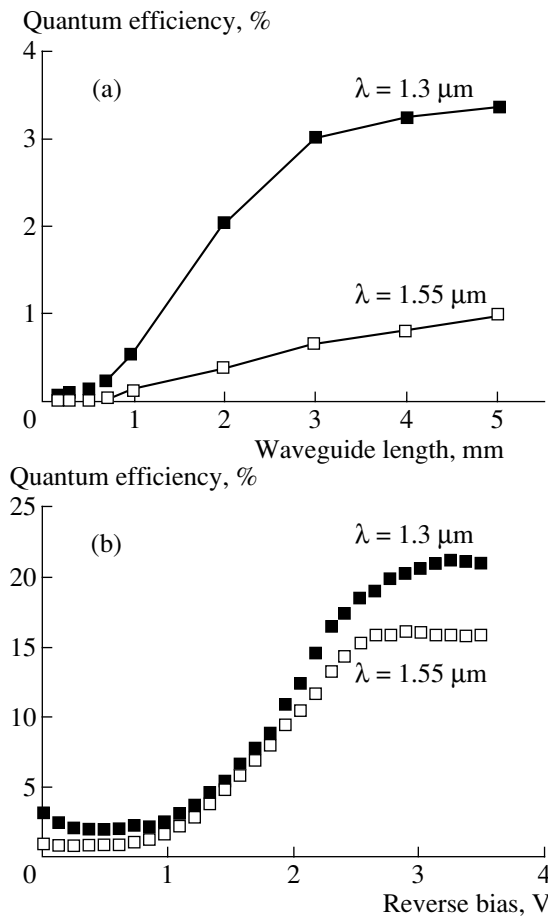


**Fig. 6.** Quantum efficiency at 1.3 and 1.55  $\mu\text{m}$  vs. (a) the waveguide length in short-circuit mode and (b) the reverse bias for the waveguide length  $L = 4 \text{ mm}$ .

conventional geometry of Ge/Si-based  $p-i-n$  photodiodes whose  $p-n$  junction side was illuminated [4]; we attributed this effect to the electric-field stimulation of ejection of photoholes localized in Ge islands into the valence band.

## 6. CONCLUSIONS

The main results of this study can be formulated as follows:

(i) A method for the production of waveguide silicon  $p-i-n$  photodiodes with built-in layers of Ge quantum dots on silicon-on-insulator substrates for the telecommunication wavelength range (1.3–1.55  $\mu\text{m}$ ) is developed. The layer density of quantum dots is  $10^{12} \text{ cm}^{-2}$ , and the dot size does not exceed 10 nm.

(ii) Due to both the effect of multiple internal reflection and the high density of Ge nanoclusters in the active region, we obtain a quantum efficiency of 21 and 16% at wavelengths of 1.3 and 1.55  $\mu\text{m}$ , respectively.

## ACKNOWLEDGMENTS

This study was supported by the Russian president's program for Young Doctors of Science (project no. MD-28.2003.02) and INTAS (grant no. 2001-0615).

## REFERENCES

1. H. Presting, *Thin Solid Films* **321**, 186 (1998).
2. W.-H. Chang, A. T. Chou, W. Y. Chen, *et al.*, *Appl. Phys. Lett.* **83**, 2958 (2003).
3. S. Tong, J. L. Wan, and K. Wang, *Appl. Phys. Lett.* **80**, 1189 (2002).
4. A. I. Yakimov, A. V. Dvurechenskiĭ, A. I. Nikiforov, *et al.*, *Fiz. Tekh. Poluprovodn. (St. Petersburg)* **37**, 1383 (2003) [*Semiconductors* **37**, 1345 (2003)].
5. M. Elcurdi, P. Boucaud, S. Sauvage, *et al.*, *Physica E (Amsterdam)* **16**, 523 (2003).
6. A. Elfving, G. V. Hansson, and W.-X. Ni, *Physica E (Amsterdam)* **16**, 528 (2003).
7. A. I. Nikiforov, V. V. Ul'yanov, O. P. Pchelyakov, *et al.*, *Fiz. Tverd. Tela (St. Petersburg)* **46**, 80 (2004) [*Phys. Solid State* **46**, 77 (2004)].
8. A. I. Yakimov, A. V. Dvurechenskii, A. I. Nikiforov, *et al.*, *Phys. Rev. B* **67**, 125318 (2003).
9. A. V. Kolobov, *J. Appl. Phys.* **87**, 2926 (2000).
10. P. M. Mooney, F. Dacol, J. C. Tsang, and J. O. Chu, *Appl. Phys. Lett.* **62**, 2069 (1993).
11. F. Cerdeira, C. J. Buchenauer, F. H. Pollak, and M. Cardona, *Phys. Rev. B* **5**, 580 (1972).
12. J. Groenen, R. Carles, S. Christiansen, *et al.*, *Appl. Phys. Lett.* **71**, 3856 (1997).

*Translated by A. Sidorova-Biryukova*

---

PHYSICS OF SEMICONDUCTOR  
DEVICES

---

# Indium Arsenide Light-Emitting Diodes with a Cavity Formed by an Anode Contact and Semiconductor–Air Interface

N. V. Zotova, N. D. Il'inskaya, S. A. Karandashev, B. A. Matveev<sup>^</sup>,  
M. A. Remennyi, N. M. Stus', and V. V. Shustov

*Ioffe Physicotechnical Institute, Russian Academy of Sciences, Politekhicheskaya ul. 26, St. Petersburg, 194021 Russia*

<sup>^</sup>*e-mail: bmat@iropt3.ioffe.rssi.ru*

Submitted March 2, 2004; accepted for publication March 4, 2004

**Abstract**—Room-temperature spectral characteristics of light-emitting diodes that are based on double InAsSbP/InAs heterostructures with an active InAs layer and a cavity formed by a wide anode contact and the structure surface and that emit near 3.3  $\mu\text{m}$  are considered. The far-field pattern and the mode structure of light-emitting diodes 7.5–45  $\mu\text{m}$  thick are reported, as well as the dependences of the mode position on the pump current. © 2004 MAIK “Nauka/Interperiodica”.

## 1. INTRODUCTION

In recent years, significant progress has been made in the development of infrared (IR) light-emitting diodes (LEDs) operating at room temperature and applicable to optical analyzers of methane that are based on absorption measurement near the fundamental band  $\nu_3$  (3.3  $\mu\text{m}$ ). The operating life of such light-emitting diodes exceeds 30000 hours [1], which is quite enough for most of applications.

Lattice-matched InAsSbP/InAs structures with an opaque InAs substrate that are grown by liquid-phase epitaxy (LPE) or metal-organic chemical vapor deposition (MOCVD) are most frequently used for the above purposes. The relevant literature contains a description of LEDs emitting at 3.3  $\mu\text{m}$  with a point top contact without antireflection coatings [2, 3]. According to [2, 3], the output power of such diodes was as high as 5 mW for pump currents of 1.4 and 12 A, respectively. This observation indicates a high internal quantum yield that far exceeds 50%, judging from the data of [2]. Due to a large refractive index ( $n = 3.52$ ) and a small angle of total internal reflection, as well as the inevitable crowding of current lines in the vicinity of the point contact, the LED designs described above are not optimal. Therefore, it can be expected that optimization of the contact configuration and antireflection of the surface will lead to a significant increase in LED power in the near future.

The development of an LED based on InAsSbP/InAs double heterostructures (DHs) grown on a transparent heavily doped  $n^+$ -InAs substrate with a wide reflecting anode contact is reported in [4]. The total internal reflection of these structures was decreased by combining the LED with immersion lenses shaped like hyperhemispheres [5]. Despite the high output power of radiation (10 mW, 5 A), such LEDs are characterized by a heavy temperature depen-

dence of power because of radiation extraction through  $n^+$ -InAs. This dependence is caused by the removal of electron degeneracy in the  $n^+$ -InAs conduction band at increased temperatures [6]. Another disadvantage is the temperature shift of the emission band, which, however, is suppressed using narrow-band filters [7, 8] with a certain loss of power in the maximum of spectrally filtered radiation.

At the same time, the development of a cavity with a thickness on the order of the emission wavelength, with faces arranged in parallel to the  $p$ - $n$  junction and integrated with it, eliminates the disadvantages mentioned above. This is achieved due to an increase in the yield of emission normal to the surface and simultaneous stabilization of the wavelength with respect to temperature variations. Corresponding LEDs with microcavities were actively studied in the near-IR spectral region (see, for example, [9, 10]); at the same time, studies of such LEDs in the mid-IR region are few in number. Microcavity LED structures of CdHgTe/HgTe with a series resistance of 80  $\Omega$  were grown by molecular-beam epitaxy (MBE) [11]. Such a high resistance combined with the low thermal conductivity of IV–VI materials results in a low efficiency of such devices. Optically excited LEDs based on lead chalcogenides, grown on BaF<sub>2</sub> or Si substrates, are described in [12, 13]. Far less attention was paid to LEDs with microcavities based on III–V materials, although they are characterized by high thermal conductivity and metallurgical stability. In [14] the output power at a wavelength of 4.2  $\mu\text{m}$  was increased twofold due to the presence of GaAs/AlAs Bragg mirrors bordering on the active region based on a superlattice of type II.

In this paper, we report on the resonant properties that appear in electroluminescence spectra near 3.3  $\mu\text{m}$  in InAsSbP/InAs DH grown by LPE on indium arsenide substrates, in which the Fabry–Perot cavity is



formed by a mirror anode contact and the surface of the semiconductor structure.

## 2. SAMPLES AND METHODS OF MEASUREMENT

The samples to be studied were prepared from InAsSbP/InAs DHs grown on (i) heavily doped  $n^+$ -InAs(Sn)(111) substrates ( $n > 10^{18} \text{ cm}^{-3}$ ) (type 1) and (ii) wide-gap buffer InAsSbP and InGaAsSb layers 2–40  $\mu\text{m}$  thick, preliminarily grown on the surface of undoped  $n$ -InAs(111) substrates ( $n \approx 2 \times 10^{16} \text{ cm}^{-3}$ ) (type 2). The DHs used were similar to those we described previously as applied to LEDs [4] and photodiodes [6] that had peaks of spectral characteristics at 3.3  $\mu\text{m}$ : the thicknesses of undoped InAs regions (active region) was 1–2  $\mu\text{m}$ , and the thicknesses of wide-gap layers (of  $n$ - and  $p$ -InAs $_{1-x-y}$ Sb $_x$ P $_y$  ( $x \approx 0.09$ ,  $y \approx 0.18$ ,  $p = 2\text{--}5 \times 10^{17} \text{ cm}^{-3}$ ) were 2–3  $\mu\text{m}$ .

To obtain structures with circular mesas 300  $\mu\text{m}$  in diameter, two-sided wet photolithography was used. Circular anode ( $D = 100$  or  $240 \mu\text{m}$ ) and U-shaped cathode contacts (Fig. 1) were deposited by sputtering followed by “hardening” using electrochemical deposition of gold. Contacts were not intentionally alloyed. In some samples, a window 100–140  $\mu\text{m}$  in diameter was etched from the substrate side above the central region of the anode contact, as shown in Fig. 2. Etching was carried out in three stages: uniform thinning of the entire substrate, etching through a mask with circular holes, and uniform thinning of the entire substrate including hollows obtained at the second stage.

Samples were cut or cleaved into chips  $0.95 \times 0.85 \text{ mm}$  in size, after which they were soldered onto silicon holders  $1.1 \times 1.6 \times 0.4 \text{ mm}$  in size with a corresponding configuration of contact regions. The assembled chips were soldered onto TO-18 headers.

Measurements were carried out at room and liquid-nitrogen (77 K) temperatures. To this end, a pulsed power supply was used with a duration of 5  $\mu\text{s}$  and a frequency of 500 Hz; cooled (77 K) InSb and CdHgTe photodiodes were used as detectors.

## 3. RESULTS AND DISCUSSION

Figure 3 shows typical electroluminescence spectra of type-2 diodes with a thickness in the window region of about 45  $\mu\text{m}$  and a wide anode contact ( $D = 240 \mu\text{m}$ ); the spectra were measured at temperatures of 77 and 300 K. The temperature shift of the contour enveloping all peaks corresponds to a change in the InAs band gap:  $dE_g/dT = 2.8 \times 10^{-4} \text{ eV/K}$ . As is evident from Fig. 3, the radiation is modulated, which is caused by the Fabry–Perot cavity, whose length is equal to the thickness of the structure on the assumption that the average refractive index in the structure is  $n = 3.5$ . This is illustrated by the data of Fig. 4, which shows that the intermode distance in the LED with  $\lambda = 3.3 \mu\text{m}$  and thicknesses of

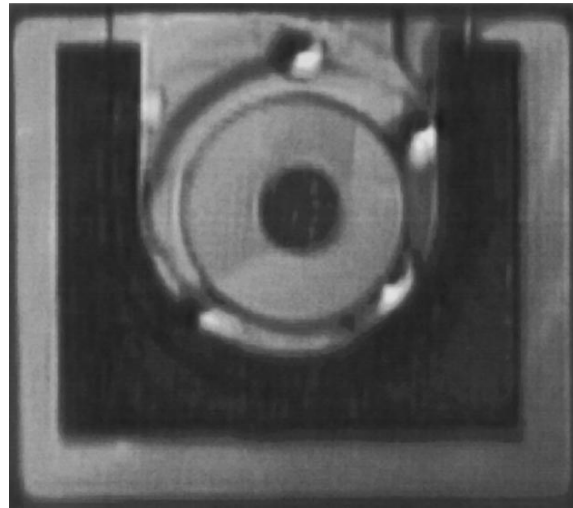


**Fig. 1.** View of the contact surface of the light-emitting diode chip with mesa and anode contact diameters of 300 and 100  $\mu\text{m}$ , respectively. The etched “window” is not seen, since it is on the opposite side of the chip.

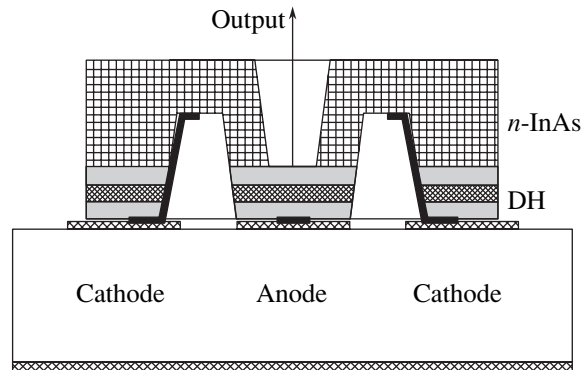


**Fig. 2.** Schematic representation of the LED fabricated using “flip-chip” technology with a “window” in the substrate:  $n$ -InAs substrate; InAs/InAsSbP double heterostructure (DH); and a silicon holder with Pb+Sn contact regions.

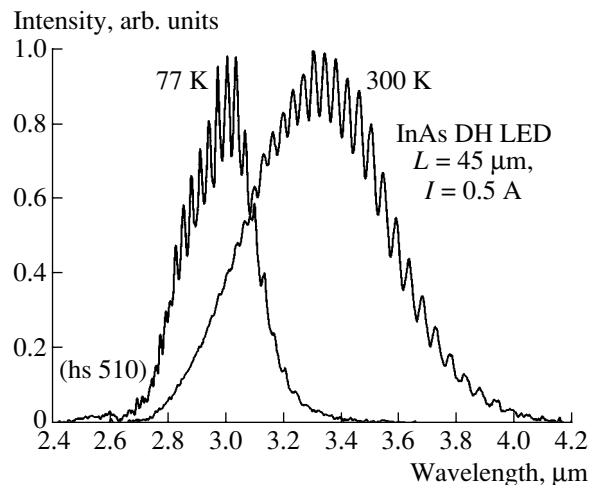


**Fig. 3.** Electroluminescence spectra of the 45- $\mu\text{m}$ -thick LED at 77 and 300 K.

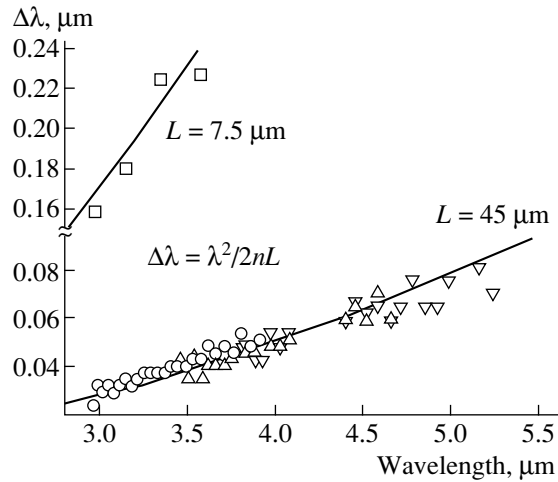


**Fig. 4.** Distance between luminescence peaks in the 45- $\mu\text{m}$ -thick LED (circles correspond to the data of Fig. 3; triangles are the data on positive/negative luminescence of the InGaAsSb LED [15]) and in the 7.5- $\mu\text{m}$ -thick LED (squares correspond to the data of Fig. 6).

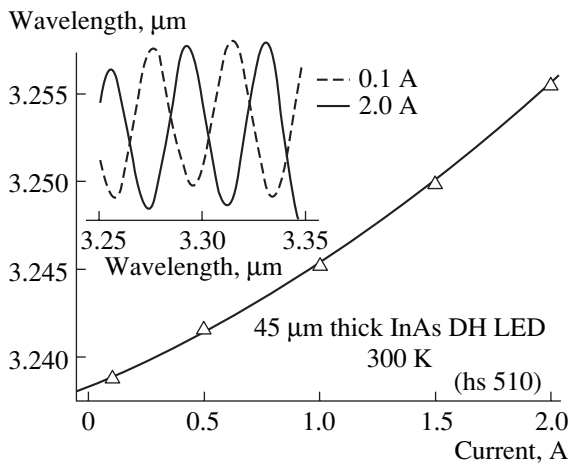


**Fig. 5.** Dependence of the spectral position of a chosen emission peak on the pump current. The inset shows the emission spectrum at currents of 0.1 and 2 A in the range from 3.30 to 3.36  $\mu\text{m}$ .

7.5  $\mu\text{m}$  (upper curve, squares) and 45  $\mu\text{m}$  (lower curve, circles), as well as in the LED with  $\lambda = 3.9 \mu\text{m}$  and a thickness of 45  $\mu\text{m}$  (lower curve, triangles [15]), are adequately described as  $\Delta\lambda = \lambda^2/2nL$ ,  $n = 3.5$ .

We note that the intermode distance in the long-wavelength region ( $\lambda > 4.5 \mu\text{m}$ , Fig. 4) was obtained by measuring the negative luminescence in InGaAsSb-based diodes at a temperature of 180°C. Thus, the monotonic variation in the intermode distance in the entire wavelength range indicates that the refractive index varies with temperature only slightly. At the same time, the spectral position of some modes shifted to longer wavelengths as current increased (at a rate of  $\sim 10 \text{ nm/A}$ ), as shown in Fig. 5. We could assume that

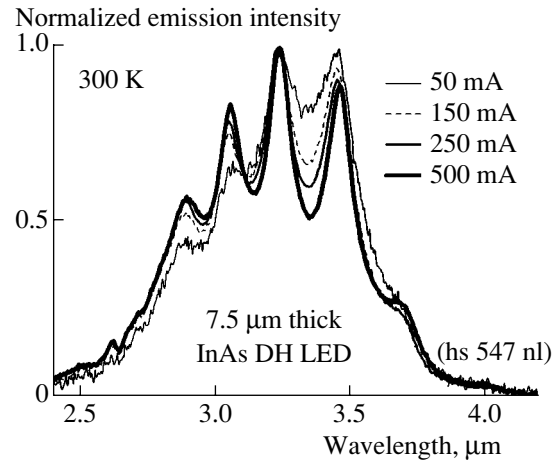


**Fig. 6.** Normalized electroluminescence spectra of the 7.5- $\mu\text{m}$ -thick LED at pump currents of 50, 150, 250, and 500 mA.

Joule heating takes place in the diodes; however, we do not expect a substantial contribution from the temperature-induced “expansion” of the cavity to the observed effect, since the active region is close to the heat sink, the series resistance is low, and the InAs linear-expansion coefficient is small. The process of current retuning of modes will be the subject of our next study, since current modulation of radiation can be very useful in fine spectral measurements.

Figure 6 shows the emission spectrum of the thinnest (in this study) LED, in which the central region of the mesa did not contain a substrate (type I) and the anode contact diameter was 100  $\mu\text{m}$ . The total thickness, including the thickness of wide-gap InAsSbP layers and the InAs active layer, was estimated at 7.5  $\mu\text{m}$ . We can see in Fig. 6 that the contrast increases with current in the range 50–500 mA, which is similar to superluminescence initiation at resonant peaks with high levels of injection. However, we cannot insist on explaining the increase in contrast by superluminescence initiation, since an important feature of this luminescence, i.e., the superlinear current–power characteristic, was not observed in the experiments we conducted. The output power in the LED under study increased with current; however, this dependence was sublinear, which is characteristic of most LEDs in this spectral region (see, for example, [2, 3]). Another observation that means that we cannot restrict our analysis to consideration of superluminescence is the fact that the contrast did not increase with current in structures with wide contacts (240  $\mu\text{m}$ ). The most probable explanation for this is the redistribution (crowding) of current lines in samples with a contact diameter of 100  $\mu\text{m}$ , which is referred to as “current crowding” and is observed in an absolute majority of LEDs with small contacts [16, 17]. Indeed, in the case under consideration, it is quite reasonable to admit that radiation is summed from two regions: (i) the region located imme-

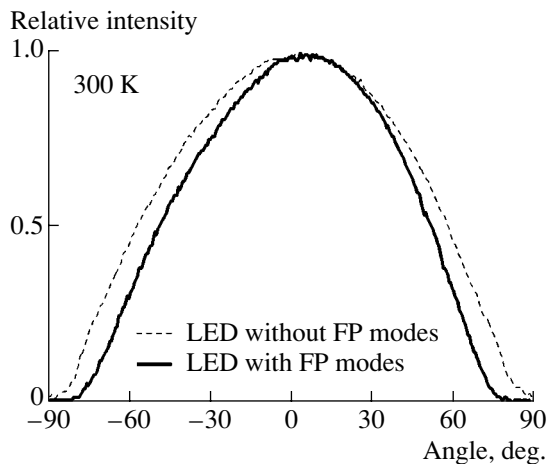


**Fig. 7.** Pattern of the electroluminescence far field of the LED with well-defined (bold curve) and poorly defined (thin curve) spectral resonances.

diately above the anode contact that is subjected to a significant effect of interference due to the high reflectance of gold and (ii) the region enveloping the former region with a ring. The second region is characterized by low reflectance from the  $p$ -InAsSbP surface without a gold coating (note that the “window” diameter was slightly larger than the contact diameter). At low currents, both regions contribute to the radiation emitted by the semiconductor, although the contribution of the first region prevails due to reflection from the contact. As the current increases, its lines crowd above the contact, which decreases the relative contribution of regions outside the contact. Hence, resonant peaks are intensified and the contrast in the spectrum increases with current, since radiation of the above-contact region of the mesa is modulated by the cavity.

The use of a transparent cavity leads to a decrease in the optical losses associated with total internal reflection. In the experiment, this effect is accompanied by a narrowing of the far-field pattern of the LED radiation, which exhibits pronounced resonant peaks in the emission spectrum (see Fig. 7) and an increase in the Q-factor with cavity length. The Q-factors for the samples with thicknesses 7.5, 13, and 45  $\mu\text{m}$  were estimated by the mode half-width as 24, 32, and 80, respectively. Incidentally, note that the actual (unnormalized) intensities of the resonant peaks shown in Fig. 6 are at least 25% higher than the corresponding intensities for similar samples exhibiting no resonant peaks. This circumstance suggests that in samples with high Q-factors an actual redistribution of radiation power occurs, which is characteristic of LEDs with microcavities (i.e., RC LEDs).

As we noted previously [6], electron degeneracy in the conduction band of heavily doped indium arsenide is eliminated as temperature increases; i.e., the Burstein–Moss effect is suppressed with a corresponding increase in absorption near the spectral band at 3.3  $\mu\text{m}$ .

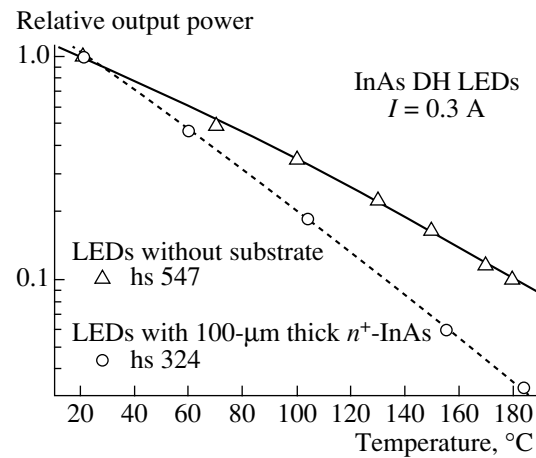


**Fig. 8.** Temperature dependence of the output power of the 3.3- $\mu\text{m}$  LED based on a InAsSbP double heterostructure with a heavily doped substrate (circles) and without a substrate (i.e., with a window) (triangles).

Therefore, it might be expected that LEDs without a substrate would have better characteristics at increased temperatures. Indeed, as can be seen from Fig. 8, the falloff of the temperature dependence of the output power in the LED without substrate (type 1) is less steep than in the LED in which radiation passes through  $n^+$ -InAs 100  $\mu\text{m}$  thick.

In conclusion, we note that, despite the thin structures in the “windows” region, only an insignificant number of LEDs had mechanical damage that prevented them from being used. In our opinion, the high reliability of the structure is caused by weak thermal stresses characteristic of the InAsSbP/InAs system.

#### 4. CONCLUSIONS

Resonant peaks and narrowing of the pattern of the far field caused by the interference of rays directed normally to the  $p$ - $n$  junction inside the Fabry–Perot cavity formed by the gold anode and the semiconductor–air interface were observed in light-emitting diodes (LEDs) 7.5–45  $\mu\text{m}$  thick based on InAsSbP/InAs DHs emitting near 3.3  $\mu\text{m}$ . The LED Q-factor was 24–80, and the rate of current retuning of the spectral peak positions of the radiation mode structure was  $\sim 10$  nm/A.

#### ACKNOWLEDGMENTS

This study was supported by the federal program “Optics and Laser Physics,” Schlumberger Oilfield Services with administrative support from the CRDF, and the SBIR/STTR program.

N. Zotova and M. Remennyi acknowledge the federal program “Support for Leading Scientific Schools” (project no. MK-1597.2003.02).

## REFERENCES

1. B. A. Matveev, G. A. Gavrilov, V. V. Evstropov, *et al.*, *Sens. Actuators B* **38–39**, 339 (1997).
2. S. S. Kizhaev, N. V. Zotova, S. S. Molchanov, and Yu. P. Yakovlev, *IEE Proc.: Optoelectron.* **140**, 36 (2002).
3. D. A. Wright, V. V. Sherstnev, A. Krier, *et al.*, *IEE Proc.: Optoelectron.* **150**, 314 (2003).
4. B. A. Matveev, N. V. Zotova, N. D. Il'inskaya, *et al.*, *J. Mod. Opt.* **49**, 743 (2002).
5. R. C. Johnes, *Appl. Opt.* **1**, 607 (1962).
6. B. A. Matveev, N. V. Zotova, S. A. Karandashev, *et al.*, *Proc. SPIE* **4650**, 173 (2002).
7. S. D. Smith, J. G. Crowder, and H. R. Hardaway, *Proc. SPIE* **4651**, 157 (2002).
8. M. Aidaraliev, N. V. Zotova, N. D. Il'inskaya, *et al.*, *Semicond. Sci. Technol.* **18**, 269 (2003).
9. T. J. Rogers, D. G. Deppe, and B. G. Streetman, *Appl. Phys. Lett.* **57**, 1858 (1990).
10. E. F. Schubert, Y.-H. Wang, A. Y. Cho, *et al.*, *Appl. Phys. Lett.* **60**, 921 (1992).
11. E. Hadji, J. Bleuse, N. Magnea, and J. L. Pautrat, *Appl. Phys. Lett.* **67**, 2591 (1995).
12. K. Kellermann, D. Zimin, K. Alchalabi, *et al.*, *IEE Proc.: Optoelectron.* **150**, 337 (2003).
13. W. Heiss, M. Bolberi, T. Schwarzzi, *et al.*, *IEE Proc.: Optoelectron.* **150**, 332 (2003).
14. D. Gevaux, A. Green, C. Palmer, *et al.*, *IEE Proc.: Optoelectron.* **150**, 360 (2003).
15. M. A. Remennyi, B. A. Matveev, N. V. Zotova, *et al.*, *Physica E (Amsterdam)* **20**, 548 (2004).
16. V. K. Malyutenko, O. Yu. Malyutenko, A. D. Podoltsev, *et al.*, *Appl. Phys. Lett.* **79**, 4228 (2001).
17. Zh. I. Alferov, A. T. Gorelenok, I. G. Gruzlov, *et al.*, *Pis'ma Zh. Tekh. Fiz.* **8**, 257 (1982) [*Sov. Tech. Phys. Lett.* **8**, 113 (1982)].

*Translated by A. Kazantsev*

## Microwave Field-Effect Transistors Based on Group-III Nitrides

S. B. Aleksandrov\*, D. A. Baranov\*, A. P. Kaïdash\*, D. M. Krasovitskii\*, M. V. Pavlenko\*,  
S. I. Petrov\*<sup>^</sup>, Yu. V. Pogorel'skii\*, I. A. Sokolov\*, M. V. Stepanov\*, V. P. Chalyi\*,  
N. B. Gladysheva\*\*, A. A. Dorofeev\*\*, Yu. A. Matveev\*\*, and A. A. Chernyavskii\*\*

\*ZAO Scientific and Technology Equipment, St. Petersburg, 194156 Russia

<sup>^</sup>e-mail: support@semiteq.ru

\*\*State Unitary Enterprise Pulsar, Moscow, 105187 Russia

Submitted February 4, 2004; accepted for publication March 17, 2004

**Abstract**—A concept for the design of experimental AlGa<sub>n</sub>/Ga<sub>n</sub>/AlGa<sub>n</sub> double heterostructures with a two-dimensional electron channel are discussed, together with their main properties. The structures were formed by ammonia molecular-beam epitaxy on sapphire substrates. The foundations for postgrowth technology are developed for microwave field-effect transistors based on Group-III nitrides, including the formation of a mesa isolation and the preparation stage of nonrectifying contacts and the Schottky barrier. The first field-effect transistors fabricated based on the above heterostructures have a complete set of static characteristics and can operate in a mode of weak microwave signals at a frequency of 8.15 GHz. © 2004 MAIK “Nauka/Interperiodica”.

### 1. INTRODUCTION

Group-III nitrides have found increasingly wide application in solid-state electronics due to the unique combination of their physical properties: wider band gaps compared to other III–V compounds, high heat conductivity, chemical and thermal stability, the presence of spontaneous polarization and piezopolarization, and so on. The high electron density in a channel combined with high breakdown fields provide a density of microwave power in GaN-based field-effect transistors that is higher than in GaAs-based devices by a factor of 5–10. This circumstance makes this class of devices promising for use in airborne radars with an active phased antenna array and in general and special purpose microwave amplifiers, namely, electronic warfare systems and surface and satellite telecommunication and communication systems. The main technologies for growing device nitride heterostructures are epitaxy from metal-organic compounds (MOVPE) and molecular-beam epitaxy (MBE). In the early 1990s, the first so-called PEFET piezotransistors (Piezoelectric Field-Effect Transistors) based on the GaAs/InGaAs/AlGaAs system [1, 2] and the first HFET (Heterostructure Field-Effect Transistors) and HEMT (High Electron-Mobility Transistors) transistors based on AlGa<sub>n</sub>/Ga<sub>n</sub> heterojunctions were reported [3, 4]. Until now, foreign companies have achieved considerable progress in fabricating high-frequency high-power field-effect transistors based on GaN. In 2000, an HFET with an output power of 2.8 W/mm,  $f_T = 43$  GHz, a transconductance of 300 mS/mm, and a drain–source breakdown voltage of 70 V was announced [5]; this transistor was formed on a SiC substrate. Recently, Oki Electric Industry Co. Ltd. (Japan) reported the fabrication of an HEMT with

a deep *T*-shaped gate [6], which has a record transconductance of 500 mS/mm and  $f_T = 126$  GHz.

In this paper, we report on a concept for the design of transistor double heterostructures based on Group-III nitrides that has been adopted at ZAO Scientific and Technology Equipment, along with the main properties of the experimental samples obtained within the framework of this concept using MBE with ammonia as the nitrogen source. We also report on the first field-effect transistors fabricated based on these heterostructures at the State Unitary Enterprise Pulsar. These transistors have a complete set of static characteristics and can operate in a mode of weak microwave signals.

### 2. SELECTION OF DESIGN FOR FIELD-EFFECT TRANSISTORS BASED ON GROUP-III NITRIDES

The most widespread design for an AlGa<sub>n</sub>/Ga<sub>n</sub> heterostructure, which is used worldwide for the fabrication of microwave HEMTs, includes a relatively thick (1–3 μm) GaN buffer layer coated with a thin (100–300 Å) Al<sub>x</sub>Ga<sub>1-x</sub>N layer (0.15 < *x* < 0.35). Due to the larger conduction-band offset compared with the GaAs/AlGaAs system combined with the piezodoping effect, a two-dimensional electron gas (2DEG) is formed at the GaN/AlGa<sub>n</sub> heterointerface. The layer density in a 2DEG is about 10<sup>13</sup> cm<sup>-2</sup>, and the mobility is about 1000 cm<sup>2</sup>/(V s). The profile of the bottom of the conduction band and the distribution of the electron density in such a structure are schematically shown in Fig. 1a. This structure is the basic concept of the design of HEMT based on Group-III nitrides. In practice, various modifications of this structure are used; for example, modulation doping of the AlGa<sub>n</sub> layer (spacer–donor layer–barrier layer) is used to increase the elec-

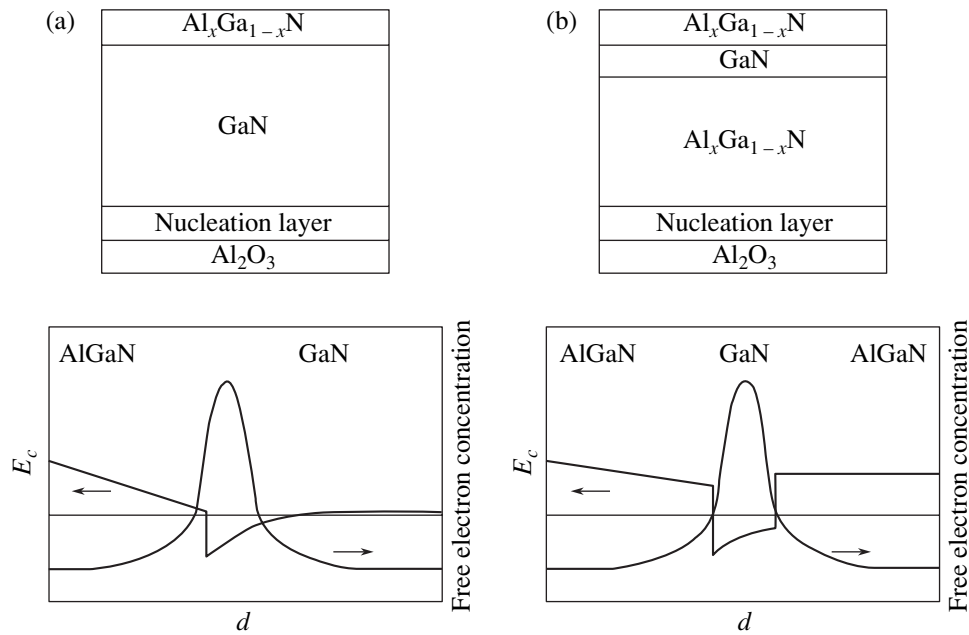


Fig. 1. Transistor structure (a) with one heterojunction and (b) with two heterojunctions.

tron density in the channel and to decrease the resistance of nonrectifying contacts.

One of the most serious requirements for all types of these heterostructures is a low (no higher than  $10^{15} \text{ cm}^{-3}$ ) carrier density in the buffer layer, which is necessary to provide interdevice isolation and to attain a complete cutoff of the drain current.

There are several reasons why the fulfillment of this requirement by growing undoped GaN (even of a high structural quality) encounters considerable difficulties. First, nucleation layers, which are used at the initial stages of growth of nitrides on lattice-mismatched substrates ( $\text{Al}_2\text{O}_3$ , SiC, Si), can form a region with conduction by defects at the interfaces of the buffer and nucleation layers [7]. Second, it was reported that donor impurities, namely, oxygen [8–10] and silicon [11, 12], diffuse into GaN from the substrate. This process can lead to the formation of shunting conduction channels in the device. In addition, the existence of spontaneous polarization and piezopolarization leads to the formation of both positive and negative induced charges at defects, at the boundaries of the blocks of the mosaic structure, and at the heterointerfaces. In turn, this phenomenon can enhance the leakage via vertical channels right up to the breakdown through the buffer layer. The combined effect of these circumstances necessitates special additional precautions to provide the required resistance of the buffer layer in real device heterostructures operating at voltages higher than 50 V.

There are several approaches to fabricating a high-resistivity buffer layer in a transistor structure. First, one must choose and optimize the growth conditions of undoped GaN. Specifically, it was shown that the resis-

tivity of the layers can vary by several orders of magnitude depending on the variation in the ratio of III/V fluxes, the thermal treatment of the nucleation layer, the temperature, and the growth rate [13]. However, such a substantial variation in the conductivity of GaN is generally associated with the variation in its other properties, namely, the structural quality, the surface profile, etc. This circumstance gives rise to certain difficulties when one combines various modes of growth of layers in a single device heterostructure. It is quite common to compensate the doping of GaN with various impurities [14–16]. As a rule, the resistance of the buffer layer in these cases is sufficient to prevent leakage and breakdown. However, this procedure includes the danger that the impurities introduced will diffuse into the transistor channel, and this effect may be enhanced by the high operating temperatures (about 300–400°C) of nitride devices. Furthermore, a wider-gap material can be used as the buffer layer, specifically,  $\text{Al}_x\text{Ga}_{1-x}\text{N}$  solid solutions right up to pure AlN, which is an excellent insulator with a band gap of 6.2 eV.

The latter of these concepts, which differs radically from those mentioned above, implies the use of double heterostructures with the additional advantages inherent in this class of device. First, in a double heterostructure, carriers are localized more strongly in a channel (right up to the formation of quantum wells) compared to a structure with a single heterojunction, which causes a necessary cutoff of the drain current. Second, unlike the structure shown in Fig. 1a that has a tensile stressed AlGaN layer on a thick relaxed GaN layer, the upper layers are compressed in the structure shown in Fig. 1b. This should be a favorable factor in overcoming the problem of relaxation of the upper barrier layer via

the formation of microcracks and the associated degradation of parameters of the channel with a 2DEG, which is often observed in traditional nitride heterostructures [17]. In addition, the use of a double heterostructure provides wide possibilities for controlling the stresses in such a structure and, consequently, for controlling the piezodoping effect due to varying the aluminum content in the bottom layer and the thickness of the channel GaN layer. Third, introducing a wide-gap material into the bottom part of the heterostructure makes it possible to further dope the channel, thus increasing the carrier density in it without the risk of worsening the gate characteristics of the transistor [18]. Moreover, doping can be completely transferred into the bottom part of the structure, which would allow a decrease in the thickness of the gate AlGaN layer in order to increase the device amplification.

These advantages were successfully realized for other III–V systems, specifically, the AlGaAs/GaAs system [19]. However, the influence of strong polarization effects should be taken into account in the nitride system. These effects significantly distort the energy-band diagram or the potential profile specified by the variation in the composition. Monitoring the stresses in a structure consisting of layers that are lattice-mismatched to each other and to the substrate calls for individual investigation. Despite the difficulties mentioned above, below we present experimental results that show that the chosen approach is promising.

### 3. EXPERIMENTAL

The AlGaN/GaN heterostructures (Table 1) were grown on sapphire (0001) substrates using an EPN-2 MBE installation. The installation was specially designed for the growth of layers of Group-III nitrides. Ammonia was used as the source of active nitrogen, and standard effusion cells were used as the source of Group-III elements and doping impurities [20]. The distinctive design feature of this equipment is the range of technology parameters, which is wider than traditional MBE systems. These are, first and foremost, the III–V flux ratio (1–1000) and the substrate temperature (as high as 1050°C).

The main difference between the heterostructures used by us [21] and the most widespread HEMT design is the presence of a relatively thick (0.6–1.0  $\mu\text{m}$ ) buffer layer that consists of layers of  $\text{Al}_x\text{Ga}_{1-x}\text{N}$  solid solutions ( $x > 0.5$ ), which provides high (over 200 V) breakdown voltages of the interdevice isolation. This is followed by a nominally undoped GaN layer (350–500 Å). This layer is coated with an  $\text{Al}_{0.3}\text{Ga}_{0.7}\text{N}$  layer, which is undoped (PEFET) or modulation-doped with Si (HFET).

According to the Hall measurements, the carrier mobility at 77 K increases to 800–1500  $\text{cm}^2/(\text{V s})$  with the conservation of the carrier layer concentration observed at room temperature, which is an indication

**Table 1.** Characteristics of the starting heterostructures and the types of fabricated devices

Transistor type	Hall mobility at 300 K, $\text{cm}^2/(\text{V s})$	Hall concentration at 300 K, $\text{cm}^{-2}$	Structure design (from top to bottom)
PEFET	360	$9 \times 10^{12}$	250 Å $\text{Al}_{0.2}\text{Ga}_{0.8}\text{N}$ 500 Å GaN Buffer $\text{Al}_{0.6}\text{Ga}_{0.4}\text{N}/\text{AlN}$
HFET	340	$2 \times 10^{13}$	80 Å $\text{Al}_{0.3}\text{Ga}_{0.7}\text{N}^*$ $100 \text{ Å } 3 \times 10^{19} \text{ cm}^{-3}$ $\text{Al}_{0.3}\text{Ga}_{0.7}\text{N}\langle\text{Si}\rangle$ 40 Å $\text{Al}_{0.3}\text{Ga}_{0.7}\text{N}^*$ 350 Å GaN Buffer $\text{Al}_{0.6}\text{Ga}_{0.4}\text{N}/\text{AlN}$

Note: An asterisk denotes an undoped layer.

**Table 2.** Static characteristics of fabricated transistors ( $W_g = 60 \mu\text{m}$ )

Transistor type	Saturation source–drain current at $U_g = 0$ , mA	Transconductance, mS/mm	Cutoff voltage, V	Saturation source–drain voltage, V
PEFET	0.1–0.05	40–50	0.6	2
HFET	30–40	92–96	6	10–12

that a 2DEG forms at the AlGaN/GaN interface. According to the data of atomic-force microscopy, the transistor heterostructures have a surface roughness of 0.9–3.3 nm (RMS by an area of  $5 \times 5 \mu\text{m}$ ). For a test GaN sample 1  $\mu\text{m}$  thick that was grown under the growth conditions of the transistor structure, the half-widths of the X-ray diffraction curves of  $\theta$ - and  $2\theta$ -scanning for the symmetric Bragg reflection were  $276''$  and  $55''$ . The total density of defects was not estimated for all the heterostructures. However, according to indirect data, this density is no lower than  $5 \times 10^9 \text{ cm}^{-2}$ . To improve the homogeneity of the layers and to decrease the defect density, we are now optimizing the design of the heterostructures and the technology for fabricating them, the results of which will be published later.

Based on these heterostructures (Table 1), we fabricated transistors with gate length  $L_g = 0.5\text{--}0.6 \mu\text{m}$ , a drain–source distance of 3  $\mu\text{m}$ , and gate widths of 60, 150, and 250  $\mu\text{m}$ . The mesa isolation was performed by plasmochemical etching with a photoresist mask. The Ti/Al/Pt nonrectifying contacts were formed using contact burst photolithography with subsequent thermal treatment in nitrogen at 700°C. For the structures under consideration, the resistivity of nonrectifying contacts was  $(2\text{--}3) \times 10^{-4} \Omega \text{ cm}^2$ . The Ni/Au gate was formed by contact burst photolithography using short-wavelength ultraviolet radiation. The static parameters of the fabri-



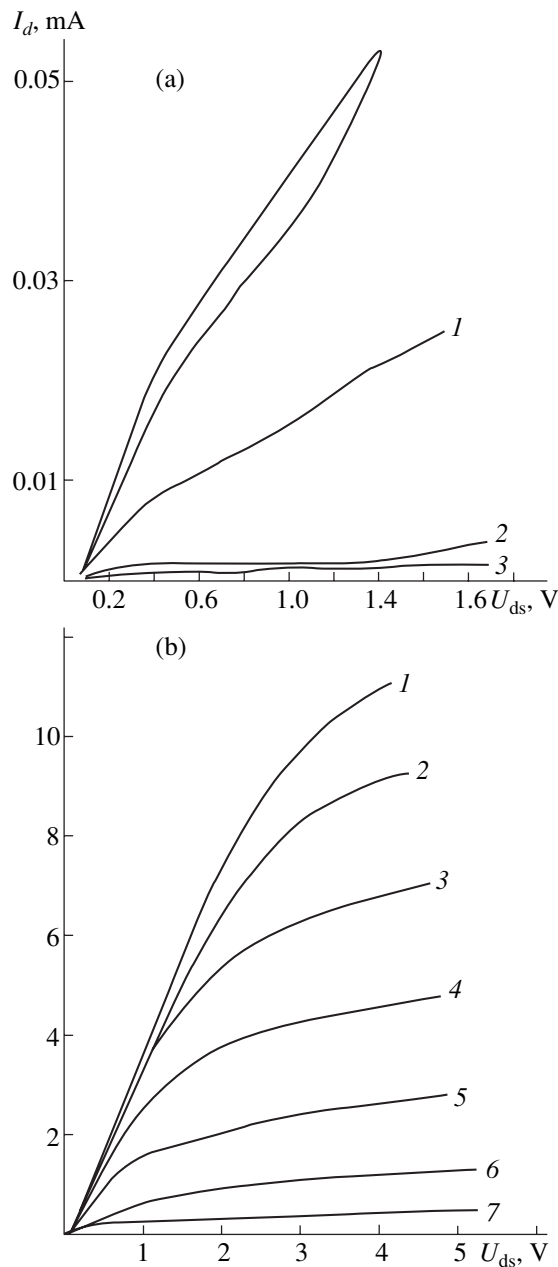


**Fig. 2.** Static current–voltage characteristics of transistors. (a) PEFET type:  $U_g = (1) -0.2$ , (2)  $-0.4$ , and (3)  $-0.6$  V. (b) HFET type:  $U_g = (1) -3.0$ , (2)  $-3.5$ , (3)  $-4.0$ , (4)  $-4.5$ , (5)  $-5.0$ , (6)  $-5.5$ , and (7)  $-6.0$  V.

cated devices are given in Table 2, and their current–voltage characteristics are shown in Fig. 2.

The fabricated devices exhibit a complete set of static characteristics. The necessary isolating properties

**Table 3.** Microwave parameters of the HFET based on the AlGa*N*/*i*-Ga*N*/*n*-AlGa*N* double heterostructure ( $W_g = 250$   $\mu$ m)

$F_{\text{meas}}$ , GHz	$K$ , dB	$U_{ds}$ , V	$U_{gs}$ , V	$I_{ds}$ , mA
8.15	4.46–4.53	12	–(3.38–3.86)	30

of the bottom part of the heterostructure provide a pronounced leveling-off of the characteristic and a complete cutoff of the drain current. However, low source–drain currents in the PEFET are inconsistent with the values expected from the measured Hall concentration. This is apparently associated with an insufficiently optimized procedure for welding the nonrectifying contacts as applied to the heterostructure with strong built-in fields. Consequently, the concentration of carriers formed due to the piezoelectric effect at the AlGa*N*/Ga*N* interface decreases. In HFETs with the modulation-doped Al<sub>0.3</sub>Ga<sub>0.7</sub>N ternary solid solution, the structure is more resistant to external effects due to the stabilization of the carrier concentration in the channel. However, doping the ternary solid solution decreases the breakdown voltage of the gate. Further optimization is necessary to reconcile the requirements for heterostructures and those for the technology of contact metallization.

One of the problems that arise in developing the technology for fabricating these transistors is the division of the wafers into individual crystals. The technologies of cutting used in fabricating other semiconductor devices lead to the emergence of inadmissible variations in the properties of the heterostructures under consideration due to the appearance of stresses (cutting with diamond discs) or thermal impact (laser cutting). This problem was not resolved at the initial stage and requires further study. Therefore, the microwave characteristics of the obtained transistors were measured directly on the wafer. Starting from the parameters of the measurement bench based on a Kh5-36 noise coefficient meter and a microwave probe contact facility developed at Pulsar, we selected for study HFET-type devices with  $W_g = 250$   $\mu$ m. The results of measurements under conditions of weak input signals are given in Table 3 (for values of  $K$  and  $U_{gs}$ , their ranges are given for three samples). As  $U_{ds}$  increased to 20 V,  $K$  was virtually constant, and the values of  $I_{ds}$  corresponded to the peak value of  $K$ . As far as we know, we are the first to demonstrate the ability of transistor structures based on Group-III nitrides fabricated in Russia to operate in a microwave mode.

#### 4. CONCLUSIONS

(i) We developed concepts of technology for fabricating field-effect transistors based on Group-III nitrides for two types of double heterostructures. These concepts include etching of a mesa isolation and the stage of fabrication of nonrectifying contacts (source and drain) and Schottky barriers (gate).

(ii) We fabricated field-effect transistors that exhibit a complete set of static characteristics. Devices of HFET type based on the AlGa*N*/*i*-Ga*N*/*n*-AlGa*N* heterostructure can operate in conditions of weak microwave signals at a frequency of 8.15 GHz.



## REFERENCES

1. X. Li, K. F. Logenbach, and W. I. Wang, *Appl. Phys. Lett.* **60**, 1513 (1992).
2. S. S. Lu and C. L. Huang, *Electron. Lett.* **30**, 823 (1994).
3. M. Asif Khan, J. N. Kuznia, D. T. Olson, *et al.*, *Appl. Phys. Lett.* **65**, 1121 (1994).
4. M. Asif Khan, A. Bhattarai, J. N. Kuznia, and D. T. Olson, *Appl. Phys. Lett.* **63**, 1214 (1993).
5. A. Wieszt, R. Dietrich, J.-S. Lee, *et al.*, in *Proceedings of European Symposium on Gallium Arsenide and Related III-V Compounds Applications* (Paris, 2000), p. 260.
6. *Oki Electric Power Transistor for Wireless Communications Achieves World's-Best Amplification Characteristics*, <http://www.oki.com/en/press/2003/z02123e.html>.
7. M. G. Cheong, K. S. Kim, C. S. Oh, *et al.*, *Appl. Phys. Lett.* **77**, 2557 (2000).
8. X. L. Sun, S. H. Goss, L. J. Brillson, *et al.*, *J. Appl. Phys.* **91**, 6729 (2002).
9. X. L. Sun, S. H. Goss, L. J. Brillson, *et al.*, *Phys. Status Solidi B* **228**, 441 (2001).
10. S. H. Goss, X. L. Sun, A. P. Young, *et al.*, *Appl. Phys. Lett.* **78**, 3630 (2001).
11. R. Armitage, Qing Yang, H. Feick, *et al.*, *Appl. Phys. Lett.* **81**, 1450 (2002).
12. S. N. Basu, T. Lei, and T. D. Moustakas, *J. Mater. Res.* **9**, 2370 (1994).
13. Z. Bougrioua, I. Moerman, N. Sharma, *et al.*, *J. Cryst. Growth* **230**, 573 (2001).
14. N. I. Kuznetsov, A. E. Nikolaev, A. S. Zubrilov, *et al.*, *Appl. Phys. Lett.* **75**, 3138 (1999).
15. H. Tang, J. B. Webb, J. A. Bardwell, *et al.*, *Solid-State Electron.* **44**, 2177 (2002).
16. R. P. Vaudo, X. Xu, A. Salant, *et al.*, *Phys. Status Solidi A* **200**, 18 (2003).
17. Z. Bougrioua, I. Moerman, L. Nistor, *et al.*, *Phys. Status Solidi A* **195**, 93 (2003).
18. Narihiko Maeda, Tadashi Saitoh, Kotaro Tsubaki, *et al.*, *Mater. Res. Soc. Symp. Proc.* **743**, L.9.3.1 (2003).
19. R. A. Keihl, P. M. Solomon, and D. J. Frank, *IBM J. Res. Dev.* **34**, 506 (1990).
20. A. V. Alekseev, A. N. Volkov, D. M. Krasovitskiĭ, *et al.*, *Izv. Vyssh. Uchebn. Zaved., Mater. Élektron. Tekh.* **1**, 32 (2001).
21. RF Patent No. 2,003,109,501/28/(010201) (August 28, 2003).

*Translated by N. Korovin*